Cranfield University

Daniel Francis

Surface strain measurement using pulsed laser shearography with fibre-optic imaging bundles

School of Engineering
PhD

Cranfield University

School of Engineering
Engineering Photonics Group

PhD Thesis

2008

Daniel Francis

Surface strain measurement using pulsed laser shearography with fibre-optic imaging bundles

Supervisors: Prof. Ralph Tatam and Dr. Stephen James

08/01/08

This thesis is submitted in partial fulfilment of the requirements
for the degree of Doctor of Philosophy

ABSTRACT

This thesis describes the development of a shearography instrument for the quantitative measurement of surface strain on dynamic test objects. Shearography is a non-contact, full-field interferometric speckle technique used for the measurement of displacement gradient. It is often used in industry for qualitative inspection of industrial components. To fully characterize the surface strain, a total of six components of displacement gradient are required. These can be measured using shearography instrumentation with at least three measurement channels. Phase measurements from each measurement channel are combined using a matrix transformation to produce the orthogonal displacement gradient measurements.

The instrument presented in this thesis possesses four measurement channels consisting of four views of the object under investigation. Images from the four views are transported to the shearing interferometer using coherent fibre-optic imaging bundles. The signals from the four views are then spatially multiplexed onto the four quadrants of a CCD camera. The optical source is a frequency doubled, pulsed Nd:YAG laser which is used to effectively ‘freeze’ the motion of the dynamic object for the duration of the laser pulse.

The optical phase difference between images recorded from two laser pulses is determined using the spatial carrier technique. This method involves introducing a carrier frequency into the recorded speckle pattern using a Mach-Zehnder interferometer. A Fourier transform is used to access the phase dependent spectral features, from which the phase distribution is calculated.

The instrument is first validated through the measurement of two static test objects. The results of these measurements are compared with modelled data and with results from a multiple-illumination-direction shearography system using a continuous-wave laser. The instrument is then used to investigate two dynamic objects; a plate rotating at 610 rpm and a speaker cone vibrating at frequencies in the range of 1 – 5 kHz.

Acknowledgements

Firstly, I would like to thank Professor Ralph Tatam and Dr. Steve James for their continual enthusiasm, guidance and support throughout the project.

I would also like to thank Dr. Tom Charrett for all his assistance in many aspects of the project, particularly in helping me get to grips with the CL programming language.

My thanks also to must go to Steve Staines for his help with all the mechanical problems I faced throughout this work.

I would like to thank Dr. Roger Groves for all his help and assistance during those difficult first months, when I was very new to the field.

I would like to thank Dackson Masiyano and Lu Zenghai for all the useful discussions on speckle, optics and the work in general.

Finally, I would like to thank all the members of the Optical Sensors Group / Engineering Photonics Group, past and present, for creating a pleasant and enjoyable working environment throughout my time in Cranfield.

Table of Contents

List of Figures

List of Tables

Symbols and abbreviations

Symbols

α	angular separation of observation positions
f	focal length
f_0	carrier frequency
γ_0	fringe modulation
I	optical intensity
i_p	illumination position
$\hat{\imath}$	illumination unit vector
J_0	Bessel function of zero order
$\mathbf{k} = (k_x, k_y, k_z)$	sensitivity vector
λ	optical wavelength
M_k	sensitivity matrix
M	optical magnification
o_p	observation position
$\hat{o}$	observation unit vector
ϕ	optical phase
ψ	random speckle phase
σ_o	objective speckle size
σ_s	subjective speckle size
t	time
θ	angle between illumination beams
(u, v, w)	displacement vector
$\partial u/\partial x$, $\partial v/\partial x$, $\partial u/\partial y$, $\partial v/\partial y$	in-plane displacement gradients
$\partial w/\partial x$, $\partial w/\partial \mathrm{y}$	out-of-plane displacement gradients
(x, y, z)	spatial coordinates
$\mathrm{d}x$, $\mathrm{d}y$	applied shear magnitudes
W	wrapping operator

Abbreviations

ASE	Amplified spontaneous emission
BS	Beamsplitter
CL	Camera lens
CCD	Charge-coupled device
DaVis	Data visualization
DLL	Dynamic link library
DOE	Diffractive optical element
DSP	Digital speckle photography
ESPI	Electronic speckle pattern interferometry
FFT	Fast Fourier transform
FSD	Frequency-guided sequential demodulation
GPIB	General purpose interface bus

GUI	Graphical user interface
He-Ne	Helium-neon
HOE	Holographic optical element
KTP	Potassium titanyl phosphate
L	Lens
LED	Light emitting diode
LabVIEW	Laboratory virtual instrument engineering workbench
M	Mirror
Matlab	Matrix Laboratory
Mch	Measurement channel
MEMS	Micro electrical-mechanical systems
MST	Minimum spanning tree
MZI	Mach-Zehnder interferometer
Nd:YAG	Neodymium: Yttrium-aluminium-garnet
ND	Neutral density
NL	Negative lens
PBS	Polarizing beamsplitter
PC	Personal computer
PCI	Peripheral component interconnect
PDV	Planar Doppler velocimetry
PTFE	Polytetraflouroethylene
PZT	Piezo-electric transducer
RPT	Regularized phase tracking
SAR	Synthetic aperture radar
SC	Spatial carrier
TIFF	Tagged image file format
TPS	Temporal phase stepped
WFF	Windowed Fourier filtering
WFR	Windowed Fourier ridges
WFT	Windowed Fourier transform

1. Introduction

Analysis of strain distributions in surfaces under an applied load is required in many branches of engineering, including mechanical, civil and aerospace. This analysis is used in the assessment of the safety, reliability and quality of engineering components such as gas turbine blades, automobile parts and composite materials. Strain is defined as the ratio of the change in length of a surface to its original length when it is deformed

$$\text{strain}\left(\varepsilon\right) = {}^{\delta L}\!\big/_{L_0} \tag{1.1}$$

Since typical strain values are often small, measurements are often given in values of microstrain, i.e. $\mu\varepsilon$ = strain x10^6.

Measurement of surface strain is often done using strain gauges. Strain gauges are actually electrical resistors which are adhered to the surface of the component at the point that is to be measured. Deformation of the component causes a change in the electrical resistance within the strain gauge. The measured resistance can be converted to a strain measurement based on the characteristics of the strain gauge. While the strain gauge offers high sensitivity measurement, it also suffers from a number of limitations. One limitation is that the strain gauge only measures the surface strain at a single point where it is attached to the component. To measure the surface strain over an area, an array of strain gauges would be required. Secondly, the measurement obtained with the strain gauge is not an exact measurement but a measurement of the strain averaged along the length of the gauge. The surface of the component to be measured often requires additional preparation before the gauge can be adhered to it. Fixing the strain gauges to the surface and soldering of the electrical connections can require skilled personnel and is often time consuming. Also, since the strain gauge is physically attached to the surface, the additional mass of the gauge may influence the result of the measurement.

Optical speckle techniques offer an attractive solution in that they are non-contact and provide a full-field measurement over the field of view of the camera. Since the discovery of laser speckle in the 1960's [1, 2], a considerable amount of research has gone into the field of speckle metrology. A range of speckle metrology techniques have been developed including electronic speckle pattern interferometry (ESPI) [3], speckle shearing interferometry (commonly known as shearography) [4, 5] and digital speckle photography (DSP) [6]. These techniques have been used to measure a wide range of parameters including:

- Out-of-plane displacement (ESPI [3])
- In-plane displacement (ESPI [7] and DSP [6])
- Derivative of displacement (shearography [5])
- Object shape (ESPI [8]) and slope (shearography [9])
- Modes of vibration (ESPI [10]) and their derivative (shearography [11])

Surface strain is a parameter that is closely related to the derivative of surface displacement. Shearography measures directly the derivative of surface displacement and is therefore an ideal technique for full-field optical strain measurement. Measurements from ESPI require numerical differentiation to determine the surface strain. Differentiation increases the error associated with the numerical strain calculations due to the fact that it amplifies any noise present within the measured phase data [12]. Another key advantage of shearography over ESPI is its resilience to vibration and rigid body motion, making it an ideal technique for use in industrial environments where it has been used experimentally for qualitative inspection [13]. To fully characterize the surface strain, measurements of six orthogonal displacement gradient components are required. It is possible to measure all of these components using shearography.

1.1 Introduction to speckle interferometry

In speckle interferometry, an optically rough test surface is illuminated with an expanded laser beam creating a laser speckle pattern in the space surrounding the illuminated region. A typical laser speckle pattern is shown in figure 1.1. The speckle pattern is optically mixed with a second coherent light field that is either another speckle pattern or a smooth light field. This produces an interferometric speckle pattern that is imaged onto a CCD (charged-coupled device) camera.

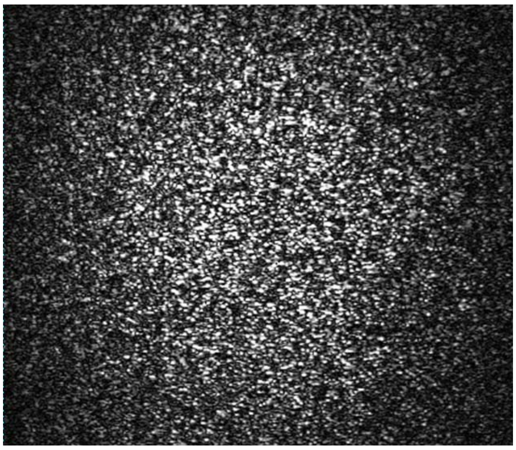

Figure 1.1 *A typical laser speckle pattern recorded by a CCD camera.*

Deformation of the test surface results in a change in the phase of the light that makes up the speckles in the pattern. This is observed as a change in the intensity of the individual speckles in the interferometric speckle pattern. When a speckle pattern recorded *before* the object is deformed is correlated with a pattern recorded *after* deformation, a two-dimensional fringe pattern is observed. These fringes are known as correlation fringes and correspond to regions on the surface experiencing equal change in displacement derivative magnitude (or displacement in the case of ESPI) between the two frames. The speckle patterns recorded before and after deformation of the object's surface are known as the reference and signal frames respectively. The correlation is commonly achieved by subtracting the signal frame from the reference frame. Typical fringe patterns obtained from a centrally loaded, out-of-plane displacement of an edge-clamped planar test object using ESPI and shearography are shown in figures 1.2(a) and 1.3(a) respectively. The plots to the right of the fringe maps show the approximate variation of displacement and displacement gradient against horizontal position for the row through the fringe map indicated by the white line. The displacement values in figure 1.2(b) are approximate values for an ESPI measurement obtained assuming a laser with a wavelength of 532 nm. Likewise, the displacement gradient values in figure 1.3(b) are approximate values for a shearography measurement assuming a laser with a wavelength of 532 nm and an applied shear of 10 mm.

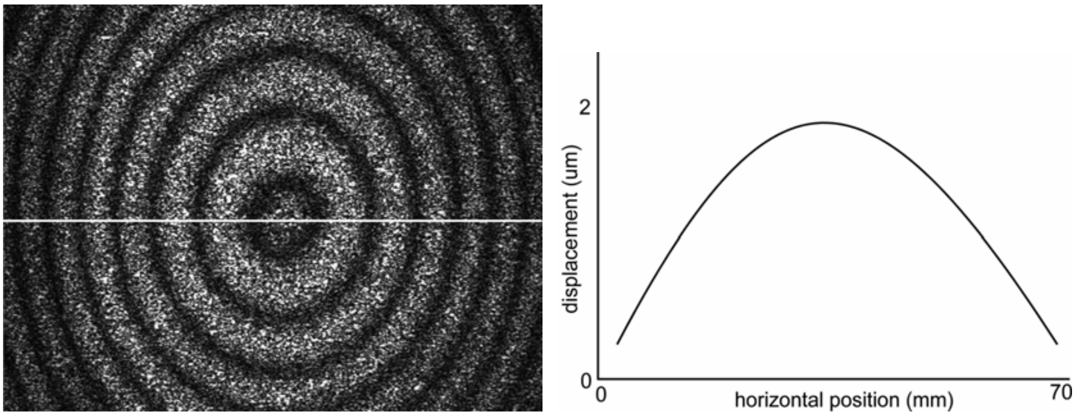

(a) **(b)**

Figure 1.2 *ESPI correlation fringes (a) and the variation of displacement against horizontal position along the white line (b).*

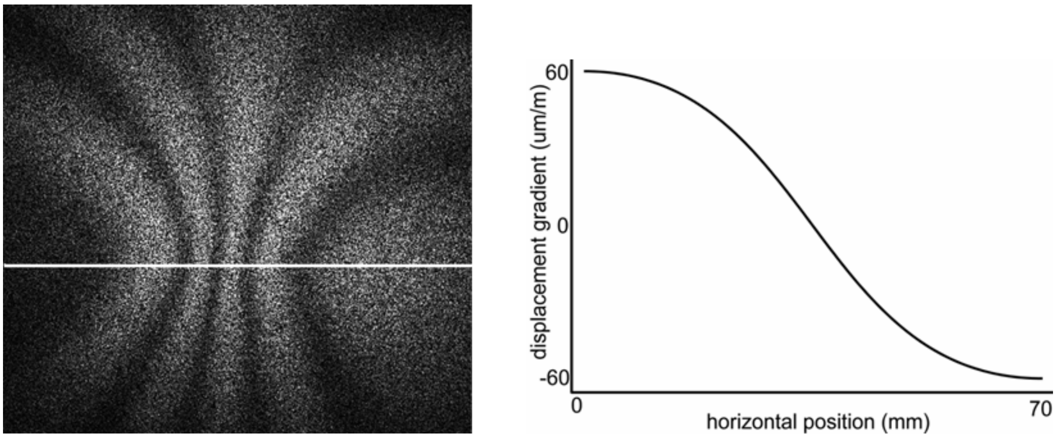

(a) **(b)**

Figure 1.3 *Shearography correlation fringes (a) and the variation of displacement against horizontal position along the white line (b).*

The component of displacement gradient that a shearography measurement is sensitive to (or displacement in the case of ESPI) is determined by the sensitivity vector. The sensitivity vector **k** is defined as the bisector of the observation vector $\hat{o}$ and the illumination vector $\hat{\imath}$. This is illustrated in figure 1.4. The figure shows a laser illuminating a test target which is viewed by a camera. The corresponding illumination and observation vectors and the sensitivity vector produced from this arrangement are also indicated. The interferometer components are omitted in this figure for clarity. A speckle interferometry fringe pattern will contain information on a single component of displacement gradient (or displacement) in the direction of the sensitivity vector. This measurement consists of contributions from the orthogonal in-plane and out-of-plane displacement gradient (or displacement) components. In order to isolate the three orthogonal components, speckle interferometry instrumentation with three measurement channels with different sensitivity vectors is required. The measurement channels can take the form of either three illumination directions and a single observation direction [14], or three observation directions and a single illumination direction [15]. The orthogonal components can be isolated from the measurements from each channel through the use of a transformation matrix based on the observation and illumination positions.

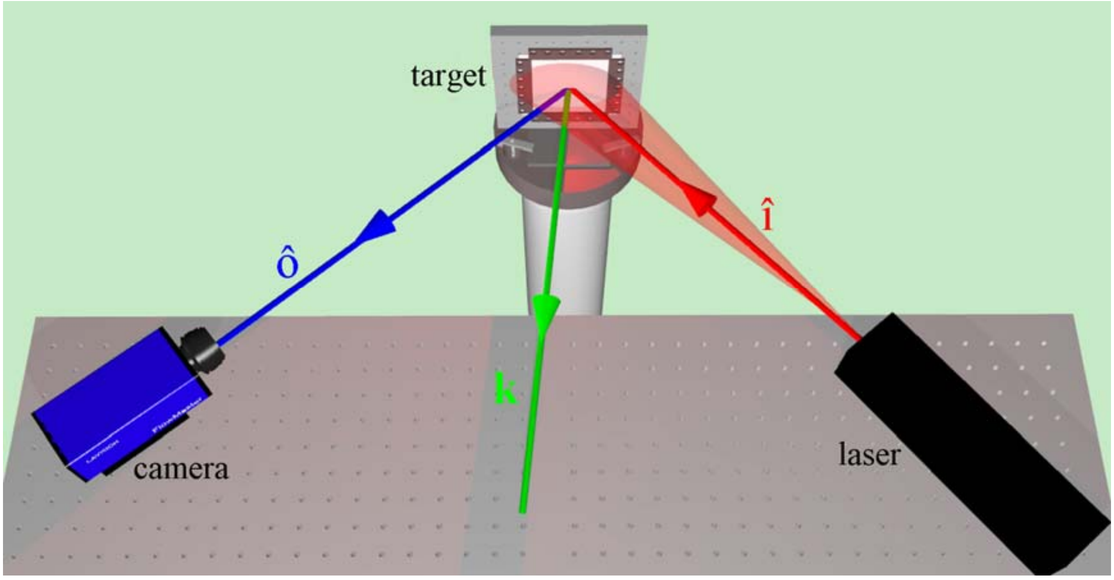

Figure 1.4 *The sensitivity vector **k** is defined as the bisector of the observation vector ô and the illumination vector î.*

1.2 Fringe analysis

The correlation fringe images obtained with speckle interferometry are arrays of numerical data whose values represent the difference in *intensity* between the signal and reference frames, at each pixel in the image. The quantitative information that is desired from a speckle interferometry measurement is actually encoded in the *phase* of the fringe pattern. The intensity at each pixel (x, y) in a correlation fringe pattern can in general be described by the equation

$$I(x,y) = I_0(x,y)\left[1+\gamma_0(x,y)\cos\left(\phi(x,y)\right)\right] \tag{1.2}$$

where $I_0(x, y)$ is the background intensity, $\gamma_0(x, y)$ is the fringe modulation and $\phi(x, y)$ is the deformation-induced local phase difference between the light reaching camera in the reference and signal frames. A necessary step towards making a measurement with speckle interferometry therefore involves a calculation of the phase variation across the image. Note that there are three unknowns in equation (1.2), $I_0(x, y)$, $\gamma_0(x, y)$ and $\phi(x, y)$. One way to determine $\phi(x, y)$ is to record at least three fringe patterns from which $\phi(x, y)$ can be calculated. This is the basic principle behind phase stepping; a commonly used method of phase analysis.

The general phase analysis process is illustrated graphically in figure 1.5. A simulated fringe pattern is shown in 1.5(a) with a plot of the intensity variation against horizontal position for the central row shown in 1.5(b). The result of most phase measurement techniques is another fringe pattern whose values are bound between –π and +π. These fringe patterns are known as wrapped phase maps. The wrapped phase map corresponding to the correlation fringe pattern in 1.5(a) is shown in 1.5(c). The plot through the central row of the wrapped phase map (figure 1.5(d)) clearly shows the fringe discontinuities that occur whenever the phase passes the values of +π or –π.

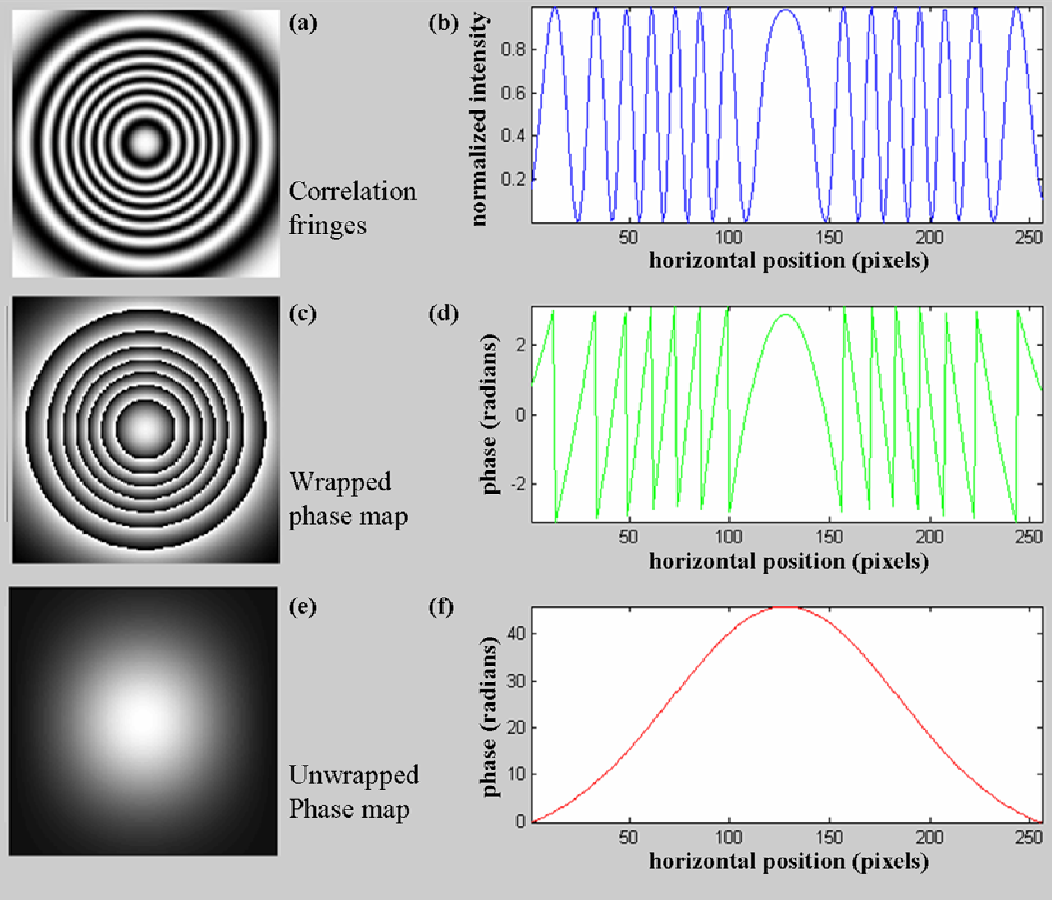

Figure 1.5 *(a) A typical correlation fringe pattern with a plot along the central row (b). The corresponding wrapped phase map is shown in (c) along with the corresponding central row (d). The unwrapped phase is shown in (e) with the central row shown in (f).*

The 2π phase discontinuities need to be removed to obtain the continuous result that is required to determine the measurand. This process is known as phase unwrapping. The unwrapped phase map corresponding to the wrapped phase map in figure 1.5(c) is shown in figure 1.5(e) along with the plot of the central row in figure 1.5(f). In this simple, noise-free example, a row-by-row phase unwrapping algorithm can be used. Speckle interferometry results, however, usually possess high frequency noise which may cause breaks in the 2π fringes in the calculated wrapped phase maps. Also, breaks in the fringes may occur, for example, by holes in the test object. In these circumstances, a more sophisticated unwrapping algorithm is required.

Figure 1.5 was produced using Matlab assuming a point out-of-plane loading at the centre of a flat plate. The illumination and observation directions were assumed to be collinear in this example. This results in an unwrapped phase distribution that represents purely out-of-plane displacement.

1.3 Aims of the work presented in this thesis

Shearography is typically used for qualitative evaluation of components from, for example, the automotive and aerospace industries [13] where it has become an important tool for qualitative non-destructive inspection. The addition of multiple measurement channels [16-18] has converted shearography from a tool for *qualitative* analysis of components to a tool capable of *quantitative* surface strain measurement. Previous shearography instrumentation developed for surface strain measurement possessed multiple measurement channels comprising three illumination directions and a single observation direction. These systems have been restricted to measurements of objects under static loading conditions, where there is no motion of the object's surface, apart from the applied deformation, between recording of the signal and reference frames.

The aim of the work presented here is, therefore, to develop a shearography instrument capable of quantitative surface strain measurement from dynamic objects. To achieve this, a novel instrument is proposed which consists of four observation directions and a single illumination direction. The additional measurement channel is beneficial because it provides redundancy of measurement and the instrument can still be used if one channel is blocked [19]. Fibre-optic imaging bundles are used to transport images from the four views to the shearing interferometer after which they are spatially multiplexed onto the four quadrants of the CCD camera. The combination of multiple observation directions and the ability to spatially multiplex the signals allows simultaneous acquisition of data from the four measurement channels. The use of a pulsed Nd:YAG laser source allows the monitoring of dynamic objects by effectively 'freezing' the motion of the object for the duration of the laser pulse. The development of the instrument is discussed in chapter 4.

One of the main obstacles to overcome is to determine a method of phase analysis that is suitable for dynamic measurements. When dynamic measurements are made, two images are recorded from two laser pulses that freeze the motion of the object at two points in time. The two images are correlated to give a measurement of the difference in displacement derivative between the two points. The phase variation must therefore be determined from just two images. The traditional method of phase analysis, temporal phase stepping, relies on the recording of a set of at least four images, and is therefore unsuitable for use in the measurement of dynamic objects. A number of phase analysis techniques were investigated with a view to solving this problem, and are discussed in chapter 5.

1.4 Structure of the thesis

The second chapter of this thesis examines the theoretical aspects of the principal speckle interferometry techniques of ESPI and shearography. The theory of surface strain measurement using multiple component shearography is described in this chapter. The use of speckle interferometry to measure the shape and slope of an object and to analyze vibrating surfaces is also discussed.

The third chapter focuses on the wide range of phase analysis techniques that have been developed and used in interferometry. In particular, the temporal phase stepping technique and the spatial carrier technique are investigated. Filtering techniques used to improve the quality of the fringe patterns are also discussed. Other techniques involving spatial phase stepping, skeletonizing and the windowed Fourier transform are also reviewed.

The fourth chapter describes the development of the multiple-viewing-direction, pulsed laser shearography system. The pulsed laser system is described, along with the viewing apparatus, fibre-bundles and the interferometer optics. The image acquisition software is explained and the processing scheme required to obtain the orthogonal displacement gradient components is presented.

The fifth chapter presents the results of the experimental investigations into some of the various phase analysis techniques. The development of phase stepping software for a single channel, laser diode based shearography system is described. Various phase-stepping algorithms and filtering methods are investigated with the aim of reducing noise in the phase measurements.

This chapter also presents results from an investigation of a diffractive optical element (DOE) with the potential to be used in a spatial phase stepping interferometer. Phase maps generated using the spatial carrier technique are also presented. Two methods of carrier fringe generation are investigated. One involves longitudinal displacement of the illuminating beam and the other is based on a Mach-Zehnder shearing interferometer. A comparison of two phase unwrapping algorithms is also presented using experimentally generated wrapped phase maps.

The sixth chapter presents the results of displacement derivative calculations for two statically loaded test objects. One is a flat aluminium plate clamped around the perimeter that is centrally loaded by turning a micrometer screw mounted on the rear of the plate. The deformation applied to this object is predominantly out-of-plane. The other object investigated is a flat Perspex plate that is deformed by turning a screw vertically through a horizontal slot in the plate. The deformation applied to this object is both in-plane and out-of-plane.

Perspective distortion, arising from the off-axis viewing arrangement, introduces errors into the measured phase variations. This is corrected for using an image ‘dewarping’ algorithm, which is discussed in this chapter.

Two methods for determining the variation of the sensitivity vector across the field of view of the camera are presented in chapter 6. One method involves the measurement of the observation and illumination positions. The other method involves calculation of the observation vectors from image dewarping mapping coefficients.

The seventh chapter presents results obtained from the measurement of two dynamic objects. The first object is a PTFE plate that was placed on a lathe rotating at 610 rpm. The rotation rate of the lathe was synchronized with the repetition rate of the pulsed laser so that images could be recorded of the object in the same location but on subsequent rotations. The second object is a speaker cone vibrating at a range of frequencies from 1.9 kHz to 4.5 kHz. Measurements from the speaker were made with the laser operating with a pulse separation of 1.6 μs.

The final chapter is dedicated to conclusions from the project and suggestions for further work in the area.

References

[1] Rigden J. D. and Gordon E. I, ‘The granularity of scattered optical maser light’, *Proc. IRE*, **50**, 6564-74 (1962).
[2] Oliver B. M. 'Sparkling spots and random diffraction', *Proc. IEEE*, **51**:1, 220-1 (1963).
[3] Leendertz J. A. and Butters J. N, ‘Speckle pattern and holographic techniques in engineering metrology’, *Opt. Laser Technol.* **3**, 26-30 (1971).
[4] Leendertz J. A. and Butters J. N, ‘An image-shearing speckle-pattern interferometer for measuring bending moments’, *J. Phys. E.* **6**, 1107-10 (1973).
[5] Hung Y. Y, ‘Shearography: a new optical method for strain measurement and non-destructive testing’, *Opt. Eng.* **21**:3, 391-5 (1982).
[6] Sjödahl M, ‘Digital speckle photography’ in *Digital speckle interferometry and related techniques*, ed. Rastogi P. K, Wiley (2001).
[7] Moore A. J. and Tyrer J. R, ‘An electronic speckle pattern interferometer for complete in-plane displacement measurement’, *Meas. Sci. Technol.* **1**, pp 1024-30, (1990).
[8] Tatam R. P, Davies J. C, Buckberry C. H. and Jones J. D. C, ‘Holographic surface contouring using wavelength modulation of laser diodes’, *Opt. Laser Technol.* **22**:5, 317-21 (1990).
[9] Huang J-R, Ford H. D, Tatam R. P, ‘Slope measurement by two-wavelength electronic shearography’, *Opt. Lasers Eng.* **27**, 321-33 (1997).
[10] Løkberg O. J. and Høgmoen K, ‘Vibration phase mapping using electronic speckle pattern interferometry’, *Appl. Opt.* **15**:11, 2701-4, (1976).
[11] Valera J. D. R and Jones J. D. C, ‘Vibration analysis by modulated time-averaged speckle shearing interferometry’, *Meas. Sci. Technol.* **6**, 965-70 (1995).
[12] Moore A. J. and Tyrer J. R, ‘Two-dimensional strain measurement with ESPI’ *Opt. Lasers Eng.* **24** 381-402 (1996).
[13] Kalms M. and Osten W, ‘Mobile shearography system for the inspection of aircraft and automotive components’, *Opt. Eng.* **42**:5, 1188-96 (2003).
[14] James S. W, Groves R. M, and Tatam R. P, ‘Surface strain characterization using time-division multiplexed 3D shearography’, *Proc. SPIE*, **4101**, 384-93 (2001).
[15] Groves R. M, James S. W. and Tatam R. P, ‘Multi-component shearography using optical fibre imaging-bundles’, *Proc. SPIE,* **5144**, 513-20 (2003).
[16] James S. W. and Tatam R. P, ‘Time-division-multiplexed 3D shearography’, *Proc. SPIE*, **3744**, 394-403 (1999).
[17] Waldner S and Brem S, ‘Compact shearography system for the measurement of 3D deformation’, *Proc SPIE*, **3745**, 141-47 (1999).
[18] Kästle R, Hack E. and Sennhauser U, ‘Multiwavelength shearography for quantitative measurements of two-dimensional strain distributions’, *Appl. Opt.* **38**:1, 96-100 (1999).
[19] Groves R. M, James S. W. and Tatam R. P, ‘Multi-component shearography employing four measurement channels’, *Proc. SPIE*, **4933**, 135-40.

2. Speckle Interferometry

Since its first demonstration, speckle interferometry has become an important diagnostic tool and has been used in many applications including the measurement of strain [1], displacement [2], vibration [3] and shape [4]. Its rise in prominence has coincided with the development of optoelectronic components such as CCD cameras, lasers and optical fibres, as well as the improvement of personal computers [5]. This chapter describes the laser speckle phenomenon, as well as the principal techniques of electronic speckle pattern interferometry (ESPI) and speckle shearing interferometry (shearography). Some of the applications that speckle interferometry has been used for are also discussed.

2.1 Laser speckle

The phenomenon of laser speckle was realized shortly after the invention of the laser. It was described as a 'granular' [6] or 'sparkling' [7] pattern of bright and dark regions. It was considered by Nobel laureate Dennis Gabor as the 'Enemy Number One' of holography [8], since speckle noise marred the quality of the holographic reconstruction. Most of the early research into laser speckle was therefore aimed at its reduction. It was later revealed that the speckle pattern contains important information about the scattering surface.

A speckle pattern (see figure 1.1) is formed whenever light from a coherent source illuminates an optically rough surface. A surface is optically rough if its surface height deviations are greater than the wavelength of the illuminating light [9]. When light illuminates an optically rough surface, each point in the illuminated region scatters light according to the topography of the surface, as shown in figure 2.1. This is known as a diffuse reflection. If it is coherent, the light scattered from different points in the illuminated region will combine producing an interference pattern. The speckle pattern is therefore the sum of the interference from all points in the illuminated region.

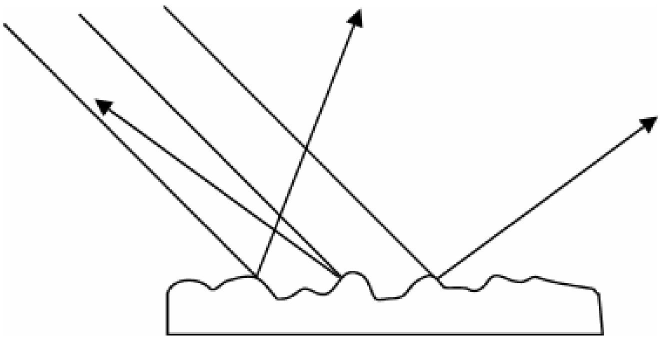

Figure 2.1 *A diffuse reflection produced by light scattering from an optically rough surface.*

A speckle pattern formed in this manner exists in all of the surrounding space and can be observed on a viewing screen placed some distance from the illuminated area.

The speckle pattern seen on the screen is known as an objective speckle pattern and its formation is illustrated in figure 2.2(a). The average speckle size in an objective speckle pattern is related to the diameter of the illuminated region D and the distance between the scattering surface and the viewing screen L by the equation [9]

$$\langle \sigma_o \rangle \approx \frac{L\lambda}{D} \tag{2.1}$$

where λ is the wavelength of the illuminating beam.

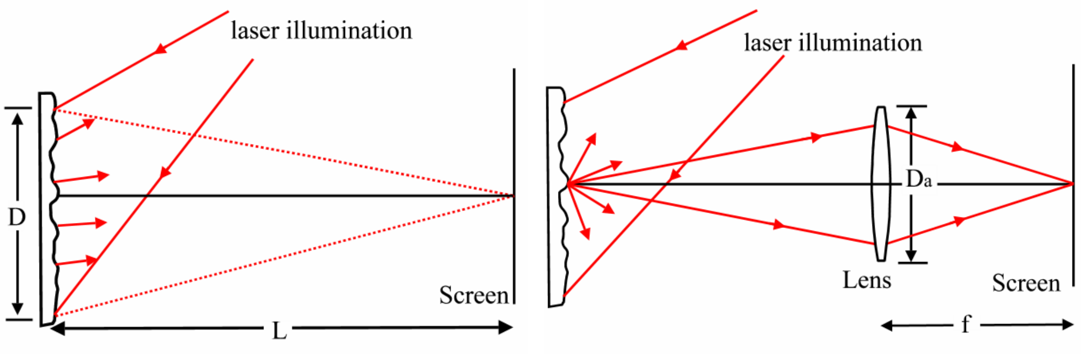

(a) **(b)**

Figure 2.2 *The formation of objective (a) and subjective (b) speckle patterns.*

If the speckle pattern is imaged onto the screen by a lens, a subjective speckle pattern is formed. Light scattered from each point on the object surface is imaged as a spot of light on the screen. The pattern on the screen is the sum of all the interference patterns produced by all illuminated points on the scattering surface that have been imaged by the lens. The size of each spot is determined by a property of the lens known as the point spread function. The point spread function is a measure of a lens' ability to image a point. Because a point source emits diverging spherical waves, a lens would need to produce converging spherical waves to perfectly image a point. A lens can only image with converging waves that are partly spherical due to its finite aperture. The resulting image is, if diffraction limited, an Airy disk spot which interferes with spots originating from other regions of the surface to form the speckle pattern. The average speckle size in a subjective speckle pattern is dependent on the focal length f and aperture diameter D_a of the imaging lens and is given by [9]

$$\langle \sigma_s \rangle \approx \frac{f\lambda}{D_a} \tag{2.2}$$

An important point to note is that the speckle size can be adjusted by varying the aperture size. This property can be important in speckle interferometry.

2.2 Electronic speckle pattern interferometry

Electronic speckle pattern interferometry (ESPI), also known as TV holography, was developed almost simultaneously in the early 1970's by research groups working in California [10], Austria [11] and the United Kingdom [2]. ESPI was the first interferometric speckle technique to use an electronic recording medium, thereby eliminating the wet processing that had been so problematic in conventional holographic interferometry. The early systems used cameras based on a vidicon tube [2] but modern day systems use semiconductor based CCD cameras or CMOS (complementary metal-oxide-semiconductor) cameras.

2.2.1 Out-of-plane ESPI

A typical ESPI system that is predominantly sensitive to out-of-plane displacement is shown in figure 2.3. Light from the laser is collimated and divided into illumination and reference beams at the first beamsplitter. The spatial filters are used to provide smooth illumination and reference beams by filtering out high frequency noise caused by dust and dirt present on the optical components. The illumination beam is expanded to illuminate the region of interest on the target's surface. The scattered light is imaged by the collecting lens and forms a subjective speckle pattern on the CCD sensor. Light from the reference beam combines with the speckle pattern to produce an interferometric speckle pattern on the CCD array. There will be a small amount of in-plane sensitivity due to the illumination and observation directions not being perfectly collinear. The angle between the observation and illumination directions is exaggerated in figure 2.3 for clarity.

In ESPI, the intensity of the reference beam needs to be approximately 3-4 times the object beam in order to obtain high contrast fringes. Light is scattered from the test object in all directions and therefore only a small amount of the object beam is returned to the camera. This can often be much less than 20 – 30% of the reference beam. For this reason beamsplitters with a split ratio of 90:10 are often used with 90% of the light going into the object beam and 10% going into the reference beam. The iris in front of the collecting lens is used to control the size of the speckles (equation (2.2)) so that the speckles match the size of the camera pixels. The reference beam should be made conjugate to the object beam in the recombining beamsplitter. That is, the image of the reference beam spatial filter aperture should appear to diverge from the centre of the imaging lens [12]. As with all interferometric systems, the optical path difference between the interfering beams needs to be less than the coherence length of the light source. For systems possessing sources with short coherence lengths and/or large object distances, a delay line can be introduced into the reference arm.

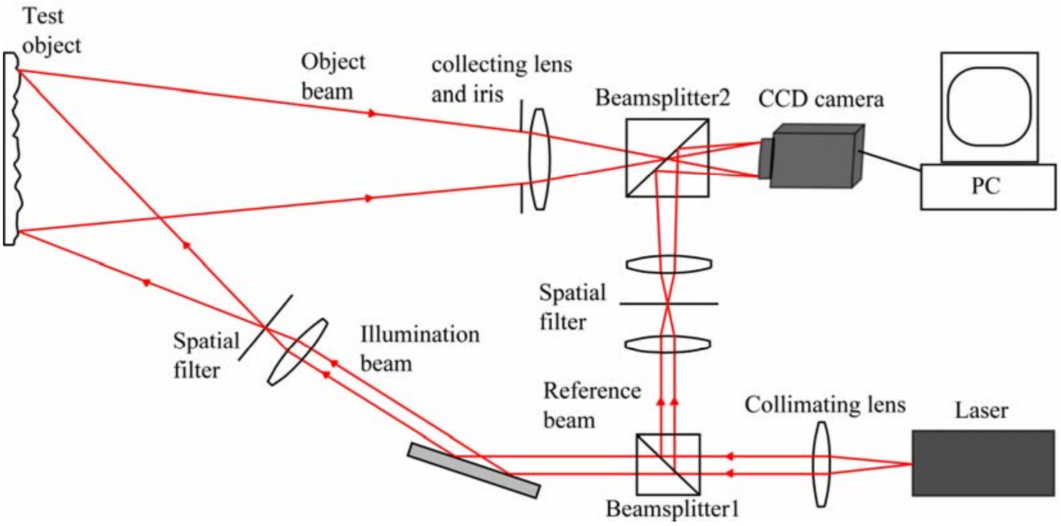

Figure 2.3 *A typical ESPI system predominantly sensitive to out-of-plane displacement [14].*

The intensity of the interferometric speckle pattern recorded by the CCD camera can be represented by [13]

$$I_1(x,y) = a_r^2(x,y) + a_o^2(x,y) + 2a_r(x,y)a_o(x,y)\cos\left(\Delta\psi(x,y)\right) \quad (2.3)$$

where a_r and a_o are the complex amplitudes of the reference and object beams respectively, $\Delta\psi$ is the phase difference between the reference and object beams and x and y are the spatial coordinates of the CCD sensor. After the target is deformed, the new interferometric speckle pattern can be expressed by [13]

$$I_2(x,y) = a_r^2(x,y) + a_o^2(x,y) + 2a_r(x,y)a_o(x,y)\cos\left(\Delta\psi(x,y) + \phi(x,y)\right) \quad (2.4)$$

where $\phi(x, y)$ is the phase change due to the displacement of the target. The two speckle patterns are subtracted to obtain

$$I_S = I_2 - I_1 = 2a_r a_o\left(\cos(\Delta\psi) - \cos(\Delta\psi + \phi)\right) \quad (2.5)$$

where the x, y dependencies have been dropped for clarity. A trigonometric identity is used to obtain

$$I_S = 4a_r a_o \sin\left(\Delta\psi + \frac{\phi}{2}\right)\sin\left(\frac{\phi}{2}\right) \quad (2.6)$$

For display, the signal is rectified so that negative values are represented correctly. The first term in equation (2.6) represents the background intensity and the second term, $\sin(\Delta\psi + \phi/2)$ represents the random speckle noise in the image. The final term, $\sin(\phi/2)$ represents a modulation in intensity where the brightness is zero whenever the condition

$$\phi = 2m\pi \qquad m = 0,1,2.... \quad (2.7)$$

is satisfied, and the brightness is a maximum whenever the condition

$$\phi = (2m+1)\pi \tag{2.8}$$

is satisfied. The resulting subtracted image results in a correlation fringe pattern where the fringes represent contours of constant phase difference. The out-of-plane displacement is given by [14]

$$w = \frac{m\lambda}{2} \tag{2.9}$$

The difference in out-of-plane displacement between adjacent fringes is equal to half the wavelength of the illuminating light. The evolution of the correlation fringes with deformation can be observed in quasi-real time if static frame subtraction is used. This involves saving the reference frame in an image buffer and continuously subtracting the reference frame from subsequently grabbed images. In this way, fringes will continue to be observed until the speckle patterns become decorrelated. Speckle decorrelation occurs when the speckles in the current frame are no longer located at the same point on the detector as their equivalent speckle in the reference frame. Speckle decorrelation can occur due to vibration or other environmental disturbances or if the displacement of the object is too great. An example of fringes generated with a predominantly out-of-plane displacement sensitive ESPI system was shown in figure 1.2(a).

2.2.2 In-plane ESPI

An ESPI configuration that is sensitive to in-plane displacements is shown in figure 2.4. The laser beam is divided into two beams which both illuminate the region of interest on the target. Light from the two object beams combine to produce an interferometric speckle pattern, therefore negating the need for a separate reference beam. If the incidence angle of the two object beams is equal and opposite then the out-of-plane displacement component is cancelled out and the system is sensitive purely to in-plane displacement. The in-plane displacement in the x direction is given by [14]

$$u = \frac{m\lambda}{2\sin\theta} \tag{2.10}$$

where θ is the incidence angle of the object beams with respect to the optical axis. In order to obtain the in-plane displacement in the y direction, the experimental arrangement needs to be rotated by 90°. A system that can measure the two in-plane components simultaneously was developed by Moore and Tyrer [15] and involves a configuration with four illumination beams. Two of the illumination beams were located in the x, z plane and the other two were located in the y, z plane.

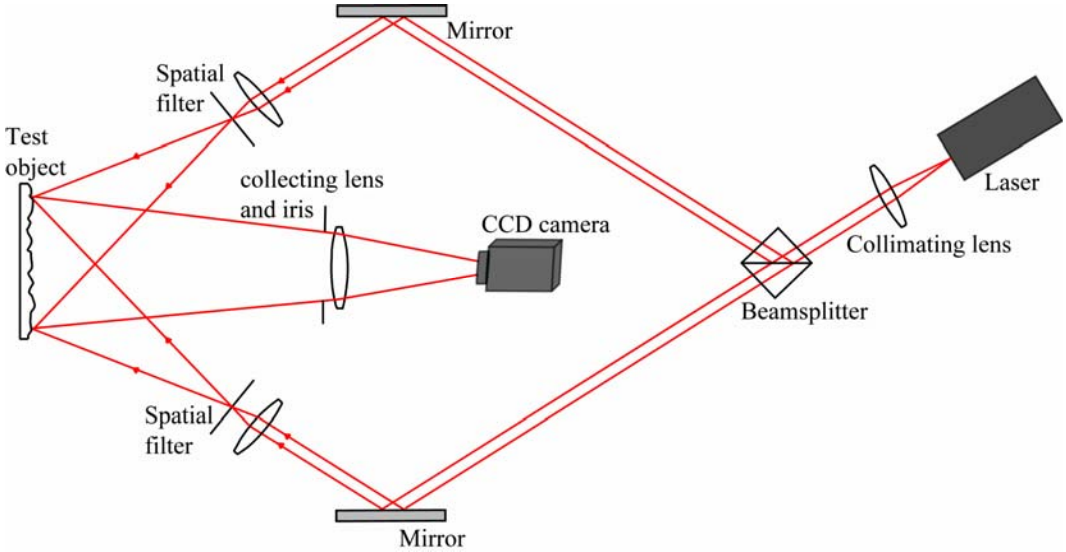

Figure 2.4 *An ESPI configuration that is sensitive to in-plane displacement [14].*

2.2.3 Multi-component ESPI

The three displacement components *u*, *v* and *w* can be isolated using an ESPI configuration with at least three object beams. The surface strain of the object under investigation can be calculated from the three displacement components but requires a numerical differentiation of the results obtained. Winther [16] measured the surface strain of a clamped pipe using an ESPI system similar to the out-of-plane configuration shown in figure 2.3, with three object beams and one reference beam. A smooth reference beam was combined with light from three object beams arranged around the target which could be selected independently. Yang and Ettemeyer [1] also discuss the application of ESPI to the measurement of three-dimensional surface strain. Their system is the basis of a commercial instrument available from Dantec dynamics.

Huang *et al* [17] used an ESPI system similar to the in-plane configuration shown in figure 2.4. One of the object beams was fixed and possessed a phase modulating device. Three other object beams are selected sequentially using a rotating mirror and combined with the fixed object beam at the target's surface. The *u*, *v* and *w* displacement components were determined from the phase measurements and the locations of the object beams. The non-fixed object beams were located at the three vertices of a triangle.

2.2.4 Fibre-optic ESPI

The use of optical fibre components in ESPI can provide a number of advantages [3, 18, 19]. Spatial filtering is automatic when single mode fibres are used which negates the need for the often tricky alignment of the bulk spatial filters shown in the previous configurations. The optical fibres can also easily be positioned at the desired locations for illumination. Also, when used in conjunction with laser diodes, compact systems can be built which do not need to be mounted on optical tables.

A fibre-optic ESPI system for out-of-plane displacement measurement is shown in figure 2.5 [3]. The input face of the optical fibre can form a conjugate point with the output of the laser, so to prevent reflections from the cleaved fibre end damaging the laser, a Faraday isolator is placed in the collimated beam path. The polarization state controller is used to ensure that the polarization states of the reference and object beams are the same. It consists of a series of three rings around which the fibre is coiled. The rings act as the fibre-optic equivalents of half and quarter wave plates [20]. The cylindrical piezoelectric transducer (PZT) in the reference arm serves as a phase modulator. This can be used to facilitate phase stepping which is used to calculate the phase change ϕ due to deformation of the object. The phase stepping technique is described in more detail in the chapter 3. The neutral density (ND) filter is used to attenuate the light in the reference beam in order to match the intensities of the reference and object beams.

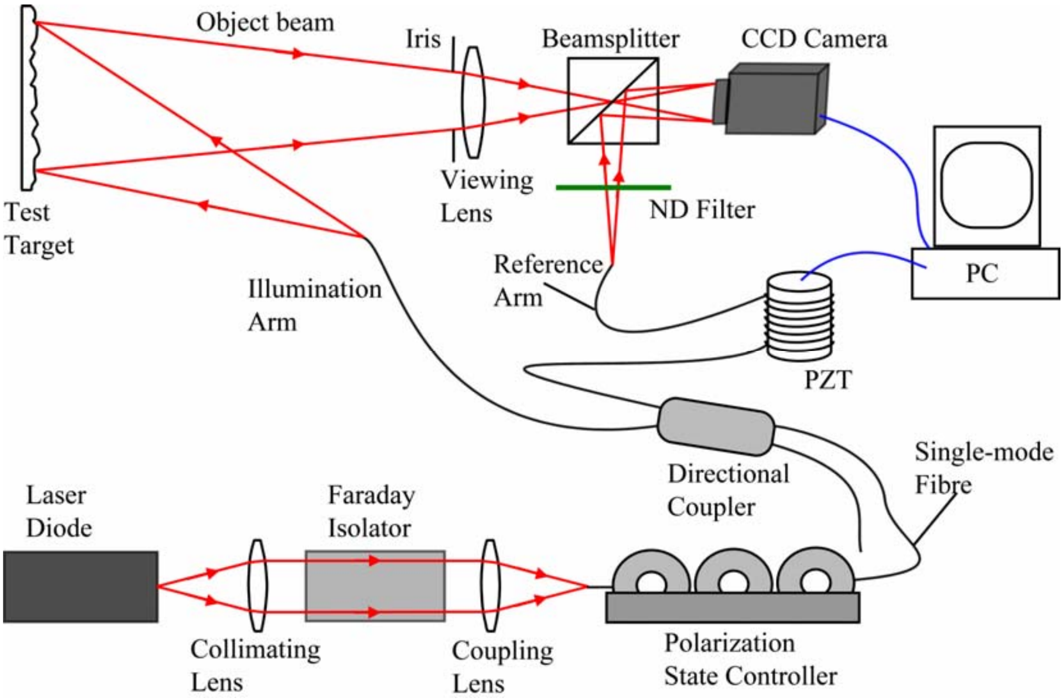

Figure 2.5 *An out-of-plane displacement sensitive fibre-optic ESPI system [3].*

2.3 Shearography

Speckle shearing interferometry, often termed ‘shearography’, was developed as an offshoot of ESPI in the early 1970’s [21]. Shearography is sensitive to the derivative of displacement, unlike ESPI which measures displacement. Unlike ESPI in its out-of-plane configuration, shearography does not utilize a smooth reference beam. Instead, the interferometric speckle pattern is produced by optically mixing the speckle pattern formed by the illuminating the object with a displaced (sheared) version of itself. The combination of sheared images means that the sensitivity of a shearography system is to the displacement difference of points on the target separated by the shear distance. If the shear is small, the displacement difference approximates to the displacement gradient. The image shear can be introduced in a number of ways, such as the image shearing camera [22-25], in which one half of the imaging lens is covered by a glass wedge that shears the image with respect to the other half. Other methods include the use of a Ronchi phase grating [26] or a diffractive optical element used in combination with ground glass [27, 28]. The most common method of image shearing is to use a Michelson interferometer where the mirror in one of the interferometer arms is tilted at a slight angle.

2.3.1 Single measurement channel shearography

Qualitative evaluation of single component of displacement gradient can be achieved with a shearography system with one illumination direction and one observation direction. A schematic showing a shearography system sensitive predominantly to out-of-plane displacement gradient is shown in figure 2.6.

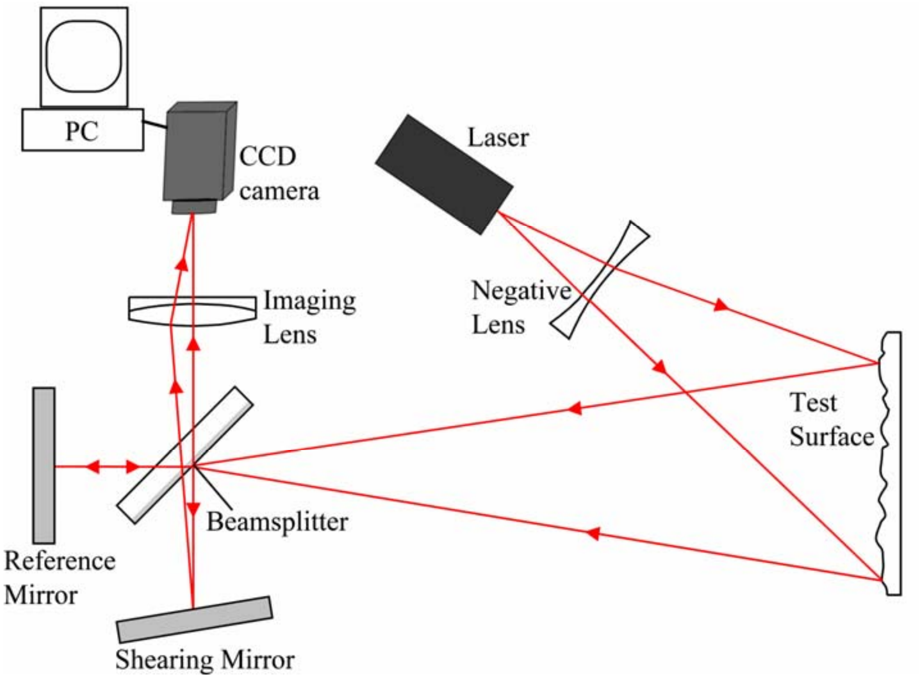

Figure 2.6 *Shearography arrangement based on a Michelson interferometer.*

Light from the laser is expanded to illuminate the region of interest on the test surface. The scattered light forms a speckle pattern which is imaged through the Michelson interferometer onto the CCD camera. The tilted mirror shears the image relative to the reference mirror so that two laterally displaced speckle patterns are imaged on the camera. Light at each pixel in the camera array is therefore made up of light that was reflected from two points on the scattering surface. This results in an interferometric speckle pattern across the CCD array. Correlation of images recorded before and after object deformation result in a fringe pattern where the fringes represent a locus of points of equal displacement gradient.

Consider a point *P* located at position (x, y, z) on the object's surface, as shown in figure 2.7. Light from the source $S(x_S, y_S, z_S)$ is scattered from *P* and is imaged onto the detector $D(x_D, y_D, z_D)$ via the reference mirror. After the object has been deformed, the point *P* is located at $P'(x+u,\ y+v,\ z+w)$, where $(u,\ v,\ w)$ is the displacement vector at the point *P*. The coordinate system that is used is also shown in figure 2.7. The origin of this coordinate system is located on the target surface at the centre of the field of view of the camera.

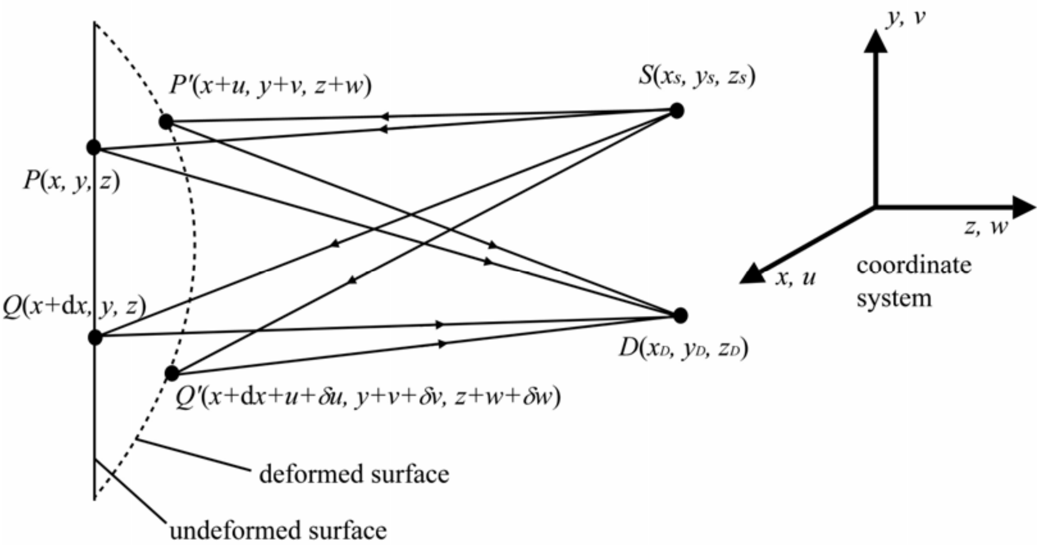

Figure 2.7 *Diagram showing the optical paths between the source S and detector D for two points on the object's surface, P and Q, before and after object deformation. The coordinate system shows that u, v and w are the displacement components in the x, y and z directions respectively.*

The change in optical path length for *P* due to the deformation is given by

$$\Delta_P = \left(SP' + P'D\right) - \left(SP + PD\right) \tag{2.11}$$

where [22]

$$\begin{aligned}
SP &= \left(\left(x-x_S\right)^2 + \left(y-y_S\right)^2 + \left(z-z_S\right)^2\right)^{1/2} \\
PD &= \left(\left(x-x_D\right)^2 + \left(y-y_D\right)^2 + \left(z-z_D\right)^2\right)^{1/2} \\
SP' &= \left(\left(x+u-x_S\right)^2 + \left(y+v-y_S\right)^2 + \left(z+w-z_S\right)^2\right)^{1/2} \\
P'D &= \left(\left(x+u-x_D\right)^2 + \left(y+v-y_D\right)^2 + \left(z+w-z_D\right)^2\right)^{1/2}
\end{aligned} \tag{2.12}$$

using a binomial expansion and taking only the first order terms we obtain [22, 29]

$$\Delta_P = \left(\frac{x-x_D}{R_D} + \frac{x-x_S}{R_S}\right)u + \left(\frac{y-y_D}{R_D} + \frac{y-y_S}{R_S}\right)v + \left(\frac{z-z_D}{R_D} + \frac{z-z_S}{R_S}\right)w \tag{2.13}$$

where

$$R_D = \left(x_D^2 + y_D^2 + z_D^2\right)^{1/2} \qquad \text{and} \qquad R_S = \left(x_S^2 + y_S^2 + z_S^2\right)^{1/2} \tag{2.14}$$

Substituting the relationships

$$A = \frac{x - x_D}{R_D} + \frac{x - x_S}{R_S} \qquad B = \frac{y - y_D}{R_D} + \frac{y - y_S}{R_S} \qquad \text{and} \quad C = \frac{z - z_D}{R_D} + \frac{z - z_S}{R_S} \tag{2.15}$$

into equation (2.14) we obtain

$$\Delta_P = Au + Bv + Cw \tag{2.16}$$

The point that is imaged onto the detector via the shearing mirror and combines with light scattered from point P is located at $Q(x+\mathrm{d}x, y, z)$, where $\mathrm{d}x$ is the magnitude of the image shear. After the object has been deformed, the point Q is located at $Q'(x+\mathrm{d}x+u+\delta u, y+v+\delta v, z+w+\delta w)$, where $u+\delta u$, $v+\delta v$ and $w+\delta w$ are the x, y and z components of the displacement of the surface at the point Q. The change in optical path length for Q due to the deformation is found in the same way as before

$$\Delta_Q = A\left(u + \delta u\right) + B\left(v + \delta v\right) + C\left(w + \delta w\right) \tag{2.17}$$

The relative optical path between the two points is found by subtracting equations (2.16) and (2.17)

$$\Delta_Q - \Delta_P = A\delta u + B\delta v + C\delta w \tag{2.18}$$

The relative phase difference between the two points is

$$\Delta\phi = \frac{2\pi}{\lambda}\left(A\delta u + B\delta v + C\delta w\right) \tag{2.19}$$

which can be written as

$$\Delta\phi = \frac{2\pi}{\lambda}\left(A\frac{\delta u}{\mathrm{d}x} + B\frac{\delta v}{\mathrm{d}x} + C\frac{\delta w}{\mathrm{d}x}\right)\mathrm{d}x \tag{2.20}$$

If the shear $\mathrm{d}x$ is small, the displacement differences approximate to the displacement gradient and equation (2.20) can be written as

$$\Delta\phi = \frac{2\pi}{\lambda}\left(A\frac{\partial u}{\partial x} + B\frac{\partial v}{\partial x} + C\frac{\partial w}{\partial x}\right)\mathrm{d}x \tag{2.21}$$

This approximation will introduce some uncertainty into the measurement of the displacement derivative. This uncertainty is reduced for smaller shear magnitudes.

The terms A, B and C are dependent on the observation and illumination positions and are equivalent to the x, y and z components of the sensitivity vector $\mathbf{k} = (k_x, k_y, k_z)$. The sensitivity vector was introduced in chapter 1 and is defined as the bisector of the observation and illumination vectors

$$\Delta\phi = \frac{2\pi}{\lambda}\left(k_x\frac{\partial u}{\partial x} + k_y\frac{\partial v}{\partial x} + k_z\frac{\partial w}{\partial x}\right)\mathrm{d}x \tag{2.22}$$

If the observation and illumination positions lie in the x, z plane and the region of the object that is imaged by the camera is small compared to the source to object and object to camera distances then the phase difference can be represented by [22]

$$\Delta\phi = \frac{2\pi}{\lambda}\left(\sin\theta\frac{\partial u}{\partial x} + (1+\cos\theta)\frac{\partial w}{\partial x}\right)\mathrm{d}x \tag{2.23}$$

where θ is the angle between the illumination and observation directions. Equivalently, if the observation and illumination positions lie in the y, z plane, then the phase is given by

$$\Delta\phi = \frac{2\pi}{\lambda}\left(\sin\theta\frac{\partial v}{\partial x} + (1+\cos\theta)\frac{\partial w}{\partial x}\right)\mathrm{d}x \tag{2.24}$$

If the $\sin\theta$ term in the above equations is made small, by making the observation and illumination directions close to collinear, then the sensitivity to the in-plane displacement gradient component becomes very small and the system is sensitive only to the out-of-plane displacement gradient component. In this case, the out-of-plane displacement derivative is given by

$$\frac{\partial w}{\partial x} = \frac{\lambda\Delta\phi}{4\pi\mathrm{d}x} \tag{2.25}$$

To isolate the in-plane displacement gradient component, a configuration with two symmetrical illumination paths, similar to the ESPI system shown in figure 2.4, can be used [30]. The processing is different to the in-plane ESPI case though. In shearography, subtracting phase measurements recorded with the two beams results in the out-of-plane component being cancelled leaving only the in-plane component. If the illumination beams lie in the x, z plane, the in-plane displacement derivative is given by

$$\frac{\partial u}{\partial x} = \frac{\lambda\left(\Delta\phi_{+\theta} - \Delta\phi_{-\theta}\right)}{4\pi\sin\theta\mathrm{d}x} \tag{2.26}$$

The $\partial v/\partial x$ component can be isolated in a similar way using a configuration that is rotated by 90° about the optical axis.

In the case of shear applied in the y-direction, the out-of-plane displacement gradient is given by

$$\frac{\partial w}{\partial y} = \frac{\lambda \Delta\phi}{4\pi \mathrm{d}y} \tag{2.27}$$

and for the in-plane sensitive configuration, the in-plane displacement gradient component is given by

$$\frac{\partial u}{\partial y} = \frac{\lambda\left(\Delta\phi_{+\theta} - \Delta\phi_{-\theta}\right)}{4\pi \sin\theta \mathrm{d}y} \tag{2.28}$$

<u>2.3.2 Multiple component shearography</u>

When the illumination and observation positions do not both lie in the x, z or y, z planes, as described above, then the phase measured with such a shearography arrangement can be described by [24]

$$\Delta\phi = \frac{2\pi}{\lambda}\left(\sin\beta\cos\theta\frac{\partial u}{\partial x} + \cos\beta\sin\theta\frac{\partial v}{\partial x} + \left(1+\cos\beta\cos\theta\right)\frac{\partial w}{\partial x}\right)\mathrm{d}x \tag{2.29}$$

where θ is the angle to the x, z plane and β is the angle to the y, z plane.

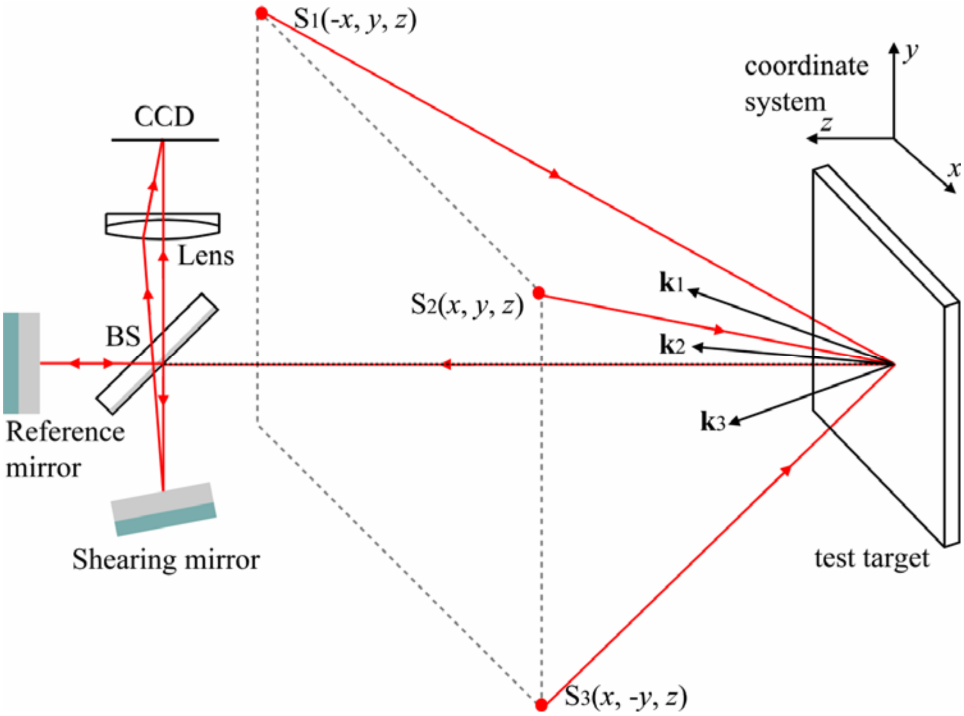

Figure 2.8: *Multi-component shearography system employing three illumination directions. (BS = beamsplitter, S_1-S_3 = source position).*

The phase measurement obtained therefore contains contributions from three components of displacement gradient. Each individual component can be isolated by employing a system that records phase measurements with three separate directional sensitivities. This has been done previously using a system with three laser sources illuminating the target from different directions [31-38]. A typical three-component system with three sources S1(-*x*, *y*, *z*), S2(*x*, *y*, *z*) and S3(*x*, -*y*, *z*) located at three corners of a square centred on the observation direction is shown in figure 2.8.

The magnitude of the sensitivity vector is expressed as

$$\mathbf{k} = \left(k_x^2 + k_y^2 + k_z^2\right)^{1/2} = \frac{2\pi}{\lambda}\left(\hat{o} - \hat{\imath}\right) \qquad (2.30)$$

where $\hat{o}$ and $\hat{\imath}$ are the unit vectors of the observation and illumination directions respectively. The phase measured by the three channels can be expressed by

$$\begin{aligned}\Delta\phi_{S1} &= \frac{2\pi}{\lambda}\left(k_{x1}\frac{\partial u}{\partial x} + k_{y1}\frac{\partial v}{\partial x} + k_{z1}\frac{\partial w}{\partial x}\right)\mathrm{d}x \\ \Delta\phi_{S2} &= \frac{2\pi}{\lambda}\left(k_{x2}\frac{\partial u}{\partial x} + k_{y2}\frac{\partial v}{\partial x} + k_{z2}\frac{\partial w}{\partial x}\right)\mathrm{d}x \\ \Delta\phi_{S3} &= \frac{2\pi}{\lambda}\left(k_{x3}\frac{\partial u}{\partial x} + k_{y3}\frac{\partial v}{\partial x} + k_{z3}\frac{\partial w}{\partial x}\right)\mathrm{d}x\end{aligned} \qquad (2.31)$$

where the numbers in the subscripts refer to the measurement channels formed by sources 1 – 3. Equation (2.31) can be represented in matrix form as

$$\begin{bmatrix}\Delta\phi_{S1} \\ \Delta\phi_{S2} \\ \Delta\phi_{S3}\end{bmatrix} = \frac{2\pi}{\lambda}\begin{bmatrix}k_{x1} & k_{y1} & k_{z1} \\ k_{x2} & k_{y2} & k_{z2} \\ k_{x3} & k_{y3} & k_{z3}\end{bmatrix}\begin{bmatrix}\frac{\partial u}{\partial x} \\ \frac{\partial v}{\partial x} \\ \frac{\partial w}{\partial x}\end{bmatrix}\mathrm{d}x \qquad (2.32)$$

The displacement gradient components are then

$$\begin{bmatrix}\frac{\partial u}{\partial x} \\ \frac{\partial v}{\partial x} \\ \frac{\partial w}{\partial x}\end{bmatrix} = \frac{\lambda}{2\pi}\begin{bmatrix}k_{x1} & k_{y1} & k_{z1} \\ k_{x2} & k_{y2} & k_{z2} \\ k_{x3} & k_{y3} & k_{z3}\end{bmatrix}^{-1}\begin{bmatrix}\Delta\phi_{S1} \\ \Delta\phi_{S2} \\ \Delta\phi_{S3}\end{bmatrix}\mathrm{d}x^{-1} \qquad (2.33)$$

If the illumination positions are located in three of the four corners of a square, so that the *x* and *y* locations of the three illuminating sources in figure 2.8 are of equal magnitude, the phase measurements from the three measurement channels can be represented by

$$\begin{aligned}
\Delta\phi_{S1} &= \frac{2\pi}{\lambda}\left(-k_x\frac{\partial u}{\partial x}+k_y\frac{\partial v}{\partial x}+k_z\frac{\partial w}{\partial x}\right)\mathrm{d}x \\
\Delta\phi_{S2} &= \frac{2\pi}{\lambda}\left(k_x\frac{\partial u}{\partial x}+k_y\frac{\partial v}{\partial x}+k_z\frac{\partial w}{\partial x}\right)\mathrm{d}x \\
\Delta\phi_{S3} &= \frac{2\pi}{\lambda}\left(k_x\frac{\partial u}{\partial x}-k_y\frac{\partial v}{\partial x}+k_z\frac{\partial w}{\partial x}\right)\mathrm{d}x
\end{aligned} \tag{2.34}$$

The displacement gradient components can then be found using [32]

$$\begin{bmatrix}\dfrac{\partial u}{\partial x}\\ \dfrac{\partial v}{\partial x}\\ \dfrac{\partial w}{\partial x}\end{bmatrix}=\frac{\lambda}{2\pi\mathrm{d}x}\begin{bmatrix}-\dfrac{1}{2k_x} & \dfrac{1}{2k_x} & 0\\ 0 & \dfrac{1}{2k_y} & -\dfrac{1}{2k_y}\\ \dfrac{1}{2k_z} & 0 & \dfrac{1}{2k_z}\end{bmatrix}\begin{bmatrix}\Delta\phi_{S1}\\ \Delta\phi_{S2}\\ \Delta\phi_{S3}\end{bmatrix} \tag{2.35}$$

This equation is only valid at the centre of the field of view. Away from the centre the zero terms in equation (2.35) become non-zero. At the centre of the field of view the displacement gradient components can be approximated by addition or subtraction of corresponding phase measurements [37]

$$\begin{aligned}
\frac{\partial u}{\partial x} &= \frac{\lambda}{4\pi k_x\mathrm{d}x}\left(\Delta\phi_{S2}-\Delta\phi_{S1}\right) \\
\frac{\partial v}{\partial x} &= \frac{\lambda}{4\pi k_y\mathrm{d}x}\left(\Delta\phi_{S2}-\Delta\phi_{S3}\right) \\
\frac{\partial w}{\partial x} &= \frac{\lambda}{4\pi k_z\mathrm{d}x}\left(\Delta\phi_{S1}+\Delta\phi_{S3}\right)
\end{aligned} \tag{2.36}$$

Arranging the three sources in this way has previously been determined to be an effective practical geometry [33]. This was achieved through analysis of the condition number of the sensitivity matrix, which determines the level of error introduced by the matrix calculation. The matrix condition number is discussed further in section 6.3.2. To fully characterize the surface strain of a test object, a total of six components of displacement gradient are required. The additional three components can be obtained using an orthogonal shear direction. The displacement gradient components can then be found from

$$\begin{bmatrix} \dfrac{\partial u}{\partial y} \\ \dfrac{\partial v}{\partial y} \\ \dfrac{\partial w}{\partial y} \end{bmatrix} = \frac{\lambda}{2\pi} \begin{bmatrix} k_{x1} & k_{y1} & k_{z1} \\ k_{x2} & k_{y2} & k_{z2} \\ k_{x3} & k_{y3} & k_{z3} \end{bmatrix}^{-1} \begin{bmatrix} \Delta\phi_{S1} \\ \Delta\phi_{S2} \\ \Delta\phi_{S3} \end{bmatrix} \mathrm{d}y^{-1} \tag{2.37}$$

The strain tensor S is given by [38]

$$S = \begin{bmatrix} \varepsilon_x & \gamma_{xy} & \gamma_{xz} \\ \gamma_{yx} & \varepsilon_y & \gamma_{yz} \\ \gamma_{zx} & \gamma_{zy} & \varepsilon_z \end{bmatrix} \tag{2.38}$$

where $\varepsilon_{x,y,z}$ are the normal strain components and $\gamma_{xy,xz,yx,yz,zx,zy}$ are the shear strain components. The strain tensor can be written in terms of the displacement gradient components as

$$S = \begin{bmatrix} \dfrac{\partial u}{\partial x} & \dfrac{1}{2}\left(\dfrac{\partial u}{\partial y}+\dfrac{\partial v}{\partial x}\right) & \dfrac{1}{2}\left(\dfrac{\partial u}{\partial z}+\dfrac{\partial w}{\partial x}\right) \\ \dfrac{1}{2}\left(\dfrac{\partial v}{\partial x}+\dfrac{\partial u}{\partial y}\right) & \dfrac{\partial v}{\partial y} & \dfrac{1}{2}\left(\dfrac{\partial v}{\partial z}+\dfrac{\partial w}{\partial y}\right) \\ \dfrac{1}{2}\left(\dfrac{\partial w}{\partial x}+\dfrac{\partial u}{\partial z}\right) & \dfrac{1}{2}\left(\dfrac{\partial w}{\partial y}+\dfrac{\partial v}{\partial z}\right) & \dfrac{\partial w}{\partial z} \end{bmatrix} \tag{2.39}$$

The shaded quantities represent those that can be measured using shearography. The other quantities represent the bulk strain components and cannot be measured using shearography. This is because they would require a measurement into the volume of the object.

In the system developed by James and Tatam [33] and by Waldner and Brem [34] the phase measurements were time-division-multiplexed. That is, the recordings were made with each illumination direction switched on sequentially. The system developed by Kästle *et al* [35] used three sources that had different wavelengths. Wavelength filters were used to direct light from each channel onto three separate CCD cameras. This system, although faster, since measurements from each channel are recorded simultaneously, is more expensive to construct, since three cameras are required. Also, the system requires the alignment of the cameras to sub-pixel accuracy in order to obtain proper registration of the images.

Often, the fringe patterns corresponding to the orthogonal shear direction are obtained simply by repeating the measurements with the new shear direction. To obtain measurements with both shear directions simultaneously, Steinchen *et al* [30] present a system with two cameras. Two beamsplitters mounted on top of each other direct light to a reference mirror and to two mirrors tilted to provide shear in the *x* and *y* directions. Light reflecting from the reference mirror and the two shearing mirrors recombine at the two beamsplitters before being directed towards the two CCD cameras. A novel system developed by Groves *et al* [39] used a polarization sensitive shearing interferometer to multiplex signals from horizontally and vertically aligned shearing mirrors. The illumination beam was coupled into a highly birefringent (hi-bi) optical fibre with each of the eigenaxes of the fibre equally populated. This was achieved by converting the linearly polarized output of the laser to circularly polarized light with a quarter-wave plate. Laser diode wavelength modulation was used to switch between orthogonal linear polarization states of the light exiting the hi-bi fibre. A polarization sensitive beamsplitter located in one arm of a Michelson interferometer was used to guide the light to the vertically or horizontally aligned mirror depending on the polarization state.

When measuring the surface strain from non-planar test objects [31, 32, 38, 40], a correction needs to be made to compensate for variation in the shear magnitude across the field of view due to the object's shape. Shearography can be used to calculate the slope of an object, where slope is the derivative of the object's shape. Slope fringes can be generated using shearography by displacement of the optical source perpendicular to the optical axis between recording frames [41]. Care needs to be taken with this method because any longitudinal displacement of the source will generate carrier fringes which will distort the slope fringes. Shape measurement is discussed further in section 2.5. Recently, surface strain measurements made with a three-component shearography system from a non-planar test object were compared to the results from fibre Bragg grating (FBG) instrumentation and resistance foil strain gauges [38]. The results from the shearography system compared well with the other, more established, strain measurement techniques.

The measurement channels in the systems described above all consist of multiple illumination directions. Equivalently, systems can be constructed whereby the measurement channels consist of multiple observation directions combined with a single illumination direction. This could be realized using three shearing interferometers with three cameras. An alternative is to use coherent fibre-optic imaging bundles to transport images from the different observation positions to a single shearing interferometer and camera [42, 43], which therefore reduces the number of optical components within the system. The advantage of a system incorporating multiple viewing directions is that only a single laser source is required and is therefore compatible with high energy pulsed lasers, which are often bulky and expensive. The use of pulsed lasers within speckle interferometry is discussed further in section 2.7.

2.4 Digital speckle photography

Digital speckle photography (DSP) [44] is a non-interferometric speckle technique that is used for measuring in-plane surface displacements. The traditional speckle photography method involved doubly exposing a photographic film to the speckle pattern before and after object deformation. The developed film is then illuminated with a narrow, collimated laser beam and a set of Young's fringes is observed in the image plane. The displacement of the surface at the point illuminated by the laser is inversely proportional to the period of the fringes and the displacement direction is perpendicular to the fringe orientation. The magnitude of the deformation needs to be of such an extent that each speckle in the second exposure has moved so that it is completely separated from its partner in the original exposure. In speckle interferometry, this would result in speckle decorrelation and no fringes would be observed. The two techniques are therefore complementary.

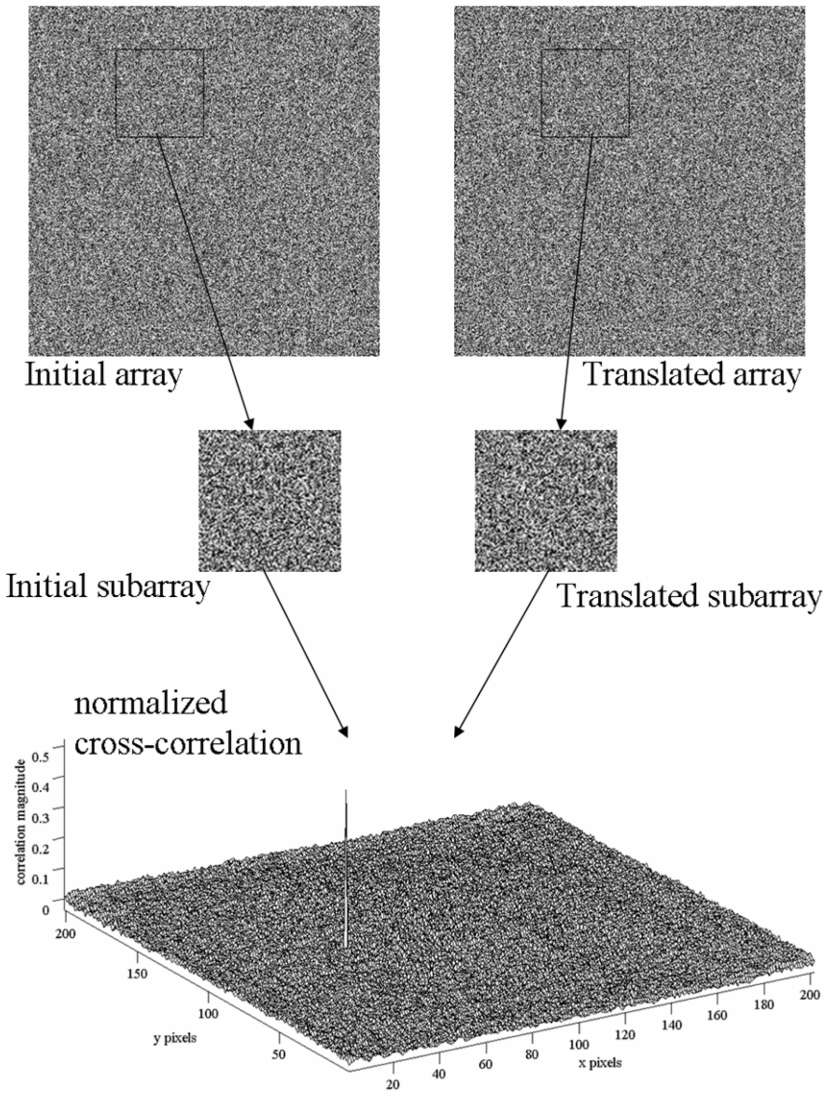

Figure 2.9 *The principle of the normalized cross-correlation, as used in digital speckle photography, for the determination of translation between two shifted images.*

Digital speckle photography is the electronic equivalent of the photographic processing speckle photography technique. In this case, the speckle pattern produced by coherent illumination of the object is imaged onto a CCD camera. Since no reference beam is required in DSP, non-interferometric speckle is imaged by the camera. Speckle patterns are recorded before and after displacement of the object and the motion of the speckles between frames is determined by comparing the speckle patterns. This comparison can be done effectively by calculating the cross-correlation between the two images [45]. The principle of cross-correlation is illustrated in figure 2.9. The figure shows a computer generated image of an array of random greyscale values. The image is then translated by 40 pixels in the *x* direction. In this example, a subarray of 100x100 pixels is chosen at an arbitrary location in the initial array and again at the same location in the translated array.

The normalized two-dimensional cross-correlation is calculated between the two subarrays resulting in a new array whose dimensions are $2x$-1, $2y$-1, where x and y are the dimensions of the subarray. The correlation peak in the array represents the magnitude and direction of the translation between the two subarrays which corresponds to the distance between the correlation peak and the centre of the array. A map of the in-plane displacement across the image can be built up point-by-point by selecting subarrays at each location in the initial image and cross-correlating them with the corresponding subarray in the translated image. The size of the subarray needs to be greater than the translation between the images in order to detect the correlation peak, so some knowledge of the displacement magnitude is required before analysis of the images.

Synnergren [46] described the use of stereoscopic DSP to measure three dimensional displacement fields. The system consisted of two CCD cameras aligned so that the image plane of each camera was parallel to the plane of the flat test object. The imaging lens of each camera was displaced laterally so that each camera viewed the same region of the target. The in-plane and out-of-plane displacement components could be isolated by addition or subtraction of the images recorded by the cameras scaled by factors due to the imaging parameters.

Three component displacement fields have also been measured using systems combining the techniques of DSP and speckle interferometry. This involves using DSP for measurement of the in-plane displacement components and using ESPI [47, 48] or shearography [49] to measure the out-of-plane component. Using this combination of techniques, three displacement components can be measured simultaneously without the need of multi-component system, all that is required is an ESPI or shearography system in the out-of-plane configuration (figures 2.3 and 2.8 respectively). The disadvantage is that the in-plane displacement needs to be large enough to translate the speckle field by at least one pixel for the correlation technique to work. Unlike with conventional in-plane speckle interferometry, very small in-plane displacements cannot be resolved. Also, the spatial resolution of the in-plane displacement measurements is less than the out-of-plane measurements due to the finite size of the correlation window.

Recently, Šmíd *et al* [50] used the speckle correlation technique to measure the in-plane velocity of a surface mounted on a motorized translation stage. Based on the knowledge of the acquisition rate of the in-plane displacement measurements, the in-plane velocity can be inferred. Velocities in the range of 10 – 100 μms^{-1} were measured using the technique.

Digital speckle photography and ESPI are complementary displacement measurement techniques. A wide range of displacements can be measured with the two techniques. ESPI has a higher sensitivity and is therefore more suitable for smaller displacements ~ 0.1 – 1.0 μm, whereas DSP is more suitable for larger displacements ~ 10 – 1000 μm [51].

2.5 Shape and slope measurement

The technique of using interferometry to measure the shape of an object is often referred to as contouring. A common method of contouring is the dual wavelength technique, introduced to holographic interferometry over 35 years ago by Zelezka and Varner [52]. In this technique, the object is illuminated with coherent light at an initial wavelength λ_1 and then illuminated at a second wavelength λ_2. The interferogram produced by subtraction is the same as that which would have been produced had the object been illuminated at a longer, equivalent wavelength λ_{eq}, given by [53]

$$\lambda_{eq} = \frac{\lambda_1 \lambda_2}{\left|\lambda_1 - \lambda_2\right|} \tag{2.40}$$

Creath *et al* [54] generated phase contours by combining two-wavelength holography with phase shifting interferometry. The method they used to generate contours of aspherics was to use a He-Ne laser and an Argon ion laser from which a number of equivalent wavelengths could be generated. The Argon ion wavelengths used were 488 nm and 514.5 nm. This was done using a Twyman-Green interferometer.

Tatam *et al* [55] reported the development of a fibre-optic ESPI system that was used to produce contour fringes generated by injection current modulation of a laser diode. In this method, the object, which was a brake disk hub, was illuminated at an initial wavelength and a speckle interferogram was saved. The injection current was then varied causing a change in the output wavelength of the laser diode. A second frame recorded at the second wavelength was then subtracted from the initial frame. The image displayed after subtraction yields contour fringes with a separation equal to the equivalent wavelength. Using this method, contour fringes with separations ranging from 0.5 – 5 mm were generated. The method is limited due to the diode laser mode hopping after the current has been tuned by a certain amount. Contour fringes obtained by laser diode current modulation obtained by Ford *et al* [4] from a gas turbine blade are shown in fig 2.10.

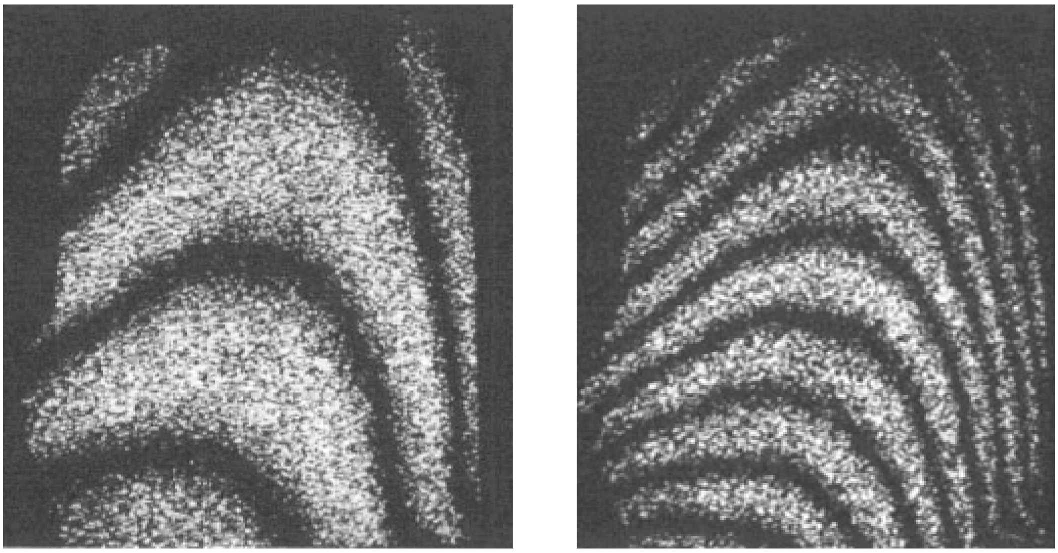

(a) (b)

Figure 2.10 *Contour fringes from a turbine blade using diode current modulated ESPI. Optical frequency differences were 32.6 GHz (a) and 42.9 GHz (b) corresponding to contour spacings of 4.7 mm and 3.5 mm respectively [4].*

Shape measurement can also be done using a fringe projection technique. In this method the fringe pattern from a Michelson interferometer or a Wollaston prism is projected first onto a flat reference surface and then on the 3-D object. Contours are generated by subtracting the digital images from each surface recorded by a CCD camera [1].

Slope, the derivative of an object's shape, can be measured using shearography. Fringes representing the slope of a surface can be generated by translating the illuminating source perpendicular to the illumination direction between recording signal and reference frames [41]. Slope measurements can also be made using shearography with the two wavelength technique, described above. This can be achieved by modulating the frequency of a laser diode between recording frames [56, 57]. Slope measurements have also been made using shearography by rotating the object. Subtraction of digital images recorded before and after object rotation result in slope sensitive correlation fringes [58].

2.6 Vibration measurement

Speckle interferometry may also be used in the analysis of vibrating surfaces. Provided the frequency of vibration is significantly greater than the refresh rate of the speckle imaging camera (25Hz in Europe) and the vibration is harmonic, then time-averaged interference fringes showing regions of equal vibration amplitude can be observed. The speckle intensity incident on the camera at any one point in time is given by

$$I(x,y,t) = a_o^2(x,y) + a_r^2(x,y) + 2a_o a_r \cos\left[\psi(x,y) + \phi(x,y,t)\right] \qquad (2.41)$$

where a_o and a_r are the object and reference beam complex amplitudes, ψ is the random speckle phase and ϕ is the change in phase due to the object vibration and is given by [59]

$$\phi(x,y,t) = \frac{4\pi A(x,y)\sin\omega t}{\lambda} \tag{2.42}$$

where A and ω are the amplitude and angular frequency of the vibration respectively. Normal viewing and illumination directions are assumed. If the vibration of the object is significantly faster than the refresh rate of the camera then the registered intensity will be averaged over the integration time of the camera. If the frame begins at $t = t$ and ends at $t = t + T$ then the time-averaged intensity will be [60]

$$I_{\text{av}} = \int_t^{t+T} a_o^2 + a_r^2 + 2a_o a_r \cos\left[\psi + \frac{4\pi A \sin\omega t}{\lambda}\right] dt \tag{2.43}$$

where the x and y dependencies have been dropped for clarity. Equation (2.43) can also be expressed as

$$I_{\text{av}} = a_o^2 + a_r^2 + 2a_o a_r \cos\psi J_0\left(\frac{4\pi A}{\lambda}\right) \tag{2.44}$$

where J_0 is the zero-order Bessel function. To generate vibration fringes, two speckle images are recorded with a π phase shift in between. This phase shift is necessary because the average intensity over many vibration cycles will be the same for the two frames, therefore subtraction would result in zero intensity [61]. With vibrational analysis, sequential subtraction can be used. With this type of subtraction, each incoming signal frame acts as the reference frame for the next so that the reference frame is constantly refreshed. The advantage of this over static subtraction is that errors due to spurious vibrations and environmental factors cause an effect between just two frames rather than over the duration of a measurement. After subtracting and squaring the reference and signal frames, the intensity distribution is given by

$$\Delta I = 4 I_r I_o \cos^2\psi(x,y) J_0^2\left(\frac{4\pi A(x,y)}{\lambda}\right) \tag{2.45}$$

for a time-averaged ESPI measurement. The fringes therefore follow a J_0^2 intensity distribution. The brightest fringe corresponds to the node of the vibration and fringe intensity decreases with increasing vibration amplitude. The brightness of the nodal fringe is approximately six times greater than the next brightest fringe. Subsequent fringe orders are therefore of low contrast and calculation of the amplitude and phase of the vibration is difficult from the time-averaged Bessel fringes. Løkberg and Høgmoen [62] used a modulated reference mirror to extend the range of vibration amplitudes that can be measured using time-averaged ESPI. In their method, the reference mirror was set to vibrate harmonically. In this set-up, the zero-order fringe no longer represents the node of vibration but regions vibrating at the same amplitude and phase as the reference mirror. They extended their technique [63] to generate a map of the vibration phase over the whole field of view. This was done by varying the amplitude and phase of the reference mirror. Atcha and Tatam [3] used laser diode wavelength modulation to heterodyne an ESPI system in order to determine the amplitude and phase of the vibration. Figure 2.7 shows some examples of time-averaged Bessel fringes generated using ESPI, from [3]. The zero-order fringe is seen at different locations in the two heterodyned examples which are 180° out of phase. Anderson *et al* [64] used a pulsed diode laser to provide stroboscopic illumination which converts the Bessel fringes to cosinusoidal fringes. Synchronization of the pulsed diode laser with the vibration of the object under investigation also allows phase stepping from which the phase can be recovered. This technique is less energy efficient than the heterodyning technique since the optical power is reduced by pulsing the laser diode.

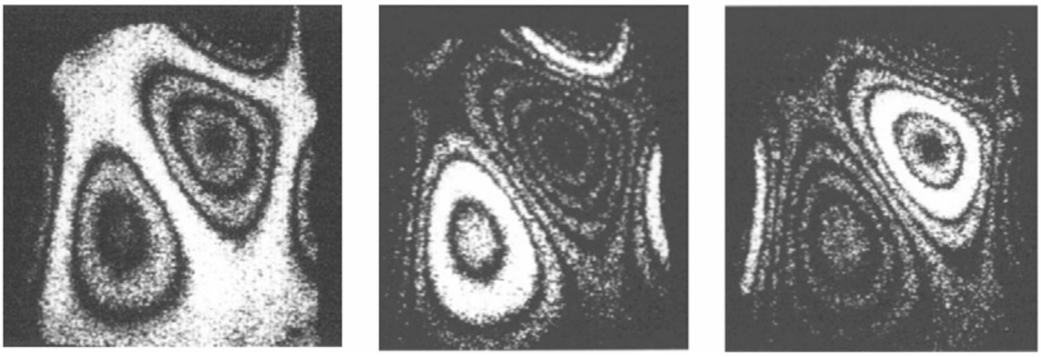

(a) **(b)** **(c)**

Figure 2.11 *Time-averaged Bessel fringes generated using ESPI from a gas turbine blade vibrating at 5.6 kHz (a). Heterodyned fringes with a phase shift of 180° between them are shown in (b) and (c). Note the change in the position of the bright zero-order fringe [3].*

When using shearography, it is the derivative of the modal displacement that is measured. Valera and Jones [65] recorded time-averaged Bessel fringes from a vibrating aluminium plate. The target was illuminated by light exiting a highly birefringent optical fibre which could be phase modulated using a PZT around which the fibre was coiled. The scattered light was imaged through a Wollaston prism which provided the image shear. Huang and Tatam [56, 66] describe a system that was heterodyned using laser diode frequency modulation. The system used a path length imbalanced Michelson interferometer as the shearing device. The size of the optical path difference determines the optical phase shift in the interferometer for a given shift in the laser diode frequency. The difference in magnifications in the two interferometer arms was corrected by placing a high refractive index glass block in the longer of the two interferometer arms. Results from a vibrating gas turbine blade were obtained and compared with results from vibration sensitive ESPI system. Time averaged Bessel fringes from a gas turbine blade vibrating at 5.6 kHz are shown in figure 2.12 [66]. Comparison of the fringe patterns in figures 2.11 and 2.12 clearly shows the improved fringe contrast of ESPI fringes over the shearography fringes which contour regions of equal displacement gradient.

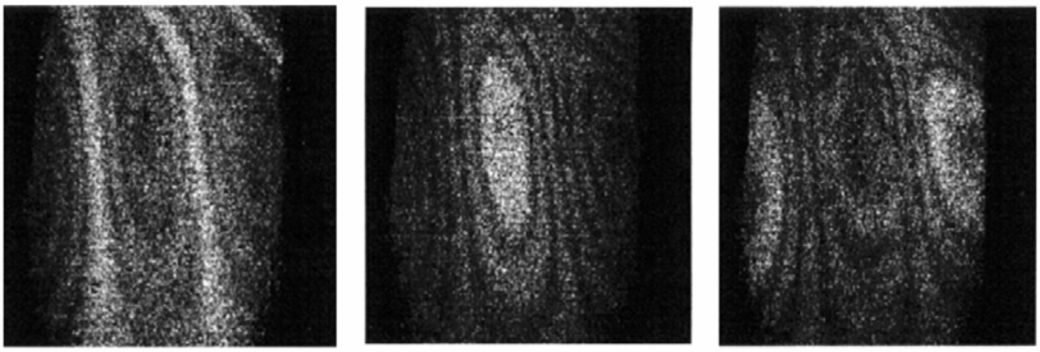

(a) **(b)** **(c)**

Figure 2.12 *Time-averaged Bessel fringes generated using shearography from a gas turbine blade vibrating at 5.6 kHz (a). Heterodyned fringes with a relative phase shift of π/2 are shown in (b) and (c) [66].*

2.7 The use of pulsed lasers in speckle interferometry

Pulsed lasers were introduced to speckle interferometry as early as 1978 [67] and present a number of advantages over continuous wave lasers. Pulsed lasers often offer higher output energies than continuous wave lasers which can be useful if large objects are to be investigated. Also, if dual-pulsed lasers are used with a short duration between the pulses, the systems developed will be much more resilient to environmental disturbances such as vibration and rigid body motion, which can cause decorrelation of the speckle patterns and therefore lose fringe visibility. This is more of a problem with ESPI than for shearography because of the separated beam paths in the ESPI interferometer due to the air path to the object being part of the ESPI interferometer.

The main advantage of pulsed lasers is in the ability to use them in the analysis of dynamic surfaces [68]. We have already seen that shearography and ESPI can be used with continuous-wave illumination to generate time-averaged Bessel fringes. When pulsed illumination is used, the fringes that are generated are cosinusoidal, which are easier to analyze. Moreover, time-averaged fringes can only be produced with continuous-wave illumination when the motion is harmonic. With pulsed lasers, surfaces can be analyzed even if the vibration is transient, provided the duration of the laser pulse is significantly shorter than the period of the vibration. Q-switched Nd:YAG lasers, for example, can have pulse durations as short as 10 ns. The motion of the surface under investigation is effectively ‘frozen’ for the duration of the laser pulse. Using a dual-pulsed laser source, speckle interferograms can be recorded from two laser pulses with very short (~20 μs) separations between them [69]. Correlation of these speckle patterns gives the relative deformation of the surface between the two pulses. One of the main issues with the dual pulsed technique is in the phase analysis. Since only two pulses are usually available for any one measurement, more sophisticated phase analysis techniques are required than the traditional phase stepping technique used in static speckle interferometry, which requires at least four frames of data. This issue is discussed in more detail in the next chapter.

The very high energy density of laser pulses can make it difficult to incorporate pulsed lasers into fibre-optic based speckle interferometers. However, Schedin *et al* [70] developed a fibre based ESPI system with a pulsed ruby laser as the optical source. Five percent of the pulse energy was separated to form the reference beam, which was coupled into a single mode fibre. The remaining pulse energy was coupled into a multimode fibre and the light scattered from the surface under investigation was imaged through a fibre endoscope before imaging onto the CCD camera.

Another application of pulsed laser based speckle speckle interferometers is in the measurement of rotating surfaces. Swain and Preater [71, 72] demonstrated an ESPI system in the in-plane configuration for the measurement of rotating components with a tangential velocity of up to 300 ms^{-1}. The system used a pulsed ruby laser to freeze to the motion of the rotating component. Pérez-López *et al* [73] measured out-of-plane displacement from a rotating surface using a single channel pulsed ESPI system. They later extended this technique to measure all three components of displacement from a rotating surface using a three channel, multiple illumination direction ESPI system [74]. Two 10 ns duration laser pulses from an Nd:YAG laser with a separation of 20 μs between them were fired at the target and speckle patterns were recorded by a CCD camera that was synchronized with the pulsing of the laser. Measurements from each channel were made sequentially for each illumination direction.

An alternative method for measuring dynamic surfaces using speckle interferometry is to use a camera with a high frame rate. A CCD camera with a frame rate of 40 kHz has previously been used with an ESPI system to investigate transient deformation with surface velocities up to 4.3 mm/s [75]. CMOS cameras with small interrogation windows have also been used for the investigation of dynamic events with speeds of up to 70 kHz [76]. The advantage of using a high speed camera is that systems can be built in conjunction with continuous wave laser sources and are therefore compatible with single mode optical fibres, which cannot tolerate very high energy laser pulses. Also, temporal phase stepping can be incorporated into speckle interferometry systems with high speed cameras [77]. A disadvantage of the technique is that short exposure times are required to achieve high frame rates, which means that a relatively low amount of optical power is available to each frame. Also, a relatively low number of pixels are used in the analysis to achieve high frame rates, which limits the spatial resolution.

2.8 Applications

Both ESPI and shearography have become important diagnostic tools in engineering. In the aerospace industry, components such as helicopter rotor blades and carbon fibre components such as aircraft wings and panels have been tested [78, 79]. In the automotive industry, speckle interferometry has been used to test components as large as the doors of cars [80]. The measurement of large scale structures is limited by the power of the optical source; therefore high power lasers are required for the measurement of these structures. At the other end of the scale, small structures such as electronics components such as MEMS (micro electrical-mechanical systems) devices [81, 82] and ball grid arrays [83], which are used for soldering printed circuit boards, have been tested for shape and deformation. A frequent application of shearography in industrial engineering is in the analysis of composite materials. These materials are known for their high strength to weight ratio and are often used, for example, in the aerospace and automotive industries. Shearography is used as a qualitative inspection tool to detect defects and disbonds in laminated structures [24]. An example of this use of shearography is shown in figure 2.13. This figure shows a shearography fringe pattern of a thermally loaded composite structure containing two defects. The location and relative magnitude of the two defects can be seen in the regions containing a higher density of fringes. This image was obtained during the course of the work presented in this thesis.

Figure 2.13 *Shearography fringe pattern showing the location and relative magnitude of two defects in a thermally loaded composite structure.*

Speckle interferometry has also found applications in field of biology and medicine. Kemper *et al* [84, 85] developed an endoscopic pulsed ESPI system for the investigation biological samples *in-vivo* and *in-vitro*. Examples of the analysis of a porcine stomach and a mucous membrane are presented in [84]. Healthy regions of tissue show correlation fringes with greater curvature than those from less healthy regions due to different elasticity in the different regions. Kishen *et al* [86] used ESPI to investigate the thermal response of human teeth. The results showed that there is significant deformation in the dental structure over a temperature range of 35 - 50°C. The out-of-plane displacement occurs along the axis of the tooth, with the in-plane deformation perpendicular to the tooth’s axis.

The vibration measurement property of ESPI has been used in the detection of buried landmines has been investigated by Sabatier *et al* [87]. In their investigation a vibration was induced in the sand close to the buried mine. A laser Doppler vibrometer was used to determine the resonant frequency of the buried mine and a dual pulsed ESPI system was used to investigate the region of interest. The pulses of the laser were synchronized with the peak and valley of the vibration. The vibration amplitude was limited to 3 μm due to decorrelation of the speckle patterns because of motion of the sand particles. The results showed a map of the vibration of the surface above the buried land mine. Another application of vibrational analysis using ESPI is in the inspection of artistic murals. Fricke-Begemann *et al* [88] used the technique to assess 14th century frescoes at St. Just church in Kamenz, Saxony. The method involved using a loudspeaker to generate an acoustic wave which caused loose sections of the plaster behind the mural to vibrate. The loose regions vibrate with a greater amplitude than stable regions and as such can be detected using a time-averaged ESPI system. The non-contact element of the optical technique is of particular advantage over the traditional tapping method which can cause further damage to the mural. Shearography has also been used in the evaluation of cultural heritage. Groves *et al* used shearography to investigate defects induced in artworks and to analyze signature features for security purposes [89].

2.9 Summary

The principal speckle interferometry techniques, shearography and ESPI, are two convenient optical tools for the non-destructive, full field evaluation of optically rough surfaces. This chapter has shown that these techniques can be used for a wide range of measurements and applications. The different parameters that can be measured are summarised below in table 2.1

Table 2.1 *Summary of measurement parameters using ESPI and shearography.*

Measurement	ESPI	Shearography	DSP
Displacement	Yes	With numerical integration	Yes
Displacement gradient	With differentiation	Yes	With numerical differentiation
Surface strain	With differentiation	Yes	Yes
Shape/slope	Yes	Yes	Yes
Vibrational modes	Yes	With numerical integration	Yes
Approximate measurement range [51]	0.1 – 1.0 μm	10 – 1000 μm/m	10 – 1000 μm

Although both techniques can be used to measure the same properties of the surface under investigation, each technique has certain relative advantages and disadvantages depending on the situation. Shearography generally uses a simpler optical configuration than ESPI, requiring only a shearing device between the object and the CCD camera. Out-of-plane ESPI requires a smooth reference beam to combine with the object beam in order to obtain the interferometric speckle pattern. This usually follows a separate beam path to the object beam. The optical path difference between these two beam paths needs to be kept below the coherence length of the source, which could potentially be a problem if a fairly wide band optical source is used. The intensity of the reference beam needs to be approximately 3-4 times that of the object beam if high contrast fringes are to be observed. Since only a small proportion of the light scattered from the object's surface is actually imaged onto the detector surface, a system of imbalanced split ratio beamsplitters or fibre-optic couplers as well as, potentially, neutral density filters are required to achieve this condition. Also, because of the comparatively low coherence requirements of shearography, it is possible to apply the technique with certain broadband sources that possess enough temporal and spatial coherence, such as a mercury arc lamp [90].

The separate beam paths in ESPI also mean that the technique is more susceptible to environmental disturbances than shearography, which can be either a common path system or have comparatively short separated beam paths in the case of a Michelson or Mach-Zehnder shearing interferometer. Also, since shearography measures the relative differences in displacement between points on the object's surface, it is relatively resilient to rigid body motion of the target, since the motion affects all points on the object. Hence, shearography is often more suitable for measurements of static surfaces in industrial environments. When dual pulsed measurements of dynamic surfaces are to made, however, these stability requirements are very much reduced since any disturbance is unlikely to have much effect in the time between recording frames, which can be of the order of microseconds.

The sensitivity (the number of fringes for any given deformation) in shearography is variable by adjusting the magnitude of the applied shear. The sensitivity variation in shearography is limited, however, because too small a shear results in a loss of fringe contrast and too great a shear leads to an increase in errors in the displacement derivative measurements. This is due to the assumptions made in the derivation of the phase equation (2.22).

For the purposes of strain measurement, shearography has a distinct advantage in that it measures directly the derivative of displacement, which is closely related to the components of surface strain (see equation (2.39)). In situations were the displacement itself is required, ESPI has the advantage. ESPI can also be beneficial when measuring the vibrational modes of surfaces because of its direct measurement of displacement. When using shearography for the measurement of vibration it is the derivative of the vibrational modes that is measured. The fringe patterns generated using shearography in this case are more difficult to interpret than the corresponding ESPI fringe patterns. Also, the contrast of the correlation fringes generated using ESPI is generally higher than those produced using shearography. Some of the various properties of the two techniques are summarized in table 2.2.

Table 2.2 *Summary properties of ESPI and shearography.*

	ESPI	**Shearography**
Optical arrangement.	Straightforward, although additional components to equalize beam polarization and intensity may be required.	Simple, only a basic Michelson interferometer or other shearing device needed between object and camera.
Resilience to environmental disturbance.	Often poor, unless pulsed laser systems are used.	Very good.
Fringe quality.	Generally excellent.	Good.
Sensitivity.	Variable in in-plane configuration.	Variable by adjusting shear magnitude.

References

[1] Yang L. and Ettemeyer A, ‘Strain measurement by three-dimensional electronic speckle pattern interferometry: potential, limitations and applications’, *Opt. Eng.* **42**:5, 1257-66 (2003).

[2] Leendertz J. A. and Butters J. N, ‘Speckle pattern and holographic techniques in engineering metrology’, *Opt. Laser Technol.* **3**, 26-30 (1971).

[3] Atcha H. and Tatam R. P, ‘Heterodyning of fibre optic electronic speckle pattern interferometers using laser diode wavelength modulation’, *Meas. Sci. Technol.* **5**, 704-9 (1994).

[4] Ford H. D, Atcha H and Tatam R. P, ‘Optical fibre technique for the measurement of small frequency separations: application to surface profile measurements using electronic speckle pattern interferometry’, *Meas. Sci. Technol.* **4**, 601-7, (1993).

[5] Tatam R. P. ‘Speckle interferometry: optoelectronic developments and applications’, *Proc. SPIE*, **3745**, 114-33 (1999).

[6] Rigden J. D. and Gordon E. I, ‘The granularity of scattered optical maser light’, *Proc. IRE*, **50**, 6564-74 (1962).

[7] Oliver B. M. 'Sparkling spots and random diffraction', *Proc. IEEE*, **51**:1, 220-1 (1963).

[8] Gabor D, ‘Laser speckle and its elimination’, *Conference on holography and the computer, IBM Journal of Research and Development*, **14** 509-14 (1970).

[9] Gåsvik K J; *Optical Metrology*, Wiley (1995).

[10] Macovski A, Ramsey S. D. and Schaefer L F, ‘Time-lapse interferometry and contouring using television systems’, *Appl. Opt.*, **10**:12, 2722-7 (1971).

[11] Schwomma. O, ‘Holographiches-interferometrisches oder moirémetrisches verfahren, *Osterreichisches Patent* **298 830**, (1972).

[12] Sharp B, ‘Electronic speckle pattern interferometry’, *Opt. Lasers Eng,* **11**, 241-55, (1989).

[13] Jones R. and Wykes C, ‘*Holographic and Speckle Interferometry*’, Cambridge University Press, Cambridge, (1989).

[14] Sirohi R. S. 'Speckle interferometry', *Cont. Phys.*, **43**:3, 161-80 (2002).

[15] Moore A. J. and Tyrer J. R, ‘An electronic speckle pattern interferometer for complete in-plane displacement measurement’, *Meas. Sci. Technol.* **1**, pp 1024-30, (1990).

[16] Winther S. ‘3D strain measurements using ESPI’, *Opt. Lasers Eng.* **8**, 45-57 (1988).

[17] Huang M. J, Liu Z-C and Jhang J-H, ‘Self-marking phase stepping electronic speckle pattern interferometry (ESPI) for 3D displacement measurement on cathode ray tube (CRT) panels’, *Opt. Lasers Eng.* **38**, 245-60 (2002).

[18] Atcha H, ‘Optoelectronic speckle pattern interferometry’, *PhD Thesis*, Cranfield University, Bedford, (1994).

[19] Liu W. and Tan Y. ‘Single mode optical fibre electronic speckle pattern interferometry’, *Opt. Lasers Eng.* **25**, 103-9 (1996).

[20] Matsumoto T. and Kano H, ‘Endlessly rotatable fractional-wave devices for single-mode-fibre optics’, *Elect. Lett.* **22**:2, 78-9 (1986).

[21] Leendertz J. A. and Butters J. N, ‘An image-shearing speckle-pattern interferometer for measuring bending moments’, *J. Phys. E.* **6**, 1107-10 (1973).

[22] Hung Y. Y. and Liang C. Y, 'Image-shearing camera for direct measurement of surface strains', *Appl. Opt.* **18**:7, 1046-51 (1979).

[23] Hung Y. Y, 'Shearography: a new optical method for strain measurement and non-destructive testing', *Opt. Eng.* **21**:3, 391-5 (1982).

[24] Hung Y. Y, Luo W. D, Lin L and Shang H. M, 'Evaluating the soundness of bonding using shearography', *Compos. Struct.* **50**, 353-62 (2000).

[25] Hung Y. Y, Ho H. P, 'Shearography: an optical measurement technique and applications, *Mater. Sci. Eng. R.* **49**, 61-87 (2005).

[26] Gundlach A, Huntley J. M, Manzke B and Schwider J, 'Speckle shearing interferometry using a diffractive optical beamsplitter', *Opt. Eng.* **36**:5, 1488-93 (1997).

[27] Mihaylova E, Naydenova I, Martin S and Toal V, 'Electronic speckle pattern shearing interferometry using photopolymer diffractive optical elements for vibration measurements', *Proc. SPIE.* **5503**, 73-8 (2004).

[28] Mihaylova E, Naydenova I, Duignan B, Martin S and Toal V, 'Photopolymer diffractive optical elements in electronic speckle pattern shearing interferometry', *Opt. Lasers Eng.* **44**:9, 965-74 (2006).

[29] Ng T. W, 'Digital speckle pattern interferometer for combined measurements of out-of-plane displacement and slope', *Opt. Comm.* **116**, 31-5 (1995).

[30] Steinchen W, Yang L. X, Kupfer G, Mäckel P and Vössing F, 'Strain analysis by means of digital shearography: potential, limitations and demonstration', *J. Strain Anal.* **33**:2, 171-82 (1998).

[31] Groves R. M, 'Development of shearography for surface strain measurement of non-planar objects', *PhD Thesis*, Cranfield University, Bedford (2001).

[32] James S. W, Groves R. M and Tatam R. P, 'Surface strain characterization using time-division multiplexed 3D shearography', *Proc. SPIE*, **4101**, 384-93 (2001).

[33] James S. W. and Tatam R. P, 'Time-division-multiplexed 3D shearography', *Proc. SPIE*, **3744**, 394-403 (1999).

[34] Waldner S and Brem S, 'Compact shearography system for the measurement of 3D deformation', *Proc SPIE*, **3745**, 141-47 (1999).

[35] Kästle R, Hack E. and Sennhauser U, 'Multiwavelength shearography for quantitative measurements of two-dimensional strain distributions', *Appl. Opt.* **38**:1, 96-100 (1999).

[36] Waldner S, Quantitative strain analysis with image shearing speckle pattern interferometry (shearography)', *PhD Thesis*, Swiss federal institute of technology, Zurich (2000).

[37] Aebischer H. A. and Waldner S, 'Strain distributions made visible with image shearing speckle pattern interferometry', *Opt. Lasers Eng.* **26**, 407-20 (1997).

[38] Groves R. M, Chehura E, Li W, Staines S. E, James S. W. and Tatam R. P, 'Surface strain measurement: a comparison of speckle shearing interferometry and optical fibre Bragg gratings with resistance foil strain gauges', *Meas. Sci. Technol.* **18**, 1175-84 (2007).

[39] Groves R. M, James S. W. and Tatam R. P, 'Polarization multiplexed and phase-stepped fibre optic shearography using laser wavelength modulation', *Meas. Sci. Technol.* **11**, 1389-95 (2000).

[40] Groves R. M, James S. W. and Tatam R. P, 'Full surface strain measurement using shearography, *Proc. SPIE*, **4448**, 142-52 (2001).

[41] Groves R. M, James S. W and Tatam R. P, 'Shape and slope measurement by source displacement in shearography', *Opt. Lasers Eng.* **41**, 621-34 (2004).

[42] Groves R. M**,** James S. W and Tatam R. P, 'Multi-component shearography using optical fibre imaging-bundles', *Proc. SPIE* **5144**, 513-20 (2003).

[43] Francis D, James S. W and Tatam R. P, 'Measurement of surface strain using multi-component pulsed laser shearography with fibre-optic imaging bundles', *Proc. SPIE* **6616**, 6616-2S (1-10) (2007).

[44] Sjödahl M, 'Digital speckle photography' in *Digital speckle interferometry and related techniques*, ed. Rastogi P. K, Wiley (2001).

[45] Sjödahl M, and Benckert L. R, 'Electronic speckle photography: analysis of an algorithm giving the displacement with subpixel accuracy', *Appl. Opt.* **32**:13 2278-84 (1993).

[46] Synnergren P, 'Measurement of three-dimensional displacement fields and shape using electronic speckle photography', *Opt. Eng.* **36**:8, 2302-10 (1997).

[47] Fricke-Begemann T. and Burke J, 'Speckle interferometry: three-dimensional deformation field measurement with a single interferogram', *Appl. Opt.* **40**:28, 5011-22 (2001).

[48] Gren P, 'Pulsed TV holography combined with digital speckle photography restores lost interference phase', *Appl. Opt.* **40**:14, 2304-9 (2001).

[49] Groves R. M, Fu S, James S. W. and Tatam R. P, 'Combined shearography and speckle pattern photography for single-access multi-component surface strain measurement, *proc. SPIE*, **5058**, 351-60 (2002).

[50] Šmíd P, Horváth P. and Hrabovsky M, 'Speckle correlation method used to measure object's in-plane velocity', *Appl. Opt.* **46**:18 3709-15 (2007).

[51] http://www.dantecdynamics.com/Default.aspx?ID=854

[52] Zelenka J. S. and Varner J. R, 'A new method for generating depth contours holographically', *Appl. Opt.* **7**:10, 2107-10 (1968).

[53] Wyant J. C. 'Testing aspherics using two-wavelength holography', *Appl. Opt.* **10**:9, 2113-8 (1971).

[54] Creath K, Chen Y-Y, Wyant J. C, 'Contouring aspheric surfaces using two-wavelength phase-shifting interferometry, *Optica Acta*, **32**:12, 1455-64 (1985).

[55] Tatam R. P, Davies J. C, Buckberry C. H. and Jones J. D. C, 'Holographic surface contouring using wavelength modulation of laser diodes', *Opt. Laser Technol.* **22**:5, 317-21 (1990).

[56] Huang J-R, 'Optoelectronic speckle shearing interferometry', *PhD Thesis*, Cranfield University, Bedford, (1996).

[57] Huang J-R, Ford H. D, Tatam R. P, 'Slope measurement by two-wavelength electronic shearography', *Opt. Lasers Eng.* **27**, 321-33 (1997).

[58] He Y. M, Tay C. J. and Shang H. M, 'Digital phase-shifting shearography for slope measurement', *Opt. Eng*, **38**:9, 1586-90 (1999).

[59] Romero G, Alvarez L, Alanís E, Nallim L. and Grossi R, 'Study of a vibrating plate: comparison between experimental (ESPI) and analytical results', *Opt. Lasers Eng.* **40**, 81-90 (2003).

[60] Wang W-C, Hwang C-H and Lin S-Y, 'Vibration measurement by the time-averaged electronic speckle pattern interferometry methods', *Appl. Opt.* **35**:22, 4502-9 (1996).

[61] Moran S. E, Law R. L, Craig P. N and Goldberg W. M, 'Optically phase locked electronic speckle pattern interferometer', *Appl. Opt.* **26**, 475-91 (1986).

[62] Løkberg O. J. and Høgmoen K, ‘Use of modulated reference wave in electronic speckle pattern interferometery’, *J. Phys. E: Sci. Instr.* **9**, 847-51, (1976).

[63] Løkberg O. J. and Høgmoen K, ‘Vibration phase mapping using electronic speckle pattern interferometry’, *Appl. Opt.* **15**:11, 2701-4, (1976).

[64] Anderson D. J, Valera J. D. and Jones J. D. C, ‘Electronic speckle pattern interferometry using diode laser stroboscopic illumination’, *Meas. Sci. Technol.* **4**, 982-7 (1993).

[65] Valera J. D. R and Jones J. D. C, ‘Vibration analysis by modulated time-averaged speckle shearing interferometry’, *Meas. Sci. Technol.* **6**, 965-70 (1995).

[66] Huang J-R, Ford H. D, Tatam R. P, ‘Heterodyning of speckle shearing interferometers by laser diode wavelength modulation’, *Meas. Sci. Technol.* **7**, 1721-7 (1996).

[67] Cookson T. J, Butters J. N. and Pollard H. C, ‘Pulsed lasers in electronic speckle pattern interferometry’, *Opt. Laser Technol.* **10**, 119-24 (1978).

[68] Moore A. J, Jones J. D. C. and Valera J. D. R, ‘Dynamic measurements’ in *Digital speckle interferometry and relatedtechniques*, ed. Rastogi P. K, Wiley (2001).

[69] Moore A. J. and Pérez-López C, ‘Low-frequency harmonic vibration analysis with double-pulsed addition electronic speckle pattern interferometry, *Opt. Eng.* **35**:9, 2641-50 (1996).

[70] Schedin S, Pedrini G, Tiziani H. J and Mendoza-Santoyo F, ‘All-fibre pulsed digital holography’, *Opt. Comm.* **165**, 183-8 (1999).

[71] Swain R. and Preater R, ‘Quantitative evaluation of speckle correlation fringes from a flat rotating specimen’, *Proc. SPIE*, **2003**, 113-23 (1993).

[72] Swain R. and Preater R, ‘Investigation of windage heating effects on rotating components using pulsed ESPI’, *Opt. Lasers Eng.* **26** 377-94 (1997).

[73] Pérez-López C, Mendoza-Santoyo F, Pedrini G, Schedin S. and Tiziani H. J, ‘Pulsed digital holographic interferometry for dynamic measurement of rotating objects with an optical derotator’, *Appl. Opt.* **40**:28, 5106-10 (2001).

[74] Pérez-López C, Mendoza-Santoyo F, and Guerrero J. A, ‘Decoupling the *x*, *y* and *z* displacement components in a rotating disc using three-dimensional pulsed digital holography’, *Meas. Sci. Technol.* **14**, 97-100 (2003).

[75] Moore A. J, Hand D. P, Barton J. S. and Jones J. D. C, ‘Transient deformation measurement with electronic speckle pattern interferometry and a high-speed camera’, *Appl. Opt.* **38**:7 1159-62 (1999).

[76] Wu T, Jones J. D. C. and Moore A. J, ‘High-speed phase-stepped digital speckle pattern interferometry using a complementary metal-oxide semiconductor camera’, Appl. *Opt.* **45**:23 5845-55 (2006).

[77] Huntley J. M, Kaufmann G. H. and Kerr D, ‘Phase-shifted dynamic speckle pattern interferometry at 1 kHz’, *Appl. Opt.* **38**:31, 6556-63 (1999).

[78] Krupka R, Walz T. and Ettemeyer A ‘Industrial applications of shearography for inspection of aircraft components’, *NDT.net*, **8**:2 (2003).

[79] Kalms M and Osten W, ‘Mobile shearography system for the inspection of aircraft and automotive components’, *Opt. Eng.* **42**:5, 1188-96 (2003).

[80] Chen F, Lou W. D, Dale M, Petnuinas A, Harwood P. and Brown G. M, ‘High-speed ESPI and related techniques: overview and its application in the automotive industry, *Opt. Lasers Eng.* **40**, 459-85 (2003).

[81] Furlong C. and Pryputniewicz R, ‘Optoelectronic characterization of shape and deformation of MEMS accelerometers used in transportation applications’, *Opt. Eng.* **42**:5, 1223-31 (2003).

[82] Pryputniewicz R, ‘Advances in optoelectronic methodology for micro- and nano- scale measurements’, *Proc. SPIE,* **6616**, 6616-2V (1-15) (2007).

[83] Madjarova V. D, Toyooka S, Chida H and Kadono H, ‘Stress behaviour of ball grid array (BGA) studied by dynamic electronic speckle pattern interferometry (DESPI)’, *Proc. SPIE,* **6616**, 6616-2R (1-5) (2007).

[84] Kemper B, Dirksen D, Avenhaus W, Merker A. and von Bally G, ‘Endoscopic double-pulse electronic-speckle-pattern interferometer for technical and medical intracavity inspection’, *Appl. Opt.* **39**:22, 3899-905 (2000).

[85] Kemper B, Kandulla J, Dirksen D. and von Bally G, ‘Optimization of spatial phase shifting in endoscopic speckle pattern interferometry’, *Opt. Comm.* **217**, 151-60 (2003).

[86] Kishen A, Murukeshan V, Krishnakumar V, Lim C. S. and Asundi A, ‘Digital speckle pattern interferometric (DSPI) and thermo-graphic investigations on the thermal responds in human teeth’, *Opt. Lasers Eng.* 489-500 (2003).

[87] Sabatier J. M, Aranchuk V, Kirkpatrick-Alberts II W. C, ‘Rapid high-spatial-resolution imaging of buried landmines using ESPI’, *Proc. SPIE*, **5415**, 14-20 (2004).

[88] Fricke-Begemann T, Gülker G, Hinsch K. D. and Joost H, ‘Mural inspection by vibration measurements with TV-holography’, *Opt. Lasers Eng.* **32**, 537-48 (2000).

[89] Groves R. M, Osten W, Doulgeridis M, Kouloumpi E, Green T, Hackney S, Tornari V, ‘Shearography as part of a multi-functional sensor for the detection of signature features in movable cultural heritage’, *Proc. SPIE*, **6618**, 6618-10 (1-9) (2007).

[90] Falldorf C, Osten W. and Kolenovic E, ‘Speckle shearography using a multiband light source’, *Opt. Lasers Eng.* **40**, 543-52 (2003).

3. Phase Analysis Techniques

The raw data obtained from a full-field interferometric system is usually a two-dimensional fringe pattern whose values represent the *intensity* of the light incident on the detector's surface. In speckle interferometry, these fringes are termed correlation fringes because they are produced by correlation of speckle interferograms recorded before and after object deformation. The desired quantity in most interferometric measurements is however, encoded in the *phase* of the detected light. In speckle interferometry, this refers to the phase difference between light scattered from the object in its reference and deformed states at each point in the CCD array. Most techniques used to determine the phase produce images in which the pixel values are bound between $-\pi$ and $+\pi$. These images are known as wrapped phase maps. In order to obtain the continuous result that is required to determine the measurand, the 2π phase discontinuities need to be removed. This process is known as phase unwrapping. In speckle interferometry, the presence of high frequency speckle noise means that sophisticated unwrapping algorithms are often required. This chapter presents some of the methods used to determine the phase and discusses some of the algorithms that are used for phase unwrapping.

3.1 Temporal phase stepping

The principle of temporal phase stepping [1] relies on the recording of a series of images with a known phase difference between them. These images are then combined using a phase stepping algorithm to determine the phase at each pixel in the image. Temporal phase stepping offers a simple, reliable and accurate method of phase determination. The limitations of the technique arise from the time required to capture the necessary images. This can prove to be a problem in certain situations, such as in the measurement of dynamic test objects, when pulsed illumination is required or in environments where the amplitude of external vibrations may be high.

3.1.1 Phase stepping techniques

There are a number of methods that have been used to shift the phase of an interferometer. Many of them involve adding a phase modulating device to one of the arms of the interferometer. A commonly used phase modulating device is a piezoelectric transducer (PZT) that is used as a mount for one of the mirrors in a Michelson interferometer. A voltage applied to the PZT causes the PZT to expand resulting in a longitudinal translation of the mirror. This results in a shift in the phase of the light propagating in that arm relative to that propagating in the other arm. Other phase modulating devices include a tilted glass plate, a rotating waveplate or analyzer, or a diffraction grating that is translated laterally [1]. In fibre optic interferometers, one of the fibre arms can be coiled around a cylindrical PZT [2]. Applying a voltage to the PZT causes it to expand thereby stretching the wrapped fibre. This causes a concomitant change in the optical phase relative to the other interferometer arm. An alternative approach exploits the fact that the phase of the output from an interferometer in which the arms are of different length is dependent on the wavelength of the illumination source. If laser diodes are used as the optical source, phase shifting can be achieved by introducing a path length imbalance between the arms of the interferometer, and modulating the modulating the injection current or temperature of the laser diode, which changes the output wavelength of the interferometer [3].

3.1.2 Phase stepping algorithms

The intensity of an interferogram can be described by the equation

$$I(x,y) = I_0(x,y)\left[1+\gamma_0(x,y)\cos\left(\phi(x,y)\right)\right] \tag{3.1}$$

where I_0 is the background intensity, γ_0 is the fringe modulation term and ϕ is the phase. The (x, y) dependencies represent the pixel locations in the image. For a phase stepped interferogram, equation (3.1) becomes

$$I = I_0\left[1+\gamma_0\cos(\phi+\alpha)\right] \tag{3.2}$$

where α represents the magnitude of the phase step. The (x, y) dependencies have been dropped for clarity. Because there are three unknowns, I_0, γ_0 and ϕ, a minimum of three phase stepped interferograms are required to calculate the phase. One of the simplest phase stepping algorithms requires three phase stepped images each with a relative phase step of $2\pi/3$ between them [4]. The three frames can be written as

$$\begin{aligned} I_1 &= I_0\left[1+\gamma_0\cos\left(\phi-\frac{2\pi}{3}\right)\right] \\ I_2 &= I_0\left[1+\gamma_0\cos(\phi)\right] \\ I_3 &= I_0\left[1+\gamma_0\cos\left(\phi+\frac{2\pi}{3}\right)\right] \end{aligned} \tag{3.3}$$

A trigonometric identity is used to obtain

$$\begin{aligned} I_1 &= I_0\left[1+\gamma_0\left(\frac{\sqrt{3}}{2}\sin\phi-\frac{1}{2}\cos\phi\right)\right] \\ I_2 &= I_0\left[1+\gamma_0\cos\phi\right] \\ I_3 &= I_0\left[1+\gamma_0\left(-\frac{\sqrt{3}}{2}\sin\phi-\frac{1}{2}\cos\phi\right)\right] \end{aligned} \tag{3.4}$$

The brackets are expanded to give

$$\begin{aligned} I_1 &= I_0 + I_0\gamma_0 \frac{\sqrt{3}}{2}\sin\phi - \frac{I_0\gamma_0}{2}\cos\phi \\ I_2 &= I_0 + I_0\gamma_0 \cos\phi \\ I_3 &= I_0 - I_0\gamma_0 \frac{\sqrt{3}}{2}\sin\phi - \frac{I_0\gamma_0}{2}\cos\phi \end{aligned} \tag{3.5}$$

The $\sin\phi$ term is then isolated by subtracting the third frame from the first frame to give

$$\sin\phi = \frac{I_3 - I_1}{\sqrt{3}I_0\gamma_0} \tag{3.6}$$

the $\cos\phi$ term is isolated in a similar way giving

$$\cos\phi = \frac{2I_2 - I_1 - I_3}{3I_0\gamma_0} \tag{3.7}$$

Equations (3.6) and (3.7) are combined to give

$$\tan\phi = \sqrt{3}\,\frac{I_3 - I_1}{2I_2 - I_1 - I_3} \tag{3.8}$$

The phase can be calculated from

$$\phi = \tan^{-1}\left(\sqrt{3}\,\frac{I_3 - I_1}{2I_2 - I_1 - I_3}\right) \tag{3.9}$$

The phase calculated in this manner is bound between the values of –π/2 and +π/2. To simplify and speed up the unwrapping process it is desirable to have the phase values bound between the values of –π and +π. To do this a modified arctangent function needs to be used which takes into account the signs of the sine and cosine values. This function is known as atan2 in many programming languages (e.g. Matlab). Simulated fringe patterns, corresponding to the three intensity distributions given in equation (3.3) are shown in top row of figure 3.1. The wrapped phase map calculated from these fringe patterns using the phase stepping algorithm in equation (3.9) is also shown. In the wrapped phase map, black pixels correspond to a wrapped phase of –π and white corresponds to a wrapped phase of +π.

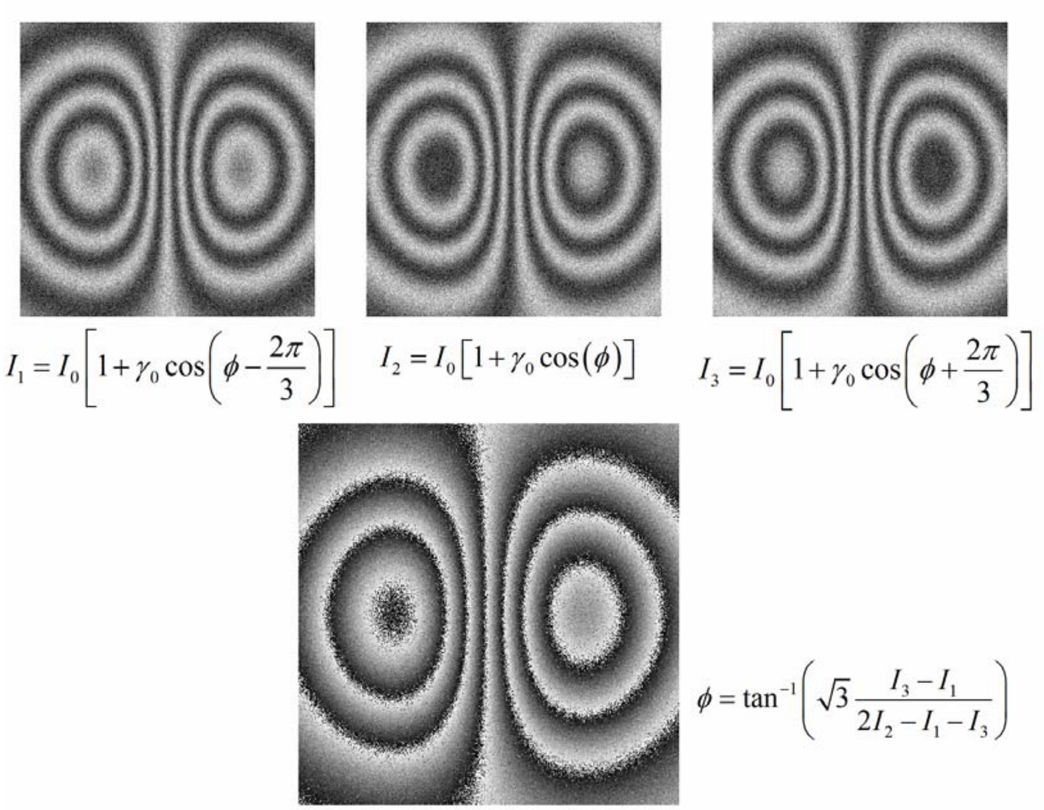

Figure 3.1 *The principle of phase stepping: Three simulated fringe patterns with a relative phase difference $2\pi/3$ between them (top row) are combined using a three step phase stepping algorithm (equation 3.9) to produce the modulo 2π wrapped phase map.*

Other phase stepping algorithms include a three-step algorithm using a π/2 phase step and a four-step algorithm [5]. The phase using the three step algorithm is calculated using

$$\phi = \tan^{-1}\left(\frac{I_3-I_2}{I_1-I_2}\right) \tag{3.10}$$

and the phase using the four-step algorithm is found by

$$\phi = \tan^{-1}\left(\frac{I_4-I_2}{I_1-I_3}\right) \tag{3.11}$$

Carré's [6] original four-step algorithm has the advantage that the exact phase step between the frames does not need to be known provided that it is consistent for each step. The phase is calculated using

$$\phi = \tan^{-1}\left\{\frac{\sqrt{\left[(I_1-I_4)+(I_2-I_3)\right]\left[3(I_2-I_3)-(I_1-I_4)\right]}}{(I_2+I_3)-(I_1+I_4)}\right\} \tag{3.12}$$

Another phase stepping algorithm that is often used is the Schwider-Hariharan algorithm [7, 8]. This algorithm requires five intensity frames with a relative phase shift of π/2 between them. The phase is calculated using

$$\phi = \tan^{-1}\left[\frac{2(I_2 - I_4)}{2I_3 - I_5 - I_1}\right] \tag{3.13}$$

This algorithm is useful because it minimizes errors due to miscalibration of the phase shifting device. A number of other phase stepping algorithms are discussed in a review by Dorrio and Fernandez [9]. De Groot [10] presents an analysis of a range of phase stepping algorithms ranging from 4 to 15 steps. He also derives a 101 step algorithm that is highly resistant to errors although not very practical in modern phase shifting interferometry.

3.1.3 Phase stepping in speckle interferometry

Temporal phase stepping was introduced to speckle interferometry in 1985 by Nakadate and Saito [11] and Creath [12]. In the method of Nakadate and Saito, phase stepping is applied to the reference frames only, and combined with a single signal frame (or vice-versa). This method is also known as the 'phase of differences' [13] method because the phase is calculated after correlation of the signal and reference frames. In the method of Creath, phase stepping is applied to both the signal and reference frames. This method is also known as the 'difference of phases' [13] method because the signal and reference phase is calculated independently. The phase difference is then determined by subtracting the signal phase from the reference phase. The 'difference of phases' method produces phase maps of a higher quality than the 'phase of differences' method. An advantage of the 'phase of differences' method is that dynamic measurements can be made provided the target is stationary for the duration required to obtain the phase stepped reference frames, since only one signal frame is needed. The phase stepped correlation fringe patterns are automatically generated with this technique.

3.2 Spatial phase stepping

Spatial phase stepping [14] involves recording a set of phase-stepped images simultaneously. This can be done either by using a system that incorporates multiple CCD cameras [15], or by spatially multiplexing the various phase-stepped images onto different regions of a single camera [16]. The phase stepped images are then recombined using the same arctangent phase stepping algorithms described above. The main advantage of spatial phase stepping over temporal phase stepping is that all the required phase information is captured within the time taken to record a single camera frame. This property is necessary for the measurement of transient, dynamic test surfaces and is also useful when making measurements in situations where there is a high degree of vibration, rigid body motion or other environmental disturbances.

The multiple camera solution is expensive because at least three cameras are required. In addition, sophisticated optical arrangements involving for example polarization optics are often required to apply the phase shift and to guide the beams to the different cameras. The phase calculation also requires that the individual images are mapped to each other to a high accuracy to avoid introducing uncertainties due to inadequate pixel registration. An advantage of this technique is that the spatial resolution associated with temporal phase stepping is retained since the whole of the CCD array can be used. Spatially multiplexing phase stepped images onto a single CCD is another method that is beneficial because it uses less optical components. However, because all of the images are recorded on the same CCD frame, the spatial resolution of each image is less than it would be if the whole CCD array was used to record each individual image. This issue can be improved by using a camera with a higher number of pixels.

3.2.1 Single camera phase stepping systems

A holographic interferometry system, developed by Kujawinska and Robinson [16], is shown in figure 3.2. In this system, spatial phase shifting is achieved by introducing a diffraction grating into the object beam in front of a holographic plate and a CCD camera. The diffraction grating serves to divide the object beam into three separate beams located in the 0 and ±1 diffracted orders. The diffracted beams interfere with light from a reference beam that illuminates the hologram plate. The three separate interferograms are then imaged onto the CCD camera. The phase shift is applied by a transverse displacement of the diffraction grating between the recording of the signal and reference frames. The relationship between the phase shift and the magnitude of the displacement is dependent on the period of the diffraction grating. The grating is displaced enough to induce a relative phase difference of $2\pi/3$ between the three images recorded by the CCD. The phase difference can then be obtained using the three-step phase stepping algorithm of equation (3.9).

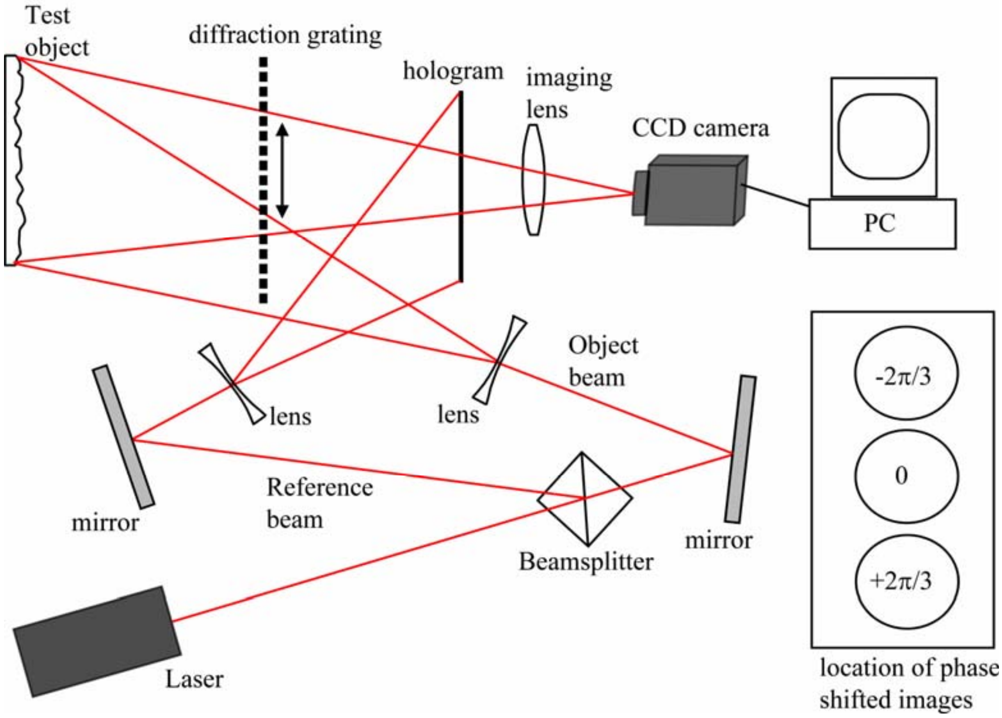

Figure 3.2 *Optical arrangement of the holographic interferometer developed by Kujawinska and Robinson for spatial phase shifting [16]. The diffraction grating is displaced between frames to induce a 2π/3 relative phase shift between the three images recorded by the CCD.*

An ESPI system incorporating spatial phase shifting was developed by García *et al* [17, 18]. This system used a holographic optical element (HOE) to achieve both beam division and phase shifting. The HOE was a computer generated hologram which was used to diffract the incident beam into four separate beams and apply a relative phase shift to each. An advantage of the method presented in this paper over the diffraction grating technique described previously [16] is that no translation of the grating is needed between exposures. The system that they used is illustrated in figure 3.3. In this system the holographic element is placed in the path of the object beam between the imaging lens and the recombining beamsplitter.

The HOE was constructed from photoresist on a glass substrate and was calculated using a Fourier transform method based on the Gerchberg-Saxton algorithm. It was calculated to provide equal intensity in each of the ±1 diffracted orders with a relative phase shift of $\pi/2$ between each of the orders. The phase step was found to be dependent on the tilt of the HOE, therefore a mount was constructed that allowed x and y rotation of the element. The mount also allowed z rotation to ensure accurate alignment of the diffracted orders with the CCD array. The distance between the HOE and the CCD was chosen to give optimum separation between the images in each quadrant of the CCD array. In order to sample the orders equally the overall magnification of the system needed to be reduced. This was achieved by placing two negative lenses, with focal lengths of -50mm, between the object and the zoom lens. Because the phase step is present in the images both before and after deformation it is necessary to subtract data from a single reference order from each object order, rather than simply subtracting corresponding orders, to generate correlation fringes. The phase was then calculated using the Carré algorithm (equation (3.12)) although other four-step algorithms with a relative phase difference of π/2 between them could be used.

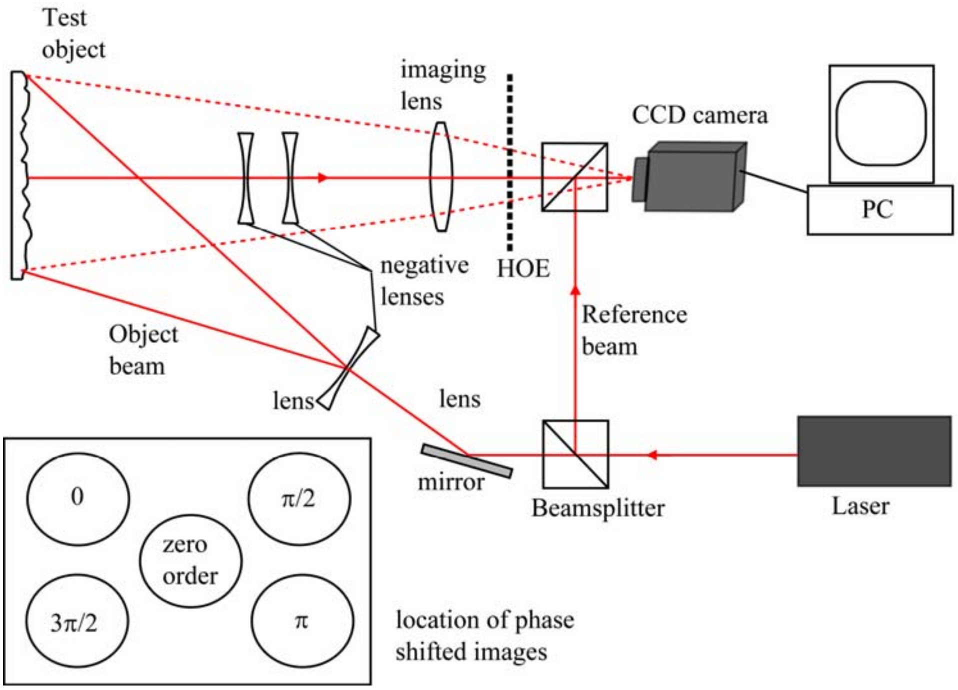

Figure 3.3 *Optical arrangement of the spatial phase shifting ESPI system based on a holographic optical element developed by García et al [17, 18]. The locations of the four phase shifted images in the ±1 diffracted orders on the CCD are shown. The central term corresponds to the zero order that is transmitted straight through the HOE and is not used in the phase calculation.*

Millerd *et al* [19] describe a polarization sensitive Twyman-Green interferometer which incorporates spatial phase shifting using a pixelated phase mask which is placed in front of the camera. This instrument was made commercially available by 4-D Technologies. The pixelated phase mask consists of a micropolarizer array divided into unit cells. Each unit cell consists of four pixels, each containing a wire grid polarizer orientated such that a relative phase shift of π/2 is induced between each pixel. The four elements of the unit cell produce phase shifts of 0, π, π/2 and 3π/2 respectively. If light incident on the phase mask is circularly polarized, the mask can be used directly, otherwise if the light is linearly polarized, a quarter-wave plate is required. The phase mask used by Millerd *et al* consists of a combination of half-wave and quarter-wave plates to achieve quarter-wave retardation over a broad range of wavelengths. The image recorded by the CCD camera was post-processed to reconstruct the four phase-stepped fringe patterns from which the phase could be calculated. An alternative processing method involved using windowed convolution algorithm can also be used to determine the phase with improved spatial resolution. Wyant [20] describes an earlier version of their Twyman-Green interferometer, which employs spatial phase shifting in similar way to that described by García *et al* [17, 18]. This interferometer uses a HOE for beam division with the phase shift being applied by a birefringent phase mask. Rather than consisting of unit cells, this phase mask is divided into four quadrants with each quadrant applying a multiple of π/2 phase shift.

Other authors who describe the use of diffractive elements in spatial phase shifting interferometry include Kitchen and Dam-Hansen [21], who used a holographic optical element to divide and phase shift a beam for the purpose of measuring angular deflections from a mirror, and Kemao *et al* [22], who used a Ronchi phase grating in conjunction with polarization optics for beam division and phase shifting in an interferometer for dynamic measurements.

3.3 Spatial carrier techniques

In the spatial carrier technique, a carrier frequency is introduced to the recorded intensity distribution producing a high frequency fringe pattern. The carrier frequency can be introduced, for example, by tilting one of the beams in the interferometer [23] or by displacing the optical source along the optical axis in the interval between recording frames [24]. The recorded carrier fringe patterns are then analyzed using a Fourier transform in order to recover the phase.

3.3.1 The Takeda method

Fringe pattern analysis techniques based on the Fourier transform were originally developed the early 1980's by Roddier and Roddier [25] and Takeda *et al* [26]. The intensity of a carrier fringe pattern can be represented by the equation

$$I(x,y) = I_0(x,y) + \gamma_0(x,y)\cos\left[\phi(x,y) + 2\pi f_0 x\right] \qquad (3.14)$$

where I_0 is the background intensity, γ_0 is the fringe modulation, ϕ is the desired phase term and f_0 is the frequency of the carrier fringes. The interferogram can be weighted with a Hanning or Hamming window to eliminate the effects of the discontinuities at the edges of the fringe pattern. The fringe pattern can be rewritten as

$$I(x,y) = I_0(x,y) + c(x,y)\exp(2\pi i f_0 x) + c^*(x,y)\exp(-2\pi i f_0 x) \qquad (3.15)$$

where

$$c(x,y) = \frac{\gamma_0(x,y)}{2}\exp\left[i\phi(x,y)\right] \qquad (3.16)$$

and the * represents the complex conjugate. The Fourier transform of equation (3.15) taken along the *x* axis gives

$$\Lambda(f_x,y) = \Lambda_0(f_x,y) + C(f_x - f_0,y) + C^*(f_x + f_0,y) \qquad (3.17)$$

where Λ and Λ_0 are the Fourier transform of I and I_0 respectively and C is the Fourier transform of c. The spatial frequency in the x direction is represented by f_x. A 1-D representation of the Fourier spectrum is shown in figure 3.4.

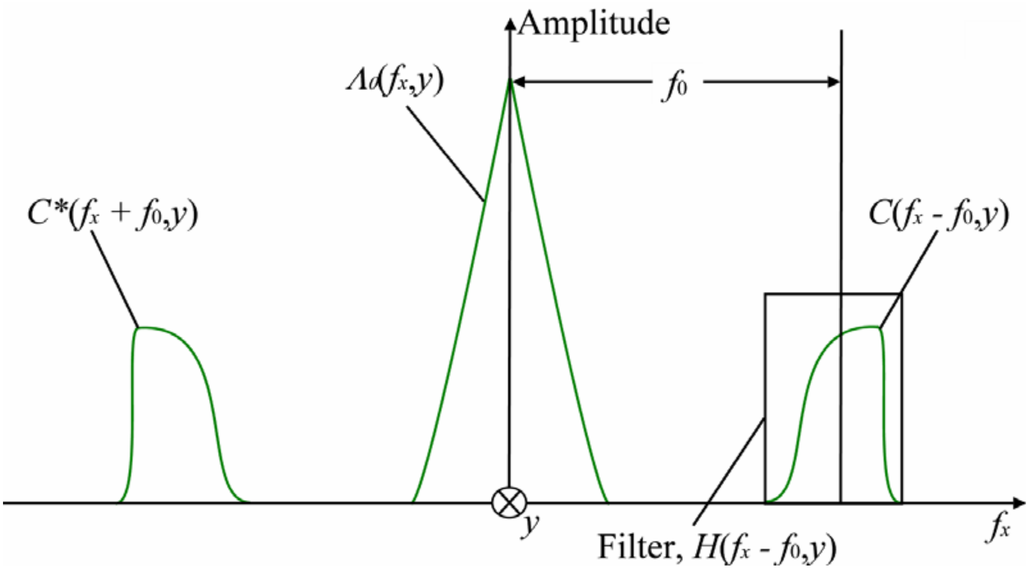

Figure 3.4 *One-dimensional representation of the Fourier transform of a carrier fringe pattern.*

The central point contains the DC term, which is equal to the sum of all the values in the original fringe pattern. This term is significantly greater than all other values in the spectrum and is therefore often deleted when visualizing the Fourier spectrum so that the spectral features can be seen in a scaled image. The region surrounding the DC term corresponds to the Fourier transform of the background term, which is the first term on the right hand side of equation (3.17). The two features to either side of the background term correspond to the second and third terms in equation (3.17) and it is these terms that contain the desired phase information. Provided that the spatial variation of the background, modulation and phase terms are small compared to the carrier frequency, then these side features will be well separated from the background term in frequency space. The magnitude of the separation is equal to the carrier frequency. To determine the phase, one of the side features is isolated and translated back to the origin by applying a filter function given by

$$H\left(f_x - f_0, y\right) \qquad (3.18)$$

Translating the isolated spectral feature removes the carrier frequency so that, when the inverse Fourier transform is calculated, the high frequency fringe pattern is no longer present. The filter function also has the effect of removing the unwanted background term and also removes noise components outside the filter function. Taking logarithms of the inverse transformed spectrum, we obtain

$$\log\left[c\left(x,y\right)\right] = \log\left[\frac{\gamma_0\left(x,y\right)}{2}\right] + i\phi\left(x,y\right) \qquad (3.19)$$

The phase contained within the imaginary part of (3.19) is now separated from the modulation term and can be obtained using

$$\phi(x,y) = \tan^{-1}\left(\frac{\text{Im}\left[c(x,y)\right]}{\text{Re}\left[c(x,y)\right]}\right) \tag{3.20}$$

The phase is obtained wrapped modulo 2π. Macy extended this technique to two-dimensional fringe patterns in 1983 [27]. An example of the technique applied to a simulated two-dimensional fringe pattern is illustrated in figure 3.5. The fringe patterns shown in figure 3.5 where simulated using Matlab. This work is described in appendix A.

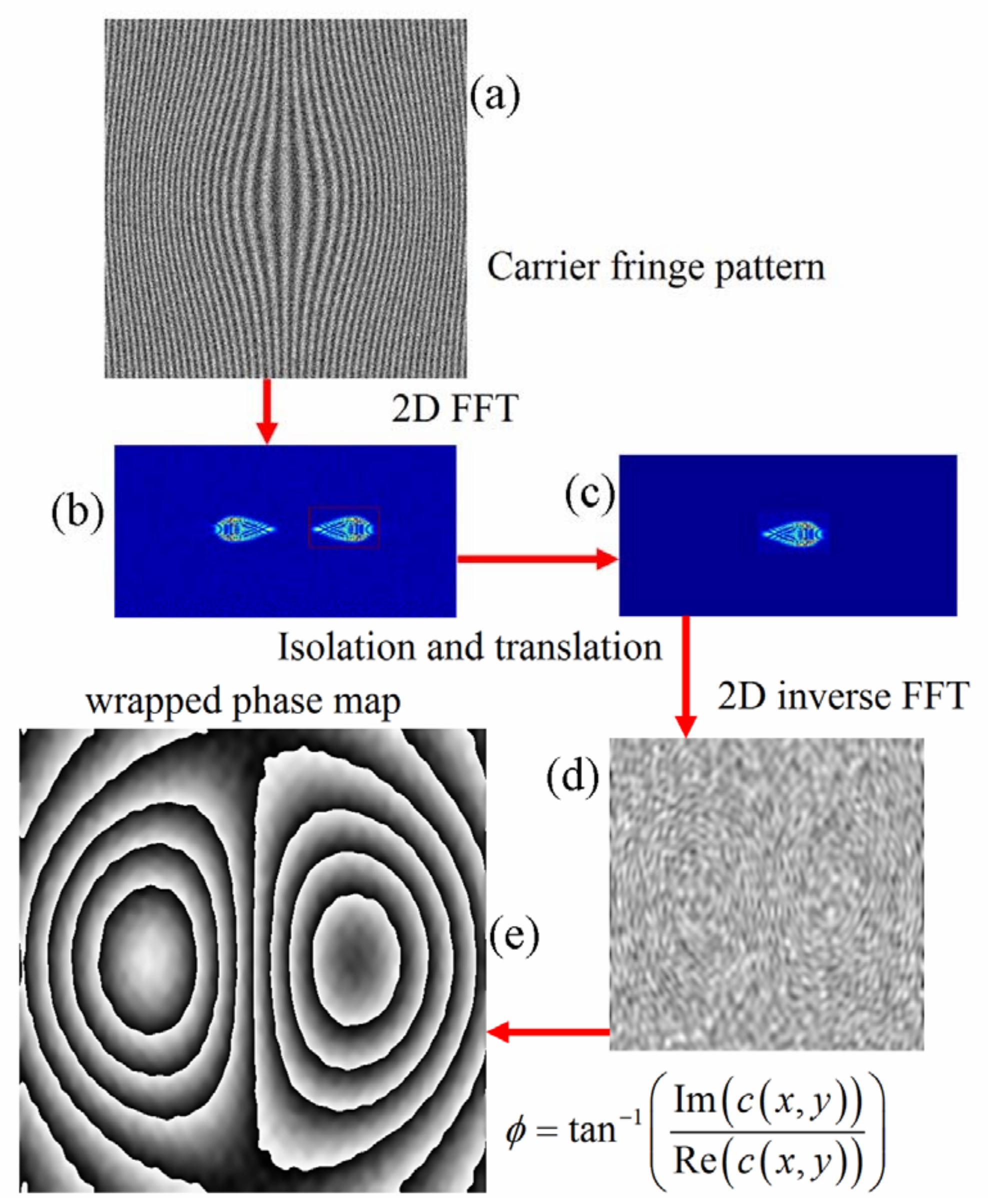

Figure 3.5 *The two-dimensional phase demodulation scheme based on the technique of Takeda: The 2-D FFT of a carrier fringe pattern is calculated and one of the side spectra is isolated and translated to the centre of the image. The inverse 2-D FFT is calculated from which the wrapped phase is obtained.*

Figure 3.5(a) shows a high frequency carrier fringe pattern modulated by a phase distribution. The two-dimensional Fourier transform is calculated using the fast Fourier transform (FFT) algorithm. The DC term is deleted to reveal the Fourier spectrum. Since the background of the fringe pattern is uniform, only the two side spectra are observed. The region surrounded by the red box in figure 3.5(b) is isolated and then translated to the centre of the image, as shown in figure 3.5(c). The inverse two-dimensional FFT of the translated spectrum is calculated and the phase is derived using equation (3.20). Figure 3.5(d) shows the magnitude of the inverse Fourier transform of the spectrum. The wrapped phase map is shown in figure 3.5(e).

Notice that the random noise present in the initial carrier fringe pattern is no longer present in the wrapped phase map, unlike in the temporal phase stepping scheme of figure 3.1. This is due to the effect of filtering in frequency space. The effect of noise in the Fourier transform technique is to introduce distortions in the phase fringe discontinuities. Figures 3.6 (a), (b) and (c) show wrapped phase maps derived from carrier fringe patterns containing no noise and added random noise that is 2.5 and 5 times the noiseless fringe amplitude, respectively. As the noise increases the distortions in the fringe discontinuities and eventually leads to breaks in the fringes which can cause problems later in the unwrapping process.

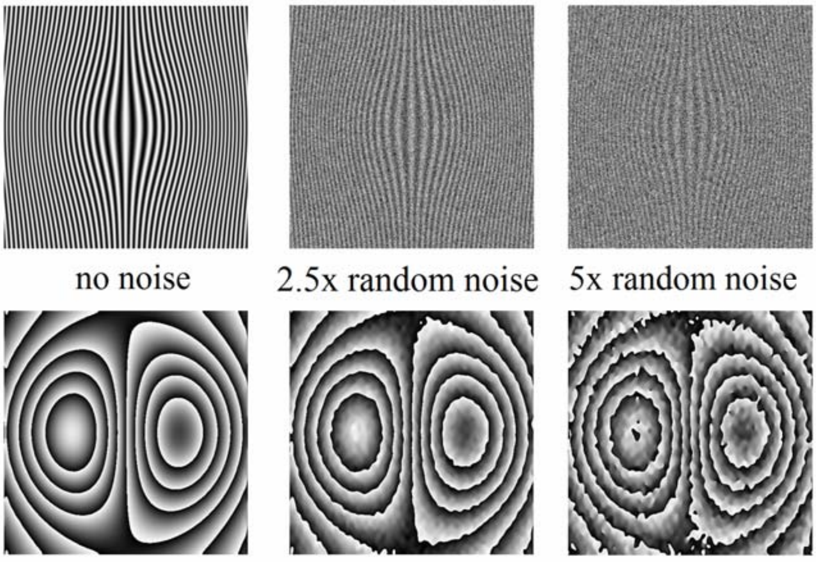

(a) **(b)** **(c)**

Figure 3.6 *The effect of noise on the wrapped phase maps obtained with the Fourier transform technique.*

<u>*3.3.2 The phase subtraction method*</u>

One of the main issues with the Takeda technique, because it was designed with one-dimensional fringe patterns in mind, is that it requires that the unmodulated carrier fringes are perfectly straight. Generating perfectly straight carrier fringes in an experimental arrangement can be problematic. If the carrier fringes are curved, the calculation cannot distinguish between the fringe curvature and the modulation of the fringes caused by the phase distribution of interest. The resulting phase map will therefore contain errors due to the fringe curvature. Figure 3.7 shows the effect of increasing curvature on the demodulated phase map. The top row shows the simulated carrier fringe patterns without the phase term present to illustrate the curvature of the fringes. The far left fringe pattern is straight with the curvature increasing from left to right. The row below shows the demodulated phase maps. It be clearly seen that as the fringe curvature increases, the further the phase fringe pattern diverges from the expected distribution.

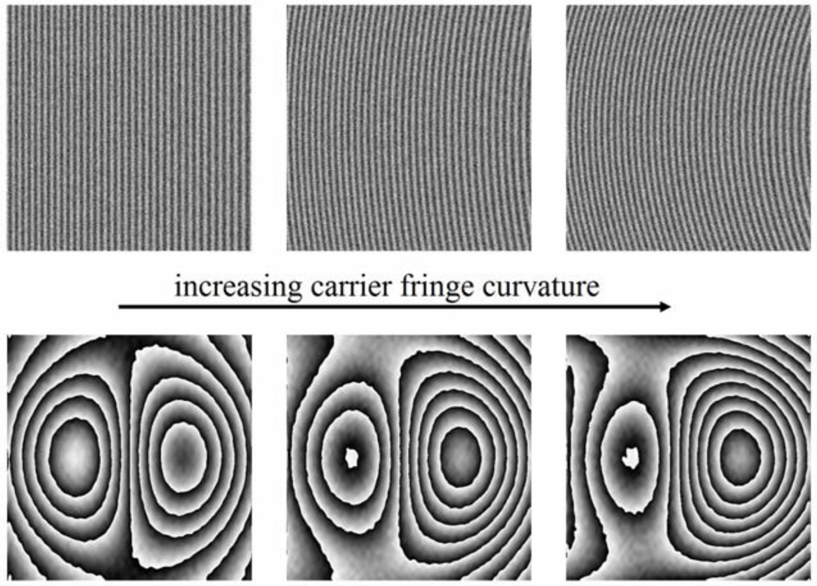

Figure 3.7 *The effect of carrier fringe curvature on the demodulated wrapped phase map using the two-dimensional Takeda technique.*

Another issue with the Takeda technique is that the carrier frequency has to be constant across the image. This is because the carrier fringes are removed by translating the side spectrum to the origin in frequency space by an amount equal to the carrier frequency. An alternative method of removing the carrier frequency involves calculating the phase independently for the fringe patterns in the reference and deformed states and obtaining the phase difference by subtracting the two [28, 29]. This method can be used even if the carrier fringes are slightly curved or of non-constant period across the image, provided that the carrier frequency remains constant between the two states, expect for the modulation due to the phase distribution. This method is illustrated in figure 3.8.

The two-dimensional FFT is calculated for both the unmodulated and modulated carrier fringe patterns, corresponding to the reference and signal images respectively. Note that in this example the unmodulated carrier fringes are slightly curved. One of the side spectra in each of the transformed images is selected and isolated. In this method the side feature is not translated and instead remains where it is in frequency space. The inverse two-dimensional FFT is calculated and the phase is calculated for both signal and reference images using equation (3.20). The phase difference contains phase jumps wrapped between the values of $\pm 2\pi$, as shown in the penultimate image in figure 3.8. These can be removed simply by rewrapping the phase to ±π. This results in the wrapped, modulo 2π, phase map.

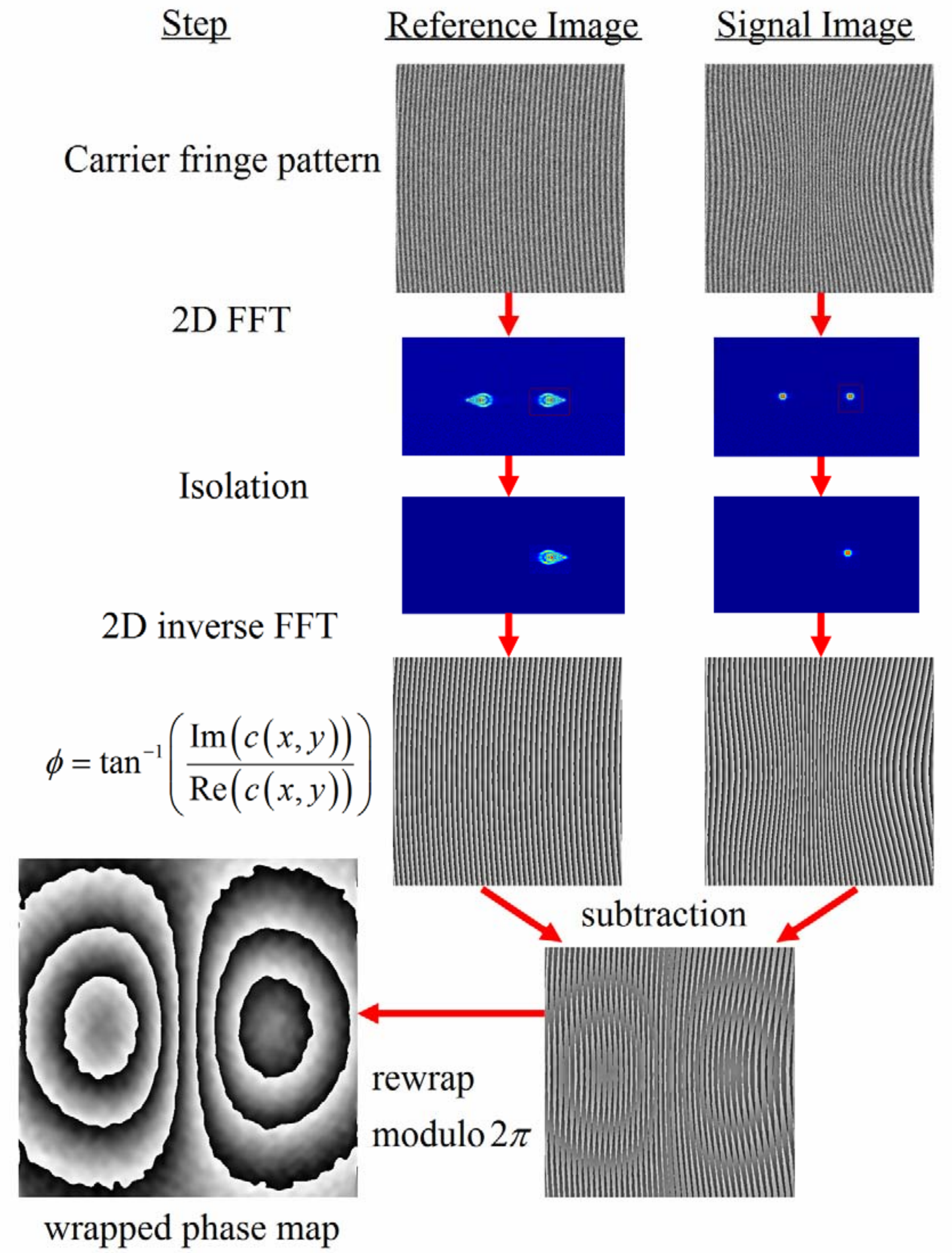

Figure 3.8 *The two-dimensional phase demodulation scheme based on the technique of phase subtraction: The 2-D FFT of carrier fringe patterns corresponding to reference and signal images is calculated. The phase from each is calculated independently from the isolated side spectrum and the phase difference is obtained by subtraction.*

3.3.3 Carrier fringe generation

One method of generating carrier fringes that is often used with shearography is to translate the optical source along its axis in between the recording of the signal and reference frames [24, 30]. In practise, this is achieved by manually translating the diverging lens that is used to expand the beam to illuminate the region of interest on the target surface. Before translating the lens, the radius of curvature of the illuminating wavefront is r_1. After translating the lens the illuminating wavefront has a radius of curvature r_2. Subtracting the speckle patterns recorded with the two different radii of curvature yields a carrier fringe pattern in which the carrier frequency is given by [24]

$$f_0 \approx \frac{d \cdot \mathrm{d}x}{MR^2\lambda} \tag{3.21}$$

where M is the magnification of the optical system, dx is the magnitude of the image shear and d is the distance between the two illumination points. R represents the radius of curvature of the illuminating wavefront at the object surface before and after translation of the lens, which are assumed to be equal for the purposes of the calculation.

One of the issues with this carrier fringe generation technique is the need to physically translate the diverging lens between signal and reference frames. This is not practical in dual-pulse speckle interferometry, as the separation between signal and reference pulses can be as short as 1 μs. A solution to this problem was presented by Fernández *et al* [31]. A schematic representation of their optical arrangement is shown in figure 3.9. In this system, light from two pulsed Nd:YAG laser cavities is recombined at beamsplitter 1. A small tilt of one of the mirrors after the output of laser cavity 1 ensures that the pulse from this source follows a different optical path to the one traversed by the pulse from laser cavity 2. The pulses are each diverged by two negative lenses located at different relative positions along the optical axis. The pulses are made collinear in beamsplitter 2 before illuminating the target. The separation d between one negative lens and its image in beamsplitter 2 determines the frequency of the carrier fringes. A similar system, using laser beam delivery arms to deliver laser pulses to a recombining polarizing beamsplitter was presented by Groves *et al* [32]. In this system, the carrier frequency was controlled by different relative divergence of the beams exiting the laser delivery arms. This was achieved by placing negative lenses of different powers at the outputs of the two laser delivery arms.

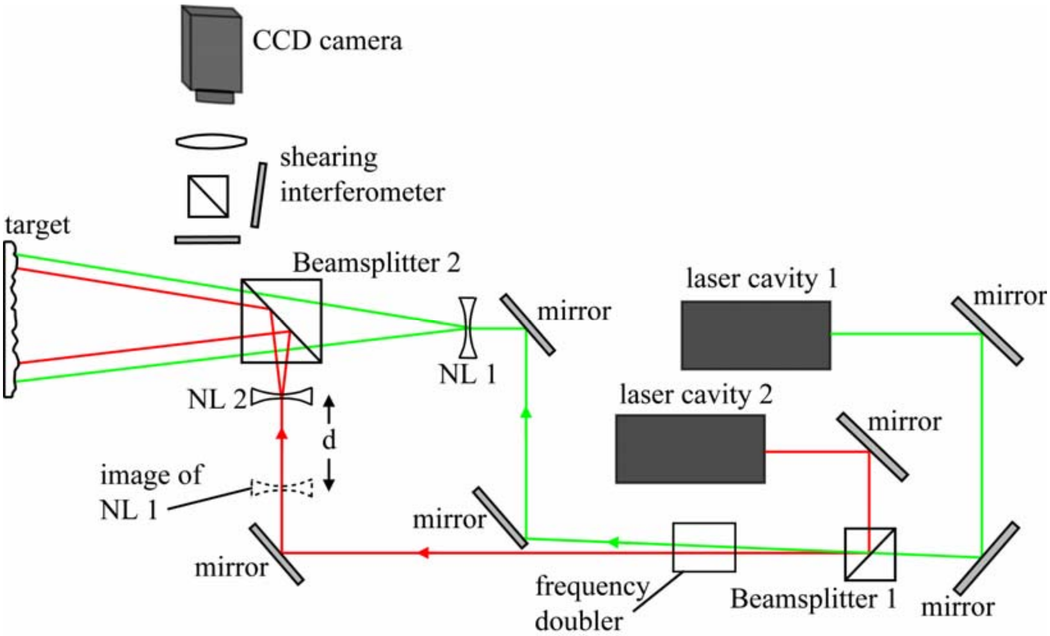

Figure 3.9 *Dual-pulsed shearography arrangement for the generation of carrier fringes [30]. NL = negative lens, d = effective lens separation. Red and green represent the different optical paths of the pulses from laser 1 and laser 2.*

Another carrier fringe generation method that is often used with ESPI involves tilting the reference beam in the interferometer. This can be done between signal and reference frames like in the source translation method. Manually tilting the reference beam is impractical when making dual pulsed measurements because of the short pulse separation. One solution previously described was to employ a Pockels cell to provide fast electro-optic switching between linear and tilted reference beams [33]. The Pockels cell was used to switch between orthogonal linear polarization states. Depending on the polarization state, light was either transmitted through or reflected from a polarizing beamsplitter after which it was directed to one of two mirrors. One mirror was aligned normally to the beam and the other was aligned at a slight angle.

Carrier fringes can also be generated by tilting the reference beam before the measurement to produce a linear phase variation across the CCD array [23, 29, 34]. If the speckle size is sufficiently large, a high frequency carrier fringe pattern is observed with the fringes crossing the individual speckles. In this way, the carrier fringe pattern is produced without the need to subtract frames. The speckle size needs to be at least six times the pixel size [35] to ensure that each speckle is sampled at least twice by the carrier fringes. The speckle size can be increased by placing an aperture in front of the imaging lens. The size and shape of the aperture determine the size and shape of the spectral features in frequency space. For this reason, rectangular apertures are often used [29, 35], because, when using a rectangular CCD array, rectangular spectral features maximize the available area in the FFT array. Variable apertures are also used and have the advantage that the optimum spectral feature size can be chosen. Circular irises are common and therefore often used for this purpose [23, 34].

It is not possible to use this spatial phase variation technique to generate the carrier frequency with conventional shearography arrangements since there is no reference beam. The technique can be introduced, however, by incorporating a Mach-Zehnder shearing interferometer [35-37] which enables independent control of the two arms of the interferometer. The carrier frequency can be generated by arranging the Mach-Zehnder so that there is sufficient angle between the beams to produce a carrier frequency. This is done by either tilting one of the mirrors [35, 37] or translating one of the mirrors [36].

The advantage of this technique is that a high carrier frequency can be generated easily so that it is straightforward to obtain a good separation of the spectral features in frequency space. The drawback is that, because a small aperture is required to increase the speckle size, high optical powers are required to compensate for light lost at the aperture.

3.4 Filtering Techniques

In speckle interferometry, filtering is often applied to improve the quality of the fringe patterns and to reduce the effect of high frequency noise. This section describes some of these filtering techniques.

3.4.1 Low pass and high pass filtering

A low pass filter blocks out high frequency components and only allows frequencies below a certain threshold to pass. In image processing, the low pass filter is used to smooth or blur images. In speckle interferometry, it can be used to remove high frequency speckle noise. It operates via the two dimensional convolution of the image with the low pass filter kernel. The simplest is the 3x3 kernel given by [38]

$$\text{Low pass filter kernel} = \frac{1}{9}\begin{bmatrix} 1 & 1 & 1 \\ 1 & 1 & 1 \\ 1 & 1 & 1 \end{bmatrix} \qquad (3.22)$$

The larger the dimensions of the filter kernel, the greater it’s smoothing effect. The low pass filter essentially works by averaging the values of pixels within a neighbourhood equal to the kernel size.

A high pass filter cuts out low frequency components and is used to enhance detail in digital images. In speckle interferometry it can be used to reduce the background and enhance fringe contrast. As with the low pass filter, it operates via the convolution of the image with a high pass filter kernel. The 3x3 high pass filter kernel is given by [38]

$$\text{High pass filter kernel} = \frac{1}{9}\begin{bmatrix} -1 & -1 & -1 \\ -1 & 9 & -1 \\ -1 & -1 & -1 \end{bmatrix} \qquad (3.23)$$

Figure 3.10 shows the effect of low and high pass filtering on a simulated fringe pattern.

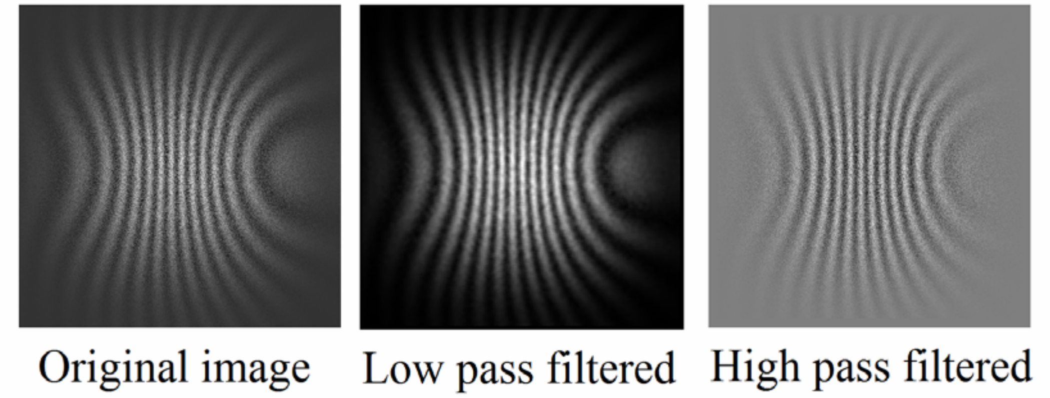
Original image Low pass filtered High pass filtered

Figure 3.10 *The effect of low pass (centre) and high pass (right) filtering on a simulated fringe pattern (left).*

Another filter of interest is the Sobel filter, which is used in image processing to detect edges. The two Sobel filter variants are used for the detection of horizontal and vertical edges and their kernels are given by [38]

$$\text{Vertical Sobel filter } = \begin{bmatrix} -1 & 0 & 1 \\ -2 & 0 & 2 \\ -1 & 0 & 1 \end{bmatrix} \quad \text{Horizontal Sobel filter } = \begin{bmatrix} 1 & 2 & 1 \\ 0 & 0 & 0 \\ -1 & -2 & -1 \end{bmatrix} \tag{3.24}$$

3.4.2 Filtering phase fringe patterns

The most common way of filtering wrapped phase fringe patterns is by the use of a sine-cosine filter. This involves calculating the sine and cosine of the wrapped phase map and applying a low pass filter two or three times to the sine and cosine fringes before recalculating the phase with the four quadrant arctangent function. The problem with this method is that over-filtering can lead to degradation of the fringe discontinuities. This degradation can often occur before the phase map has been adequately filtered. Adequate filtering is required to effectively unwrap the phase map using an unwrapping algorithm. The effect of raw and filtered phase maps on different unwrapping algorithms is investigated in chapter 5. Aebischer and Waldner [39] introduced a simple modification to the technique that gives an improvement in performance. Their method is to apply a small low pass filter kernel up to 20 or 30 times to the sine and cosine fringes with an intermediate phase recalculation after each filter iteration. This technique has the effect of an adaptive filter whereby regions of low fringe density are more heavily filtered than regions of high fringe density. Figure 3.11 shows the effect of applying Aebischer and Waldner’s iterative sine-cosine filter to a noisy simulated phase stepped phase map. For comparison, phase maps are shown after the application of a single pass of a 19x19 low pass filter and 30 passes of a 3x3 low pass filter. Over filtering is observed to smear out the high fringe density regions at the centre of the image unless the intermediate phase recalculation is made.

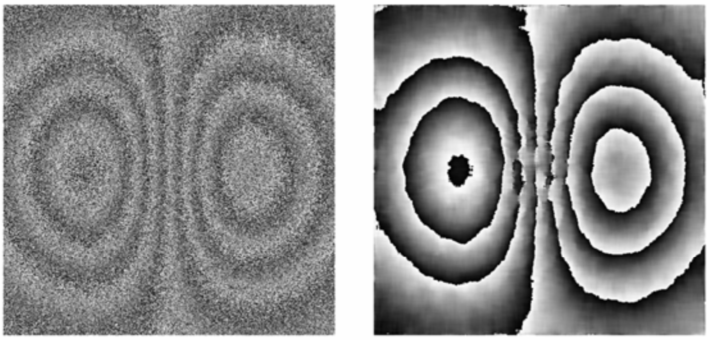

Original phase map 1 pass of 19x19 low pass filter

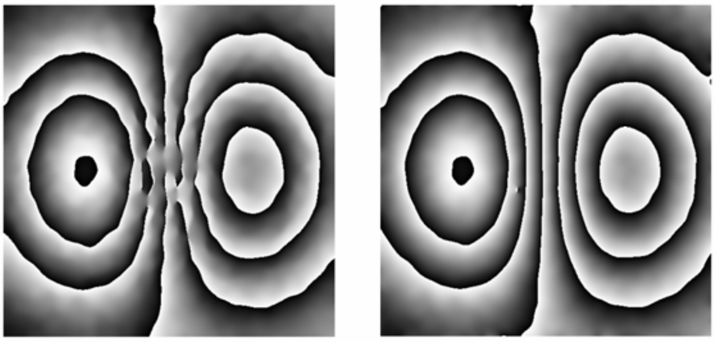

30 passes of 3x3 low pass filter 30 passes of 3x3 low pass filter with intermediate phase calculation

Figure 3.11 *Filtering a noisy phase map with different low pass filters. Over filtering leads to degradation of the central high density fringes unless an intermediate phase recalculation is made between repetitive applications of a small filter kernel.*

Kemao *et al* [40] discuss the relative merits of filtering the constituent fringe patterns in a phase stepped map or filtering the final phase map. They concluded that filtering the fringe patterns before application of the phase stepping algorithm was the better method for wrapped phase maps which possess fringe discontinuities, since filtering the phase map blurs the fringe discontinuities.

3.4.3 Windowed Fourier filtering

Windowed Fourier filtering (WFF) is a powerful filtering method based on the windowed Fourier transform (WFT). The use of the WFT to process two-dimensional interferometric data was developed by Kemao [41-44]. The windowed Fourier transform, also known as the short-term Fourier transform, in one dimension is written as [41]

$$Sf\left(u,\omega_x\right)=\int_{-\infty}^{\infty} f\left(x\right)g\left(x-u\right)\exp\left(-i\omega_x x\right)\mathrm{d}x \tag{3.25}$$

where $f(x)$ is the signal to be transformed, ω_x is the spatial frequency in the x direction and $g(x-u)$ is a window function of spatial extent u which is often chosen to be Gaussian. The inverse WFT is given by [41]

$$f\left(x\right)=\frac{1}{2\pi}\int_{-\infty}^{\infty}\int_{-\infty}^{\infty}Sf\left(u,\omega_x\right)g\left(x-u\right)\exp\left(\mathrm{i}\omega_x x\right)\mathrm{d}\omega_x\mathrm{d}u \qquad (3.26)$$

The main difference between the windowed Fourier transform and the standard Fourier transform is the window function which allows the signal to be broken down into blocks and processed separately. The advantage of processing individual blocks is that the signal in one position will not affect the signal in another position [41], unlike with the global operation of the standard Fourier transform. To use the WFT for the purpose of filtering, the spectrum is thresholded so that low amplitude frequency components are set to zero. Figure 3.12 shows the use of windowed Fourier filtering on simulated phase maps obtained using temporal phase stepping and the spatial carrier technique. The Matlab code for the windowed Fourier transform is provided in [44] and the algorithm for generating the fringe patterns used in this example is given in [41].

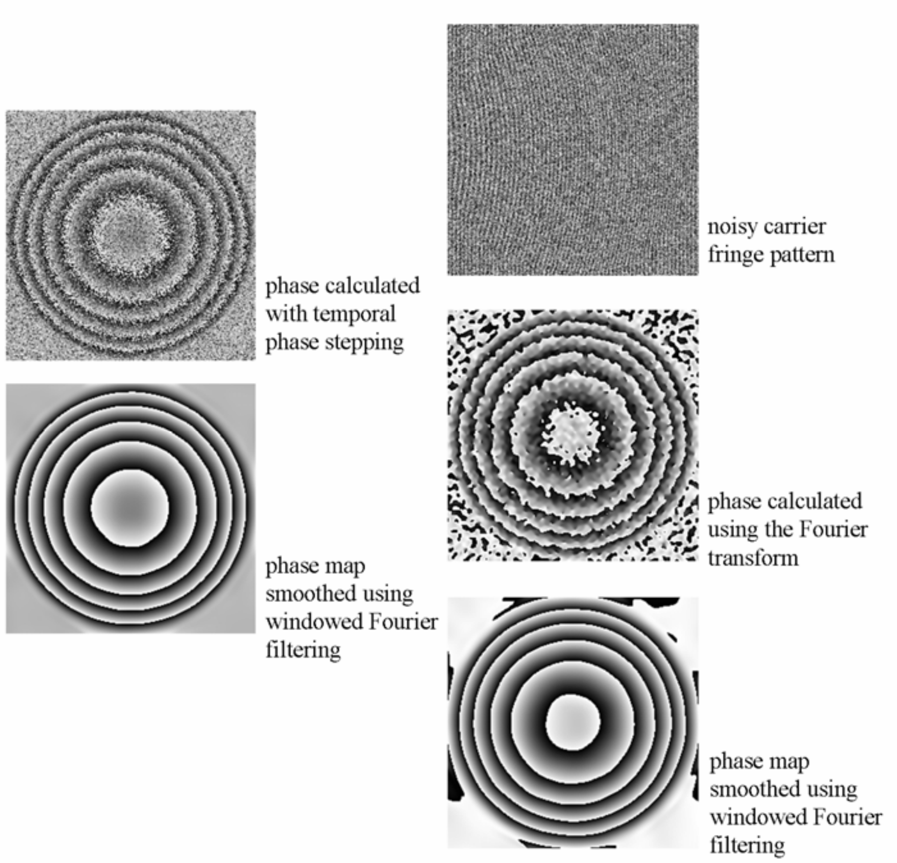

Figure 3.12 *The effect of windowed Fourier filtering on simulated phase maps calculated using temporal phase stepping (left) and the spatial carrier technique (right) [41, 44].*

3.5 Single fringe pattern demodulation

This section discusses some of the techniques that may be used to demodulate the phase from a single fringe pattern. These techniques are beneficial because they require just a single interferogram and do not need a carrier frequency. The disadvantage is that they are often complex and require more computer processing time than the techniques discussed previously. In addition, the fringe patterns that are used often need to possess low noise levels and be of high contrast for the techniques to work.

3.5.1 Skeletonizing

Skeletonizing [45–48] involves scanning the interferogram and reducing the fringes to the thickness of one pixel. This can be done using a peak detection algorithm and setting all pixels as +1 or -1 for pixels where fringe maxima or minima are located respectively and 0 for all other pixels. The resulting greyscale image shows a grey background with alternate black and white fringes that are only one pixel thick. The phase difference between a peak and valley is equal to π and can be approximated by a linear interpolation of the values between the fringe skeletons. The problem with the technique is that it can be difficult to apply an accurate peak detection algorithm that results in single line fringes with no breaks in them, which can be an issue with noisy fringe patterns [47].

Tay *et al* [46, 47] present a number of improvements to the technique, including an adaptive weighted filter to smooth the fringe patterns, an algorithm to detect breaks in the fringe skeletons and the use of an arctangent function to calculate the phase from the interpolated values. Zhang *et al* [48] present a method of skeletonizing based on determination of the fringe orientation. The fringe orientations were used in combination with a filtered binary image of the fringe pattern to determine the fringe skeletons.

3.5.2 Windowed Fourier ridges

Windowed Fourier ridges (WFR) is a technique based on the windowed Fourier transform that can be used to demodulate the phase from a single fringe pattern [42, 44]. The technique works by calculating the windowed Fourier transform for a region of the fringe pattern determined by the window function $g(x - u, y - v)$. The region of the fringe pattern determined by the window is compared to the WFT spectrum at a range of spatial frequencies. The spatial frequencies that maximize the similarity between the region of the fringe pattern within the window and the WFT spectrum are taken as the local frequency values for the pixel at the centre of the predefined window. The phase at that pixel is calculated from angle (the arctangent of the ratio of real to imaginary parts) of the windowed spectrum with these local frequencies. The phase at each pixel is calculated with the window centred at each point the fringe pattern.

Figure 3.13 shows the use of the WFR technique on the demodulation of an open and closed fringe pattern. A closed fringe pattern is a fringe pattern where at least some of the fringes are completely contained within the image. The demodulated phase from the closed fringe pattern contains error due to sign ambiguities that manifests itself as a vertical discontinuity through the fringe map. The sign ambiguity exists because, for a pair of local frequencies ω_x, ω_y that are chosen, the frequencies $-\omega_x$, $-\omega_y$ are also a valid solution. The discontinuity can be removed by forcing the continuity of the local frequency values in the direction perpendicular to the discontinuity [44]. The examples shown in figure 3.13 were calculated using Matlab code provided in reference [44].

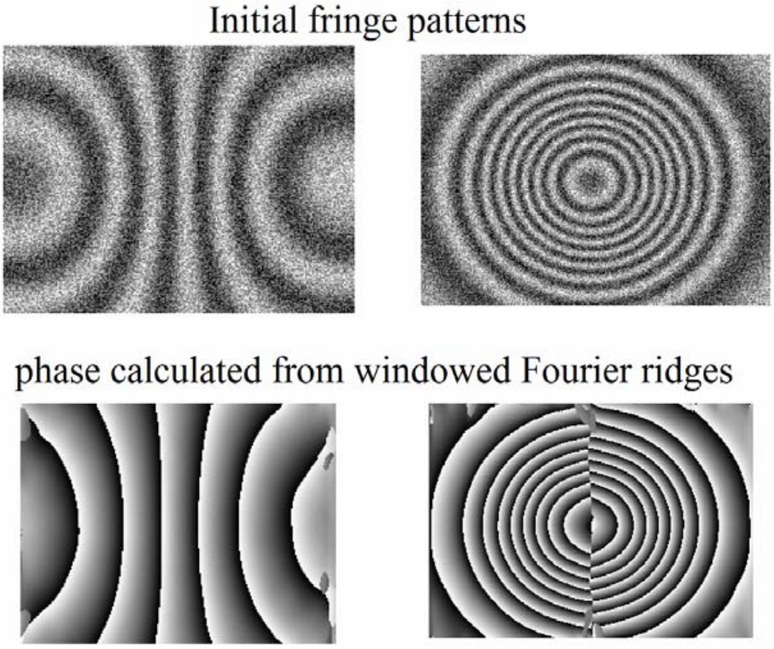

Figure 3.13 *Phase calculated using the WFR technique from an open (left) and closed (right) fringe pattern. Note the vertical discontinuity through the phase map from the closed fringe pattern.*

3.5.3 Regularized phase tracking

The regularized phase tracking (RPT) technique [49-51] is another method for demodulating single fringe patterns. The phase at a pixel (x, y) is determined by finding the solution $U(\phi, \omega_x, \omega_y)$ within a small surrounding neighbourhood of pixels $N_{x,y}$ that minimizes the cost function [49]

$$U(x,y) = \sum_{(\varepsilon,\eta)\in N_{x,y}} \left\{ f(\varepsilon,\eta) - \cos\left[\omega_x(x,y)(\varepsilon - x) + \omega_y(x,y)(\eta - y) + \phi(x,y)\right]\right\}^2 \quad (3.27)$$

where $f(\varepsilon, \eta)$ represents the fringe pattern at the point (ε, η) within the neighbourhood $N_{x,y}$, which is often chosen to be between 5x5 or 9x9 pixels. The phase and local frequencies are initially estimated and are then optimized iteratively according to a gradient descent algorithm. The pixel is then flagged as demodulated and the algorithm moves on to the next pixel. The demodulated phase and local frequency of the previous pixel start as the initial estimate for the next pixel. One of the improvements of the technique was to assess pixels according to the direction of the fringes instead of on a row-by-row basis. This improvement allowed even complicated closed-fringe patterns to be demodulated correctly.

A similar method, developed by Kemao [52], is the frequency-guided sequential demodulation (FSD) technique. In this method, the initial phase estimate is made by calculating the cosine of the initial fringe pattern. For this to work, however, the background term needs to be removed, for example by high-pass filtering, and the noise needs to be removed. The fringe pattern also needs to be normalized, which can be achieved with the application of a Hilbert transform [53]. The local frequency at each pixel is then estimated by testing all combinations of the frequencies from ω_{x1} to ω_{x2} and ω_{y1} to ω_{y2} within a predefined pixel neighbourhood to find a solution to equation (3.27). A typical frequency range would be -1 rad/pixel to +1 rad/pixel in steps of 0.1 [52]. The sign of the phase is then found for each pixel in order of highest to lowest frequency.

3.6 Phase unwrapping

The phase maps presented thus far in this chapter are known as wrapped phase maps because the phase values within the images are wrapped between $-\pi$ and $+\pi$. To obtain a continuous phase measurement, the 2π discontinuities need to be removed. The process of removing these discontinuities is known as phase unwrapping and the result is an unwrapped phase map. Figure 3.14(a) shows a plot of the phase across a single row of a wrapped phase map. In this simple case, the phase can be unwrapped by scanning along the row and adding 2π to the pixel value whenever the difference between the current pixel and the next is greater than $-\pi$, or subtracting 2π whenever the difference is greater than $+\pi$. The resulting unwrapped phase for the row shown is displayed in figure 3.14(b).

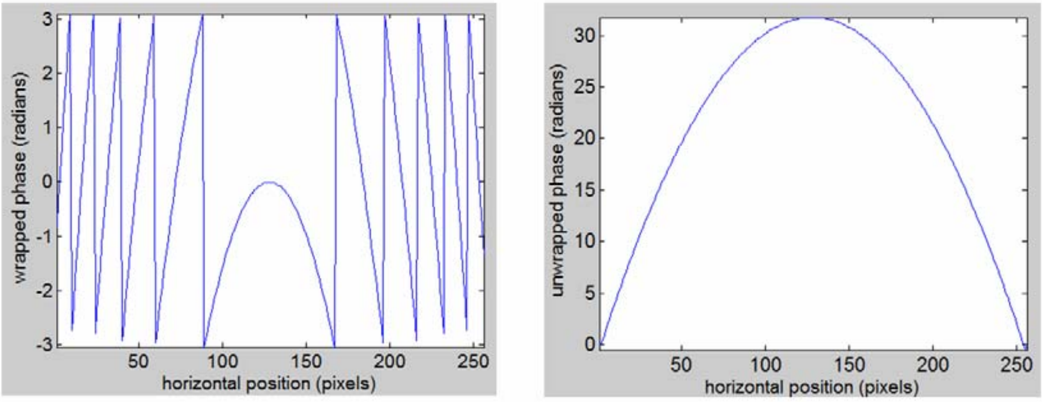

(a) **(b)**

Figure 3.14 *A single row of a wrapped phase map (a) and the same row after phase unwrapping.*

If a phase map is of very good quality, phase unwrapping can be achieved using the principle described above, on a row-by-row basis. If, however, the phase map contains breaks in the 2π fringe discontinuities or is affected by high frequency noise, the phase map cannot be unwrapped using the simple row-by-row method. A small region of a wrapped phase map is shown in figure 3.15(a) which contains breaks in the fringes. The effect of unwrapping the phase with the row-by-row method is shown in figure 3.15(b). The errors due to the breaks in the fringes are observed to propagate through the image. A more sophisticated unwrapping algorithm is therefore required to unwrap phase maps that contain noise induced errors due to, for example, speckle decorrelation, or discontinuities occurring, for example, due to a hole in the object.

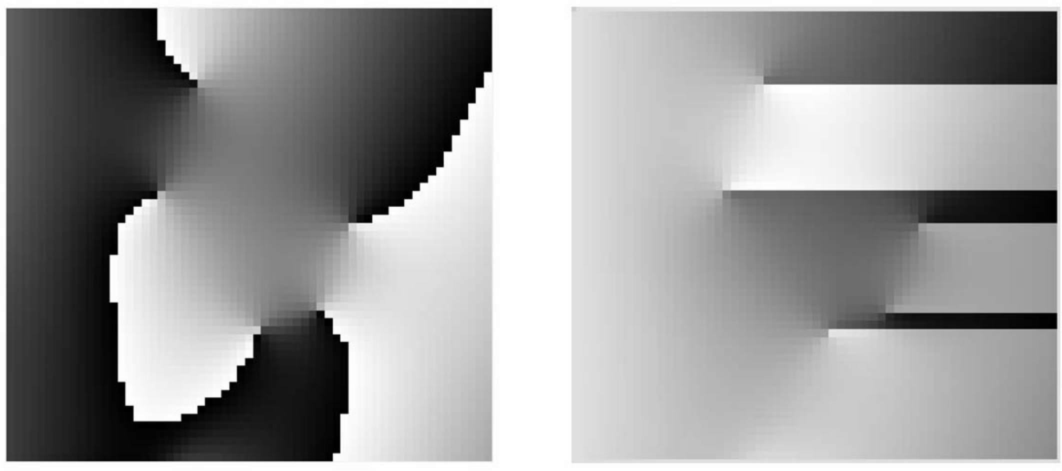
(a) (b)

Figure 3.15 *A small region of a wrapped phase map in which the* 2π *fringe discontinuities contain breaks (a). The result of unwrapping this phase map contains errors that propagate through the image.*

3.6.1 Minimum spanning trees

One method of processing wrapped phase maps that contain errors or discontinuities is to unwrap pixels in order of quality. One method of determining the quality of the data is to determine the absolute difference in phase between each pixel and its neighbours. Pixels with lower phase gradients are considered to contain higher quality data than pixels of high phase gradient. Unwrapping along the path of minimum phase gradient corresponds to the principle of the minimum spanning tree (MST) [54-57], which comes from graph theory. A graph is an array of points known as vertices which are connected by edges. A tree corresponds to a graph were all vertices are connected by one route only. If the graph is weighted, in that the edges of the graph have a specific value attached to them then there exists a route along which the sum of all the edges is a minimum. This route is the minimum spanning tree of the graph. An array of wrapped phase data can be considered as a graph, with the pixels being the vertices of the graph. The absolute phase difference between a pixel and its neighbour can be considered to be the weights of the graph's edges.

The MST technique has been improved by dividing the wrapped phase map into equal regions known as tiles [55-57]. The phase is unwrapped within each tile and then the tiles are assembled using the MST principle. There are a number of factors that determine the quality of data within the tile, and therefore its position in the tile queue, including its agreement with neighbouring tiles, the fringe density within the tile and the density of low modulation points within the tile [56]. The size of the tiles needs to be chosen carefully for optimum performance. The tiles need to contain as few fringes as possible but also need to be large enough to contain any phase errors completely within one tile. This will obviously depend on the particular phase map to be unwrapped but a typical size is 20x20 pixels [56].

3.6.2 Goldstein's branch cut algorithm

Goldstein's branch cut algorithm [58, 59] is a procedure for processing wrapped phase maps involving the detection of the phase residues within the wrapped phase map. Phase residues are located at the points were the breaks in the fringes occur, for example, there are five residues in the phase map segment shown in figure 3.15(a). The phase residues can be detected by calculating the sum of the wrapped phase differences for every pixel in a 2x2 region around the pixel using the equation [58]

$$\sum \Delta\phi = \Delta\phi_1 + \Delta\phi_2 + \Delta\phi_3 + \Delta\phi_4 \tag{3.28}$$

where the $\Delta\phi$ terms for a particular pixel (x, y) are given by

$$\begin{aligned} \Delta\phi_1 &= W\left\{\phi(x, y-1) - \phi(x, y)\right\} \\ \Delta\phi_2 &= W\left\{\phi(x+1, y+1) - \phi(x, y+1)\right\} \\ \Delta\phi_3 &= W\left\{\phi(x+1, y) - \phi(x+1, y+1)\right\} \\ \Delta\phi_4 &= W\left\{\phi(x, y) - \phi(x+1, y)\right\} \end{aligned} \tag{3.29}$$

where W is the wrapping operator. Whenever the sum of the wrapped phase differences is equal 2π, the pixel contains a positive residue and whenever it is equal to -2π the pixel contains a negative residue. For all other cases the phase differences sum to zero. The detected residues for the phase map in figure 3.15(a) are shown in figure 3.16(a). The white pixels correspond to positive residues and the black pixels correspond to negative residues.

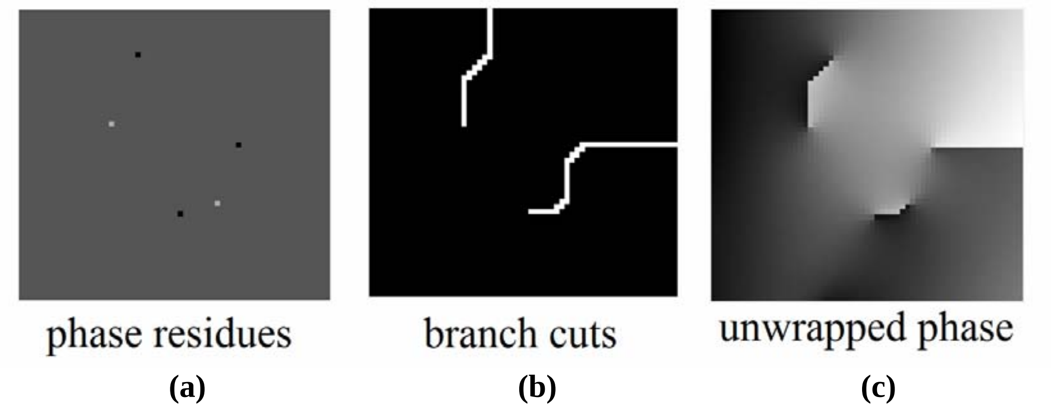

(a) **(b)** **(c)**

Figure 3.16 *The residues in the phase map in figure 7(a) are detected (a) and branch cuts are placed between them (b). The phase is unwrapped around the branch cuts(c)*[*].

The next step in Goldstein's algorithm is to connect the residues in such a way that the residues balance. This is done by placing branch cuts between the residues such that the sum of the residues along the branch is equal to zero. Positive residues have

---

[*] *The version of Goldstein's algorithm used here was coded in Matlab by Wu Nan and posted on a forum at www.cv.tu-berlin.de/rat*

a value of +1 and negative residues have a value of -1. To place the branch cuts, the residue image is then scanned row-by-row until a residue is detected. When this occurs, a 3x3 box is then centred on the residue. This box is scanned until another residue is detected. If no residue is detected in the box, the box is enlarged to 5x5 and then 7x7 and so on.

When a second residue is detected a branch cut is placed between the two residues. If the residues balance then the scan of the image continues. If the residues do not balance then the 3x3 box is moved to be centred on the second residue. The process of scanning and enlarging the box is repeated on the second residue and subsequent detected residues until either the residues balance or the box encounters the image border. If the border is encountered, a branch cut is placed between the residue at the centre of the box and the border. All residues connected to this branch cut are then declared balanced.

If a residue is found within the search box, it is always connected to the residue at the centre of the box even if it is already connected to another residue by a branch cut. The branch cuts corresponding to the phase map in figure 3.15(a) is shown in figure 3.16(b). Once all the residues in the image have been balanced, the phase is unwrapped pixel-by-pixel around the branch cuts. The unwrapped phase map is shown in figure 3.16(c). The phase errors are now confined to the regions of the branch cuts rather than propagating across the image as was seen in figure 3.15(b).

A large number of techniques have been developed to solve the problem of phase unwrapping. The two procedures presented here, Goldstein's algorithm and the minimum spanning tree principle, are described here because they provide the basis of the phase unwrapping software used in the experimental work presented in this thesis. The book, 'Two dimensional phase unwrapping: theory, algorithms and software' by Ghiglia and Pritt, provides a detailed description of a range of phase unwrapping algorithms of varying complexity along with C code implementations of each of them.

3.7 Summary

Determination of the optical phase of an interferogram is an essential processing step in most applications of full-field interferometry. In many cases, temporal phase stepping is the method of choice, particularly in the analysis of static test objects, since it is a fast, accurate and simple technique to implement. Temporal phase stepping, however, requires a minimum of four frames of data from which to calculate the phase. This requirement precludes temporal phase stepping from being the analysis method of choice when making pulsed illumination measurements of objects undergoing transient vibration or rotation. This is because the laser pulses are used to effectively freeze the motion at two points in the cycle of the object's motion. Only two frames of data are therefore available from which the phase can be determined.

One method is to record all the phase stepped intensity frames simultaneously. This technique, known as spatial phase stepping, can be realized by using a system incorporating multiple cameras or a diffraction grating. The diffraction grating serves to divide the interferometer output so that the phase-stepped signals can be spatially multiplexed onto different regions of one camera. The disadvantage of this method is that either a complex optical system is required, in the case of the multiple camera solution, or the results suffer a reduction in spatial resolution, in the case of the diffraction grating solution.

Another technique is to introduce a carrier frequency into the measurement. This can be done by translating the optical source between frames or by tilting the interfering beams to produce a linear phase variation across the CCD sensor. The phase can be demodulated from the carrier fringe pattern by using a Fourier transform to isolate the phase dependent side band in frequency space. In the method of Takeda [25], the carrier frequency is removed from the final wrapped phase result by translating the side band to the origin. When applied to two-dimensional fringe patterns, this method breaks down if the carrier fringes are not perfectly straight. An alternative is to calculate the phase from reference and signal carrier fringe patterns independently. The carrier frequency can then be removed by subtracting the two phase fringe patterns modulo 2π. The spatial carrier technique suffers from reduced spatial resolution relative to phase stepping techniques because only the data within the filter window is used in the phase calculation. Also, noise can have a more detrimental effect with the spatial carrier technique since it can cause breaks and distortions of the fringe discontinuities.

Another option is to demodulate the phase from a single fringe pattern. This can be done by reducing the fringes to single pixel thick fringe skeletons and interpolating the phase values between the fringe maxima and minima. This technique requires very smooth fringe patterns for the edge detection algorithm to work correctly. Windowed Fourier ridges is a technique that can be used to demodulate the phase from a single fringe pattern by considering regions of the fringe pattern within a particular neighbourhood of pixels. This method suffers from a sign ambiguity however, and cannot be used to demodulate closed fringe patterns without further post-processing. The regularized phase tracking and frequency guided sequential demodulation techniques operate by initially estimating the phase and frequency values within a small region of a fringe pattern. These values are then optimized until a solution to a cost function is found. These techniques are computationally heavy and require high quality fringe patterns to start with which generally require pre-processing before the phase is demodulated.

The phase analysis methods described in this chapter fall into three groups: phase stepping, spatial carrier techniques and single fringe pattern demodulation. The output of each of these techniques is a wrapped phase map (with the exception of the RPT technique). To obtain a continuous phase measurement, the wrapped 2π discontinuities need to be removed. This can be achieved using a phase unwrapping algorithm. Some of the properties of the phase analysis chapter are summarized in table 3.1.

In chapter 5, some of these phase analysis techniques are investigated using experimental shearography instruments. The aim of the work is to determine the most suitable phase analysis technique for the measurement of dynamic objects using the multiple-viewing-direction, pulsed laser shearography instrument described in chapter 4.

Table 3.1 *Summary of properties of different phase analysis techniques.*

	Phase Stepping			**Spatial carrier**		**Single pattern**		
	phase of differences	**difference of phases**	**spatial phase stepping**	**Takeda method**	**subtraction method**	**Skeletonizing**	**WFR**	**RPT**
camera frames required	4 (min)	6 (min)	2	2	3(2)*	2	2	2
fringe patterns required	3(min)	3(min)	1	1	2	1	1	1
computational complexity	low	low	low	moderate	moderate	high	high	high
additional requirements	phase shifter	phase shifter	diffraction grating or multiple cameras	carrier generation	carrier generation	none	none	none
noise influence	low	low	low	moderate	moderate	high	high	high
live phase maps	yes	yes	yes	possible	possible	no	no	no
closed fringe patterns	yes	yes	yes	yes	yes	yes	no	yes

* Depends on carrier fringe generation. 3 if correlation of speckle patterns is required to produce carrier fringes.

References

[1] Creath K. 'Temporal phase measurement methods', in *Interferogram analysis: digital fringe pattern measurement techniques*, ed. Robinson D. W. and Reid G. T, Institute of Physics, Bristol (1993).

[2] Atcha H. 'Optoelectronic speckle pattern interferometry' PhD Thesis, Cranfield University, Bedford, UK (1994).

[3] Tatam R. P, Davies J. C, Buckberry C. H. and Jones J. D. C, 'Holographic surface contouring using wavelength modulation of laser diodes', *Opt. Laser Technol.* **22**:5, 317-21 (1990).

[4] Wyant J. C, Oreb B. F. and Hariharan P, 'Testing aspherics using two wavelength holography: use of digital electronic techniques' *Appl. Opt.* **23**:22, 4020-3 (1984).

[5] Wyant J. C, 'Use of an ac heterodyne lateral shear interferometer with real-time wavefront correction systems' *Appl. Opt.* **14**:11, 2622-6 (1974).

[6] Carré P, 'Installation et utilisation du comparateur photoélectric et interferéntiel du bureau de pois et mesures' *Metrologia* **2**:1, 13-23 (1966).

[7] Schwider J, Burow R, Elsner K-E, Grzanna J, Spolaczyk R. and Merkel K, 'Digital wavefront measuring interferometry: some systematic error sources' *Appl. Opt.* **22**:21, 3421-32 (1983).

[8] Hariharan P, Oreb B. F. and Eiju T, 'Digital phase shifting interferometry: a simple error compensating algorithm' *Appl. Opt.* **26**:13, 2504-6 (1987).

[9] Dorrio B. V. and Fernandez J. L, 'Phase-evaluation methods in whole-field optical measurement techniques' *Meas. Sci. Technol.* **10,** R33-R35 (1999).

[10] De Groot P, '101-frame algorithm for phase shifting interferometry', *EUROPTO preprint 3098-33*, 1-10 (1997).

[11] Nakadate S. and Saito H, 'Fringe scanning speckle pattern interferometry' *Appl. Opt.* **24**:14, 2172-80 (1985).

[12] Creath K, 'Phase-shifting speckle interferometry' *Appl. Opt.* **24**:18, 3053-8 (1985).

[13] Huntley J. M, 'Automated analysis of speckle interferograms', in *Digital speckle interferometry and related techniques*, ed. Rastogi P. K, Wiley (2001).

[14] Kujawinska M, 'Spatial phase measurement methods' in *Interferogram analysis: digital fringe pattern measurement techniques*, ed. Robinson D. W. and Reid G. T, Institute of Physics, Bristol (1993).

[15] Smythe R, and Moore R, 'Instantaneous phase measuring interferometry', *Opt. Eng.* **23**:4 361-4 (1984).

[16] Kujawinska M. and Robinson D. W, 'Multi-channel phase-stepped holographic interferometry' *Appl. Opt.* **27**:2, 312-20 (1988).

[17] García B. B, Moore A. J, Pérez-López C, Wang L. and Tschudi T, 'Transient deformation measurement with electronic speckle pattern interferometry by use of a holographic optical element for spatial phase stepping, *Appl. Opt.* **38**:28, 5944-7 (1999).

[18] García B. B, Moore A. J, Pérez-López C, Wang L. and Tschudi T, 'Spatial phase-stepped interferometry using a holographic optical element', *Opt. Eng.* **38**:12, 2069-74 (1999).

[19] Millerd J, Brock N, Hayes J, North-Morris M, Novak M. and Wyant J, 'Pixelated phase-mask dynamic interferometer', *proc. SPIE*, **5531**, 304-14 (2004).

[20] Wyant J, ‘Going through a phase – dynamic phase-shifting interferometry beats vibration’, *SPIE’s OE magazine*, 20-2, (August 2005).

[21] Kitchen S. R. and Dam-Hansen C, ‘Holographic common-path interferometer for angular displacement measurements with spatial phase stepping and extended measurement range’, *Appl. Opt*, **42**:1, 51-9 (2003).

[22] Kemao Q, Xiaoping W. and Asundi A, ‘Grating-based real-time polarization phase-shifting interferometry: error analysis’, *Appl. Opt*, **41**:13, 2448-53 (2002).

[23] Fricke-Begemann T and Burke J, ‘Speckle interferometry: three-dimensional deformation field measurement with a single interferogram’, *Appl. Opt.* **40**:28, 5011-22 (2001).

[24] Dávila A, Kaufmann G. H. and Pérez-López C, ‘Transient deformation analysis by a carrier method of pulsed electronic speckle-shearing pattern interferometry’, *Appl. Opt.* **37**:19, 4116-22 (1998).

[25] Roddier C. and Roddier F, ‘Interferogram analysis using Fourier transform techniques’, *Appl. Opt*, **26**:9, 1668-73 (1987).

[26] Takeda M, Ina H. and Kobayashi S, ‘Fourier-transform method of fringe-pattern analysis for computer-based topography and interferometry’, *J. Opt. Soc. Am*, **72**:1, 156-9 (1982).

[27] Macy Jr. W. W, ‘Two-dimensional fringe-pattern analysis’, *Appl. Opt.* **22**:23, 3898-901 (1983).

[28] Waldner S, Quantitative strain analysis with image shearing speckle pattern interferometry (shearography)’, *PhD Thesis*, Swiss federal institute of technology, Zurich (2000).

[29] Saldner H. O, Molin N-E and Stetson K. A. ‘Fourier-transform evaluation of phase data in spatially phase biased TV holograms’, *Appl. Opt.* **35**:2, 332-6 (1996).

[30] Martínez-Celorio R. A, Dávila A, Kaufmann G. H. and Mendiola G, ‘Extension of the displacement measurement range for electronic speckle shearing interferometry using carrier fringes and a temporal-phase-unwrapping method’, *Opt. Eng.* **39**:3, 751-7 (2000).

[31] Fernández A, Doval A. F, Dávila A, Blanco-García J, Pérez-López C. and Fernández J. L, ‘Double-pulsed carrier speckle shearing pattern interferometry for transient deformation analysis’, *Proc. SPIE*, **3478**, 352-8, (1998).

[32] Groves R. M, James S. W, Barnes S. E, Fu S, Furfari D, Irving P. and Tatam R. P, ‘Multi-component laser shearography for the investigation of defects in rotating machinery’, *Proc. SPIE*, **5058**, 351-60, (2002).

[33] Davila A, Kerr D. and Kaufmann G. H, ‘Fast electro-optical system for pulsed ESPI carrier fringe generation’, *Opt. Comm.* **123**, 457-64, (1996).

[34] Kemper B, Kandulla J, Dirksen D. and von Bally G, ‘Optimization of spatial phase shifting in endoscopic electronic speckle pattern interferometry’, *Opt. Comm.* **217**, 151-60 (2003).

[35] Pedrini G, Zou Y-L and Tiziani H. J, ‘Quantitative evaluation of digital shearing interferogram using the spatial carrier method’, *Pure Appl. Opt.* **5**, 313-21 (1996).

[36] Santos F, Vaz M, and Monteiro J, ‘A new set-up for pulsed digital shearography applied to defect detection in composite structures’, *Opt. Lasers Eng.* **42**, 131-40 (2004).

[37] Francis D, James S. W and Tatam R. P, ‘Measurement of surface strain using multi-component pulsed laser shearography with fibre-optic imaging bundles’, *Proc. SPIE* **6616**, 6616-2S (1-10) (2007).

[38] Crennell K, ‘Introductory digital image processing’, in *Interferogram analysis: digital fringe pattern measurement techniques*, ed. Robinson D. W. and Reid G. T, Institute of Physics, Bristol (1993).

[39] Aebischer H. A, Waldner S, ‘A simple and effective method for filtering speckle-interferometric phase fringe patterns’, *Opt. Comm.* **162**, 205-10 (1999).

[40] Kemao Q, Hock-Soon S. and Asundi A, ‘Smoothing filters in phase-shifting interferometry’, *Opt. Laser Technol.* **35**, 649-54 (2003).

[41] Kemao Q, ‘Windowed Fourier transform for fringe pattern analysis’, *Appl. Opt.* **43**:13, 2695-702 (2004).

[42] Kemao Q, ‘Windowed Fourier transform for fringe pattern analysis: addendum’, *Appl. Opt.* **43**:17, 3472-3 (2004).

[43] Kemao Q, ‘Windowed Fourier transform for demodulation of carrier fringes’, *Opt. Eng.* **43**:7, 1472-3 (2004).

[44] Kemao Q, ‘Two-dimensional windowed Fourier transform for fringe pattern analysis: principles, applications and implementations’, *Opt. Lasers. Eng.* **45**, 304-17 (2007).

[45] Yatagai T, ‘Intensity based analysis methods’, in *Interferogram analysis: digital fringe pattern measurement techniques*, ed. Robinson D. W. and Reid G. T, Institute of Physics, Bristol (1993).

[46] Tay C. J, Quan C, Yang F. J. and He X. Y, ‘A new method for phase extraction from a single fringe pattern’, *Opt. Comm.* **239**, 251-58 (2004).

[47] Quan C, Tay C. J, Yang F. J. and He X. Y, ‘Phase extraction from a single fringe pattern based on guidance of an extreme map’, *Appl. Opt.* 44:23, 4814-21 (2005).

[48] Zhang D, Ma M. and Arola D. D, ‘Fringe skeletonizing using an improved derivative sign binary method’, *Opt. Lasers Eng.* **37** 51-62 (2002).

[49] Servin M, Marroquin J. L. and Cuevas F. J, ‘Demodulation of a single interferogram by use of a two-dimensional regularized phase tracking technique’, *Appl. Opt.* **36**:19, 4540-8 (1997).

[50] Servin M, Marroquin J. L. and Cuevas F. J, ‘Fringe-follower regularized phase tracker for demodulation of closed-fringe interferograms’, *J. Opt. Soc. Am. A.* **18**:3, 689-95 (2001).

[51] Servin M, Marroquin J. L. and Quiroga J. A, ‘Regularized quadrature and phase tracking from a single closed-fringe interferogram’, *J. Opt. Soc. Am. A.* **21**:3, 411-9 (2004).

[52] Kemao Q. and Hock-Soon S, ‘Sequential demodulation of a single fringe pattern guided by local frequencies’, *Opt. Lett.* **32**:2, 127-9 (2007).

[53] Quiroga J. A, Gómez-Pedrero J. A. and García-Botella A, ‘Algorithm for fringe pattern normalization’, *Opt. Comm.* **19**, 43-51 (2001).

[54] Robinson D. W, ‘Phase unwrapping methods’, in *Interferogram analysis: digital fringe pattern measurement techniques*, ed. Robinson D. W. and Reid G. T, Institute of Physics, Bristol (1993).

[55] Judge T. R. and Bryanston-Cross P. J, ‘A review of phase unwrapping techniques in fringe analysis’, *Opt. Lasers Eng.* **21**, 199-239 (1994).

[56] Towers D. P, Judge T. R. and Bryanston-Cross P. J, ‘Automatic interferogram analysis techniques applied to quasi-heterodyne holography and ESPI’, *Opt. Lasers Eng.* **14**, 239-81 (1991).

[57] Sawaf F. and Tatam R. P, ‘Finding minimum spanning trees more efficiently in tile-based phase unwrapping’, *Meas. Sci. Technol.* **17**, 1428-35 (2006).
[58] Goldstein R. M, Zebker H. A. and Werner C. L, ‘Satellite radar interferometry: two-dimensional phase unwrapping’, *Radio Sci.* **23**:4, 713-20 (1988).
[59] Ghiglia D. C. and Pritt M. D, ‘Two-dimensional phase unwrapping: theory, algorithms and software’, Wiley, Chichester (1998).

4. Multi-component, pulsed laser shearography

In this chapter, the components used in the development of the multiple-viewing-direction, pulsed-laser shearography system are presented. The components include the pulsed Nd:YAG laser system, the viewing apparatus, fibre-optic imaging bundles and the CCD camera. The test objects that are used in the measurement of static deformations are also introduced. The software used to acquire images from the CCD camera is discussed and the image processing scheme that is used to obtain three-component surface strain measurements is presented. Finally, a laser diode based, multiple-illumination-direction shearography system, developed previously at Cranfield University [1, 2] is described. This instrument was used for the temporal phase stepping analysis in chapter 5 and previous results obtained with the system were used for static strain measurement comparison in chapter 6.

4.1 Overview of the multiple-viewing-direction shearography system

The multiple-viewing-direction pulsed laser shearography system is shown in figure 4.1. The viewing apparatus consists of two pairs of aluminium beams arranged to form a cross. The structure is mounted on a tripod and is arranged so that the tips of the cross are located at the four corners of a square. At these corners are positioned four camera lenses, referred to as CL1-4 in figure 4.1, which view the test object from different locations.

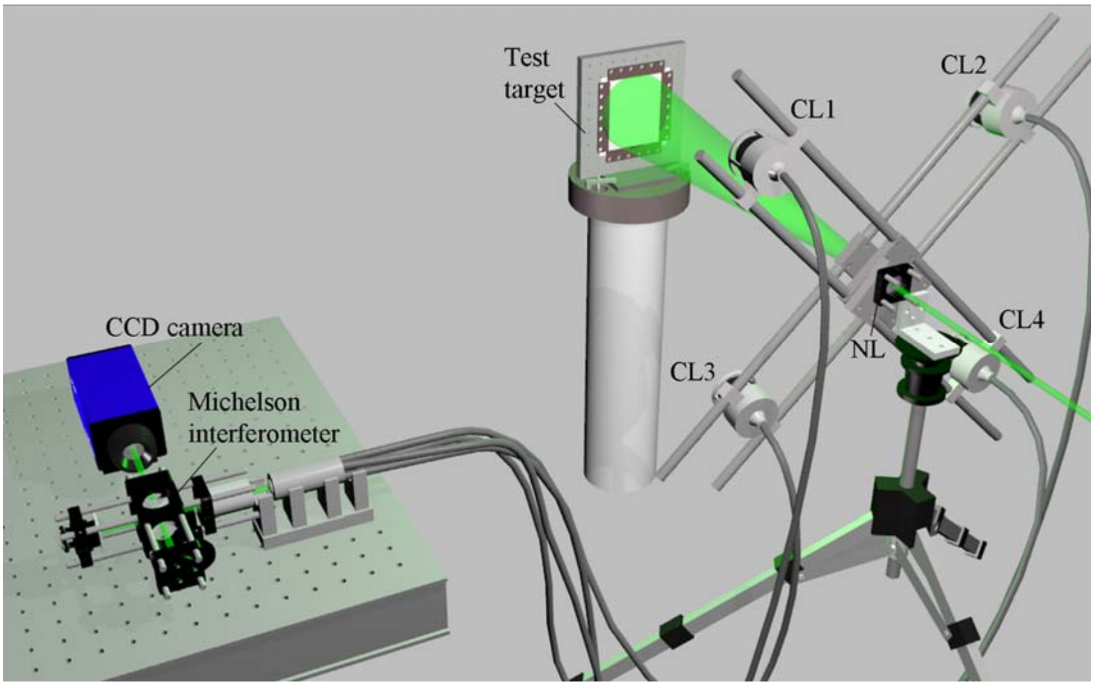

Figure 4.1 *Arrangement of the multiple viewing direction, pulsed laser shearography system. CL = camera lens.*

A negative lens is housed within the centre of the cross structure. This lens serves to diverge light from the pulsed Nd:YAG laser to illuminate the surface of the object under investigation. Light scattered from the test surface is imaged by each of the camera lenses onto the input face of a coherent fibre-optic imaging bundle. The fibre bundles guide the images from each of the camera lenses to the shearing interferometer located remotely on an optical bench. Light exiting the interferometer is imaged onto the surface of a CCD camera.

4.2 The pulsed Nd:YAG laser system

The laser system used in this work is a custom made Continuum 150 ns long pulse Nd:YAG laser with a pulse repetition rate of 10 Hz. The laser optics are mounted on an optical bench that is located on a portable trolley. The arrangement of the optical components is illustrated in the schematic diagram shown in figure 4.2. A large number of optical components make up the laser system, therefore for clarity many have been omitted from figure 4.2.

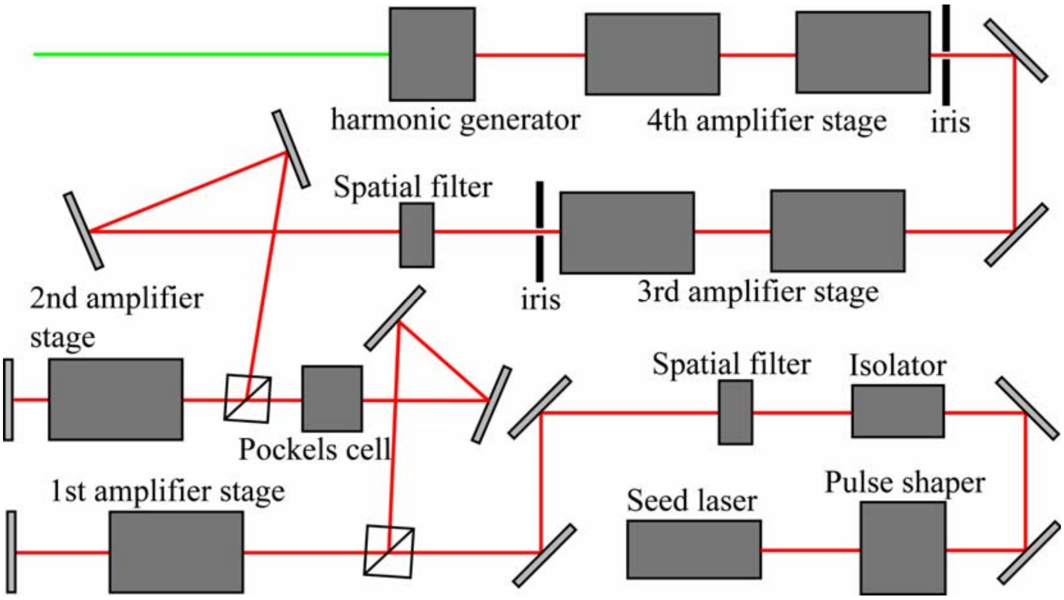

Figure 4.2 *Schematic showing the arrangement of components within the pulsed laser system.*

The light source within the system is a Lightwave 126 series seed laser that emits continuous-wave infra-red radiation at a wavelength of 1064 nm. The output power of the seed laser is 700 mW. A Kentech programmable pulse shaper is used to divide the input continuous wave radiation into the desired pulse shape. The pulse shaper is based around a Li:Tantalate double Pockels cell [3] and can be used to provide single pulse emission or dual pulse emission with a pulse separation of in the range of approximately 0.5-2.0 μs. Pulse trains consisting of more than two pulses can also be generated using the pulse shaper. After exiting the pulse shaper, light pulses pass through a Faraday isolator and a spatial filter. The isolator prevents light being reflected back into the seed laser. The spatial filter is used to ensure that the beam profile is clean and free of diffraction rings caused by dust and imperfections in the optical components prior to the spatial filter. The seed pulse then passes through the first and second amplifier stages. These amplifiers consist of a 6 mm Nd:YAG rod and pulses pass through these amplifiers twice. A double Pockels cell located between the first and second amplifier stages is used to decrease the amplified spontaneous emission (ASE) background [4]. Further Faraday isolators are installed to prevent any feedback from amplification stages located further down the beam path. After exiting the 6 mm amplification stages the beam profile has a characteristic ring structure. This is removed by a second spatial filter positioned after the second amplification stage. The pulses then pass through the third and fourth amplifier stages, each of which contain a 9 mm Nd:YAG rod. Infra-red laser pulses exiting the fourth amplifier stage have a pulse energy of up to 3 J at a wavelength of 1064 nm. The harmonic generator consists of a 13 mm long KTP (potassium titanyl phosphate) crystal and is used to double the frequency of the laser pulses. Green light with a wavelength of 532 nm exits the harmonic generator. The crystal has a maximum efficiency of over 50% and therefore can provide more than 1.5 J of green laser light. A photograph of the pulsed laser system indicating the locations of some of the significant components is shown in figure 4.3. The dimensions of the laser optics bench are approximately 2.5 x 0.75 m.

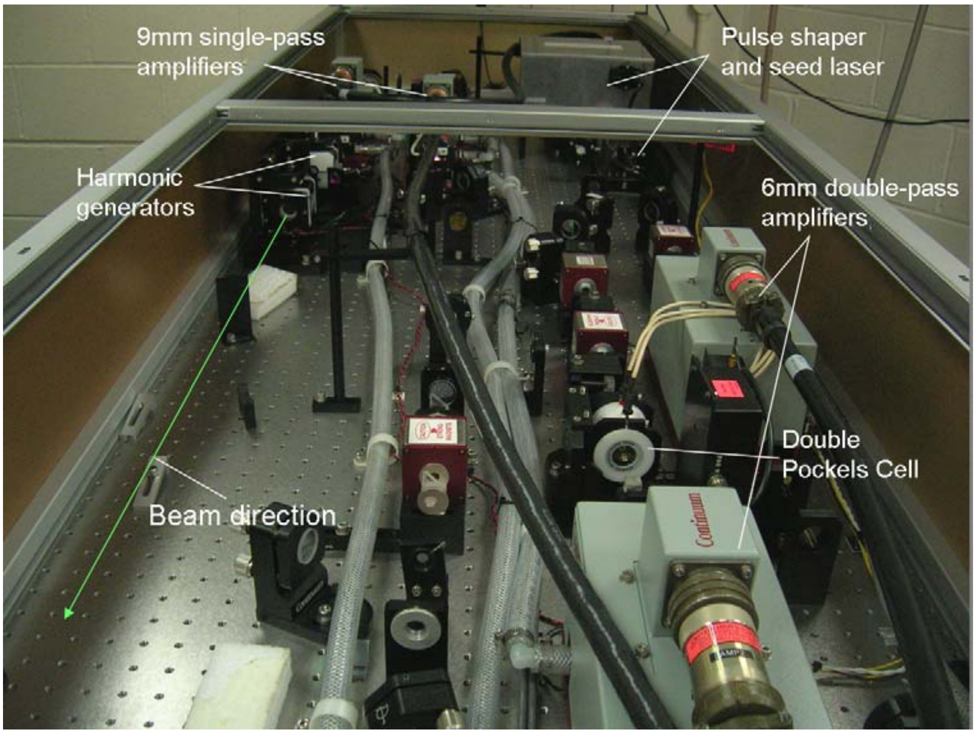

Figure 4.3 *Photograph showing the arrangement of components within the pulsed laser system. The bench dimensions are approximately 2.5 x 0.75 m.*

The minimum pulse width of this custom designed Nd:YAG laser system is 150 ns. This is significantly longer than the pulse width of conventional Nd:YAG lasers which is typically 10 ns or so. The advantage of having a long pulse width is that the linewidth of the laser is reduced relative to the conventional Nd:YAG laser. This is significant in applications that require a narrow linewidth, such as planar Doppler velocimetry (PDV) [5]. Another advantage of this laser system is that it has no external cavity. The only laser cavity is within the seed laser. The lack of an external cavity means that the laser does not suffer from the effects of spatial hole burning. This is a phenomenon caused by interference of counter-propagating light beams with the same polarization. This produces a standing wave pattern, the result of which can cause multimode operation of the laser system [6]. Also, no cavity jitter results in a more stable output wavelength.

4.3 The viewing apparatus

The viewing apparatus, shown in figure 4.4(a), consists of a cross structure built from two pairs of 1m long aluminium bars. This cross structure is used to hold the four camera lenses (CL) that are used to view the object under investigation. At the centre of the cross is housed the negative lens (NL) that is used to diverge the laser light to illuminate the target. The camera lenses (Helios 44-2 (focal length 58 mm)) are held within aluminium lens holders which slide onto the bars of the cross structure. The lens holders can be rotated in two orthogonal directions to ensure accurate positioning of the lenses. This enables the lenses to view the same region of the test surface. A photograph of one of the lens holders is shown in figure 4.4(b).

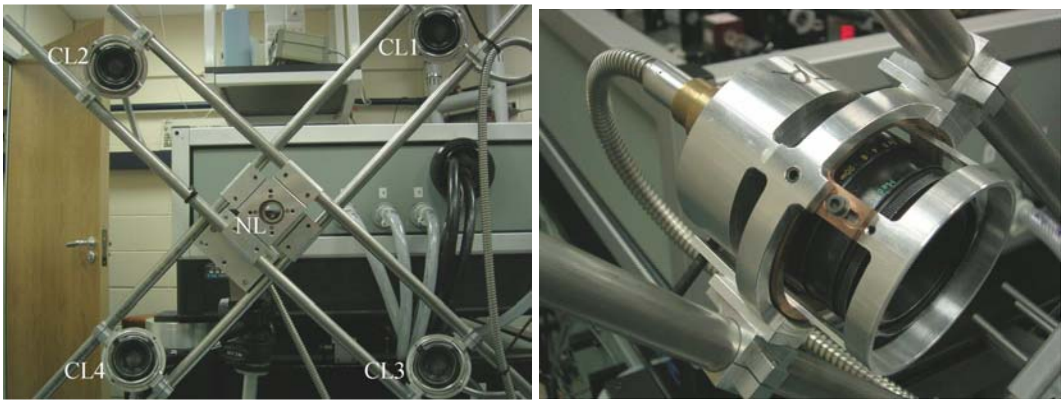

(a) **(b)**

Figure 4.4 *Photographs showing the viewing apparatus (a) used to hold the four camera lenses (CL) and the negative lens (NL) and a close-up of one of the camera lens holders (b). The length of the bars is approximately 1 m.*

The use of four camera lenses to view the object from four directions allows the calculation of displacement gradient with four different sensitivity vectors. Only three measurement channels are required for a full analysis of the surface strain, as was explained in section 2.3.1. The use of a fourth measurement channel therefore gives redundancy of measurement and the ability to select the best three data sets [7]. Also, measurements can still be made if one of the views is obscured. Light collected by each of the camera lenses is imaged onto the input face of a fibre optic imaging bundle, which is attached to the rear of each of the camera lens holders. The input ends of the fibre bundles are shown in figure 4.5(a).

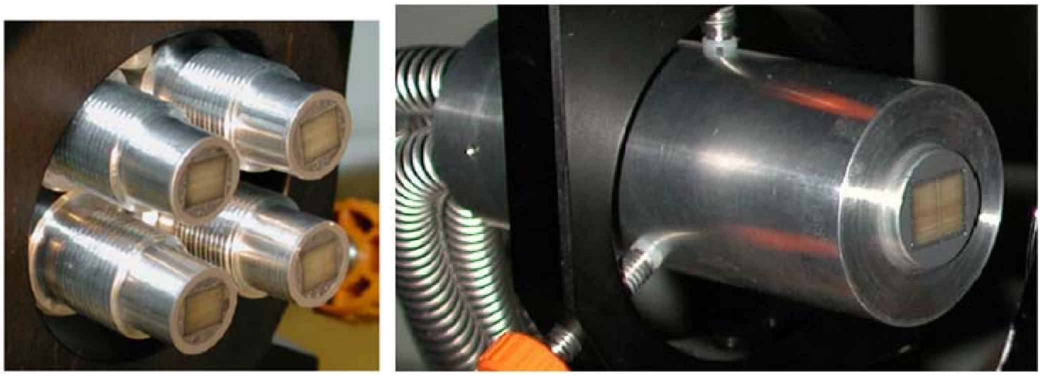

(a) **(b)**

Figure 4.5 *Photographs showing the input ends of the fibre-optic imaging bundles (a) and the distal end (b) where images from the four bundle arms are combined to form a composite image, which is then imaged onto the camera.*

Each bundle arm is 4 m long and consists of a matrix of 500 x 600 optical fibres. Each individual fibre has a core diameter of 8 μm and the fibres are spaced on 10 μm centres. The fibres are grouped into subarrays consisting of 5x5 optical fibres within the bundles. An armoured sheath is used to prevent damage to the fibres. At the distal end, the four bundle arms are combined to form a composite array of 1000x1200 optical fibres. The fibre bundle distal end module is shown in figure 4.5(b).

An image recorded by a CCD camera through the bundles is shown in figure 4.6(a). This image was recorded with a sheet of paper with the ‘Measurement Science and Technology’ logo printed on it placed in the focal plane of the four camera lenses. The paper was illuminated with a desk lamp and the image was captured with the camera with an exposure time of 0.1 s. The structure of the 5x5 fibre subarrays can be seen within the image. Figure 4.6(b) shows a magnified region of an image recorded through the fibre bundles which clearly shows the structure of the subarrays. The fringes are due to the image being recorded through a Mach-Zehnder interferometer. The subarrays are formed during the fabrication process due to winding a multi-fibre array one layer at a time onto a drum. The final imaging bundle is comprised of individual multi-fibres bound only at the ends and separate between, making the bundle flexible [8].

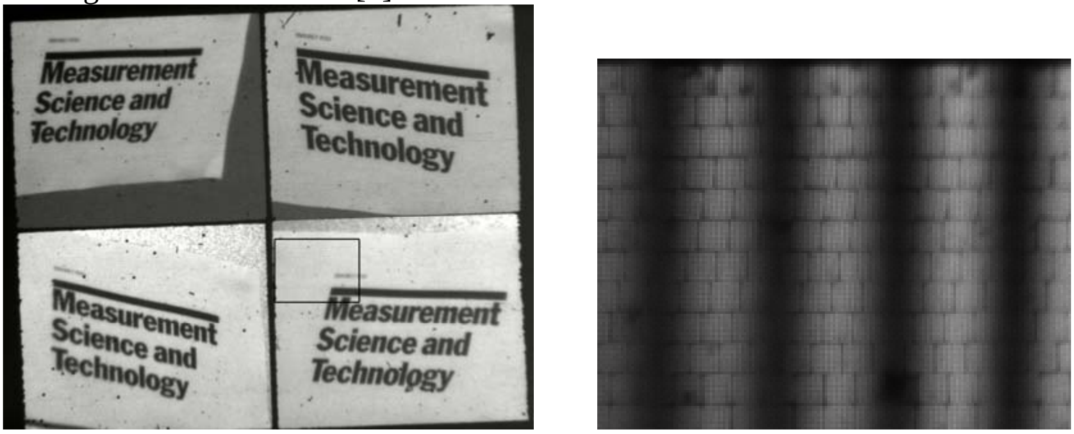

(a) **(b)**

Figure 4.6 *Image recorded by a CCD camera through the fibre bundles (a). The enlarged region enclosed by the box shows the structure of the bundle subarrays (b).*

The use of the fibre-optic imaging bundles to guide and spatially multiplex the four separate views means that multi-component measurements can be made using just one CCD camera. The alternative would be to use multiple cameras with multiple interferometers which would be expensive since more components are required. Fibre-optic imaging bundles have previously been used at Cranfield University to make multi-component measurements of flow velocity using planar Doppler velocimetry (PDV) [5]. One of the aims of this project is to apply this technology that was successful previously in PDV to multi-component shearography.

One of the disadvantages of using fibre bundles in shearography is that the bundles need to be mechanically stable for the duration of the measurement. Motion of the bundles during the recording will result in speckle decorrelation, which will destroy the correlation fringe patterns. This is an issue when measurements of static test surfaces are being made, where the measurement time is of the order of seconds. Static measurements can only be realistically made within the laboratory environment where the bundles can be kept in controlled conditions. For dynamic measurements, however, this is not an issue, since within the time between recording images, of the order of microseconds, the motion of the bundles is likely to be minimal, even outside of the laboratory.

4.4 The CCD camera and interferometer

The camera and Michelson interferometer are shown in figure 4.7. The shearing Michelson interferometer is constructed using Linos Microbench® opto-mechanical components. These components are used for constructing both the Michelson and Mach-Zehnder shearing interferometers used in this thesis. In the system shown in figure 4.7, light exiting the bundle distal end is collimated by an Olympus PlanApo large aperture microscope objective. Light then passes through the shearing Michelson interferometer before being imaged onto the CCD camera.

The camera is a 12 bit LaVision Flowmaster 3 CCD camera. The CCD chip has a spatial resolution of 1024 x 1280 pixels. The size of each pixel is 6.7 μm^2, giving a total chip size of approximately 6.9 x 8.6 mm^2. The camera is capable of operating in a dual-frame mode, where two frames can be recorded with a separation of 200 ns. The response linearity of a similar camera system has been measured previously [9] and was found to be linear for over 90% of the full range. Measurement intensities should therefore be kept below about 3800 counts (of a maximum of 4095). Operating at intensities higher than this, i.e. within the non-linear region, would introduce uncertainties in the measured phase distributions since the intensity would be higher than that measured. The image acquisition software can be set to display pixels that are close to saturation as red within a greyscale image which helps to ensure that the camera is in the linear region.

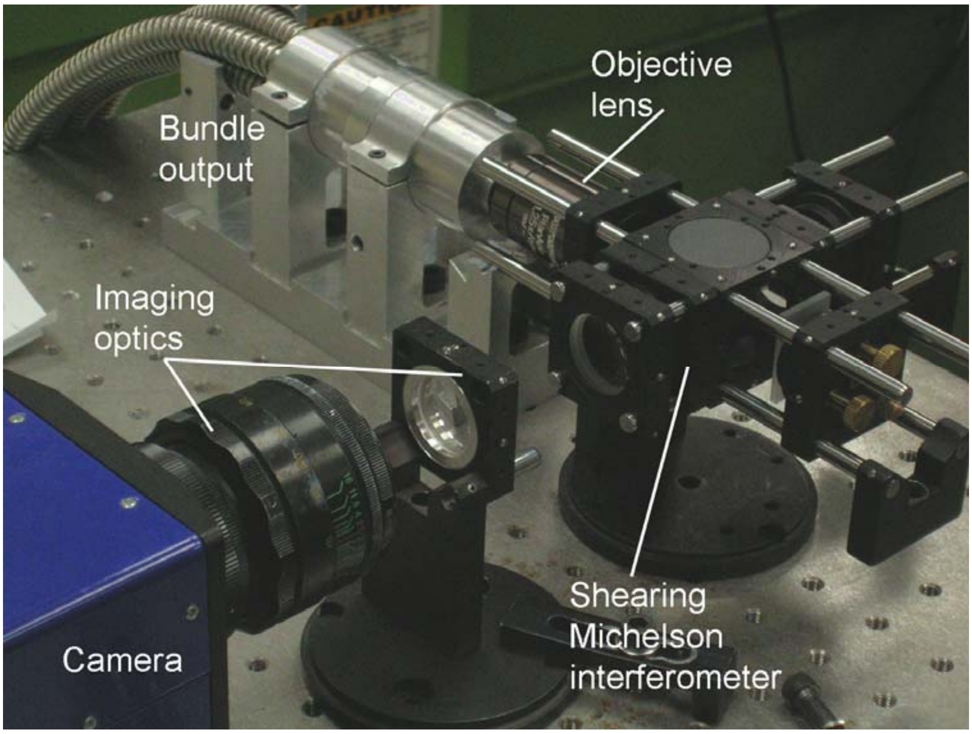

Figure 4.7 *CCD camera, bundle output and shearing Michelson interferometer constructed using Microbench®.*

4.5 Static test objects

This section introduces the test objects used in surface strain measurements under static loading conditions. The first object is a flat aluminium plate coated with ROCOL retro-reflective paint. This object is shown in figure 4.8(a).

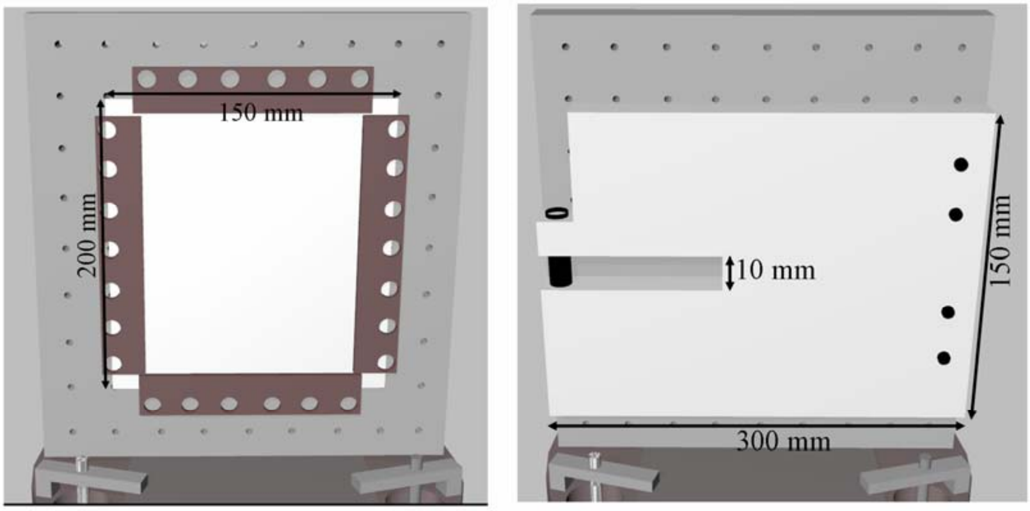

(a) **(b)**

Figure 4.8 *The flat aluminium plate (a) and the flat Perspex plate containing a horizontal slot.*

The plate measures 200 mm x 150 mm and was clamped around its perimeter to a section of aluminium breadboard. The breadboard was, in turn, clamped to large steel pipe which was approximately the same height above the ground as the aperture of the pulsed laser. The plate was deformed by turning a micrometer screw mounted on the rear of the breadboard section. Turning this screw produces an out-of-plane displacement of the order of a few micrometers in the centre of the plate. This test object was used in the phase analysis work presented in the next chapter.

The second test object, shown in figure 4.8(b), is a flat Perspex plate of dimensions 300 mm x 150 mm x 10 mm. A 10 mm wide horizontal slot was cut out of the plate. The object was loaded by turning a screw vertically through the slot which opens or closes the slot. Turning this screw produces a predominantly in-plane deformation. This object was also fixed to the section of breadboard that was clamped to the pipe. The Perspex plate was used because it exhibits in-plane strain as well as out-of-plane strain when deformed.

4.6 Image acquisition

A frame grabber card located within a PC was used to acquire images from the camera. This is controlled using LaVision's software package *DaVis* (Data Visualisation). A BNC (Berkeley Nucleonics Corporation) 555 pulse generator is used to synchronise the camera with the laser pulses. A TTL pulse from the lasers timing circuit is used to trigger the pulse generator. The pulse generator then triggers the frame grabber card and the camera acquires an image.

Figure 4.9 shows an image captured with the camera whilst synchronized with the laser. In this figure one of the mirrors in the shearing interferometer was blocked, hence only one image is seen. This image was recorded from light scattered from the aluminium plate, which was mounted on the pipe at a distance of approximately 1 m from the tripod mounted cross structure. At this distance the diameter of the diverging laser beam was approximately 30 cm. The field of view on the object's surface is 60 mm x 80 mm. In this image some of the ring structure within the pulse from the amplifier stages can be seen. This can be a problem in speckle interferometry. If the viewing apparatus on the tripod moves between the recording of the two frames, then the position of these rings will move within the image. When the two frames are correlated the rings will influence the resulting image and obscure the desired correlation fringe pattern. The effect of the rings can be reduced by decreasing the diameter of the irises before the third and fourth amplifier stages (see figure 4.2). This can be used to produce a clean beam profile at the test object but comes at a cost of reduced optical power. The laser is however, of sufficient power for this to not be a significant issue.

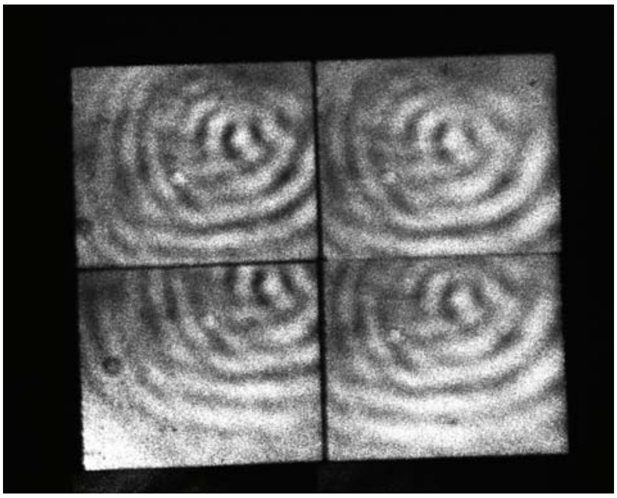

Figure 4.9 *Image captured through the fibre bundle of a laser pulse scattered from the aluminium test plate. Note the ring structure present within the laser pulse. This can be reduced using the irises within the laser.*

To obtain correlation fringes from the object under investigation, a speckle interferogram was acquired with the object in its undeformed state. The object was deformed and a second speckle interferogram was captured. The two interferograms were then correlated by digitally subtracting the two images. The resulting image was then rectified and correlation fringes were displayed on the monitor. Figure 4.10 shows correlation fringes obtained from the system using the flat aluminium plate object with shear applied in the *x*-direction (horizontally across the image) (a) and in the *y*-direction (vertically across the image) (b). The magnitude of the applied shear in each case was approximately 10 mm. The camera lens (CL) used to acquire each fringe pattern is indicated in the figure. In regions where there is no overlap between light from corresponding channels from the two interferometer arms there is no valid data. This can be seen as vertical bands of higher frequency fringes oriented vertically through the centre of figure 4.10(a) and horizontally through the centre of figure 4.10(b). This is due to mixing of light from different measurement channels. The images were obtained from the object under static loading conditions with a duration of more than 0.1 s between the frames.

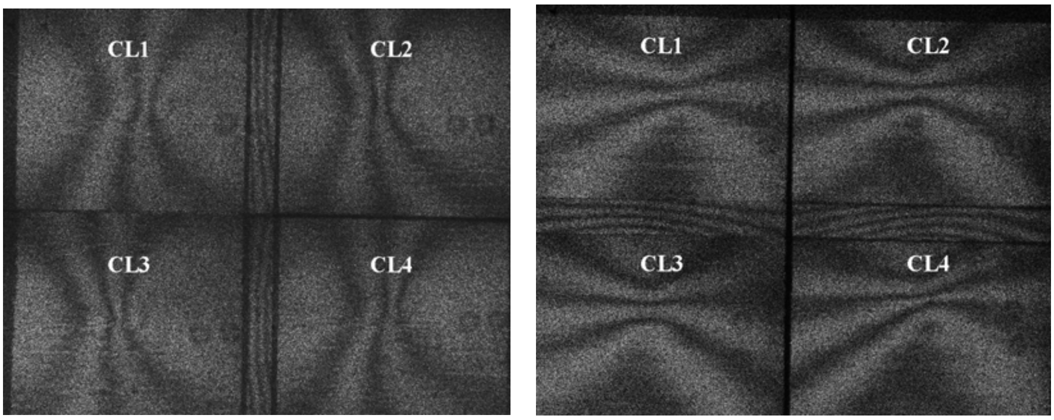

(a) **(b)**

Figure 4.10 *Correlation fringes generated with shear applied in the x-direction (a) and y-direction (b). CL1-4 represents the camera lens used to acquire each image.*

4.7 The DaVis interface

This section examines the interface of the camera control software package from LaVision, DaVis. Figure 4.11 shows a section of a screenshot of the DaVis interface. The camera can be controlled easily using the 'Camera', 'Take' and 'Grab' buttons (1). 'Camera' is used to set up the camera, 'Take' captures a single image and 'Grab' continuously acquires images until the 'Stop' button is pressed. The buffer list (2) shows all the buffers that are currently being used. When an image is captured, or loaded into the program, it is stored within a buffer. One buffer holds one image. A total of 200 image buffers are available within DaVis. An image can be viewed by selecting it from the buffer list. The image is then seen in a window (3). The size and zoom level of the window currently being used to view an image is controlled by the buttons under label (4). The resolution of the image being viewed can be set using the buttons under label (5). The camera that is used is 12 bit, so a maximum of 4096 grey levels can be used to display the image. A colourmap can be selected using (6). The colourmap shown in this example is a conventional greyscale colourmap with black representing zero counts and white representing the maximum number of counts determined by the image resolution.

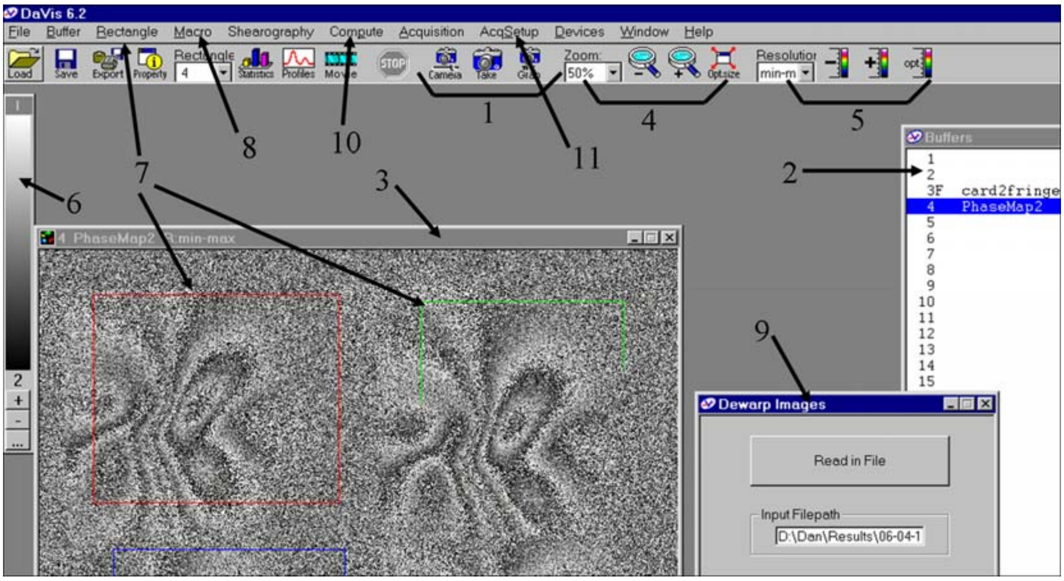

1
2
3F card2fringe
4 PhaseMap2
5
6
7
8
9
10
11
12
13
14
15

Input Filepath: D:\Dan\Results\06-04-1

Figure 4.11 *A screenshot showing the DaVis interface. The numbers indicate some of the important features of DaVis that are described in the text.*

The 'rectangle' menu (7) is used to select a rectangular region within an image. The selected region can then be copied into another image buffer. A total of 8 rectangles can be saved in DaVis and can be used on any image. This function is useful, within the context of this work, for dividing the composite images into their individual image quadrants.

The 'macro' menu can be used to load user defined macros created with the DaVis command language. The command language is a text based programming language similar in structure to the C language. The ability to create macros is useful for performing sequences of image processing. For example, the static frame subtraction routine used to generate the correlation fringes shown in figure 4.10 was achieved using a DaVis macro. All DaVis functions are defined within the command language. Additional functions can be programmed in C++ and called from the main CL program as a DLL (dynamic link library). CL contains functions that can be used to build a graphical user interface (GUI) for a macro. An example of a macro GUI is shown under label (9) in figure 4.11.

The ‘compute’ menu (10) contains a number of image processing functions such as image filtering and Fourier transform calculations. Some of the features that can be accessed from the ‘compute’ menu are the functions that are used to correct images for perspective distortion. This is important within the context of this work because each of the camera lenses views the target at an angle, introducing perspective distortion into the recorded images. The effect of perspective distortion can be seen in figure 4.6, for example. Errors will be present in the results of calculations made from images obtained with the system if this distortion is not corrected for. The process of correcting for perspective distortion, known as image ‘dewarping’, requires the calibration of a test grid. The calibration process is carried out using the functions in the ‘compute’ menu. The dewarping process is described in more detail in section 6.1.

Functions within the ‘acquisition set up’ menu (11) can be used to select which camera to use (if more than one camera is connected to the PC) and to set the exposure time of the camera. The background subtraction function can be toggled on or off under this menu. The background subtraction function works by averaging a series of 10 images recorded sequentially with the laser beam switched off. The resulting image is saved and subtracted from all subsequent recorded images. Background subtraction is used to remove sources of background noise from the recorded images. Sources of background noise include ambient light, such as light from the PC monitor, and CCD dark current.

4.8 Image processing

The image processing scheme used to calculate the orthogonal displacement gradient components is illustrated in figure 4.12. First, images are captured before (reference frame) and after (signal frame) deformation of the test object. The signal and reference frames are used to calculate the wrapped phase distribution across the field of view. The phase analysis techniques used with this system are discussed in chapter 5. The wrapped phase maps are filtered to remove high frequency noise. The images are then separated into their individual image quadrants using the DaVis rectangle functions described above. The phase maps are unwrapped before being dewarped to remove the effects of perspective distortion. The sensitivity vectors are then calculated across the field of view for each image quadrant. Finally, the sensitivity vector maps are combined with the unwrapped phase maps to calculate the orthogonal displacement gradient components. Only the results from three of the four measurement channels are required for the displacement gradient calculation.

The capture of images, separation of individual measurements and image dewarping are all achieved using DaVis macros. Image filtering, phase unwrapping and the displacement gradient calculation are done using Matlab. The calculation of wrapped phase and the calculation of the sensitivity vectors are done either with Matlab or with DaVis depending on the method used. The methods used for calculating the wrapped phase and the sensitivity vectors are discussed in chapters 5 and 6 respectively. Matlab, an acronym for matrix laboratory, is a software package designed for the manipulation of matrices. Since a digital image can be considered as a large matrix, Matlab is powerful tool for digital image processing. It is relatively easy to use and it is often more convenient to program image processing functions in Matlab than in the DaVis command language.

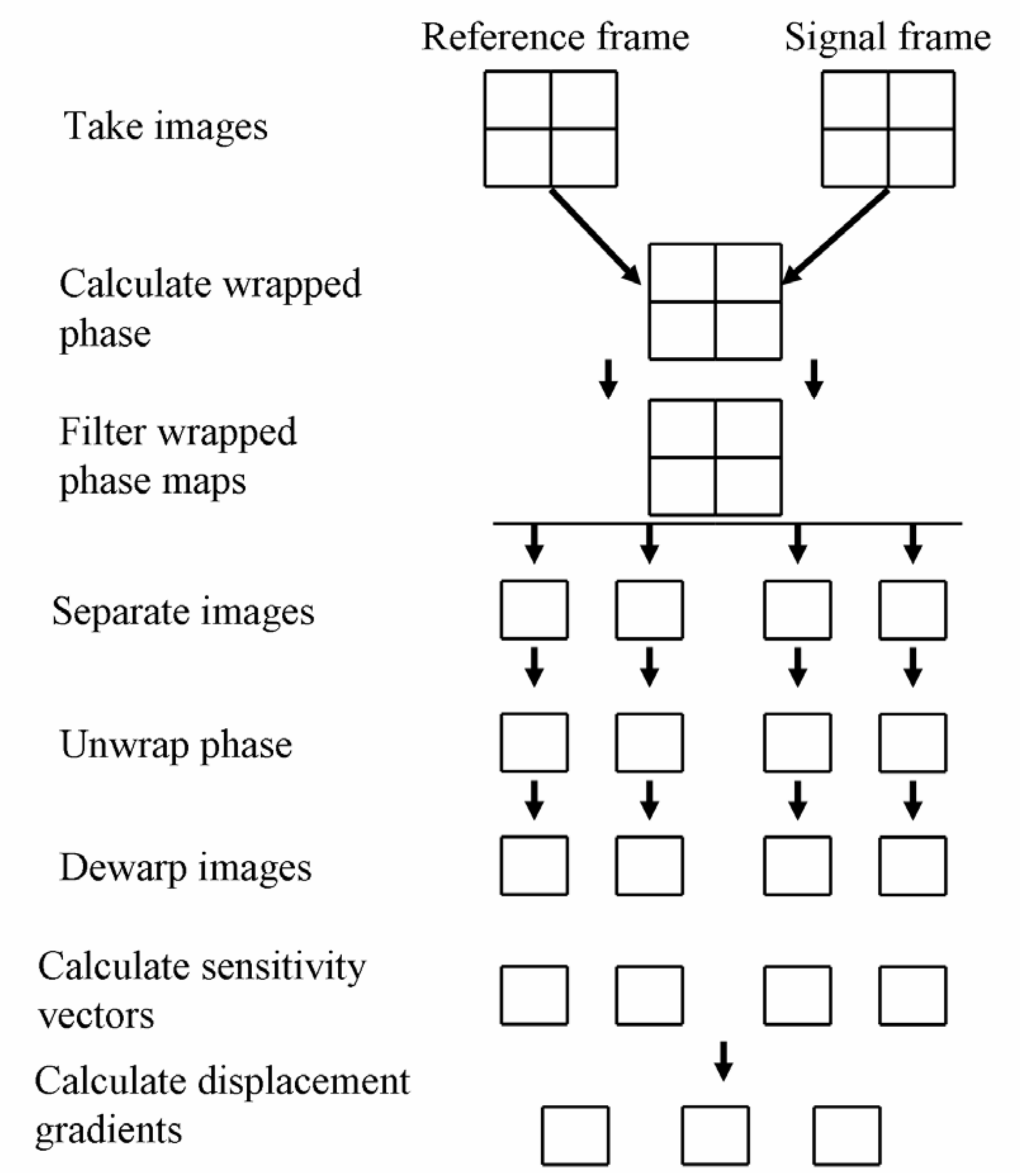

Figure 4.12 *The image processing scheme used to calculate the orthogonal displacement gradient components.*

4.9 Multiple-illumination-direction shearography

This section introduces a multiple-illumination-direction shearography system developed previously at Cranfield University to measure surface strain from static, non-planar objects [1, 2]. This instrument was used previously to make static surface strain measurements from the flat Perspex plate (figure 4.8(b)) [10]. These results are compared with results obtained from the multiple-viewing-direction system in section 6.4.2. This instrument was also used, operating with a single measurement channel, in the temporal phase stepping analysis presented in section 5.1. The system, shown in figure 4.13(a), contains three laser diodes (SDL model 5410 series) operating at a wavelength of 810 nm and an output power of 100 mW. Light from each of the diodes is guided to the three illumination positions, located at three corners of a square, by single mode optical fibres. The frequency of each laser is stabilized by fibre Bragg gratings (FBGs) written into the input end of the delivery fibres. Negative lenses positioned at the fibre outputs serve to diverge the laser beams to illuminate the region of interest on the targets surface. Measurements made using the system are time-division-multiplexed. That is, images are recorded with light from each position illuminating the target sequentially. Illumination from each direction can be toggled by switching the electronic shutters positioned between the fibre outputs and the negative lenses.

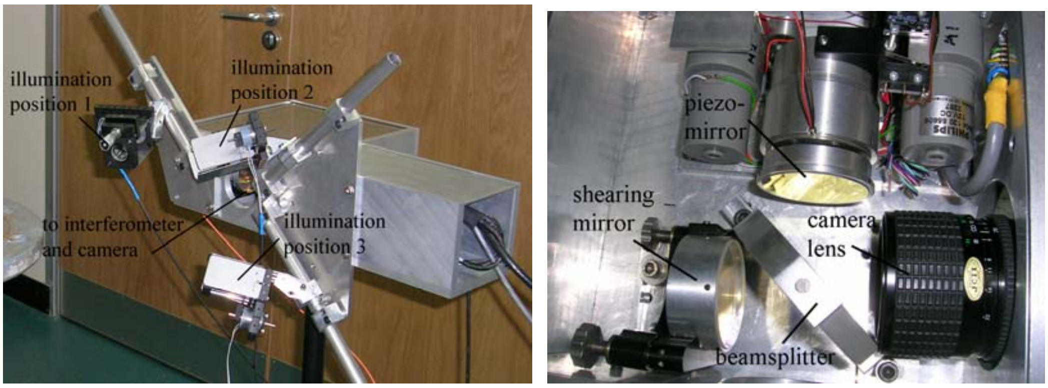

(a) **(b)**

Figure 4.13 *The laser diode based multiple illumination direction shearography system (a) and the shearing interferometer within this system (b).*

The illumination modules, consisting of the negative lenses and the electronic shutters, are mounted on aluminium bars which are fixed onto the box that contains the shearing interferometer and the CCD camera. This box is mounted on a tripod which can be used to adjust the height of the instrument for each particular application. The position of the illumination modules along the bars can be adjusted so that a range of illumination angles can be achieved. An aperture at the front of the box allows light scattered from the object to be imaged onto the camera via the shearing Michelson interferometer. The shearing interferometer, shown in figure 4.13(b), consists of a beamsplitter, a reference mirror and a shearing mirror. The shearing mirror can be adjusted in two orthogonal directions to allow image shearing in either the x or y direction. The reference mirror is mounted on a piezo-electric transducer (PZT) to facilitate phase stepping. A camera lens is used to image light propagating through the interferometer onto the camera. The camera is an 8-bit Dalsa (model CA-D4-0512A) CCD camera with spatial resolution of 512 x 512 pixels. Acquisition of images is achieved using a Bitflow Roadrunner framegrabber PCI card. Image acquisition, phase stepping and the electronic shutters are all controlled by software written in labVIEW.

Examples of the correlation fringes obtained with this instrument are shown in figure 4.14. These fringe patterns were obtained from static frame subtraction of images recorded before and after object deformation. The object used in this case was the flat aluminium plate shown in figure 4.8(a). The magnitude of the applied shear in both the *x*-direction (figure 4.14(a)) and the *y*-direction (figure 4.14(b)) was approximately 8 mm on the object's surface. The field of view in both figures is approximately 10 cm x 10 cm.

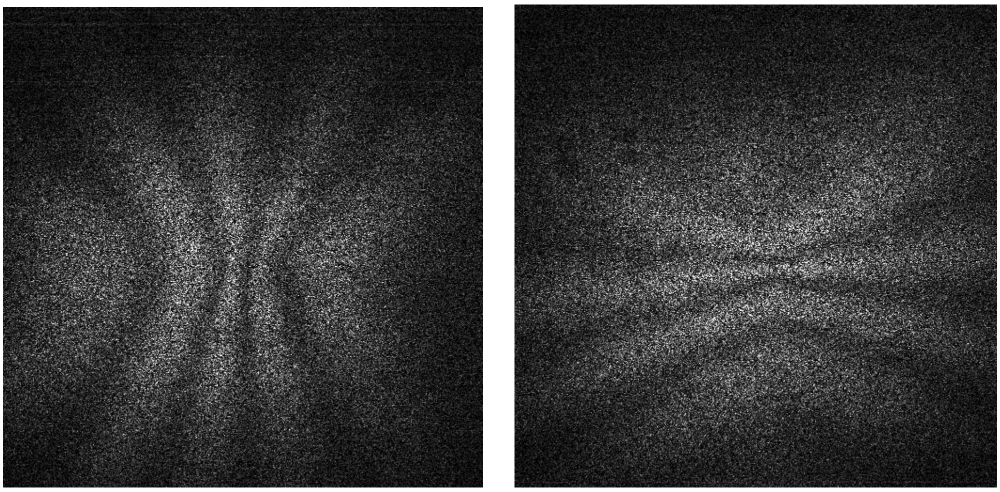

(a) **(b)**

Figure 4.14 *Correlation fringes recorded using a single measurement channel of the laser diode shearography system with shear applied in the x-direction (a) and in the y-direction (b).*

4.10 Summary

In this chapter, the components used in the development of the multiple-viewing-direction, pulsed-laser shearography system have been presented. These components include the pulsed Nd:YAG laser system, the coherent fibre-optic imaging bundles and the CCD camera. The software used to control the CCD camera was presented. The processing scheme used to obtain surface strain measurements from the images recorded using the shearography system was illustrated. A multiple-illumination-direction shearography system, developed previously at Cranfield University was also introduced.

References

[1] James S. W. and Tatam R. P, 'Time-division-multiplexed 3D shearography', *Proc. SPIE*, **3744**, 394-403 (1999).
[2] Groves R. M, 'Development of shearography for surface strain measurement of non-planar objects', *PhD Thesis*, Cranfield University, Bedford (2001).
[3] Kentech pulse shaping software manual, Kentech Instruments Ltd, Oxford, UK.
[4] Operation and maintenance manual, Custom 150 ns long pulse laser, Continuum, Santa Clara, CA, USA.
[5] Nobes D. S, Ford H. D and Tatam R. P, 'Instantaneous, three component planar Doppler velocimetry using imaging fibre bundles', *Exp. Fluids* **36**, 3-10 (2004).
[6] Operation and maintenance manual, NY60 and NY61 lasers, Continuum, Santa Clara, CA, USA.
[7] Groves R. M, James S. W and Tatam R. P, 'Multi-component shearography employing four measurement channels, *Proc. SPIE* **4933**, 135-40 (2003).
[8]http://www.us.schott.com/fiberoptics/english/products/imaging/flexiblecomponents/wound.html
[9] Charrett T. O. H, Ford H. D, Nobes D. S, and Tatam R. P, 'Two-frequency planar Doppler velocimetry (2ν-PDV)', *Rev. Sci. Instrum.* **75**:11, 4487-96 (2004).
[10] James S. W, Groves R. M. and Tatam R. P, ''Surface strain characterization using time-division multiplexed 3D shearography', *Proc. SPIE*, **4101**, 384-93 (2001).

5. Experimental investigations into phase measurement techniques

One of the key processing steps in quantitative shearography is the determination, across the field of view, of the optical phase difference before and after object deformation. In this chapter, a selection of the phase measurement techniques that were described in chapter 3 are experimentally investigated using the shearography systems presented in chapter 4. Temporal phase stepping was investigated using a single channel of the laser diode shearography system described in section 4.9. This technique was then incorporated into the processing procedure for the pulsed laser shearography system. The motivation for exploring further phase analysis techniques is due to the need to determine the phase from only two frames from the CCD camera. This requirement is imposed when dynamic test surfaces are to be analyzed. Two techniques that fulfil this requirement are spatial phase stepping and the spatial carrier technique. The investigation of these two techniques is described in sections 5.2 and 5.3. Phase unwrapping was achieved using ISTRA software, which is based on the minimum spanning tree principle [1], and with Goldstein's branch cut algorithm [2]. These algorithms are compared in section 5.4. Each of the phase analysis techniques that are discussed in this chapter were investigated using data obtained using the flat aluminium plate test object described in section 4.5.

5.1 Temporal phase stepping

Temporal phase stepping [3], described in section 3.1, is a convenient method of phase analysis for displacement derivative measurement of static test objects. The principle relies on the recording a series of at least three images with a known phase step between each of them. The phase can then be calculated using an arctangent function known as a phase stepping algorithm. The work presented here was conducted using a single channel of the multiple-illumination-direction laser diode based shearography system described in section 4.9. In this system, the phase shift is applied by translating one of the mirrors in a shearing Michelson interferometer. In this interferometer, the reference mirror is mounted on a piezo-electric transducer (PZT). Applying a voltage to the PZT causes it to expand, which translates the mirror causing a concomitant shift in the phase of that arm relative to the other. Section 5.1.4 describes the incorporation of this technique into the pulsed laser shearography system.

5.1.1 Calibration of the PZT

Each of the phase stepping algorithms discussed here requires a specific, known phase step between each of the recorded images. It was therefore necessary to calibrate the PZT so that, for a particular voltage applied to the PZT, the phase shift in the interferometer is known. The calibration of the PZT was achieved using a program written in LabVIEW. Using this program to control an analogue-to-digital card located in the PC, the voltage applied to the PZT was initially set to zero. A speckle pattern was recorded and saved as a reference image. The voltage was then incremented and another speckle pattern was recorded with no deformation applied to the object. This speckle pattern was subtracted from the reference speckle pattern and the resulting image was rectified. The average of all pixel values within a 350x350 pixel box in the centre of the 512x512 image was calculated and this value was saved. This box size was chosen to obtain a good estimate of the average intensity within the image and also window out lower intensity regions around the edges of the image that exist because of the Guassian beam profile. This procedure was repeated until the voltage applied to the PZT had reached 10 V, which is the maximum voltage output from the analogue-to-digital card. The average value within the 350x350 box at each voltage step was then plotted against the applied voltage and a curve was fitted. This curve is shown in figure 5.1. When the phase has been shifted by 2π, the speckle pattern should be the same as the reference speckle pattern at zero phase shift. Subtracting from the reference gives a minimum average pixel value within the 350x350 box. This value is not quite zero because of background noise sources such as fluctuations in ambient light in the time between acquisition of the two images. The voltage required to provide a phase shift of 2π was found to be 5.8 V ± 0.1 V. This was determined from repeated runs of the program to obtain an increased confidence. The uncertainty in the voltage measurement corresponds to an uncertainty of ±6.2° for a 2π phase shift. This calibration method is similar in principle to the method used by Olszak and Tatam [4] to determine the path length imbalance in fibre-optic ESPI systems.

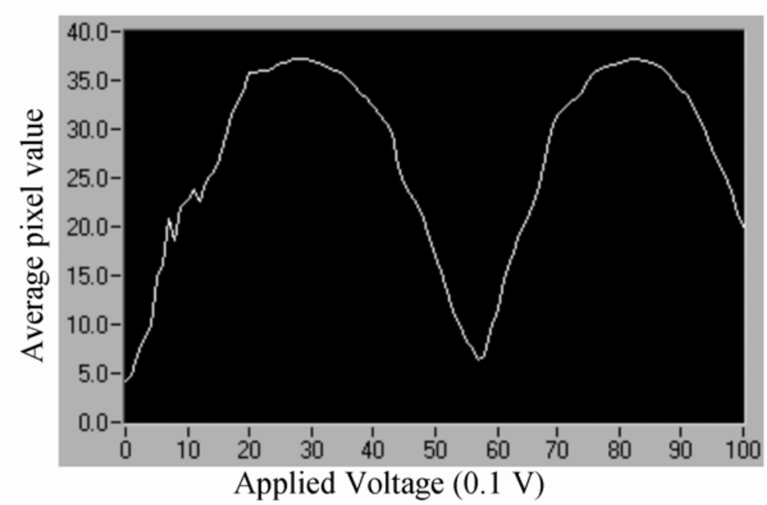

Figure 5.1 *PZT calibration curve showing the average pixel counts vs. applied voltage V within a 350x350 box in the centre of the image generated by subtraction of speckle patterns recorded with a voltage of 0 and V volts applied to the PZT.*

5.1.2 Development of a three-step algorithm

The phase can be calculated from three phase-stepped fringe patterns with a phase step of 2π/3 between them. This is done using a three-step algorithm given by [5]

$$\phi = \tan^{-1}\left(\sqrt{3}\,\frac{I_3 - I_1}{2I_2 - I_1 - I_3}\right) \tag{5.1}$$

The phase shift versus applied voltage to the PZT was assumed to be linear across the voltage range of the analogue-to-digital card. The voltage steps required for three 2π/3 steps is therefore 0 V, 1.93 V and 3.87 V for phase steps 1 to 3 respectively. Three fringe patterns with a 2π/3 phase shift between them are shown in figure 5.2. In this example, phase stepping was applied to the reference frames only. The signal frame was then subtracted from each of the phase stepped reference frames to generate the fringe patterns. The fringe patterns were then smoothed through the application of a 3x3 low pass filter. The phase was calculated from the phase stepped fringe patterns using equation (5.1). The wrapped phase map calculated from the three phase stepped fringe patterns is shown in figure 5.2. This method of phase stepping is known as the 'phase of difference' method [6] because the subtraction was carried out *before* the phase was calculated.

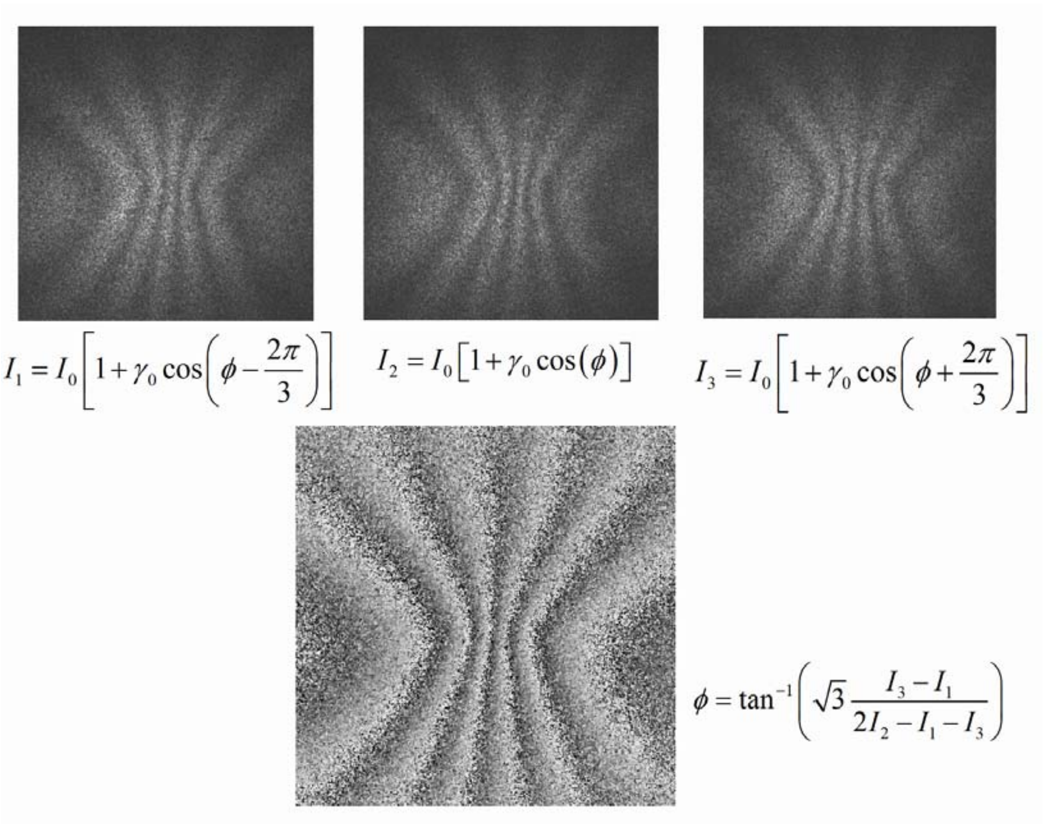

Figure 5.2 *Three phase stepped fringe patterns are combined using a three-step algorithm (equation 5.1) to yield a wrapped phase map.*

An alternative method involves phase stepping both the reference and signal frames. In this case, the phase is calculated for the signal and reference frames independently and then subtracting to obtain the phase difference. This method is known as the 'difference of phases' method [6] because the subtraction is calculated *after* the phase is calculated. The 'difference of phases' method is often favourable because there is less noise present in the calculated phase map than with the 'phase of differences' method [6]. The 'phase of differences' method is sometimes favourable when faster processing speed is required because only a single signal frame is necessary. Wrapped phase maps calculated using the two methods are shown in figure 5.3. The wrapped phase map calculated using the 'difference of phases' method was processed through the application of a 3x3 low pass filter applied to the sine and cosine of the wrapped phase map.

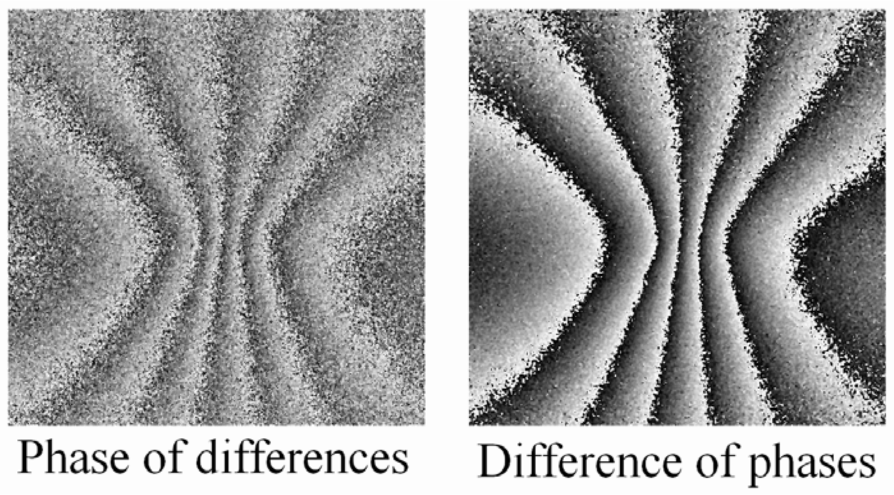

(a) (b)

Figure 5.3 *Wrapped phase maps calculated using the 'phase of differences' method (a) and the 'difference of phases' method (b).The 'difference of phases' method produces an improved quality phase map of that produced by the 'phase of differences' method.*

5.1.3 Comparison of phase stepping algorithms

A program was developed using LabVIEW to compare qualitatively a number of different phase stepping algorithms. This program acquired the necessary phase stepped frames for each algorithm simultaneously so that the results from each algorithm were obtained from the same deformation of the object. Each of the phase maps were calculated using the 'difference of phases' method described above. The images were processed by the application of a 3x3 low pass filter to the sine and cosine of the wrapped phase maps. The first algorithm implemented in the program was the three-step algorithm with a phase step of 2π/3 given in equation 5.1. The other algorithms were a three-step algorithm with a π/2 phase step [7]

$$\phi = \tan^{-1}\left(\frac{I_3 - I_2}{I_1 - I_2}\right) \tag{5.2}$$

and a four-step algorithm also with a π/2 phase step

$$\phi = \tan^{-1}\left(\frac{I_4 - I_2}{I_1 - I_3}\right) \tag{5.3}$$

Also implemented was the Schwider-Hariharan five-step algorithm [8, 9] with a π/2 phase step,

$$\phi = \tan^{-1}\left[\frac{2\left(I_2 - I_4\right)}{2I_3 - I_5 - I_1}\right] \tag{5.4}$$

a six-step algorithm with a π/2 phase step [10]

$$\phi = \tan^{-1}\left(\frac{3I_1 - 5I_2 + 5I_5 - 3I_6}{I_1 + 3I_2 - 4I_3 - 4I_4 + 3I_5 + I_6}\right) \tag{5.5}$$

and a seven-step algorithm with π/2 phase step [11]

$$\phi = \tan^{-1}\left[\frac{-\left(I_1 - I_7\right) + 7\left(I_3 - I_5\right)}{-4\left(I_2 + I_6\right) + 8I_4}\right] \tag{5.6}$$

Wrapped phase maps calculated using the six algorithms given above are shown in figure 5.4. The phase maps calculated using the two three-step algorithms appear to possess slightly higher levels of noise than the other phase maps. There does not appear to be much improvement in the quality of the wrapped phase map after about 4 or 5 phase steps.

3-step ($2\pi/3$) 3-step ($\pi/2$) 4-step

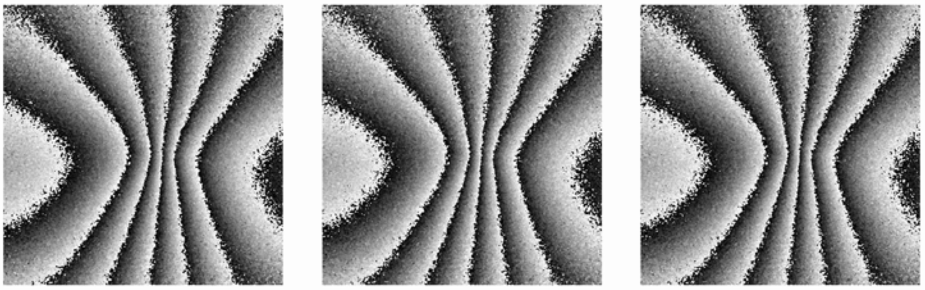

5-step 6-step 7-step

Figure 5.4 *Wrapped phase maps calculated using six different phase stepping algorithms.*

5.1.4 Phase stepping in the pulsed laser shearography system

Phase stepping was used in the analysis of static objects with the pulsed laser shearography system. This was also achieved using a PZT mounted mirror in the reference arm of the shearing Michelson interferometer. The voltage required to translate the PZT mounted mirror was generated using a Keithley 230 programmable voltage source. The voltage source was controlled externally using a GPIB (general purpose interface bus) card housed within the image acquisition PC. The PZT mirror was calibrated in the same manner as described in section 5.1.1. The phase stepping algorithm that was used was the five-step algorithm presented in the previous section. This algorithm was chosen because it seemed to perform well in comparison to the other algorithms investigated in the previous section. This algorithm also compensates for errors due to PZT miscalibration [9] which may be introduced as a consequence of the assumption of the linearity of the PZT. The main phase stepping program was written as a macro in the DaVis command language. The phase stepping algorithm was coded in C++ which was called by the DaVis macro as a DLL (dynamic link library). The algorithm was coded in C++ because pixel-wise calculations can be performed considerably faster than in DaVis command language. This allows for quasi-real time acquisition of wrapped phase maps. An example of the raw, unfiltered phase maps obtained from the system is shown in figure 5.5(a). This image was processed using the iterative sine-cosine filtering method developed by Aebischer and Waldner [12] and the result is shown in figure 5.5(b). This filtering method was described previously in section 3.5.2.

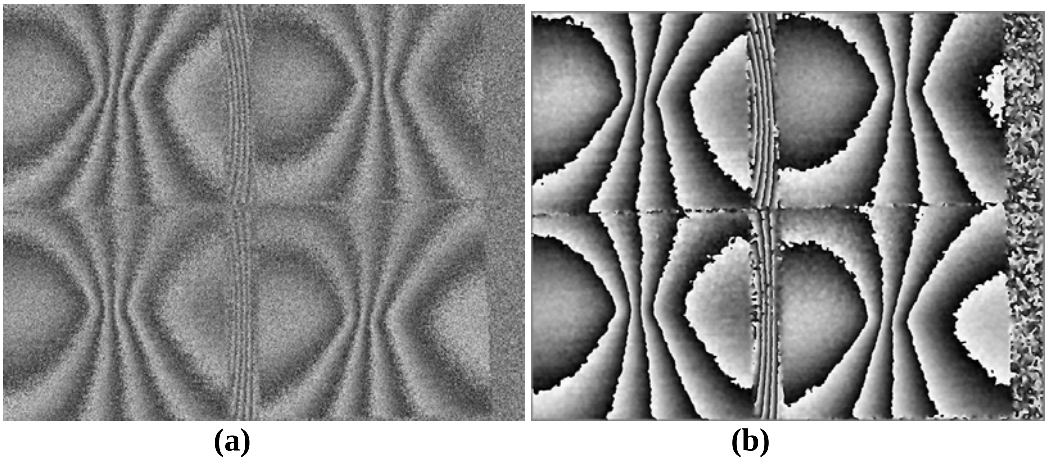
(a) **(b)**

Figure 5.5 *Wrapped phase maps obtained from the multiple viewing direction shearography system using temporal phase stepping using the 5-step algorithm [9]. The wrapped phase maps are unprocessed in (a) and processed using an iterative sine-cosine filter in (b) [12].*

5.2 Spatial phase stepping using a diffractive optical element

Temporal phase stepping is not a feasible technique when dynamic surfaces are to be measured due to the limitation that only two frames of data can be used in the phase calculation. Spatial phase stepping was therefore investigated as a potential solution for phase analysis within the pulsed laser shearography system. Spatial phase stepping involves recording a series of phase stepped speckle patterns simultaneously. One method of achieving this is to use a diffractive optical element (DOE) to divide the incident beam into four separate beams in the ±1 diffracted orders. A relative phase shift can then be applied to each of the diffracted beams, which are spatially multiplexed onto the four quadrants of a CCD camera. The use of a single camera results in a cheaper and simpler optical arrangement relative to the alternative multiple camera solution, at the cost of reduced spatial resolution. DOEs have previously been used successfully with spatial phase stepping in ESPI [13, 14], as was described in section 3.2.1.

5.2.1 Mach-Zehnder shearing interferometer for spatial phase stepping

To achieve phase shifting in interferometry, the DOE needs to be placed in one of the arms of the interferometer so that a relative phase shift is introduced between light propagating through the two arms of the interferometer. This requirement becomes an issue when using a conventional Michelson interferometer in shearography. This is because the phase shift would be reversed on the second pass through the DOE after reflection at the mirror, as illustrated in figure 5.6. Also the diffracted beams would be diffracted an undesired second time at the DOE.

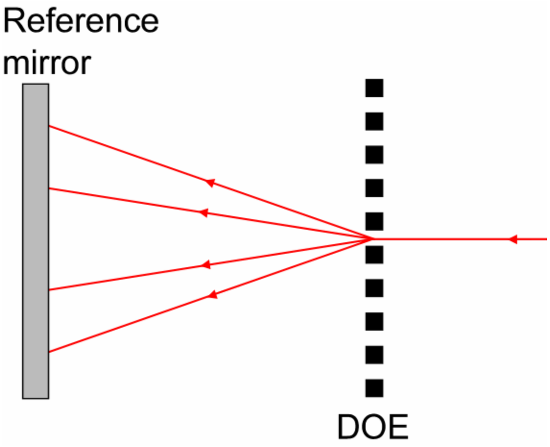

Figure 5.6 *The DOE located in one arm of a Michelson interferometer. After reflection at the mirror the applied phase shift will be reversed after a second pass through the DOE. The diffraction would also occur a second time.*

To overcome this problem, a Mach-Zehnder shearing interferometer is proposed. In a Mach-Zehnder interferometer light propagates only once through each of the interferometer arms. The problem of the double pass that occurs in the arm of a Michelson interferometer is therefore not an issue. The proposed interferometer is shown in figure 5.7. The interferometer contains a DOE within each of the interferometer arms. The DOE in one arm is used to divide the incident beam into four diffracted beams as well as applying a relative phase shift of $\pi/2$ between each of the diffracted orders. The DOE in the second arm is required only for beam division and applies no phase shift. This way, a relative phase difference is introduced between the diffracted beams propagating through the two arms of the interferometer. The interferograms produced by combination of the diffracted beams from each of the interferometer arms are imaged onto the CCD camera by the imaging lens. The four images recorded will have a relative phase difference of $\pi/2$ and the wrapped phase can be calculated from the four images using the four step algorithm given in equation 5.3.

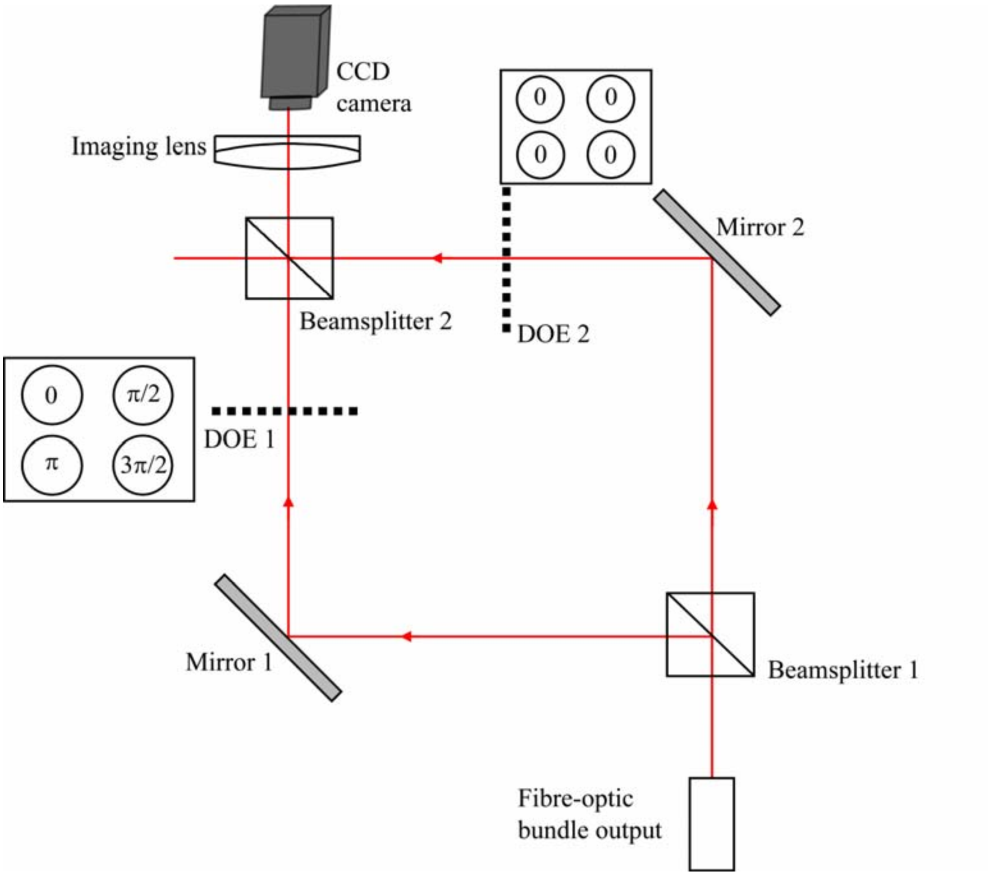

Figure 5.7 *Proposed Mach-Zehnder shearing interferometer for spatial phase stepping using a diffractive optical element.*

5.2.2 Preliminary results from DOE investigation

In order to investigate the proposed system, a DOE was borrowed from SILIOS technologies in France [15]. The DOE was a cross binary grating and was a combination of an amplitude and phase grating. A silica substrate was etched to produce the phase grating and a metal layer was then deposited and etched to produce the amplitude grating. The dimensions of the grating were optimized so that the intensity within the zero diffraction order and orders greater than 1 are minimized. The diffraction angle of the grating was 0.35°. The DOE served only to divide the beam into the four separate orders. It is apparently difficult to manufacture a DOE that performs both beam division and produces a controlled phase shift between each of the diffracted orders. Stéphane Tisseraud, of SILIOS technologies, suggested a revision of the proposed interferometer whereby beam division is performed by a single DOE located at the input of the interferometer and the phase shifting is performed by phase screens located in the interferometer arms. This system would also be cheaper to develop than the one shown in figure 5.7 since only one DOE is required. The phase screens are manufactured by SILIOS and could be delivered with a DOE if it was decided that this system offers the best solution to the phase analysis problem.

The next step in the investigation of the DOE was simply to image the diffracted orders onto the camera so that images within each of the orders were well separated. By placing the DOE at the output of the fibre bundles and imaging light diffracted by the grating the diffracted images were found not to be well separated as shown in figure 5.8(a). The separation of the orders in the image plane was found to be dependent on the distance between the grating and the bundle output. The further from the bundle output that the DOE is located the greater the separation of the diffracted orders in the image plane. The separation can also be increased by placing a negative lens between the bundle output and the DOE. Figure 5.8(b) shows the diffracted orders well separated by the introduction of the negative lens. The use of the negative lens introduces another problem, however, in that only a small proportion of the light exiting the bundle output is captured by the imaging lens and focused onto the camera. This is not so much of a problem when using a high power laser such as the long pulse Nd:YAG but could prove to be an issue when using lower power laser systems.

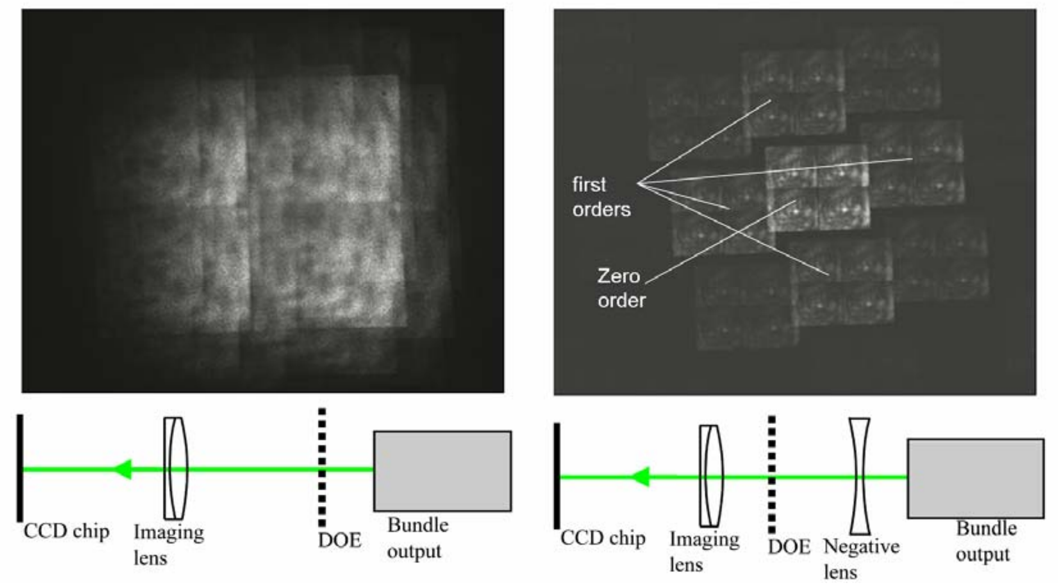

(a) **(b)**

Figure 5.8 *Image recorded with the camera with the DOE placed just after the bundle output (a). The diffracted orders overlap in the image plane. Increasing the separation between the bundle output and DOE and placing a negative lens between the output and the DOE results in well separated images in the focal plane (b).*

The next step was to observe shearography fringe patterns produced within the diffracted images. To do this a Michelson shearing interferometer was placed between the DOE and the imaging lens, as shown in figure 5.9. The reference mirror in figure 5.9 was equipped with a PZT to facilitate phase stepping. Temporal phase stepping was used because wrapped phase maps tend to be of better contrast than correlation fringe patterns generated in shearography. Figure 5.10 shows some wrapped phase maps obtained with the DOE and Michelson interferometer. The phase maps shown in the figure have been processed with the application of the iterative sine-cosine filter. In the figure, the diffraction terms higher than the first order have been masked out for clarity. The images shown were obtained with increasing deformation applied to the flat aluminium plate giving a range of fringe densities across the field of view of each individual measurement channel.

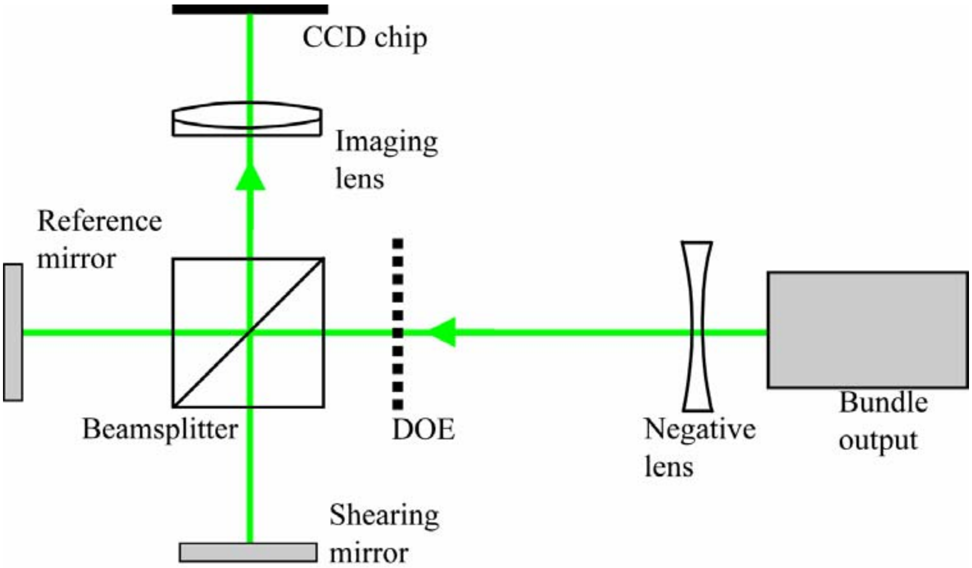

Figure 5.9 *Michelson interferometer used with the DOE to investigate fringe patterns within the diffracted images.*

The images presented in figure 5.10 display approximately one, two and three fringes across each individual view, respectively. It can be seen from figure 5.10 that as the fringe density across each image increases, the more the fringes become corrupted by noise. This is most likely due to the reduced spatial resolution of each image quadrant. In figure 5.10, the image from each view is sampled by only approximately 50x50 pixels. This could be improved by using a camera with a larger number of pixels. For example, if a camera with 4000x4000 pixels were used, each view within each diffracted order would be sampled by approximately 200x200 pixels. The number of pixels within the image from each view could be increased further by using a DOE and imaging optics that makes better use of the available space on the CCD sensor. The fringe density for a particular deformation could also be reduced by reducing the magnitude of the applied shear. The fringe patterns shown in this thesis obtained using temporal phase stepping show fringe densities of up to 6 fringes across each individual view with each view sampled by approximately 500x500 pixels. The spatial phase stepping technique should work as well as temporal phase stepping if each view is sampled by the same number of pixels. However, a new camera plus the cost of the DOE was beyond the budget of this project, but not too expensive relative to the fibre bundles and pulsed laser which were already available so would therefore be a good approach to investigate in another project. It would therefore be convenient to use an alternative phase analysis technique that does not require such expensive components.

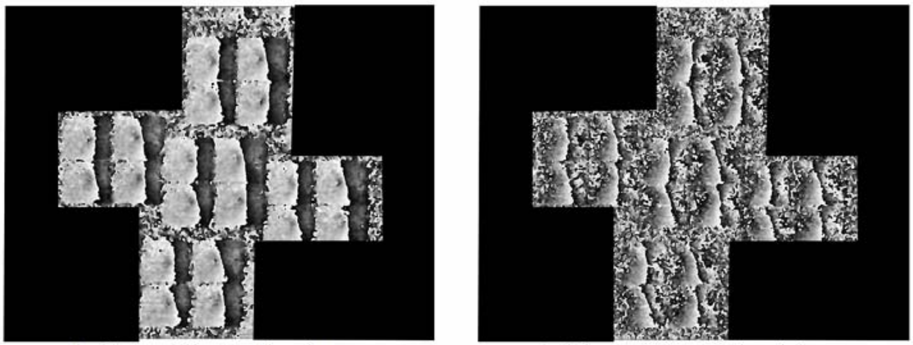

1 fringe discontinuity 2 fringe discontinuities

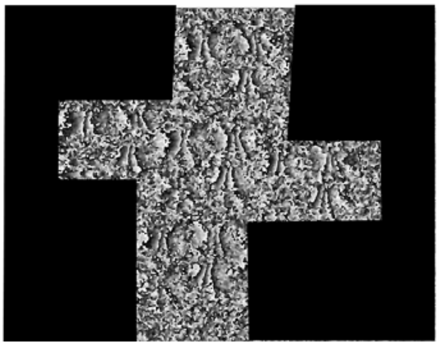

3 fringe discontinuities

Figure 5.10 *Wrapped phase maps generated using temporal phase stepping in a Michelson interferometer positioned between the DOE and the imaging lens. The fringes become more corrupted by noise as the fringe density increases. The images from the diffracted orders higher than ±1 have been masked out for clarity.*

5.3 Phase analysis using the spatial carrier technique

The spatial carrier technique [16] involves introducing a carrier frequency into the recorded speckle pattern so that the desired phase information is spatially separated from the DC term in frequency space. The frequency distribution of an image can be accessed easily using a two-dimensional FFT (fast Fourier transform) algorithm included in software such as Matlab. One of the phase-encoded side-bands is isolated in frequency space and the carrier fringes are removed either by translating the side-band to the origin or by subtracting the inverse transformed spectra of images recorded before and after object deformation.

5.3.1 The spatial carrier technique using source displacement

The required carrier frequency can be introduced to the speckle pattern by translating the source along the optical axis in the duration between recording signal and reference frames [17]. This can be done easily by physically translating the negative lens that is used to diverge the beam to illuminate the target. This method was investigated using a single channel of the multiple-illumination-direction shearography system, described in section 4.9.

First, a reference speckle pattern was recorded and saved as a digital array. The illuminating lens was translated by approximately 10 mm and a second speckle pattern was recorded. Subtraction and rectification of the two speckle patterns results in a series of carrier fringes across the field of view, as shown in figure 5.11(a). Note that the carrier fringes are neither perfectly straight nor of constant period across the field of view. This is due to the oblique angle of illumination. The method of removing the carrier frequency involving translation of the side spectra to the origin will therefore not be suitable for correct phase determination, as was shown in section 3.3.2.

The Fourier transform of the carrier fringe pattern of figure 5.11(a) is shown in figure 5.11(b). The spectral features are small in the image so only the central 100x100 pixels are shown in order to see the spectral features clearly. The central DC term has been deleted so that the spectral features can be observed within the scaled image. The magnitude of the lens translation controls the frequency of the carrier fringes and therefore the separation of the spectral features in frequency space. It is important, therefore, that the translation of lens is sufficient that the side bands are well separated from the background (DC) term in frequency space. However, if the translation is too great then the contrast of the carrier fringes will be lost in the speckle noise. In the example shown, the lens was translated by approximately 10 mm.

After the object was deformed, a second speckle pattern was recorded and subtracted from the reference speckle pattern. This results in the phase modulated carrier fringe pattern, shown in figure 5.11(c). The magnitude of the Fourier spectrum is shown in figure 5.11(d). The phase was then calculated independently for the two carrier fringe patterns by isolating one of the side bands in frequency space and then calculating the inverse Fourier transform. The phase was obtained using the equation

$$\phi(x,y) = \tan^{-1}\left(\frac{\operatorname{Im}\left[c(x,y)\right]}{\operatorname{Re}\left[c(x,y)\right]}\right) \tag{5.7}$$

where *c* represents the inverse transformed spectrum at each pixel location *x*, *y*. The wrapped phase map was then obtained by subtraction and rewrapping modulo 2π, as shown in figure 5.11(e).

The wrapped phase map contains more noise around the periphery of the image. This is due to the Gaussian profile of the laser beam which means that the intensity at edges of the image is less that at the centre, resulting in a lower signal/noise in these regions. There are also some rippling effects in the phase map and distortions of the fringe discontinuities. This may be due to the fact that the side features in frequency space are so small, therefore only a small amount of information is isolated and used in the reconstruction of the phase. The effect of the rippling in the phase map can be reduced somewhat by processing the carrier fringe patterns with windowed Fourier filtering [18] prior to the phase calculation. This filtering technique was described previously in section 3.4.3. The central regions of the filtered phase map, shown in figure 5.11(e) are slightly improved, in that there is less rippling, but no signal is observed at the edges of the image where the laser intensity was relatively low.

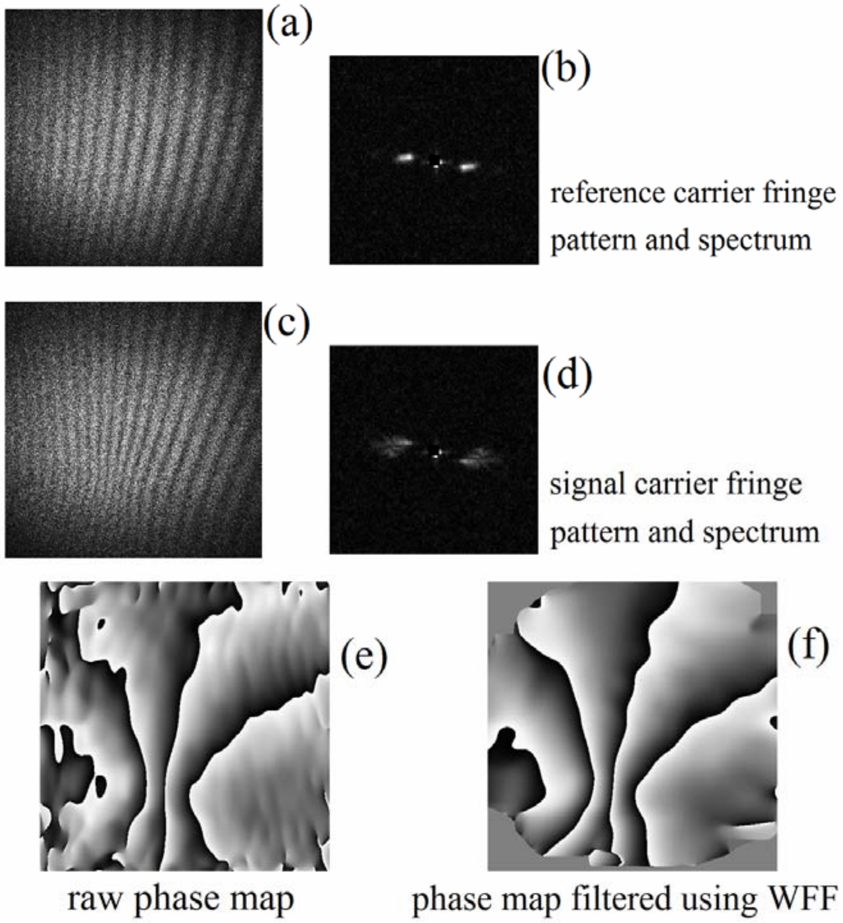

Figure 5.11 *Carrier fringe patterns recorded before (a) and after (c) object deformation and the magnitude of their Fourier transforms (b) and (d). The wrapped phase map calculated from these carrier fringe patterns (e) and the phase map after processing the carrier fringe patterns with windowed Fourier filtering (f).*

This method of carrier fringe generation cannot be directly applied to dual pulsed measurements using the pulsed laser shearography system due to the need to physically translate the illuminating lens. The time difference between the two pulses is too short to be able to achieve this. One solution to this problem involves using the Mach-Zehnder interferometer shown in figure 5.12. Light exiting a laser beam delivery arm passes through a Pockels cell. The first pulse to pass the Pockels cell is transmitted through the polarizing beamsplitter PBS_1 and arrives at the second polarizing beamsplitter PBS_2 via the negative lens NL_1 and the mirror M_2. In the time before the next pulse arrives, a voltage is applied to the Pockels cell. This switches the pulse to an orthogonal polarization and the pulse is reflected from PBS_1 and arrives at PBS_2 via the mirror M_1 and the negative lens NL_2. Since the two negative lenses are located at different distances from PBS_2 the divergence caused by each one will be different and is therefore equivalent to translating the lens between the pulses. Correlation of speckle patterns produced by the two pulses will result in a carrier fringe pattern. This technique is similar in principle to the solution presented by Fernández *et al* [19] for a dual cavity pulsed laser system illustrated in figure 3.9.

Another problem with the method shown in figure 5.11 is that three frames are required; two to generate the reference carrier fringe pattern and another to generate the signal carrier fringe pattern. If the Takeda method of translating the side band to the origin was used instead, only two frames would be necessary. This leads back to the problem of generating perfectly straight carrier fringes, however.

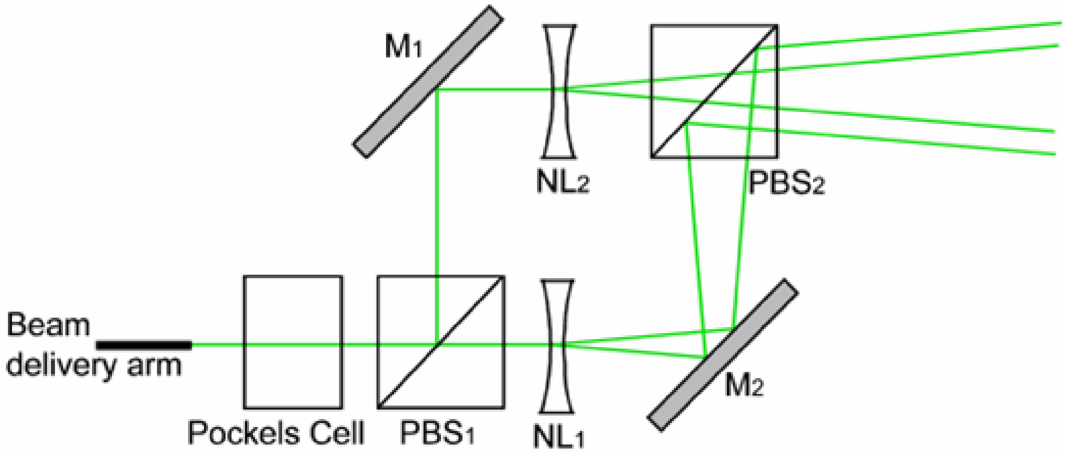

Figure 5.12 *Arrangement suitable for carrier fringe generation in a pulsed laser system. NL = negative lens, M = mirror and PBS = polarizing beamsplitter.*

5.3.2 The spatial carrier technique using a Mach-Zehnder shearing interferometer

Another method of generating carrier fringes involves introducing a tilt between the interfering beams within the interferometer. This can be achieved in shearography using a Mach-Zehnder interferometer. The problem with using a Michelson interferometer is that the tilt required to generate the carrier fringes is much greater than the tilt used to generate the shear and thus the images from the two arms would not overlap in the image plane. A Mach-Zehnder interferometer can be arranged with the tilt required to generate the carrier frequency as well as producing the required image shear. This technique, originally presented by Pedrini *et al* [20], was investigated using the pulsed laser system.

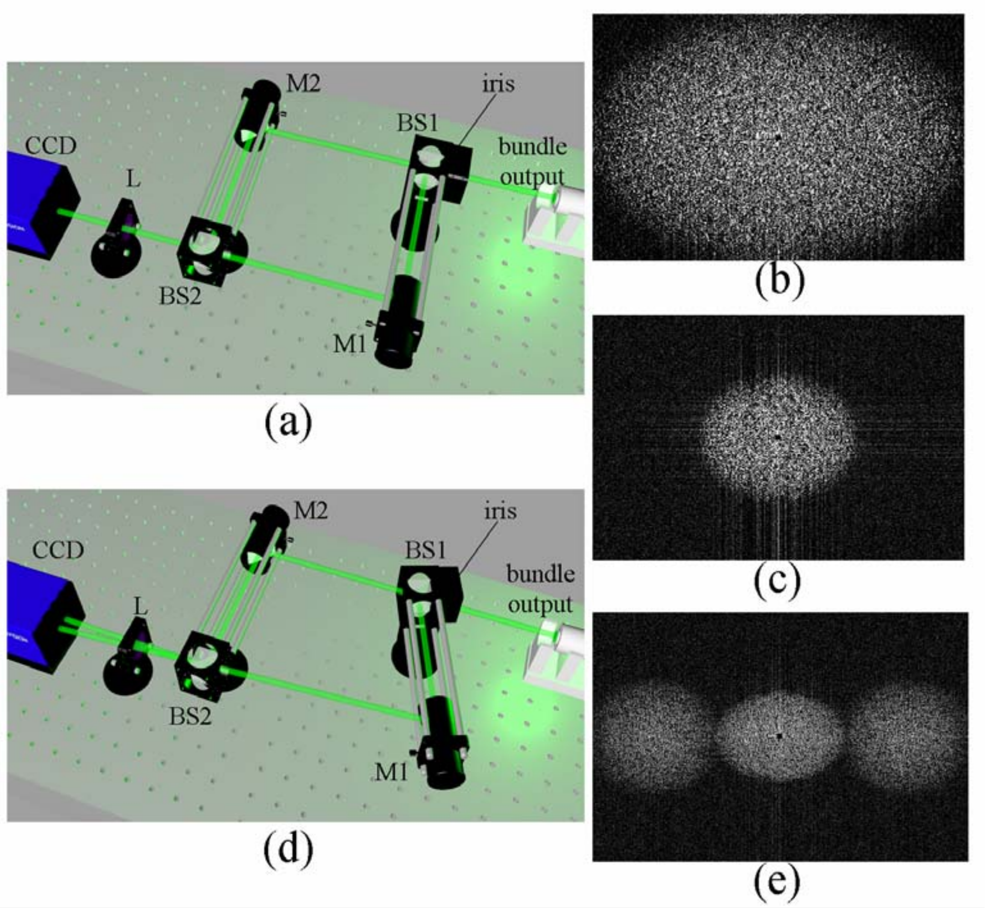

Figure 5.13 *A Mach-Zehnder shearing interferometer located at the output of the fibre bundle (a). The spectral feature observed in the Fourier transform is shown with the large initial aperture (b) and after reduction of the aperture diameter (c), which also increases the speckle size. If a tilt is introduced between the interfering beams (d) a carrier frequency is introduced and the phase dependent side bands are separated from the central term in frequency space (e). L = imaging lens, BS = beamsplitter and M = mirror.*

Figure 5.13(a) shows a conventional Mach-Zehnder interferometer located at the output of the fibre bundle. The lengths of the interferometer arms in the figure are exaggerated for clarity. An iris located at the entrance of the interferometer was used to control the size of the speckles recorded by the camera. Reducing the diameter of the iris aperture also reduces the size of the spectral feature (figure 5.13(b)) observed in frequency space so that a single feature is contained within the Fourier transform image (figure 5.13(c)). Arranging the Mach-Zehnder interferometer in such a way that a tilt is introduced between the interfering beams produces a linear phase variation between the beams incident on the CCD chip. This can be achieved by adjusting the angle of the beamsplitter BS1 and the mirror M1, as shown in figure 5.13(d). The image shear can be adjusted using the mirror M2. The tilt introduces the carrier frequency which causes the phase dependent side bands to become separated from the central term in frequency space, as shown in figure 5.13(e).

The size and shape of the features in the Fourier transform of the recorded intensity distribution are determined by the diameter and shape of the aperture in the optical system. The imaging lens L, works as a transform lens, therefore the intensity distribution recorded by the camera can be considered itself as the Fourier transform of the light passing the aperture. The Fourier transform of the recorded image that is performed computationally can be considered as the inverse transform of the aperture function. The shape of the aperture is therefore observed in the Fourier transform image. The aperture used in this system was circular; therefore circular features are expected in the Fourier transform as shown in figures 5.13(c) and 5.13(e). This image was obtained with the diameter of the iris aperture set to approximately 3 mm.

The alignment of the optical system was optimized by adjusting the magnitude of the tilt and the diameter of the iris aperture. The optimum position occurs when the side bands occupy as much of the available space as possible but are still contained within the perimeter of the image and are well separated from the central term. A DaVis macro was written that enabled quasi-real-time display of the Fourier transform of the recorded intensity. This allowed for easy optimization of the interferometer alignment. Figure 5.14 shows a photograph of the Mach-Zehnder interferometer. The green line shows the direction of light propagation from left to right through the interferometer from the bundle output to the CCD camera.

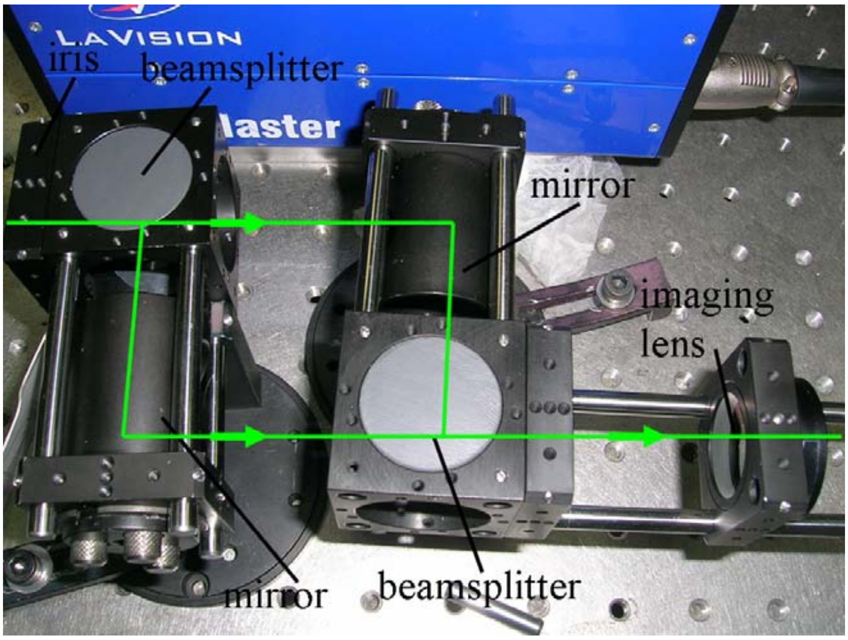

Figure 5.14 *Photograph showing the Mach-Zehnder interferometer used for carrier fringe generation. The green line indicates the path of light propagation through the interferometer.*

With the interferometer correctly aligned, a series of fine carrier fringes can be seen within the recorded speckle pattern. In order to observe the carrier fringes a minimum speckle size of 6x6 pixels is required [20] to ensure that the carrier fringes are adequately sampled. The speckle size is controlled by the iris aperture. A typical speckle pattern obtained with this interferometer is shown in figure 5.15(a). The region enclosed by the white box is shown enlarged in figure 5.15(b) illustrating the carrier fringe pattern.

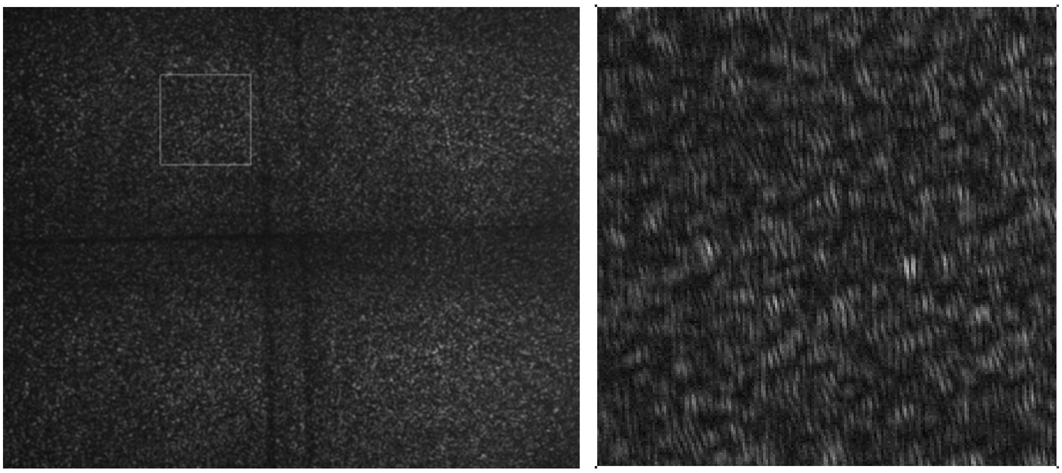

(a) **(b)**

Figure 5.15 *Speckle patterns recorded through the tilted Mach-Zehnder interferometer from each fibre bundle arm (a). The enlarged region enclosed by the white box (b) clearly shows the fine structure of the carrier fringes.*

Carrier fringe patterns were recorded before and after deformation of the object and the Fourier transform was calculated for each. The magnitude of the Fourier transform of the figure 5.15(a) is shown in figure 5.16. The high magnitude values at the centre of the image have been deleted for clarity. The orientation of the spectral features is determined by the direction of the carrier fringes. The imaginary line connecting the centres of the three features in figure 5.16 is perpendicular to the direction of the carrier fringes. The carrier fringes used to obtain figure 5.16 are tilted slightly away from vertical, as can be seen in figure 5.15(b).

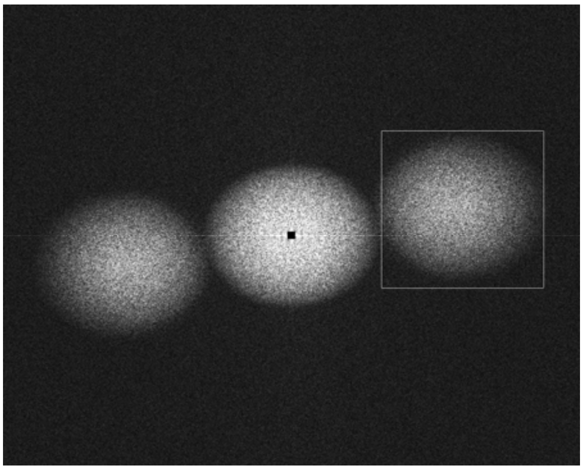

Figure 5.16 *The Fourier transform of figure 5.15(a). The black square in the centre is a region of high values that have been deleted. The white box around the right hand side feature corresponds to the region that was isolated for the phase calculation.*

The region enclosed by the white box corresponds to the data that was used in the phase calculation. This region was isolated in both the signal and reference images and the inverse Fourier transform was calculated. The phase was determined from the result of the inverse transformation of the signal and reference images independently using equation (5.7). The wrapped phase map was then obtained by subtracting the signal phase from the reference phase and then rewrapping the result modulo 2π. Figure 5.17(a) shows a raw wrapped phase map obtained using this technique. The raw phase maps generated using this method possess high noise levels but the filtering process effectively removes much this. The reason that figure 5.17(a) is much noisier than the result shown in figure 5.11(e) is that the isolated side bands are much larger here. Information at much higher spatial frequencies were therefore used in the reconstruction of the wrapped phase map. There are still some phase errors as can be seen in figure 5.17(b) and some of these errors result in breaks in the 2π fringe discontinuities. An unwrapping algorithm that is immune to these breaks in the fringes is therefore required in order to use the phase measurements obtained with this method in further calculations.

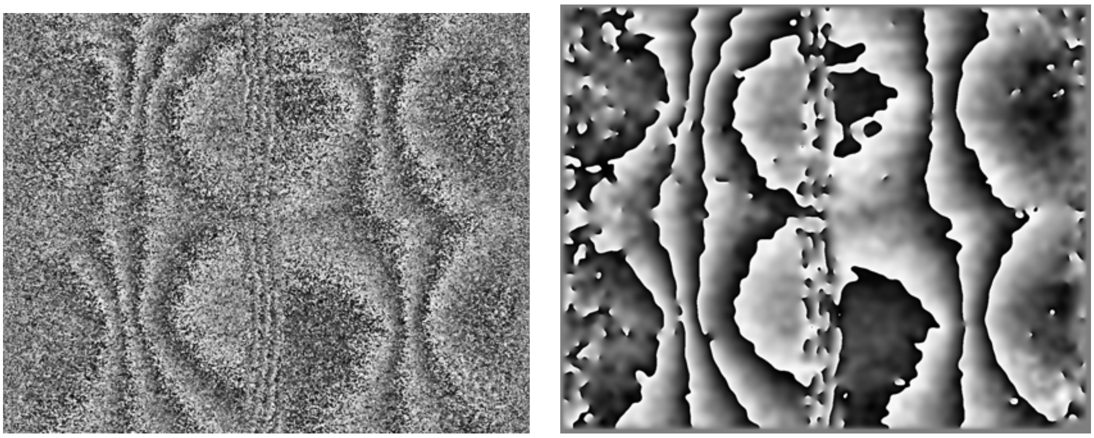
(a) **(b)**

Figure 5.17 *Raw wrapped phase map obtained using the spatial carrier technique with a tilted Mach-Zehnder interferometer (a). The same phase map after processing with an iterative sine-cosine filter (b).*

The main disadvantage with this technique is that it is not very light efficient. The iris needs to be placed some distance (between 10 – 15 cm in the examples shown) away from the bundle output to allow rays from the edges of bundle output to pass through aperture and thus avoid the effects of vignetting from the periphery of the aperture. This constraint, coupled with the relatively small iris diameter, means that only a small proportion of light emitted from the bundle output is collected by the imaging lens and captured by the camera. This can be a problem if a low power laser source is used but it is not a significant problem when using a high power laser. The requirement for large speckles also means that the spatial resolution of the wrapped phase maps generated using this technique is reduced compared to the wrapped phase maps generated using temporal phase stepping. This means that this technique works better for phase maps with a lower fringe density. The fringe density for a particular magnitude of deformation can be reduced by reducing the magnitude of applied shear at the cost of reduced sensitivity.

5.4 Phase unwrapping

Two phase unwrapping algorithms were used in the work presented in this thesis. The first algorithm is based on the minimum spanning tree principle and is found within ISTRA, a standalone fringe analysis software package produced by Dantec-Ettemeyer. The second algorithm is a version of Goldstein's branch cut algorithm [2] coded in Matlab that was available from a synthetic aperture radar (SAR) interferometry forum at www.cv.tu-berlin.de/rat.

In this section, these two algorithms are compared using four wrapped phase maps obtained from a single channel of the multiple-viewing-direction pulsed laser shearography system. The wrapped phase maps used in this investigation are shown in the top row of figure 5.18. The wrapped phase maps were obtained using two techniques, temporal phase stepping and the spatial carrier technique based on the Mach-Zehnder interferometer. Examples of both raw and filtered phase maps obtained with the two techniques are used. The results of unwrapping using ISTRA and Goldstein's branch cut algorithm are shown in the middle and bottom rows of figure 5.18 respectively. Both of the algorithms are able to effectively unwrap the filtered phase stepped map. Goldstein's branch cut algorithm fails to unwrap the raw phase stepped map. ISTRA can unwrap this phase map albeit with large regions of erroneous data around the edges of the image. Neither of the algorithms are capable of unwrapping the noisy raw phase map calculated using the spatial carrier technique, but both can unwrap the filtered spatial carrier phase map. However, a region to the right of the filtered spatial carrier map was incorrectly unwrapped by ISTRA.

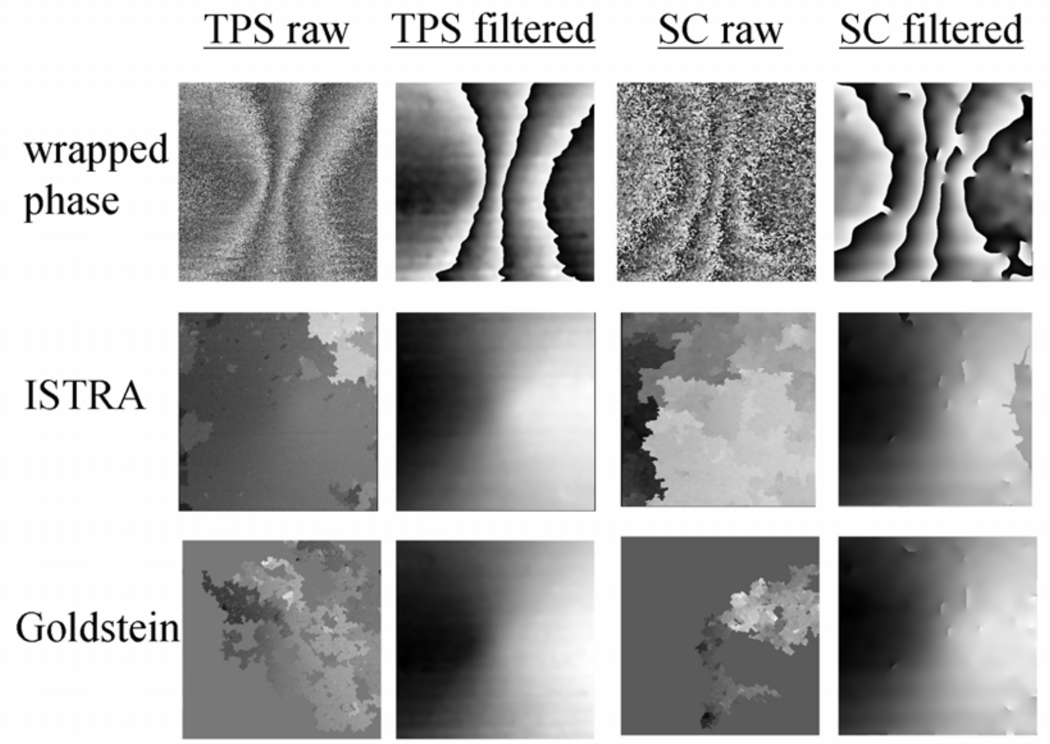

Figure 5.18 *Comparison of phase unwrapping algorithms. TPS = temporal phase stepped. SC = spatial carrier.*

ISTRA appears to be a better algorithm for unwrapping phase maps containing high levels of high frequency noise, as was seen from the raw phase stepped map, but Goldstein’s branch cut algorithm appears more effective for unwrapping maps that contain phase errors and breaks in the 2π phase discontinuities. Goldstein’s branch cut algorithm also offers a number of other advantages. Because it is coded in Matlab it is easy to incorporate with further image processing functions that are also coded in Matlab. The version of ISTRA that we have at Cranfield University, on the other hand, only operates on PCs running windows ’98 and requires images to be saved as text files or as TIFF (Tagged Image File Format). Goldstein’s algorithm is therefore more user friendly. Also, ISTRA operates only on a central region of the input image determined by a user defined window. The output image is therefore smaller than the input image which can be a problem if the unwrapped image needs to be the same size as the input image. With Goldstein’s algorithm, the output image is the same size as the original image.

5.5 Summary

In this chapter a number of phase analysis techniques have been investigated. These include temporal and spatial phase stepping and the spatial carrier technique with two methods of carrier fringe generation. Table 5.1 summarizes the relative advantages and disadvantages of the techniques investigated in this chapter. Temporal phase stepping has proved to be a simple and effective phase analysis technique, but relies on the recording of four or more camera frames. It is therefore unsuitable for dual pulsed measurements of dynamic test surfaces; however, it is the method of choice when measuring static test surfaces. Measurements of static surfaces using temporal phase stepping will be presented in chapter 6.

Spatial phase stepping is a potential solution to the problem of calculating the phase with just two camera frames. A diffractive optical element has been investigated with the aim of incorporating it within a Mach-Zehnder interferometer for the purpose of spatial phase stepping. It was found during the investigation of the DOE that the spatial resolution of each image was quite low with the camera currently available. The components required for the system are also quite expensive so it was decided to investigate other techniques.

The spatial carrier technique was investigated using two methods of carrier fringe generation. The first method involved translating the illuminating lens along the optical axis after deformation of the object. With this method it can be difficult to generate a high enough carrier frequency to separate the side bands from the DC term in frequency space. It is also difficult to generate perfectly straight carrier fringes with this method. The fringes need to be straight to correctly demodulate the phase by translating the side band to the origin in frequency space. The results presented were obtained from the subtraction of two carrier fringe patterns. These fringe patterns required three camera frames to produce and therefore would not be suitable for dual pulse measurements.

Table 5.1 *Comparison of phase analysis techniques investigated in this chapter.*

Technique	Advantages	Disadvantages
Temporal phase stepping	Simple to implement. High resolution phase maps produced.	Unsuitable for dual pulsed dynamic measurements.
Spatial phase stepping	Potentially high resolution phase maps obtained with a high resolution camera.	Expensive components required. Low spatial resolution of images recorded by one camera.
Spatial carrier: Source translation method	Can operate under comparatively low light levels.	Straight carrier fringes required. Difficulty generating high enough carrier density. Additional components required for use in dual pulsed measurements.
Spatial carrier: Tilted MZI method	No additional components required. Only two frames required.	Poor light efficiency. Reduced spatial resolution compared to temporal phase stepping.

The second method of carrier fringe generation that was investigated involved introducing a tilt between the interfering beams using a Mach-Zehnder interferometer. Reducing the diameter of an iris positioned at the input of the interferometer increased the size of the speckles in the pattern. Arranging the interferometer so that a carrier frequency was introduced between the interfering beams resulted in a carrier fringe pattern that was observed across the enlarged speckle pattern. Only a single frame was required to record a carrier fringe pattern, therefore wrapped phase maps could be generated from just two carrier fringe patterns recorded before and after object deformation. Other than the iris, no additional components are required for this method of phase analysis. The technique is somewhat light inefficient, however, but this is not a significant issue with the high power pulsed Nd:YAG laser that was available during the course of this work. The raw wrapped phase maps generated using this technique are noisy but after processing with an iterative sine-cosine filter the results can be effectively unwrapped using either ISTRA or Goldstein’s branch cut algorithm. This is therefore the technique chosen for phase analysis in the measurement of dynamic surfaces. Measurements of dynamic surfaces will be presented in chapter 7.

References

[1] Robinson D. W, 'Phase unwrapping methods', in *Interferogram analysis: digital fringe pattern measurement techniques*, ed. Robinson D. W. and Reid G. T, Institute of Physics, Bristol (1993).

[2] Goldstein R. M, Zebker H. A. and Werner C. L, 'Satellite radar interferometry: two-dimensional phase unwrapping', *Radio Sci.* **23**:4, 713-20 (1988).

[3] Creath K. 'Temporal phase measurement methods', in *Interferogram analysis: digital fringe pattern measurement techniques*, ed. Robinson D. W. and Reid G. T, Institute of Physics, Bristol (1993).

[4] Olszak A. and Tatam R. P, 'The calibration of the path-length imbalance in optical fibre ESPI systems employing source-wavelength modulation', *Meas. Sci. Technol*, **8**, 759-63 (1997).

[5] Wyant J. C, Oreb B. F. and Hariharan P, 'Testing aspherics using two wavelength holography: use of digital electronic techniques' *Appl. Opt.* **23**:22, 4020-3 (1984).

[6] Huntley J. M, 'Automated analysis of speckle interferograms', in *Digital speckle interferometry and related techniques*, ed. Rastogi P. K, Wiley (2001).

[7] Wyant J. C, 'Use of an ac heterodyne lateral shear interferometer with real-time wavefront correction systems' *Appl. Opt.* **14**:11, 2622-6 (1974).

[8] Schwider J, Burow R, Elsner K-E, Grzanna J, Spolaczyk R. and Merkel K, 'Digital wavefront measuring interferometry: some systematic error sources' *Appl. Opt.* **22**:21, 3421-32 (1983).

[9] Hariharan P, Oreb B. F. and Eiju T, 'Digital phase shifting interferometry: a simple error compensating algorithm' *Appl. Opt.* **26**:13, 2504-6 (1987).

[10] Dorrio B. V. and Fernandez J. L, 'Phase-evaluation methods in whole-field optical measurement techniques' *Meas. Sci. Technol.* **10,** R33-R55 (1999).

[11] De Groot P, '101-frame algorithm for phase shifting interferometry', *EUROPTO preprint 3098-33*, 1-10 (1997).

[12] Aebischer H. A, Waldner S, 'A simple and effective method for filtering speckle-interferometric phase fringe patterns', *Opt. Comm.* **162**, 205-10 (1999).

[13] García B. B, Moore A. J, Pérez-López C, Wang L. and Tschudi T, 'Transient deformation measurement with electronic speckle pattern interferometry by use of a holographic optical element for spatial phase stepping, *Appl. Opt.* **38**:28, 5944-7 (1999).

[14] García B. B, Moore A. J, Pérez-López C, Wang L. and Tschudi T, 'Spatial phase-stepped interferometry using a holographic optical element', *Opt. Eng.* **38**:12, 2069-74 (1999).

[15] SILIOS Technologies, Z. I. Peynier-Rousset, Rue Gaston Imbert prolongée, 13 790 Peynier, France. Web www.silios.com.

[16] Takeda M, Ina H. and Kobayashi S, 'Fourier-transform method of fringe-pattern analysis for computer-based topography and interferometry', *J. Opt. Soc. Am*, **72**:1, 156-9 (1982).

[17] Dávila A, Kaufmann G. H. and Pérez-López C, 'Transient deformation analysis by a carrier method of pulsed electronic speckle-shearing pattern interferometry', *Appl. Opt.* **37**:19, 4116-22 (1998).

[18] Kemao Q, 'Windowed Fourier transform for fringe pattern analysis', *Appl. Opt.* **43**:13, 2695-702 (2004).

[19] Fernández A, Doval A. F, Dávila A, Blanco-García J, Pérez-López C. and Fernández J. L, ‘Double-pulsed carrier speckle shearing pattern interferometry for transient deformation analysis’, *Proc. SPIE,* **3478**, 352-8 (1998).
[20] Pedrini G, Zou Y-L and Tiziani H. J, ‘Quantitative evaluation of digital shearing interferogram using the spatial carrier method’, *Pure Appl. Opt.* **5**, 313-21 (1996).

6. Surface strain measurements from static objects

In the previous chapter, the processing steps taken to derive unwrapped phase distributions from the raw images obtained from the multiple-viewing-direction pulsed laser shearography system were described. These steps constitute the first five steps given in the processing scheme shown in figure 4.12. In this chapter, the final three processing steps shown in figure 4.12 that are required to calculate the orthogonal displacement gradient component are described.

The unwrapped phase maps determined using the instrument possess errors due to perspective distortion. This is due to the viewing angle of each of the camera lenses and is corrected for using a process known as image 'dewarping'. This process is described in the first section of this chapter.

Two methods of calculating the sensitivity vector across the field of view are presented. The first method is based on measurements of the physical locations of the four camera lenses and of the central negative lens with respect to the centre of the test target. In the second method, the sensitivity vectors are obtained from the mapping coefficients generated in the image dewarping process. The sensitivity vector measurements provide the elements of a matrix transformation that is used to determine the orthogonal displacement gradient components. The first of these two methods for calculating the sensitivity vector was used determine the optimum viewing configuration based on the condition number of the transformation matrix.

The remainder of the chapter presents the results of surface strain measurements from the two test objects introduced in section 4.5. Measurements made using the flat aluminium plate are compared with the results obtained from simulated phase distributions. Measurements made using the flat perspex plate are compared with results obtained previously using the laser diode based, multiple-illumination-direction shearography system [1]. These measurements were made using phase maps calculated using temporal phase stepping. The final section presents results from the flat aluminium plate that were calculated using phase maps generated using the spatial carrier technique. These measurements were made using an image cross-correlation technique to calculate the variation in the shear magnitude across the field of view.

6.1 Image dewarping

This section describes the image dewarping process that is used to correct images for errors introduced due to perspective distortion. Radial distortion is also corrected for using this algorithm. This method is also used to align the four views to sub-pixel accuracy which is essential for the calculation of the orthogonal displacement gradient components. The process is achieved using a dewarping algorithm that is built into the DaVis software package.

The first step in the dewarping process was the calibration of the dewarping target. This target consists of a regular array of white dots on a black background. The calibration target was placed in the focal plane of the four camera lenses and was illuminated with a 60 W desk-lamp. Figure 6.1(a) shows an image of the dewarping target viewed through the fibre-bundles and imaged onto the CCD camera with one of the interferometer mirrors blocked.

The target in figure 6.1(a) consists of an orthogonal array of white dots with a diameter 0.5 mm that are separated by 2.5 mm. This image was divided into the four separate views using the DaVis rectangle function, which were then stored in separate image buffers. The DaVis rectangle function was described previously in section 4.7. The first view, chosen to be the top-left image quadrant in figure 6.1(a), was then selected. A reference dot in the centre of this image was then selected. The reference dot has a small dot located below it to the right. This is so that the same dot can easily be identified in the other three images. This dot can be seen near the centre of each of the image quadrants in figure 6.1(a). The adjacent dot to the right of the reference dot was then selected. After the two dots were selected, the algorithm scans the image and detects the other dots in the image using an image correlation process. Based on the prior knowledge of the dot separation, the algorithm dewarps the image to a flat plane. After dewarping, the image of the calibration target appears as though viewed perpendicularly, as shown in figure 6.1(b).

Next, the image from the second view, chosen to be the top-right image quadrant in figure 6.1(a), was selected and the reference dot within this image selected. It is important to select the same reference dot in this image as was chosen in the first image, to ensure that both dewarped images are centred at the same point. Again, the adjacent dot to the right was selected and the algorithm detects the remaining dots. This image was dewarped and mapped to the first dewarped image so that both were centred at the same point. This process was then repeated for the final two images. The four dewarped images were then overlaid as shown in figure 6.1(c). This image demonstrates the ability of the dewarping algorithm to align the four views. The region of the image that is common to all four views is then windowed using a fifth DaVis rectangle.

The calibration process generates a dewarping mapping function for each of the four views. The mapping function is a third order polynomial consisting of 20 coefficients in x and y [2]. These coefficients arise from the fact that there are 10 coefficients each in x and y and are necessary to correct for radial and perspective distortion. These mapping functions are saved and can be applied later to the unwrapped phase measurements obtained with the shearography system. The dewarping of unwrapped phase maps was performed using a macro programmed in the DaVis command language. The dewarping process also generates a millimetre to pixel scaling which gives the area in mm^2 on the target viewed by each pixel. This can be useful, for example, when calculating the shear magnitude from a recorded image.

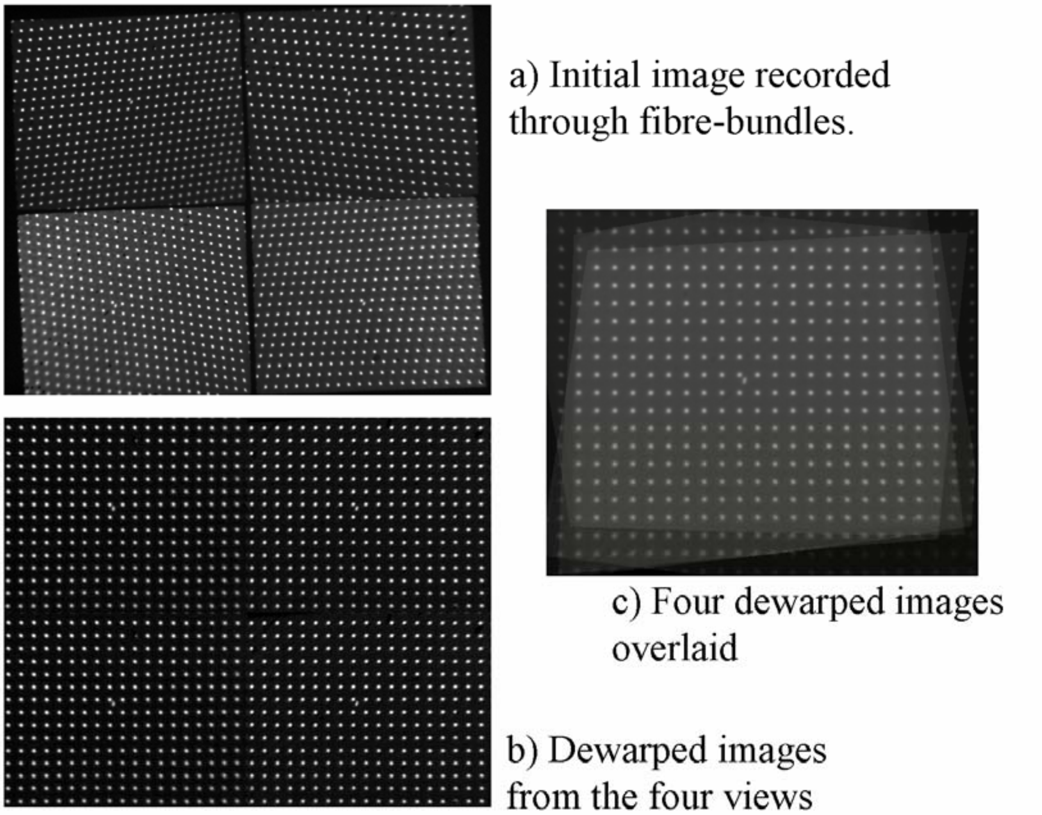

a) Initial image recorded through fibre-bundles.

b) Dewarped images from the four views

c) Four dewarped images overlaid

Figure 6.1 *The calibration target viewed through the four fibre bundles (a). Each view is separated and dewarped to a flat plane. The dewarped images from the four views are shown in (b). The target now appears as though viewed perpendicularly. The four dewarped views are overlaid (c) and the region of the overlaid views common to each view is selected.*

The uncertainties in the dewarping procedure arise from the fact that the calibration target needs to be placed in the plane of the test object. The target is placed in the object plane of the four camera lenses by hand and as a consequence will generally not be perfect. For effective dewarping, good image quality with uniform illumination of the target is desired. If this is not the case, some of the dots may not be clear in the image and may not be detected in the correlation process. The more dots that are missed, the more uncertainty is introduced to the dewarping. This may be tolerable if only one or two dots are missed but may not be tolerable if many dots are missed. As a general rule, the dewarping is considered acceptable if all four views match well when overlaid, as is seen in figure 6.1(c). If this is not the case, steps should be taken to improve the quality of the image of the calibration target. This may include adjusting the illumination and adjusting the viewing lenses to ensure the target is well focused.

6.2 Calculation of sensitivity vectors

The component of displacement gradient that a shearography measurement is sensitive to is determined by the sensitivity vector. The sensitivity vector is defined as the bisector of the observation and illumination vectors of the shearography system, and is represented by the equation

$$\mathbf{k} = \hat{o} - \hat{\imath} \qquad (6.1)$$

where $\hat{o}$ and $\hat{\imath}$ are the observation and illumination unit vectors respectively. Each pixel in the CCD camera makes its own independent measurement of the displacement gradient at a different location on the object's surface. Each pixel therefore has its own sensitivity vector. It is therefore necessary to determine the sensitivity vector across the field of view in order to make a quantitative measurement.

6.2.1 Calculation of sensitivity vectors from observation and illumination positions

One method of determining the sensitivity vector across the field of view is based on the measurement of the observation and illumination positions. The observation positions are taken to be at the centre of the four camera lenses and the illumination position is taken to be at the centre of the negative lens mounted in the centre of the cross structure. These positions were measured within a three-dimensional Cartesian coordinate system whose origin is taken to be the point on the target at the centre of the field of view of the four camera lenses. The following coordinate locations are given in the form (x, y, z) and were measured in centimetres with an uncertainty of ±0.5 cm. This uncertainty corresponds to a maximum error in the measured displacement gradient of 0.4%. The locations of each of the observation positions were measured to be (-25, 25, 62) for camera lens 1, (25, 25, 62) for camera lens 2, (-25, -25, 62) for camera lens 3 and (25, -25, 62) for camera lens 4. The illumination position was measured to be (0, 0, 62). These coordinate locations are indicated in figure 6.2. The coordinate system is also shown, with the positive z direction coming out of the page.

The first step in the calculation of the sensitivity vector is to determine the observation and illumination unit vectors $\hat{o}$ and $\hat{\imath}$. For the moment we shall consider just the central observation vector and assume that the illumination vector does not vary across the field of view. In this case $\hat{\imath}$ = (0, 0, -1). The z component of the sensitivity vector is negative because the illumination vector points in the negative z direction, as shown in figure 6.3. If the observation and illumination directions were collinear, then the observation unit vector would be $\hat{o}$ = (0, 0, 1). The sensitivity vector in this case is

$$\mathbf{k} = (0,0,1) - (0,0,-1) = (0,0,2) \qquad (6.2)$$

and its magnitude is |k| = 2. This is the maximum magnitude that the sensitivity vector can possess and illustrates that the highest sensitivity is obtained with collinear observation and illumination.

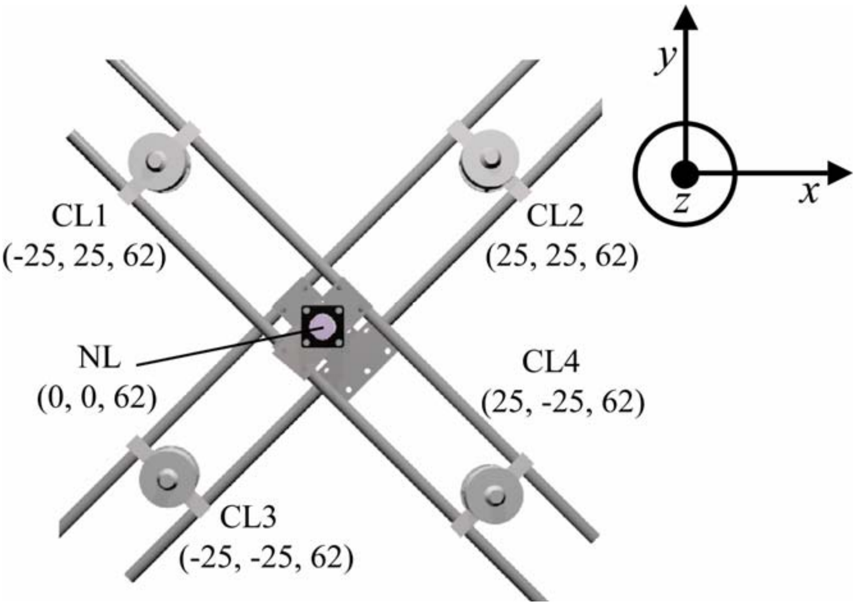

Figure 6.2 *Coordinate locations of the observation and illumination positions given in centimetres. These were measured relative to the point on the target's surface at the centre of the field of view of the four camera lenses (0, 0, 0). The coordinate system is shown with the positive z direction coming out of the page. CL1-4 = camera lens, NL = negative lens.*

Now consider the central observation vector from camera lens CL2, which is o = (25, 25, 62). The unit vector for this observation direction is calculated using

$$\hat{o} = \frac{o}{|o|} = \left(\frac{25}{71.4}, \frac{25}{71.4}, \frac{62}{71.4}\right) = \left(0.35, 0.35, 0.87\right) \tag{6.3}$$

where $|o|$ is the magnitude of o and is equal to $(25^2 + 25^2 + 62^2)^{1/2}$. The sensitivity vector in this case is

$$\mathbf{k} = (0.35, 0.35, 0.87) - (0, 0, -1) = (0.35, 0.35, 1.87) \tag{6.4}$$

and its magnitude is |k| =1.93. The calculation of this vector is illustrated in figure 6.3. Notice that the magnitude of the sensitivity vector is less than in the collinear case. As the observation vector moves further away from the collinear condition, the magnitude of the sensitivity vector decreases.

We now consider how the sensitivity vector varies across the field of view. The field of view for each of the camera lenses in the experimental configuration is approximately 6 cm x 8 cm on the target surface. The observation vectors at the extreme left and right are given by o_L = (29, 25, 62) and o_R = (21, 25, 62) respectively and are illustrated in figure 6.4. The sensitivity vectors for these two cases are $\mathbf{k}_L$ = (0.4, 0.34, 1.85) and $\mathbf{k}_R$ = (0.3, 0.36, 1.88) and their magnitudes are $|k_L|$ = 1.92 and $|k_R|$ = 1.94 respectively. The sensitivity vectors for the points at the extreme top and bottom of the field of view calculated similarly are $\mathbf{k}_T$ = (0.36, 0.31, 1.88) and $\mathbf{k}_B$ = (0.34, 0.39, 1.86) and their magnitudes are $|k_T|$ = 1.94 and $|k_B|$ = 1.93 respectively. The sensitivity vector for camera lens 2 is therefore expected to increase from left to right across the field of view and decrease from top to bottom across the field of view.

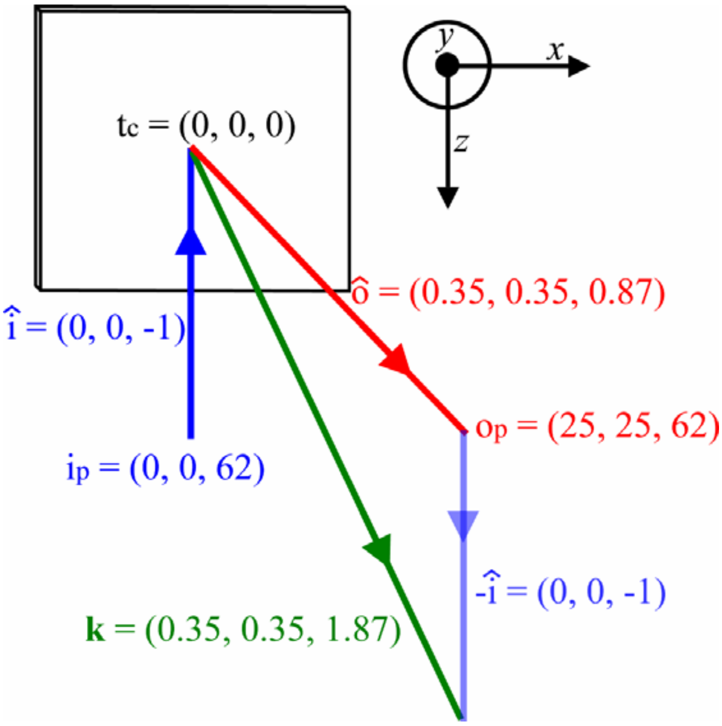

Figure 6.3 *Calculation of a single sensitivity vector at the centre of the field of view of camera lens 2. The observation and illumination positions are represented by o_p and i_p respectively, the observation and illumination unit vectors are ô and î respectively and **k** is the sensitivity vector. The transparent blue vector is the projection of the illumination vector onto the observation vector. The coordinate system is shown with the positive y direction coming out of the page. The centre of the target is represented by t_c.*

The observation unit vector across the field of view was computed using

$$\hat{o}(x,y)=\left(\frac{o_x-xd_x}{|o(x,y)|},\frac{o_y-yd_y}{|o(x,y)|},\frac{o_z}{|o(x,y)|}\right) \tag{6.5}$$

where d_x and d_y are the x and y distances on the target from the centre viewed by each pixel respectively, $|o(x, y)|$ is the magnitude the observation vector at each pixel location (x, y) and (o_x, o_y, o_z) is the observation position, shown in figure 6.2. This calculation was performed using Matlab. The illumination vector also varies across the field of view due to the fact that the illuminating beam is diverging from the negative lens. The illumination unit vector across the field of view was computed using

$$\hat{\imath}(x,y)=\left(\frac{i_x-xd_x}{|i(x,y)|},\frac{i_y-yd_y}{|i(x,y)|},\frac{i_z}{|i(x,y)|}\right) \tag{6.6}$$

The illuminating beam is assumed to have a spherical wavefront diverging from a point source located at the centre of the negative lens.

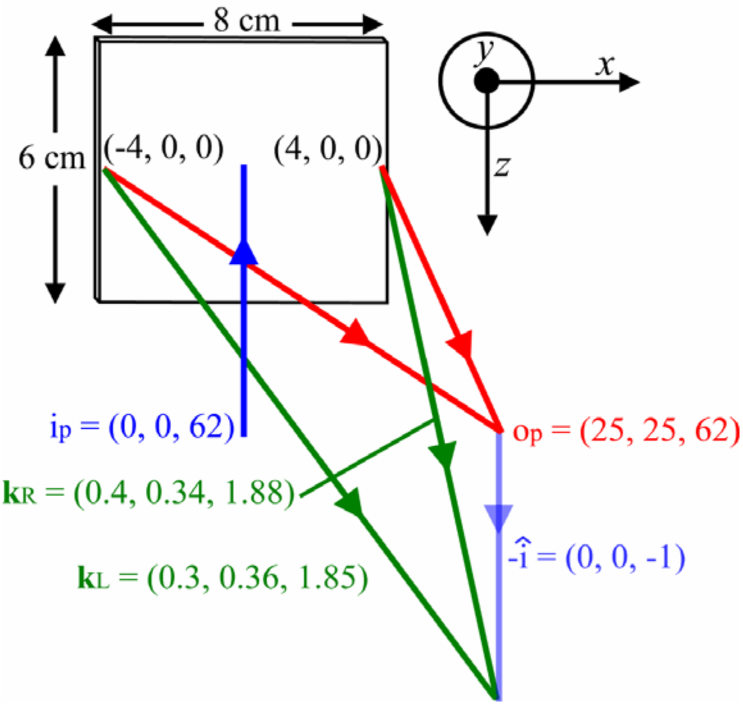

Figure 6.4 *Calculation of a single sensitivity vectors at the extreme left and right of the field of view of camera lens 2. The observation and illumination positions are represented by* o_p *and* i_p *respectively;* $\mathbf{k}_L$ *is the left hand sensitivity vector and* $\mathbf{k}_R$ *is the right hand sensitivity vector. The transparent blue vector is the projection of the illumination vector onto the observation vector. The coordinate system is shown with the positive y direction coming out of the page.*

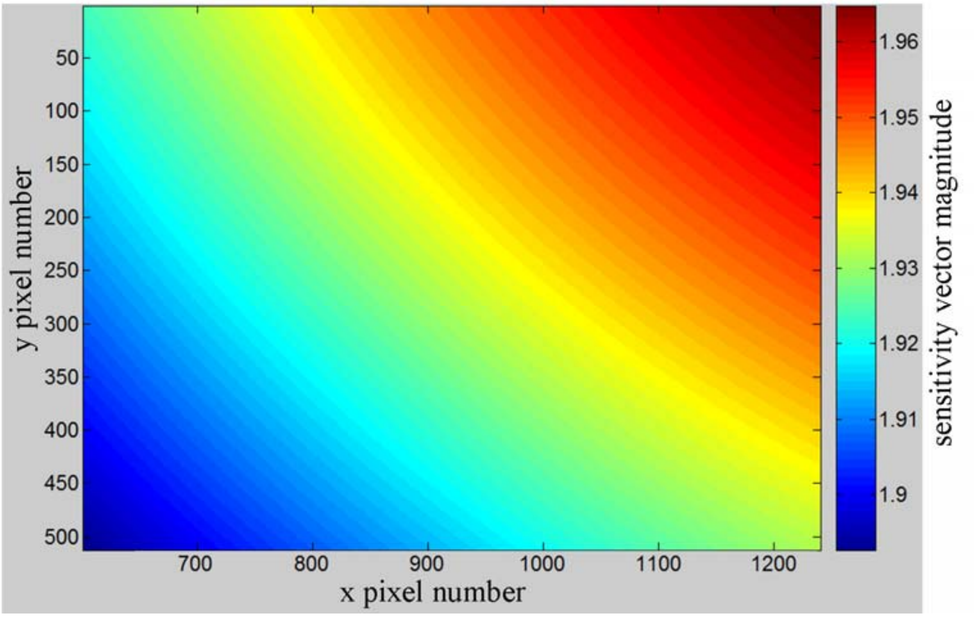

Figure 6.5 *Variation of the sensitivity vector magnitude across the field of view of camera lens 2.*

The sensitivity vector was then calculated by applying equation (6.1) to each pixel in the image. The magnitude of the sensitivity vector for each pixel across the field of view of camera lens 2 is shown in figure 6.5. The resolution of the colour map used in the generation of this figure corresponds to one colour for each sensitivity vector magnitude range of 0.001. This finite resolution causes the lines that can be seen in the image.

The variation of the sensitivity vector across the field of view shows the expected form based on the individual vector calculations presented previously. The sensitivity vector magnitude increases from left to right and decreases from top to bottom across the field of view as predicted. The sensitivity vector magnitude is lower at the bottom and left and higher at the top and right of the image than predicted. This is because the image was calculated taking the variation of the illumination vector into consideration. This was omitted previously. Figure 6.6 shows the variation of the sensitivity vector across the field of view for all four camera lenses, shown here combined into a composite image for presentation. The maximum error introduced into the displacement gradient measurements if a single sensitivity vector magnitude were to be assumed across the image would be 3.9% for a field of view of 6 cm x 8 cm.

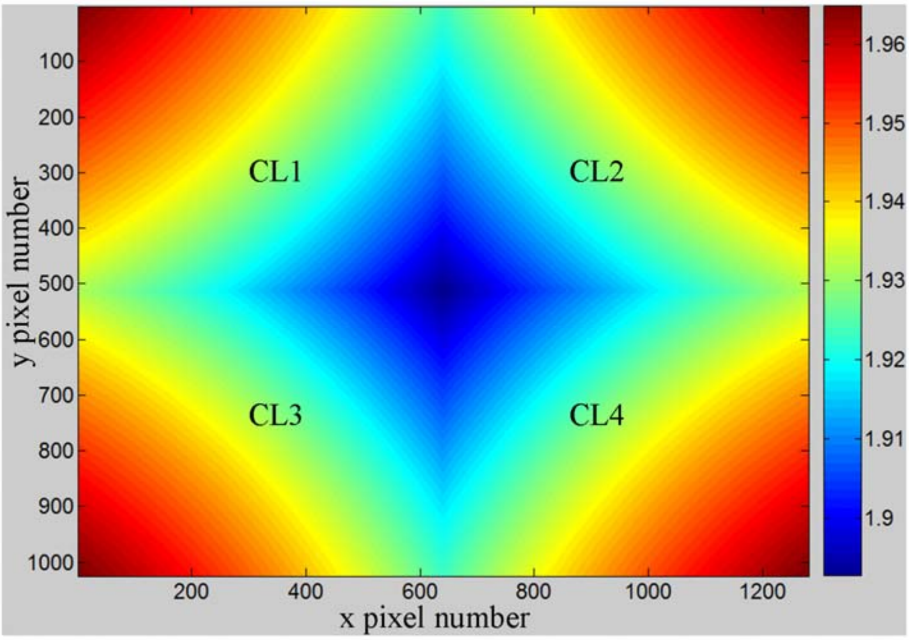

Figure 6.6 *Variation of the sensitivity vector magnitude across the field of view for all four camera lenses (CL1-4).*

<u>6.2.2 Determination of sensitivity vectors from dewarping mapping coefficients</u>

In this section, an alternative method of calculating the sensitivity vector is presented. This method, developed by Nobes *et al* [3], involves the calculation of the observation vector across the field of view from the mapping coefficients generated during the dewarping process. The method of calculating the sensitivity vector based on the observation and illumination positions described above does not take into consideration any of the optics in the imaging system. Any imaging distortions that alter the observation vectors will therefore not be detected with this method. The dewarping process corrects for perspective and radial distortion as well as aberrations induced by the optical components [2, 3]. The dewarping mapping coefficients therefore contain information on the distortion induced by the imaging optics. The observation vectors calculated using the method described in the previous section are dependent on the accurate measurement of the observation positions. Inaccurate measurements of these positions will introduce errors into the measurements of the sensitivity vector. The method of determining the sensitivity vectors based on the dewarping coefficients requires a measurement of the illumination position but not the observation positions. Uncertainty in the measurement of the observation positions is therefore not an issue with this technique. The accuracy of this method is dependent on the accuracy of the dewarping technique. The uncertainties in the dewarping technique were discussed in section 6.1. The image of the calibration target needs to be of high quality for this technique to be successful. Any degradation of this image due to noise, blurring or poor illumination will adversely affect the performance of the dewarping procedure and lead to errors in the calculated mapping function and hence the determined observation vectors [3].

The x, y and z components of the observation unit vectors, $\hat{o}_x$, $\hat{o}_y$ and $\hat{o}_z$, were calculated from the dewarping mapping coefficients using a system of simultaneous equations presented in reference [3]. This calculation was performed using a C++ DLL that was written by Dr. D. S. Nobes. This DLL was called from a macro written in the DaVis command language. The next step was to determine the sign of the $\hat{o}_x$ and $\hat{o}_y$ components of the observation vectors. It was not necessary to determine the sign of the $\hat{o}_z$ components because $\hat{o}_z$ was positive across the field of view for all four camera lenses. The signs of the $\hat{o}_x$ and $\hat{o}_y$ components of the observation vectors were determined using horizontal and vertical Sobel filters (see section 3.4.1), respectively. The Sobel filter was used to determine the local image gradients from which the signs of the observation vector could be determined. The illumination vectors were determined in the same manner as in the previous section by assuming that the illumination has a spherical wavefront diverging from a point source located at the centre of the negative lens shown in figure 6.2. The sensitivity vectors were then calculated by subtracting the illumination vectors from the observation vectors for each of the four camera lenses. The magnitude of the sensitivity vector across the field of view for each of the four camera lenses is shown in figure 6.7. The results of the two techniques shown in figures 6.6 and 6.7 compare well in that both show a similar variation across the image and have similar sensitivity vector magnitudes.

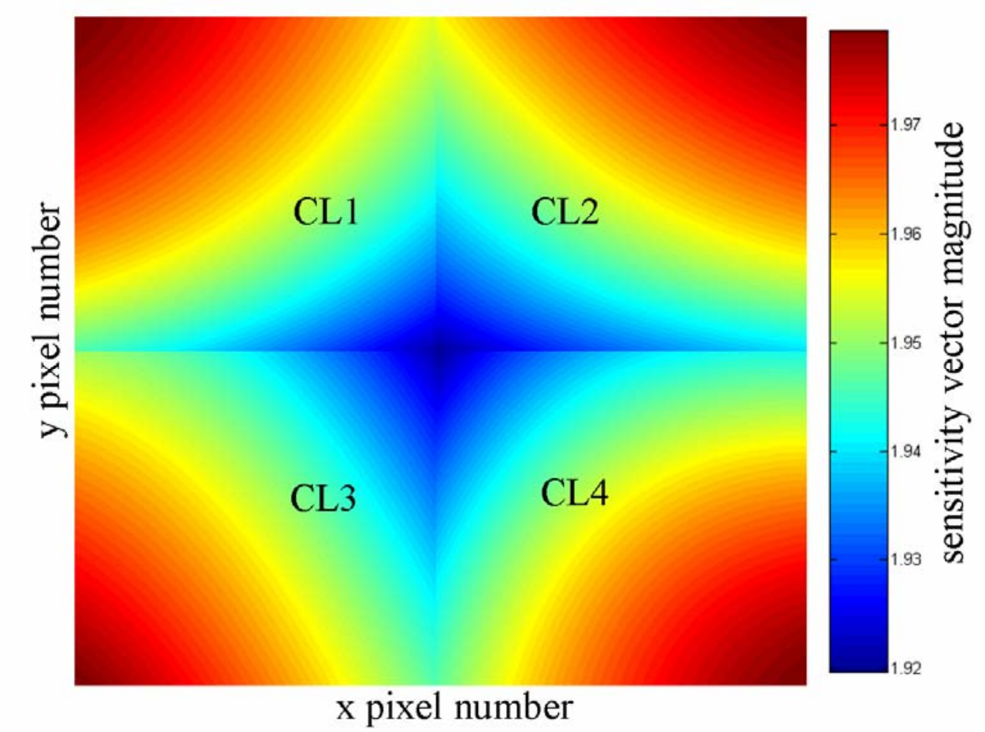

Figure 6.7 *Variation of the sensitivity vector magnitude across the field of view for the four camera lenses (CL1-4) determined using observation vectors calculated from the dewarping mapping coefficients.*

6.3 Calculation of orthogonal displacement gradient components

The orthogonal displacement gradient components are calculated from the unwrapped phase and the sensitivity vector maps at each pixel using the matrix transformation

$$\begin{bmatrix} \frac{\partial u}{\partial x} \\ \frac{\partial v}{\partial x} \\ \frac{\partial w}{\partial x} \end{bmatrix} = \frac{\lambda}{2\pi} \begin{bmatrix} k_{x1} & k_{y1} & k_{z1} \\ k_{x2} & k_{y2} & k_{z2} \\ k_{x3} & k_{y3} & k_{z3} \end{bmatrix}^{-1} \begin{bmatrix} \Delta\phi_1 \\ \Delta\phi_2 \\ \Delta\phi_3 \end{bmatrix} \mathrm{d}x^{-1} \tag{6.7}$$

where $\partial u/\partial x$ and $\partial v/\partial x$ are the in-plane displacement gradient components and $\partial w/\partial x$ is the out-of-plane displacement gradient component. The x, y and z components of the sensitivity vector are represented by k_{xi}, k_{yi} and k_{zi} respectively, where $i = 1, 2, 3$. The unwrapped phase is given by $\Delta\phi$. The numbers in the subscripts refer to the particular measurement channel. The source wavelength is represented by λ and dx is the magnitude of the shear applied in the x direction. For shear applied in the y direction, the orthogonal displacement gradient components are given by

$$\begin{bmatrix} \dfrac{\partial u}{\partial y} \\ \dfrac{\partial v}{\partial y} \\ \dfrac{\partial w}{\partial y} \end{bmatrix} = \frac{\lambda}{2\pi} \begin{bmatrix} k_{x1} & k_{y1} & k_{z1} \\ k_{x2} & k_{y2} & k_{z2} \\ k_{x3} & k_{y3} & k_{z3} \end{bmatrix}^{-1} \begin{bmatrix} \Delta\phi_1 \\ \Delta\phi_2 \\ \Delta\phi_3 \end{bmatrix} \mathrm{d}y^{-1} \tag{6.8}$$

where dy is the applied shear in the y direction.

6.3.1 The sensitivity matrix

The sensitivity matrix M_k is given by

$$M_k = \begin{bmatrix} k_{x1} & k_{y1} & k_{z1} \\ k_{x2} & k_{y2} & k_{z2} \\ k_{x3} & k_{y3} & k_{z3} \end{bmatrix} \tag{6.9}$$

The displacement gradient calculation requires the calculation of the inverse of the sensitivity matrix. The inverse of the sensitivity matrix is represented by [4]

$$M_k^{-1} = \frac{1}{\det(M_k)} \mathrm{adj}(M_k) \tag{6.10}$$

where det(M_k) is the determinant of the matrix M_k and is given by [5]

$$\det(M_k) = \left(k_{x1}k_{y2}k_{z3} + k_{x2}k_{y3}k_{z1} + k_{x3}k_{y1}k_{z2}\right) - \left(k_{x1}k_{y3}k_{z2} + k_{x2}k_{y1}k_{z3} + k_{x3}k_{y2}k_{z1}\right) \tag{6.11}$$

and adj(M_k) is the adjoint of the matrix M_k. The adjoint of a matrix is a matrix where the elements are cofactors of the original matrix. The adjoint of the sensitivity matrix is given by [6]

$$\mathrm{adj}(M_k) = \begin{bmatrix} \left(k_{y2}k_{z3} - k_{y3}k_{z2}\right) & -\left(k_{x2}k_{z3} - k_{x3}k_{z2}\right) & \left(k_{x2}k_{y3} - k_{x3}k_{y2}\right) \\ -\left(k_{y1}k_{z3} - k_{y3}k_{z1}\right) & \left(k_{x1}k_{z3} - k_{x3}k_{z1}\right) & -\left(k_{x1}k_{y3} - k_{x3}k_{y1}\right) \\ \left(k_{y1}k_{z2} - k_{y2}k_{z1}\right) & -\left(k_{x1}k_{z2} - k_{x2}k_{z1}\right) & \left(k_{x1}k_{y2} - k_{x2}k_{y1}\right) \end{bmatrix} \tag{6.12}$$

The matrix inverse can be calculated in Matlab using the function inv(M_k). It can be seen from equation (6.10) that the inverse of a matrix will be infinite if the determinant is equal to zero. If the determinant is close to zero, the matrix is said to be ill-conditioned. An ill-conditioned matrix will result in greater uncertainty than a well conditioned matrix. The conditioning of a matrix is determined by the condition number. A well-conditioned matrix has a low condition number, close to 1, and an ill-conditioned matrix has a high condition number [7]. The condition number is given by

$$\kappa(M_k) = \|M_k\| \cdot \|M_k^{-1}\| \tag{6.13}$$

where $||M_k||$ is the norm of the matrix M_k and represents the magnitude of the elements of M_k. Since the multiple-viewing-direction pulsed-laser shearography system possesses four measurement channels, we therefore need to select three of the channels for the calculation. If we select, for example, the measurement channels comprising camera lenses CL1, CL2 and CL4 and label them as measurement channels 1, 2 and 3 in equation (6.9) respectively (as shown in figure 6.8(a)), the inverse of the sensitivity matrix for the central pixel of the images from each of the camera lenses is given by [1]

$$M_k^{-1} = \begin{bmatrix} -\frac{1}{2k_x} & \frac{1}{2k_x} & 0 \\ 0 & \frac{1}{2k_y} & -\frac{1}{2k_y} \\ \frac{1}{2k_z} & 0 & \frac{1}{2k_z} \end{bmatrix} \tag{6.14}$$

The x, y and z components of the sensitivity vector for the central pixel of the image from camera lens CL2 (measurement channel 2) using the positions shown in figure 6.2 were calculated previously (section 6.2.1) and were given in equation (6.4). The sensitivity vector components for the central pixel for camera lenses CL1 and CL4 (measurement channels 1 and 3 respectively) can be calculated similarly. The sensitivity matrix for this configuration is

$$M_k = \begin{bmatrix} -0.35 & 0.35 & 1.87 \\ 0.35 & 0.35 & 1.87 \\ 0.35 & -0.35 & 1.87 \end{bmatrix} \tag{6.15}$$

The inverse of this matrix is

$$M_k^{-1} = \begin{bmatrix} -1.43 & 1.43 & 0 \\ 0 & -1.43 & 1.43 \\ 0.27 & 0 & 0.27 \end{bmatrix} \tag{6.16}$$

which agrees with equation (6.13). The condition number of this matrix, calculated using the Matlab function cond(M_k), is 8.08.

6.3.2 Effect of viewing configuration on the sensitivity matrix condition number

The effect of the experimental configuration on the condition number of the sensitivity matrix has been investigated previously [8, 9]. It was shown that condition number is dependent on the diameter of the circle encompassing the observation positions and the working distance of the instrument.

The effect of the viewing configuration on the condition number is examined in figure 6.8. This figure shows three example configurations. The coordinate locations of the viewing and observation positions for each configuration are shown. Configuration 1 is the configuration presented previously with camera lenses 1, 2 and 4 located at three of the four corners of a square. The measurement channels formed by these three camera lenses are labelled Mch1 - Mch3 respectively. The condition number for this configuration is 8.08. The angular separation, α, of the measurement channels is 90° and for this configuration 1. Configurations 2 and 3 are arbitrarily chosen to have an angular separation of 45° and 135°. These configurations have condition numbers of 28.64 and 6.54 respectively. The condition number of the configuration is therefore dependent on the angular separation of the observation positions.

The variation of condition number against angular separation of the observation positions is shown in figure 6.9. This plot was produced by fixing the position of Mch2 at position (0, 35.4, 62) and rotating Mch3 clockwise and Mch1 counter-clockwise from this position over a range of 180°. The distance from the observation positions to the illumination position was kept constant. At an angular separation of 0° the condition number is infinite. This is because determinant of the sensitivity matrix is zero since the sensitivity vectors for the three channels are the same. The condition number is a minimum when the angular separation of the three channels is 120°, which is the maximum angular separation between all three channels. This position is indicated by the green line. At this point the condition number is 5.33.

The locations of the three configurations shown in figure 6.8 are indicated by the red lines. The optimum arrangement, based on the sensitivity matrix condition number, for the observation positions in a three-component system is therefore at the three vertices of an equilateral triangle. In general a condition number less than 20 can be considered to provide adequate performance [9]. The condition number provides a convenient figure for comparison of prospective viewing configurations, but does not take into consideration the relative magnitudes of the measurand being determined, which can have a considerable impact on the uncertainties in the results [9]. Configuration 1 is therefore considered to provide adequate performance and is also easier to implement in a practical system [8]. It is also a convenient configuration for the subsequent construction of a four-channel system.

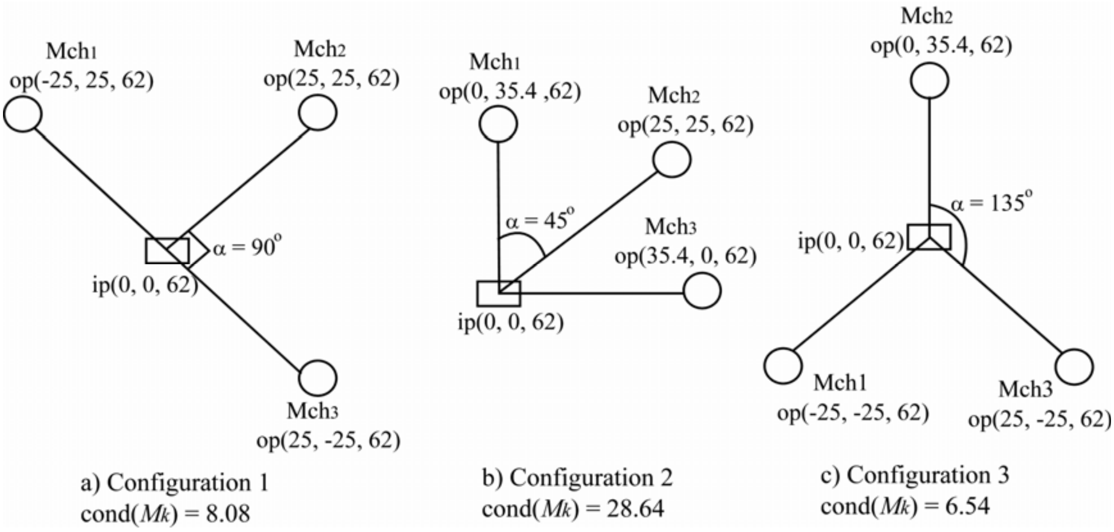

Figure 6.8 *Experimental configuration using camera lenses CL1, CL2 and CL4 (a) and the condition number of the sensitivity matrix for these observation and illumination positions. Two alternative configurations (b and c) and the condition number for the sensitivity matrix in these cases. Mch1-3 = measurement channel 1-3, op = observation position, ip = illumination position and* M_k *= sensitivity matrix.*

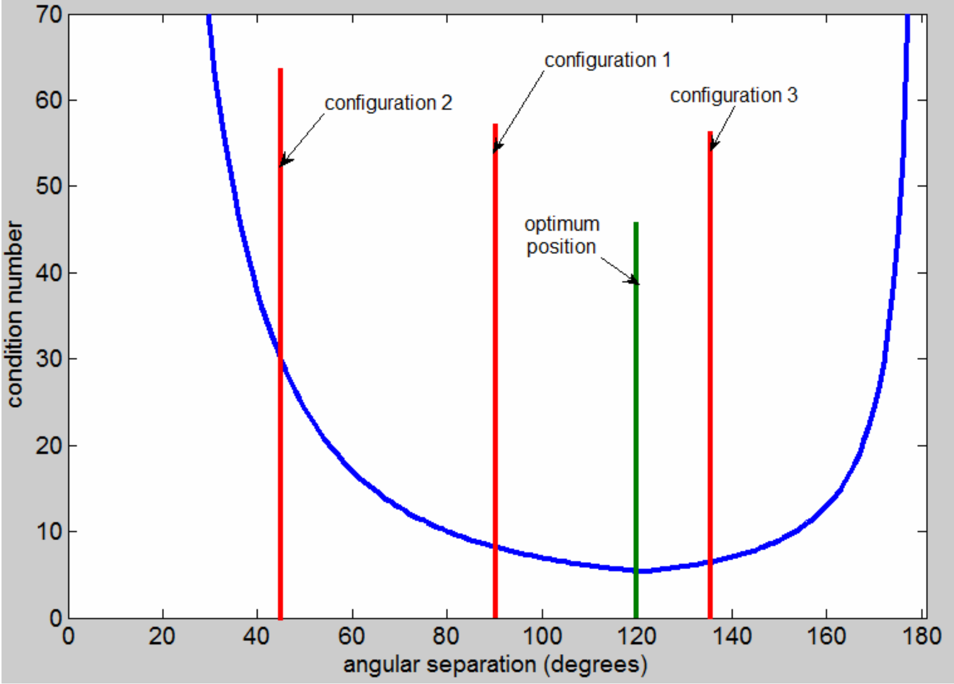

Figure 6.9 *Variation of the condition number vs. angular separation between channels 1 and 3 and channel 2. The minimum condition number occurs when the angular separation between the three channels is equal, at 120°. The locations of the three configurations shown in figure 6.8 are indicated.*

Figure 6.10(a) shows the variation of the condition number against the working distance of the configuration. The graph was calculated by assuming a constant separation between the observation positions and the illumination position and an angular separation of 120° between the three observation positions. It can be seen from the graph that the condition number decreases as the configuration is brought closer to the object. A similar plot can be generated by keeping the working distance fixed and varying the separation between the observation and illumination positions. Figure 6.10(b) shows the graph of condition number against observation angle (the angle of the observation position from the *z*-axis) and it can be seen that the condition number decreases as the observation angle increases.

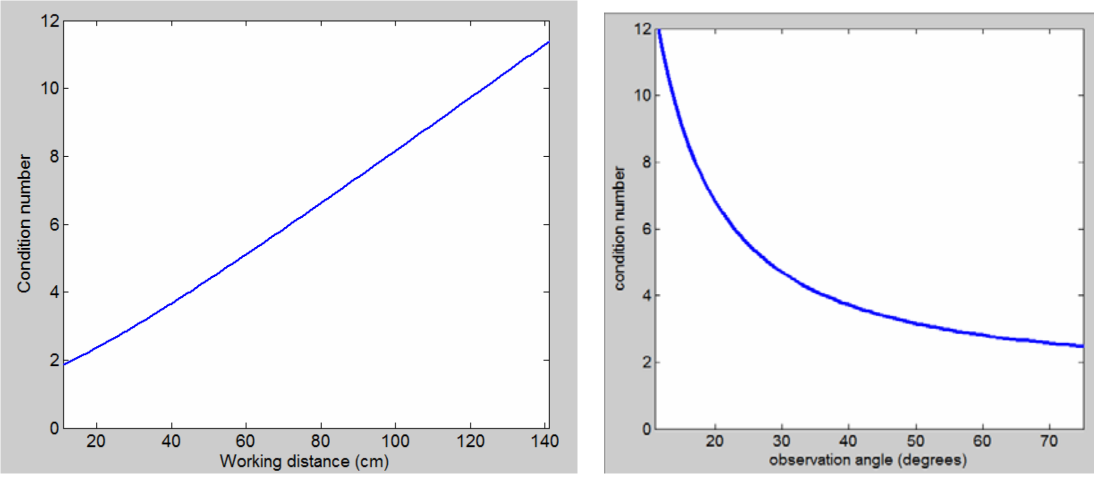

(a) **(b)**

Figure 6.10 *Variation of the condition number of sensitivity matrix against working distance (a) and observation angle (b) of the viewing configuration.*

6.3.3 Calculation of orthogonal displacement derivatives using simulated phase maps

The displacement gradient calculation (equations (6.7) and (6.8)) was investigated using simulated phase maps. The phase maps were calculated by assuming a point out-of-plane loading at the centre of a flat plate. The displacement distribution was assumed to be Gaussian across the field of view. The Gaussian distributions were differentiated with respect to *x* and *y* to simulate *x* and *y* shear respectively. The simulated phase maps are shown both wrapped and unwrapped, in figure 6.11. The phase maps were calculated for the four measurement channels with observation positions at the locations given in figure 6.2. The phase variation across the unwrapped maps, figures 6.11(a) and 6.11(b) is approximately ±17.5 radians for each phase map. There is a slight variation in the phase magnitude for each phase map due to the different sensitivity vector for each map. The out-of-plane displacement gradient across the field of view can be estimated, if we assume for the moment collinear observation and illumination, using the equation

$$\frac{\partial w}{\partial x} = \frac{\lambda \Delta \phi}{4\pi \mathrm{d}x} \qquad (6.17)$$

for shear applied in the *x* direction. Assuming a shear of 10 mm and a wavelength of 532 nm, equation (6.16) gives a variation in out-of-plane displacement gradient of ±74 μm/m over the field of view. The in-plane displacement gradient components are expected to be minimal due to the simulated displacement being purely out-of-plane.

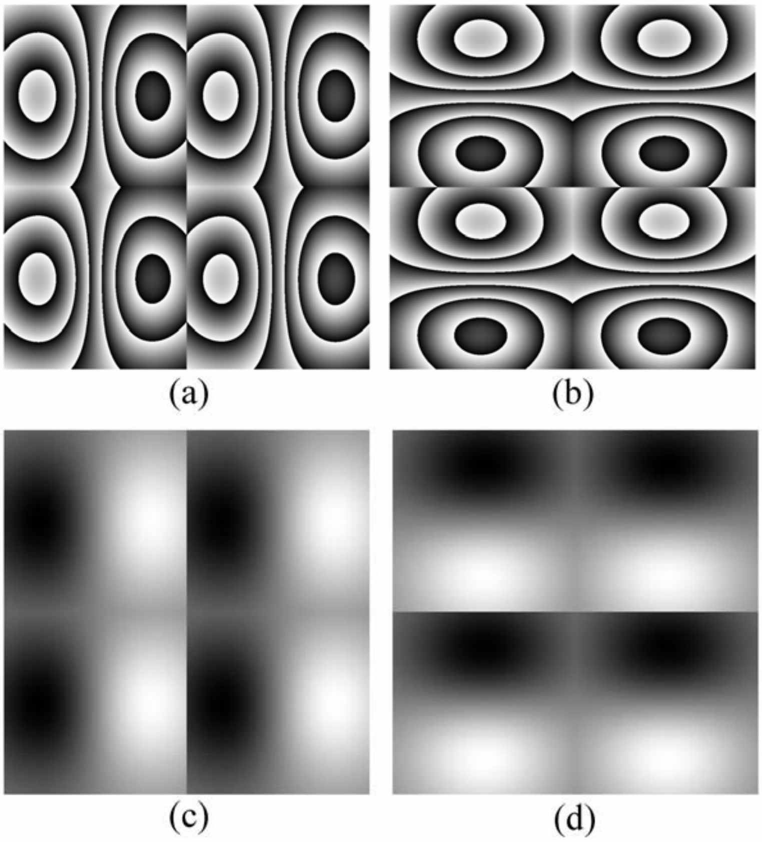
(a) (b)

(c) (d)

Figure 6.11 *Simulated phase maps for the four measurement channels calculated by assuming a Gaussian displacement distribution from a point out-of-plane deformation of a flat plate. The phase maps are shown wrapped with x-shear (a) and y-shear (b) and unwrapped with x-shear (c) and y-shear (d).*

The orthogonal displacement gradient components calculated using the phase maps shown in figure 6.11 are shown in figure 6.12. The in-plane displacement gradient components are represented by $\partial u/\partial x$, $\partial v/\partial x$, $\partial u/\partial y$ and $\partial v/\partial y$ and the out-of-plane displacement gradient components are represented by $\partial w/\partial x$, $\partial w/\partial y$. The sensitivity vector maps used in the calculation were determined from the measurements of the observation and illumination positions that were shown in figure 6.6. The variation in the out-of-plane displacement gradient magnitude, across the field of view in figure 6.11 is ±78 μm/m. This value agrees well with the prediction calculated using equation 6.16. The discrepancy of ±4 μm/m is due to the assumption of collinear observation and illumination that was made in the previous calculation. The in-plane displacement gradients are minimal, as expected.

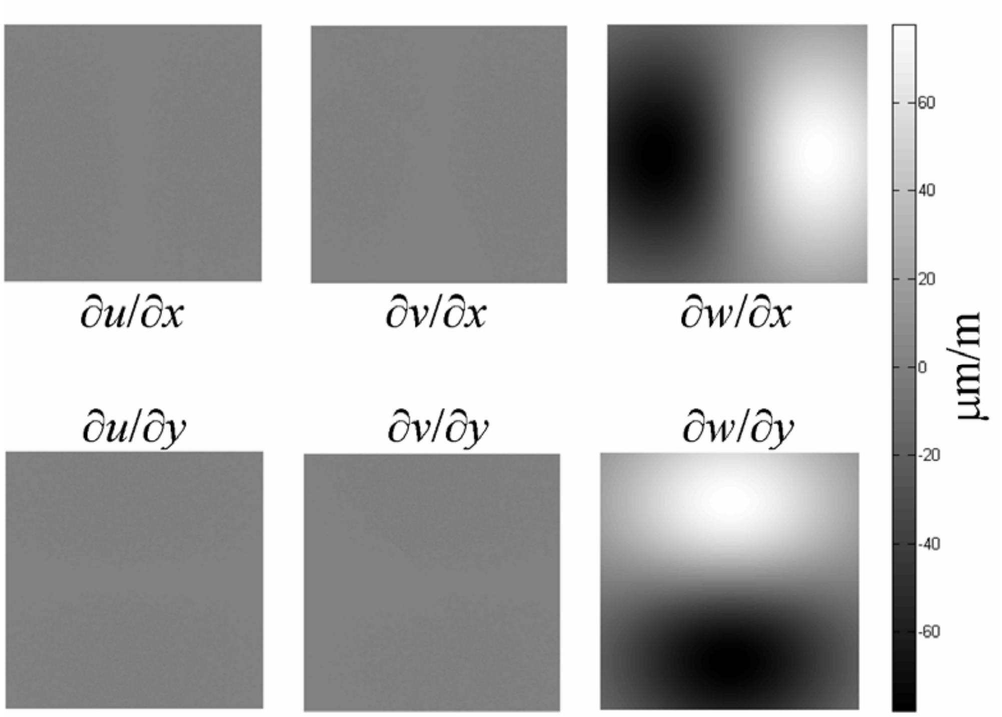

Figure 6.12 *Orthogonal displacement gradient components calculated from the simulated phase maps shown in figure 6.11 and sensitivity vector components calculated from the measured observation and illumination positions (figure 6.6).*

6.4 Displacement gradient measurements of statically loaded objects

This section presents the results of displacement gradient measurements made with the flat aluminium and perspex plate objects that were introduced in section 4.5 using temporal phase stepping.

6.4.1 Measurements from the aluminium plate using temporal phase stepping

Measurements from the flat aluminium plate were made using the observation and illumination positions shown in figure 6.2. Wrapped phase maps were generated from phase stepped speckle patterns recorded before and after object deformation. The five-step phase stepping algorithm, discussed in sections 3.1.2 and 5.1.3, was used to calculate the phase maps. The displacement applied at the centre of the object was of the order of a few micrometres. Wrapped phase maps recorded with *x* and *y* shear are shown in figures 6.13(a) and 6.13(b) respectively. The magnitude of the applied shear was 7 mm in each case, measured at the centre of the image. The shear magnitude was determined using the scaling information generated in DaVis during the dewarping process, from which the distance in millimetres per pixel is known. The wrapped phase maps are shown after the application of an iterative sine-cosine filter [10]. This filtering technique was discussed previously in section 3.4.2 and was used to remove high frequency noise from the wrapped phase maps. The phase maps from each individual view were isolated and then unwrapped using Goldstein's branch cut algorithm [11]. The unwrapped phase maps were then dewarped to remove perspective distortion using the previously calibrated dewarping mapping functions. The dewarping was also used to align the four unwrapped phase maps from each shear direction so that each was centred at the same point. The unwrapped phase maps were then overlaid and the region common to all four phase maps was selected. This resulted in the image size being the same for all four unwrapped phase maps. The unwrapped and dewarped phase maps with shear applied in the *x* and *y* direction are shown in figures 6.13(c) and 6.13(d) respectively. In the figures, the unwrapped maps from each view have been re-joined to form a composite image for the purpose of presentation.

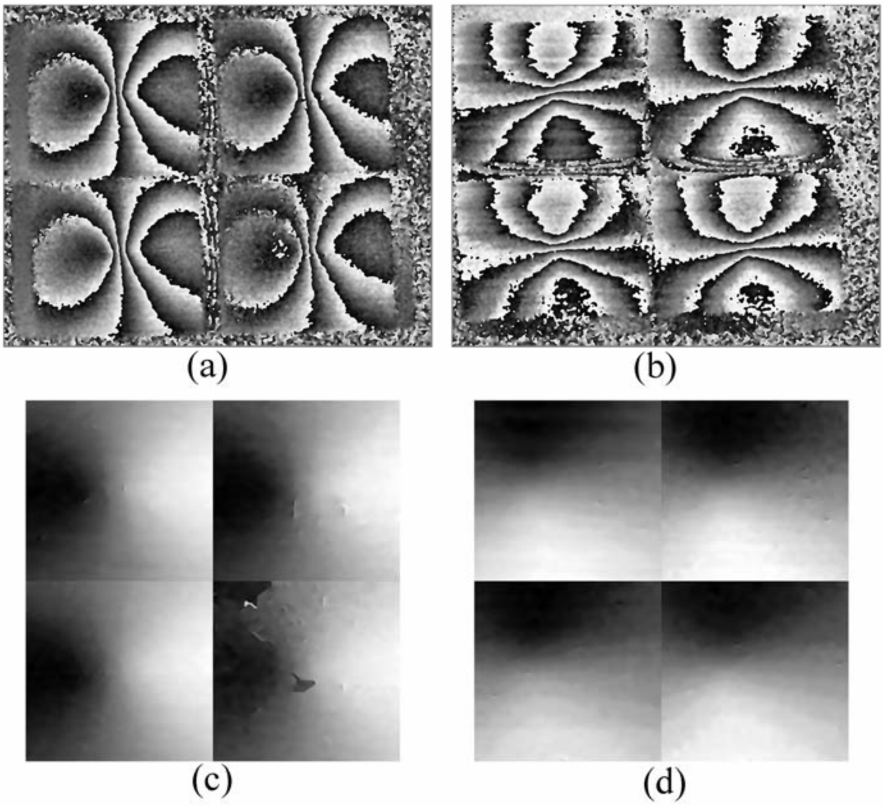

Figure 6.13 *Phase maps obtained using temporal phase stepping after deformation of the flat aluminium plate. The filtered wrapped phase maps obtained with x-shear (a) and y-shear (b). The unwrapped and dewarped phase maps obtained with x-shear (c) and y-shear (d).*

The orthogonal displacement gradient components calculated using the unwrapped phase maps shown in figures 6.13(c) and 6.13(d) are shown in figure 6.14. The three best data sets were selected for the displacement gradient calculation, highlighting the benefit of redundancy of measurement of the four-channel configuration [12]. The calculation was performed using sensitivity vectors calculated using the dewarping mapping functions, which were presented in figure 6.7. The region shown in each of the images corresponds to an area of approximately 35 x 30 mm^2 on the target's surface.

The results of the displacement gradient components produced using simulated phase data that were shown in figure 6.12 can be used as a qualitative comparison to the results shown in figure 6.14. They cannot be used for a quantitative comparison because it cannot be assumed that the distribution of displacement across the field of view in the experiment is perfectly Gaussian.

The in-plane displacement gradient components show low strain distributions across the field of view in comparison to the out-of-plane displacement gradient components. This is to be expected considering the nature of the deformation, which was predominantly out-of-plane. Thresholding was applied to the in-plane components to remove high noise regions. These regions can be seen in the in-plane displacement gradient maps in figure 6.14. The variation in out-of-plane displacement gradient across the field of view is similar to that predicted by the simulated results shown in figure 6.12. The RMS error within the in-plane components of figure 6.14 is approximately ±1 μm/m.

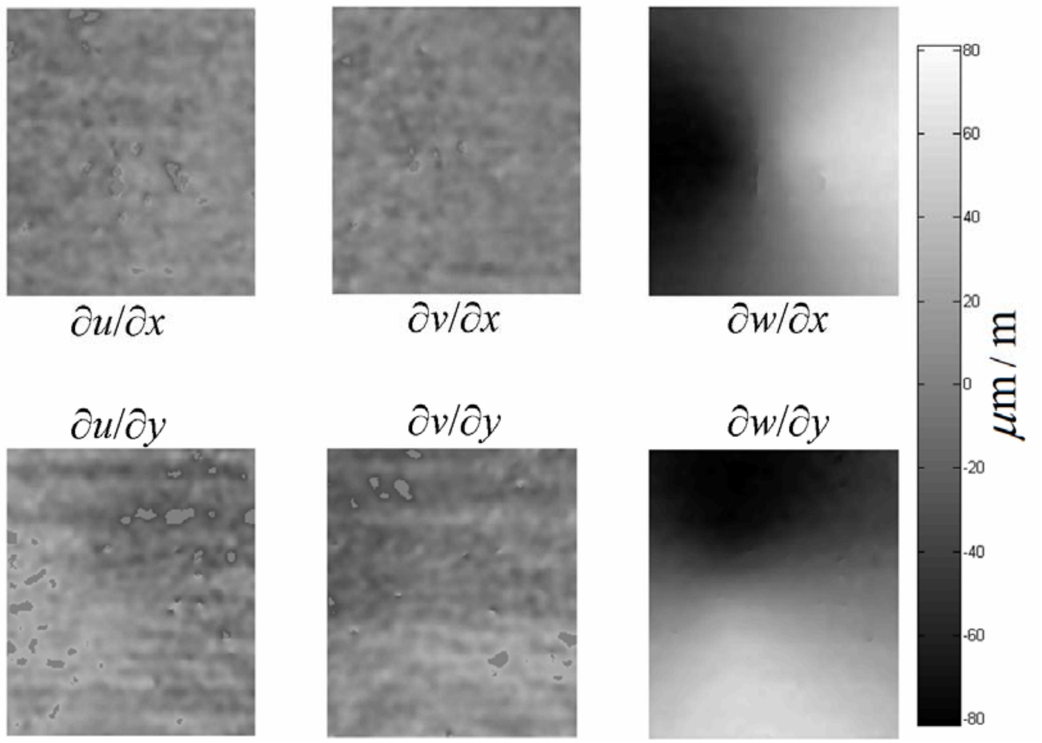

Figure 6.14 *Orthogonal displacement gradient components calculated using the experimentally determined phase maps shown in figures 6.13(c) and 6.13(d) and sensitivity vectors calculated using the dewarping mapping functions (figure 6.7).*

6.4.2 Measurements from the perspex plate

The second object that was investigated was the flat perspex plate, illustrated in figure 4.8(b). This object was selected for analysis due to the fact that it exhibits in-plane strain when deformed. Deformation was applied to the object by turning a screw vertically through a horizontal slot cut out of the plate.

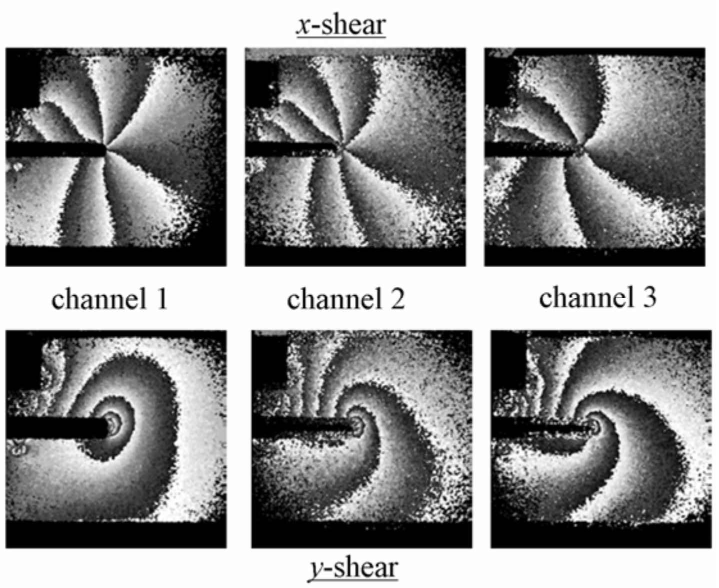

Figure 6.15 *Wrapped phase maps obtained from the three measurement channels of the laser diode based multiple-illumination-direction shearography system [1].*

Surface strain analysis of this object has been performed previously using the laser diode based multiple-illumination-direction shearography system presented in section 4.9. Results from that investigation were published in [1]. Figure 6.15 shows the wrapped phase maps that were obtained using temporal phase stepping. Results obtained using *x*-shear and *y*-shear are shown in the top and bottom rows respectively. The magnitude of the applied shear was 10 mm in each case. The field of view across each of the images is approximately 9 cm x 10 cm. The phase maps were unwrapped and the orthogonal displacement gradient components were calculated using the matrix transformation (equations (6.7) and (6.8)). The displacement gradient components are shown in figure 6.16.

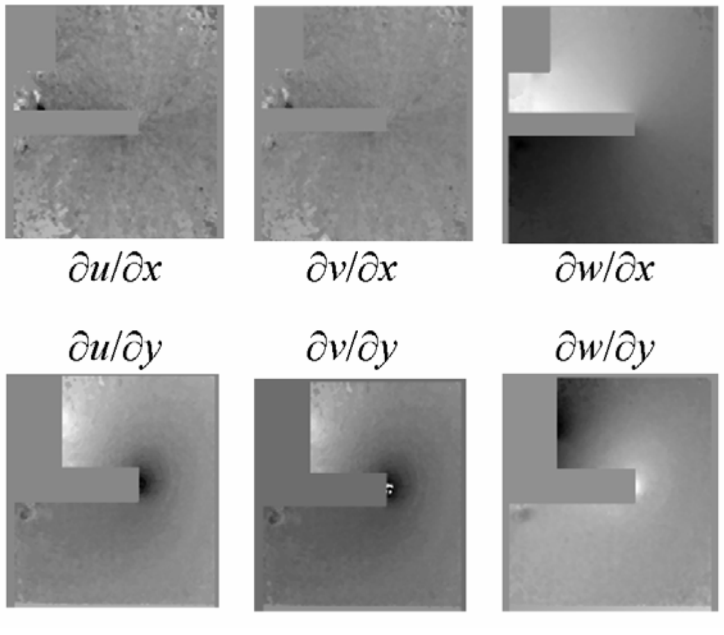

Figure 6.16 *Orthogonal displacement gradient components calculated using the phase maps shown in figure 6.15 after unwrapping [1].*

The wrapped phase maps obtained using the multiple-viewing-direction pulsed laser shearography system after loading the object are shown in figure 6.17. These wrapped phase maps were obtained using a shear of 9 mm. The field of view across each of the images is approximately 6 cm x 7 cm.

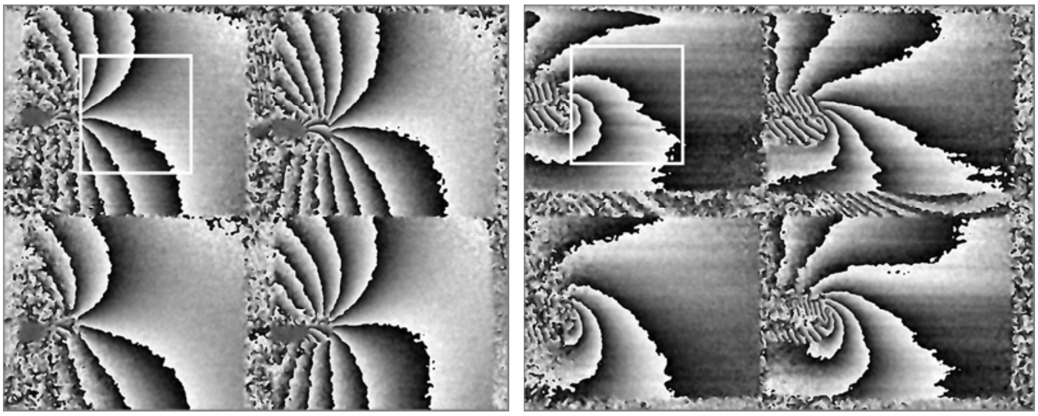

(a) **(b)**

Figure 6.17 *Wrapped phase maps obtained using the multiple-viewing-direction pulsed laser shearography system with shear applied in the x-direction (a) and the y-direction (b). The white box indicates the approximate region used for the strain calculation.*

The white box in the top-left wrapped phase map indicates the approximate region that was isolated from each of the four views and used in the displacement gradient calculation. The apex of the horizontal slot is located to the left of the white box. The orthogonal displacement gradient components calculated from these phase maps after unwrapping are shown in figure 6.18.

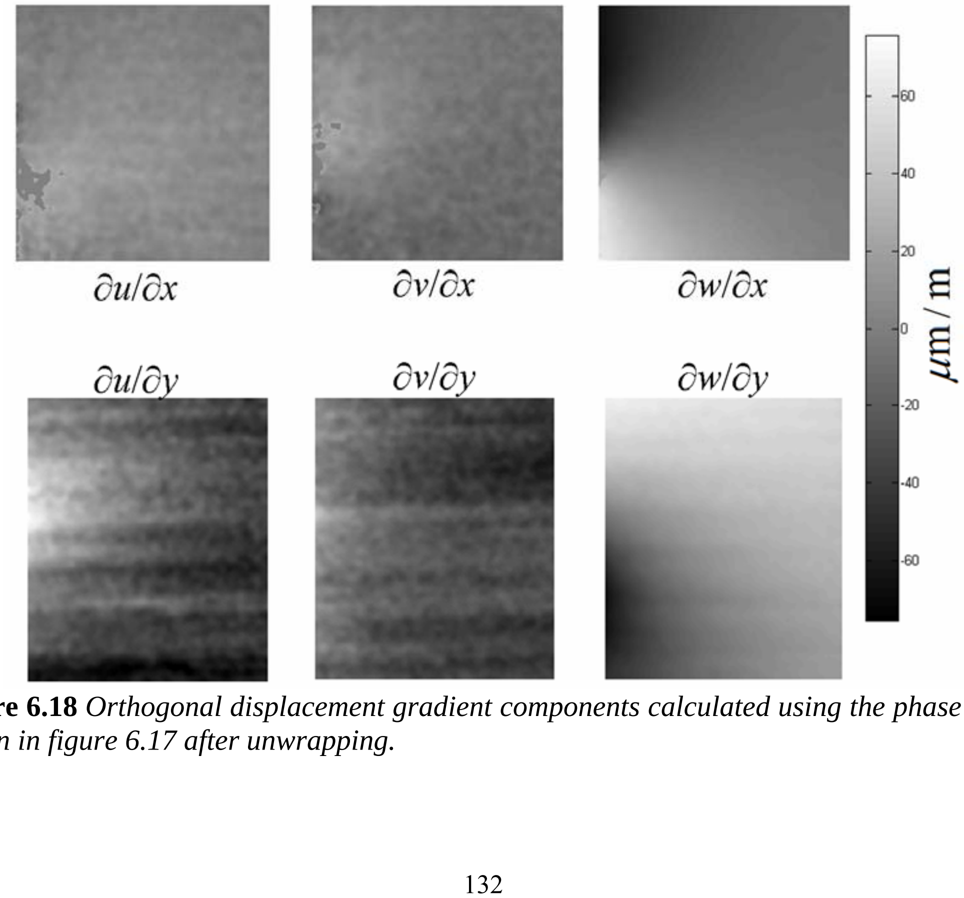

Figure 6.18 *Orthogonal displacement gradient components calculated using the phase maps shown in figure 6.17 after unwrapping.*

With shear applied in the *x*-direction, predominantly out-of-plane strain is observed, with low strain distributions in the in-plane displacement gradient components. When shear is applied in the *y*-direction, however, both in-plane and out-of-plane strain is observed, with the greatest strain concentrations located near the apex of the slot. This is to be expected considering the nature of the loading, which was in the *y*-direction. The results also agree with those presented in figure 6.16, although the direction of the applied deformation was opposite in the two cases, which can be seen from the opposite colour map gradient in the two cases. For example, the region of high strain concentration near the apex of the slot in the $\partial w/\partial y$ component is represented by black in figure 6.18 and by white in figure 6.16.

6.4.3 Horizontal lines through subtracted images

One problem that was encountered during the course of this work was the presence of horizontal lines that sometimes were observed in images obtained from subtraction of speckle patterns. These lines resulted in the distortion of the fringe discontinuities of the wrapped phase maps. This phenomenon was more prevalent when image shear was applied in the *y*-direction. The distortion of the wrapped phase fringes can be seen, in particular, in the wrapped phase maps recorded with *y*-shear in figures 6.13(b) and 6.17(b).

It was discovered that these lines are due to the structure of the fibre subarrays that can be seen in images recorded through the fibre bundles, such as in figure 4.6(b). This explains why they are more prevalent when shear is applied in the *y*-direction since in this case the fibre subarrays are imaged twice onto the camera. Only horizontal lines are seen, which is due to the fibre subarrays being well-aligned in rows but not columns. To illustrate this, figure 6.19(a) shows an image generated by static subtraction of speckle patterns recorded from the flat aluminium plate with no deformation applied to the object. In this image, shear is applied in the *y*-direction. Figure 6.19(b) shows an image that was also generated by static subtraction with shear applied in the *y*-direction although this time the output of the fibre bundle has been rotated by approximately 35° about the optical axis. The lines remain aligned with the orientation of the bundle output.

The reason for the appearance of the lines is due to mechanical instability of the viewing apparatus during the recording period. Motion of the viewing apparatus after recording the first frame may result in light coupling into rows of fibres with different transmission to the first frame. The rows of fibres will then be revealed when the two images are subtracted. This problem can be reduced by fixing the viewing apparatus more securely so that it is less susceptible to vibration, such as in the experiments presented in section 7.1. This phenomenon should not cause any problem when dual pulsed illumination is used since the time between frames is not sufficient for the motion of the viewing apparatus to be noticed.

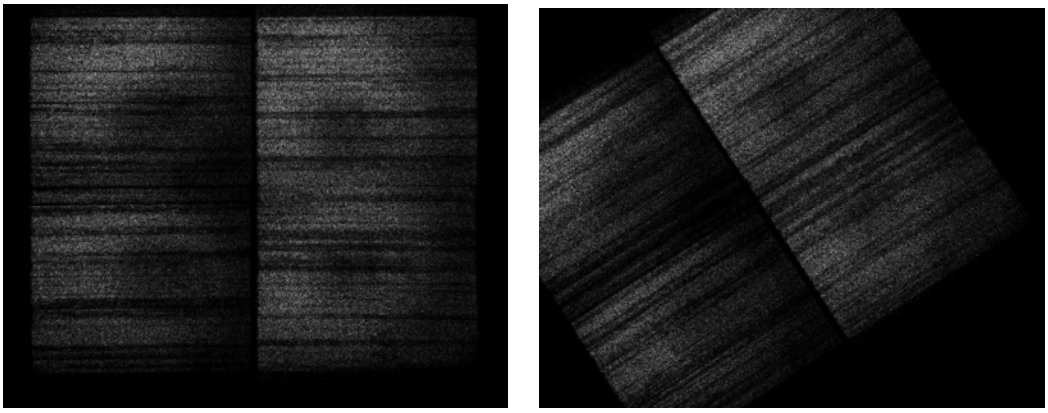
(a) **(b)**

Figure 6.19 *Static subtraction of speckle patterns sometimes reveals lines across images recorded through the fibre bundles (a).This is due to the structure of the fibre subarrays. After rotating the bundle output and recording subsequent images (b), the lines remain orientated parallel to the x-axis of the bundle output.*

6.5 Measurements using the spatial carrier technique

Measurements made on the flat aluminium plate test object were repeated using the spatial carrier technique in order to verify that this phase analysis technique is suitable for use in multi-component surface strain analysis. The spatial carrier technique was performed with the aid of a tilted Mach-Zehnder shearing interferometer; the principle of which was discussed in section 5.3.2. Wrapped phase maps obtained using the spatial carrier technique are shown in figures 6.20(a) and 6.20(b) for shear applied in the x and y directions respectively. The wrapped phase maps were divided into their individual image quadrants, unwrapped and then dewarped. The unwrapped phase maps obtained with shear applied in the x and y directions are shown in figures 6.20(c) and 6.20(d) respectively. The unwrapped phase maps have been recombined into a composite image here for the purpose of presentation.

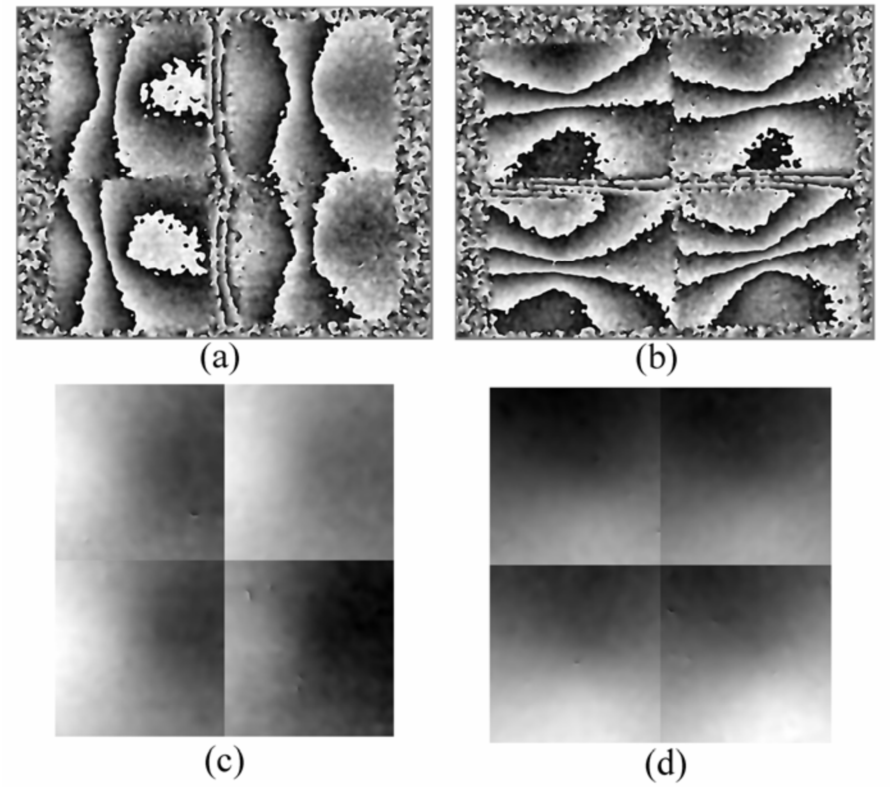

Figure 6.20 *Phase maps obtained using the spatial carrier technique after deformation of the flat aluminium plate. The filtered wrapped phase maps obtained with x-shear (a) and y-shear (b). The unwrapped and dewarped phase maps obtained with x-shear (c) and y-shear (d).*

6.5.1 Calculation of shear magnitude variation using image correlation

An issue that was noticed with the wrapped phase maps generated using the spatial carrier technique was that the density of fringes was not constant for each measurement channel. The left hand phase maps in figure 6.20(a) have a higher fringe density than the right hand phase maps and bottom row of phase maps in figure 6.20(b) have a higher fringe density than the top row of phase maps. This was believed to be due to a variation in the shear magnitude across the image caused by the tilt of the Mach-Zehnder interferometer. A measurement of the shear magnitude across the image was therefore required in order to correct for the variation in shear prior to the displacement gradient calculation.

The shear magnitude across the image was measured using a method based on the principle of digital cross-correlation [13, 14]. The image correlation process was described in section 2.4 and illustrated in figure 2.9. The shear measurement method involves recording a pair of images through the interferometer with each interferometer arm blocked in turn. In references [13] and [14] the images recorded were speckle patterns obtained by illuminating a diffuse surface with a continuous wave laser. The cross correlation of subarrays within the two images was calculated and a correlation peak was observed. When using the pulsed Nd:YAG laser system no correlation peak was observed from speckle patterns recorded with each mirror blocked. To combat this, a target was produced consisting of a random pattern. This was generated using Matlab by building an array of random numbers. A grey-scale array produced from the numerical array was printed and placed in focal plane of the four camera lenses. The target was illuminated using a 60 W desk lamp and imaged through the fibre bundles and shearing interferometer. A pair of images was then recorded sequentially with each interferometer arm blocked in turn. The images from each interferometer arm are shown in figures 6.21(a) and 6.21(b) respectively.

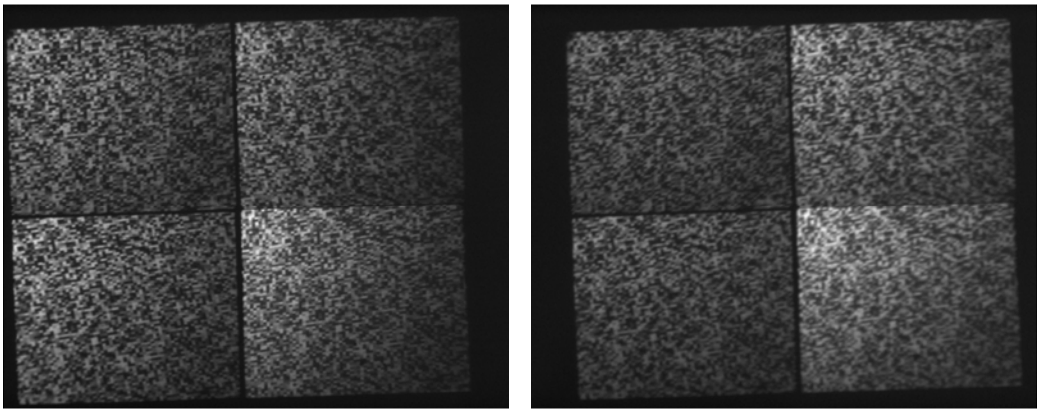

(a) **(b)**

Figure 6.21 *Images taken of a target consisting of a random grey-scale array recorded through each individual interferometer arm.*

A Canny edge detection filter was applied to the images shown in figure 6.21 to enhance the features within the images. This helps the correlation process by increasing the likelihood that a strong correlation peak is detected at each location in the image. The shift of the pattern features between each image was determined by calculating the cross-correlation of subarrays selected from the same location in each of the two images. A correlation window subarray of 150x150 pixels was chosen for this application. This subarray size was chosen to be large enough to ensure that features contained within one subarray were still contained within the other. The image resulting from the correlation calculation contains a correlation peak. The distance between the correlation peak and the centre of the resulting image is equal to pixel displacement of the features between the two subarrays. Figure 6.22(a) shows a typical image of the correlation calculation obtained from subarrays taken from the images in figure 6.21. The red spot to the left of centre is the correlation peak. The correlation peak can be seen more clearly in the mesh plot shown in figure 6.22(b).

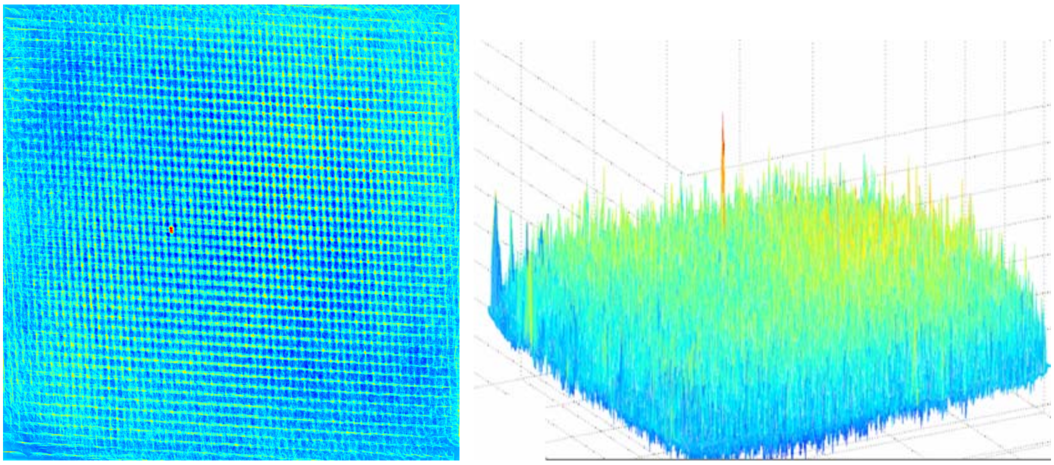
(a) (b)

Figure 6.22 *A typical image resulting from the cross-correlation of subarrays taken from the two images shown in figure 6.21. The red dot to the left of centre is the correlation peak (a). A mesh plot of the same image shows the correlation peak more clearly (b).*

The first correlation calculation was made from subarrays taken from the top-left corner of the images shown in figure 6.21. A single measurement of the pattern translation was obtained from the calculation and this value was inserted into another array. The correlation window was then translated by 20 pixels in the *x*-direction and a second measurement was made from the correlation of subarrays obtained at that location. This process was repeated until the end of the row was reached. Correlation measurements were then measured along the next row, which was chosen to be located 32 pixels below the top row. This was repeated until measurements had been made across the entire image. The values of 20 and 32 pixels between each measurement in the *x* and *y* directions were chosen to obtain a good compromise between resolution of measurement across the image and processing speed. These values are also required to be integer divisible by the number of pixels in the full image, i.e. 1024x1280.

The final image shows the translation of the pattern features in pixels between the two images. To obtain the shear magnitude, the pixel shift was multiplied by the pixel scaling factor. The pixel scaling factor was obtained during the image dewarping process and was found to be 0.158 mm. The result of the shear measurement across the image for shear applied in the *x*-direction (using the images shown in figure 6.21) is shown in figure 6.23(a). The results show a shear variation of approximately 1 mm across the image. This shear variation could introduce significant uncertainty into the displacement derivative calculations if a single shear value were used. Measurements made with a ruler placed in the focal plane of the four camera lenses confirmed this shear variation to be accurate.

A second pair of images of the random pattern target was recorded for shear applied in the *y*-direction. The same processing described above was applied to these images to determine the variation of the *y*-shear across the field of view. The result of this analysis is shown in figure 6.23(b). Regions where no correlation peak was detected resulted in erroneous measurements of the pattern feature translation. These regions are windowed out in figure 6.23(b). The measurements show a variation in the applied shear magnitude of approximately 0.35 mm across the image. This is an improvement on the results obtained with *x*-shear but nonetheless would introduce uncertainty into the displacement derivative calculation if a single shear value were to be used.

The maximum error introduced into the final displacement gradient calculations if just the central shear magnitude were used in the calculation would be 5.7% for the shear variation obtained for *x*-shear and 2.3% for the shear variation obtained for *y*-shear.

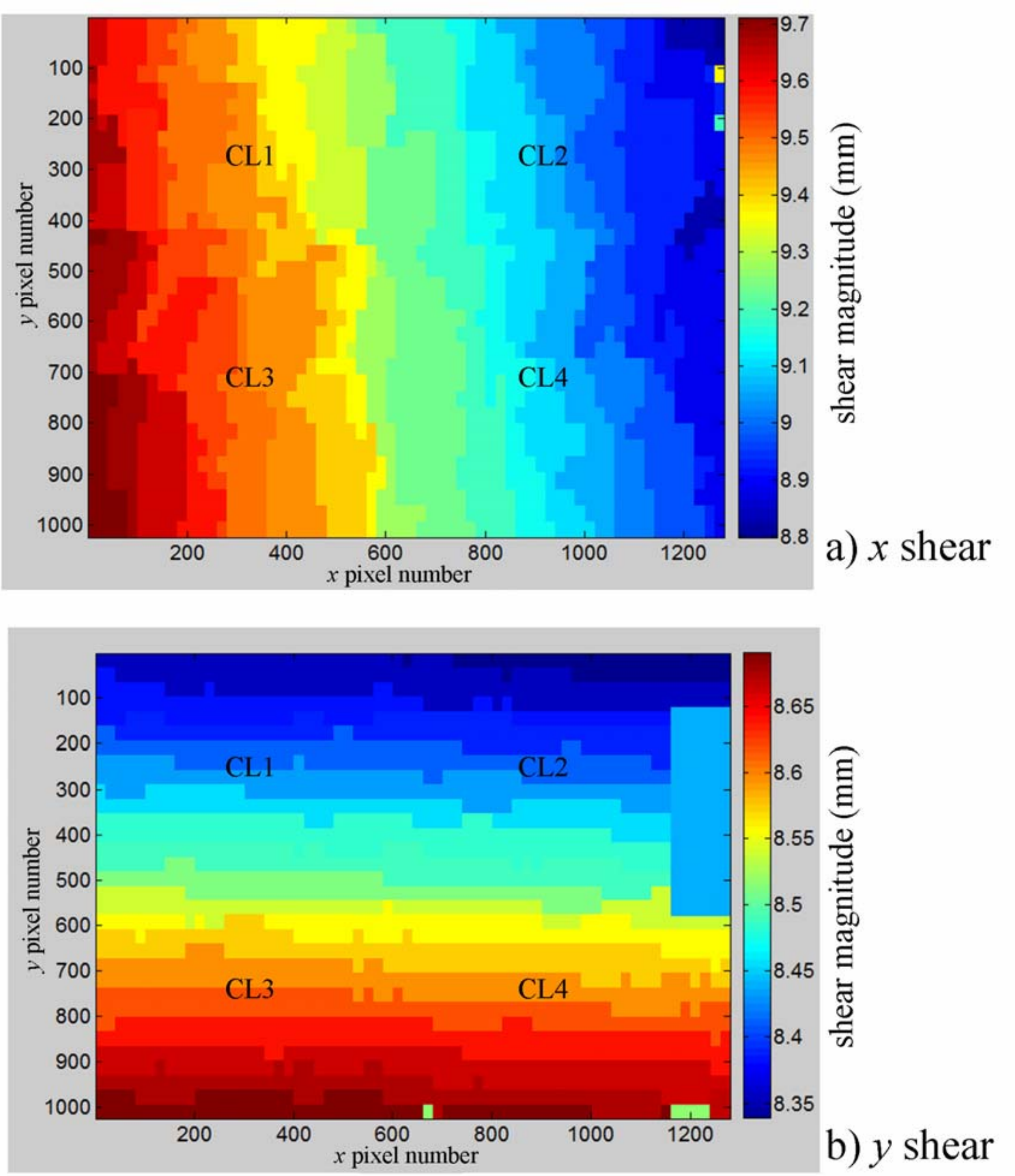

a) *x* shear

b) *y* shear

Figure 6.23 *Measurements of the shear magnitude across the image for shear applied in the x-direction (a) and y-direction (b) obtained using the image cross-correlation technique.*

6.5.2 Orthogonal displacement gradient components

The orthogonal displacement gradient components were calculated from equations (6.7) and (6.8) using the unwrapped phase maps shown in figure 6.20(c) and 6.20(d), the sensitivity vectors across the field of view (figure 6.6) and the measurements of the shear magnitude (figures 6.23(a) and 6.23(b)). The results of this calculation are shown in figure 6.24. The results show a similar form to those presented in figure 6.14 with the strain being predominantly out-of-plane. The variation in out-of-plane displacement gradient is approximately ±30 μm/m for the measurements made with shear applied in the *x*-direction and ±40 μm/m for the measurements made with shear applied in the *y*-direction. The reason for this difference is due to the measurements for *x* and *y* shear being made sequentially, therefore the loading might differ between the *x* and *y* shear results.

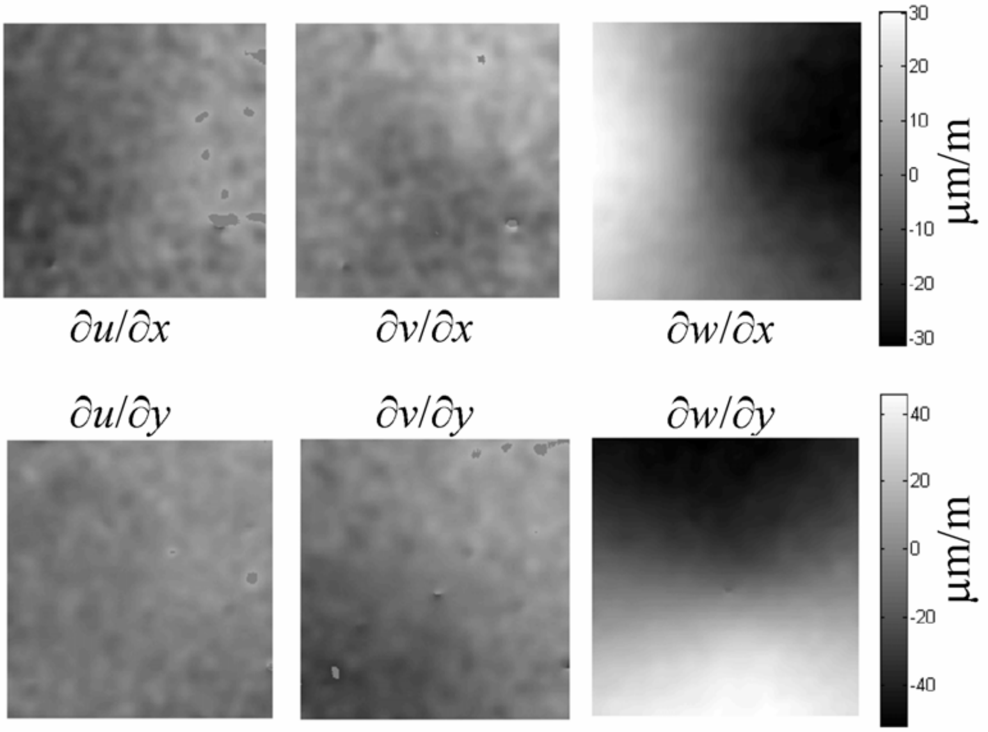

Figure 6.24 *Orthogonal displacement gradient components calculated using the unwrapped phase maps shown in figures 6.20(c) and 6.20(d), the measurements of the sensitivity vector (figure 6.6) and the measurements of the shear magnitude (figures 6.23(a) and 6.23(b)).*

6.6 Summary

In this chapter, the technique used for dewarping images recorded using the multiple-viewing-direction pulsed laser shearography system was presented. This technique is used to correct the images obtained for errors introduced due to perspective distortion and to centre the images obtained from the four views at the same point. The variation of the sensitivity vector was calculated across the field of view from measurements of the relative locations of the illumination and observation positions. An alternative method of calculating the sensitivity vector across the field of view involving the use of the dewarping mapping coefficients was also presented. The sensitivity matrix was investigated and an analysis of the condition number of this matrix showed that the viewing configuration used with the system is adequate for multi-component measurements.

Measurements of orthogonal displacement gradient components from two test objects were presented. These measurements were calculated from unwrapped phase maps obtained from the system and the measurements of the sensitivity vector across the field of view. The first object, a flat aluminium plate, illustrated in figure 4.8(a), was qualitatively compared with results obtained from simulated phase maps. The second test object, a flat perspex plate, illustrated in figure 4.8(b), was compared with results obtained using the multiple-illumination-direction shearography system that were presented previously in reference [1]. Phase measurements obtained using the spatial carrier technique were found to possess a variation in fringe density across the image. This was discovered to be due to a variation in the shear magnitude across the image. The shear magnitude was measured using an image cross-correlation technique.

All the results presented in this chapter were obtained from objects under static loading conditions. In the next chapter, the results obtained from dynamic test objects are presented.

References

[1] James S. W, Groves R. M. and Tatam R. P, ‘‘Surface strain characterization using time-division multiplexed 3D shearography’, *Proc. SPIE*, **4101**, 384-93 (2001).
[2] Tools for DaVis, Pro-package user manual, LaVision GmbH, Goettingen, Germany.
[3] Nobes D. S, Weineke B. and Tatam R. P, ‘Determination of View Vectors from Image Warping Mapping Functions’, *Opt. Eng*, **43**:2, 407-14 (2004).
[4] http://www.mathwords.com/i/inverse_of_a_matrix.htm
[5] http://www.mathwords.com/d/determinant.htm
[6] http://www.mathwords.com/c/cofactor_matrix.htm
[7] http://en.wikipedia.org/wiki/Condition_number
[8] James S. W. and Tatam R. P, ‘Time-division-multiplexed 3D shearography’, *Proc. SPIE*, **3744**, 394-403 (1999).
[9] James S. W, Tatam R. P. and Elder R. L, ‘Design considerations for a three dimensional fiber optic laser Doppler velocimeter for turbomachinery applications’, *Rev. Sci. Instrum*, **68**:8, 3241-6, (1997).
[10] Aebischer H. A, Waldner S, ‘A simple and effective method for filtering speckle-interferometric phase fringe patterns’, *Opt. Comm.* **162**, 205-10 (1999).
[11] Ghiglia D. C. and Pritt M. D, ‘Two-dimensional phase unwrapping: theory, algorithms and software’, Wiley, Chichester (1998).
[12] Groves R. M, James S. W. and Tatam R. P, ‘Multi-component shearography using four measurement channels’, *Proc. SPIE*, **4933**, 135-40 (2003).
[13] Ng T. W, ‘Shear measurement in digital speckle shearing interferometry using digital correlation’, *Opt. Comm.* **115**, 241-4 (1995).
[14] Andersson A, Krishna Mohan N, Sjödahl M. and Molin N-E, ‘TV-shearography: quantitative measurement of shear magnitude by use of digital speckle photography’, *Appl. Opt.* **39**:16, 2565-8 (2000).

7. Measurement of surface strain from dynamic objects

In this chapter, the results of measurements made from dynamic test objects are presented. The use of the pulsed laser system allows the measurement of dynamic surfaces by effectively freezing the motion of the object for the duration of the laser pulse. The use of multiple-viewing-direction configuration and the spatial multiplexing of signals from the four measurement channels allows the simultaneous acquisition of data from the four observation positions. The spatial carrier technique was used to calculate the phase distribution from just two images recorded sequentially at different points in the object's cycle. Two dynamic test objects are investigated: The first is a flat PTFE plate that is mounted on a lathe and set to rotate at 610 rpm and the second is a speaker cone that is subjected to vibrational frequencies ranging from 1.9 – 4.5 kHz.

The analysis of rotating components using speckle interferometry was previously investigated by Swain and Preater [1]. They used an ESPI system to measure the in-plane displacement field of a rotating object and used a pulsed ruby laser to freeze the motion of the object. The phase was evaluated using Fourier transform techniques. More recently, Pérez-López *et al* [2] used a multiple-illumination-direction ESPI system to determine the three orthogonal displacement components of a rotating object. Data from each measurement channel was acquired sequentially. The results presented in section 7.1.4 were made from a rotating object with measurements made with different sensitivity vectors simultaneously, thus allowing the computation of the orthogonal displacement gradient components that characterize the surface strain.

The vibrating speaker cone used in the measurements presented in section 7.2 was non-planar. Accurate surface strain measurement was therefore not possible using this object without a calculation of the object's shape. The main purpose of the investigation into the vibrating object was to prove that the image processing procedure could be successfully applied to images recorded with the laser operating in dual-pulse mode.

7.1 Measurements from a rotating test object

This section describes the application of the multiple-viewing-direction shearography system to the measurement of surface strain on a rotating test object. The test object, a flat PTFE plate, was mounted on a WARCO GH1322 gear head lathe. The lathe was set to rotate at 10 Hz, matching the repetition rate of the laser. A signal from an optical rev counter connected to the lathe was used to trigger the laser and the image acquisition of the camera. A signal from the lathe triggered a pulse generator, which in turn triggered the laser and CCD camera. This ensured that the object was illuminated once on each revolution and each time the object was illuminated it was at the same point in its cycle. Fringe patterns were obtained from sequential subtraction of images captured with the object located at the same position on subsequent revolutions. The object was thermally loaded and fringe patterns were continually acquired as the object cooled.

An alternative to recording speckle patterns on subsequent rotations is to use dual-pulsed illumination and record speckle patterns with a short delay between them. For example the results presented in reference [2] were derived from images recorded 20 μs apart. The difficulty with this approach, however, is the application of a deformation that is measurable on this timescale. The thermal loading approach would not induce sufficient strain between frames to observe fringes; therefore measurements were made with images recorded on subsequent revolutions at a rate of 10 Hz.

7.1.1 The test object

The object used in this investigation was a flat PTFE (polytetraflouroethylene) plate, as shown in figure 7.1. The plate has dimensions of 100x240 mm^2 and a thickness of 3 mm. A 3 mm thick aluminium disk with a diameter of 20 mm was bonded to the rear of the PTFE plate. The holes to the left and right of the aluminium disk in figure 7.1 were used to bolt the object to the lathe.

The PTFE and aluminium have different coefficients of thermal expansion. At room temperature the coefficient of thermal expansion for PTFE is $\alpha = 120 \times 10^{-6} k^{-1}$ [3] and for aluminium is $\alpha = 23 \times 10^{-6} k^{-1}$ [4]. When the object is thermally loaded, the PTFE will expand more than the aluminium and a strain variation will be observed around the periphery of the aluminium disk.

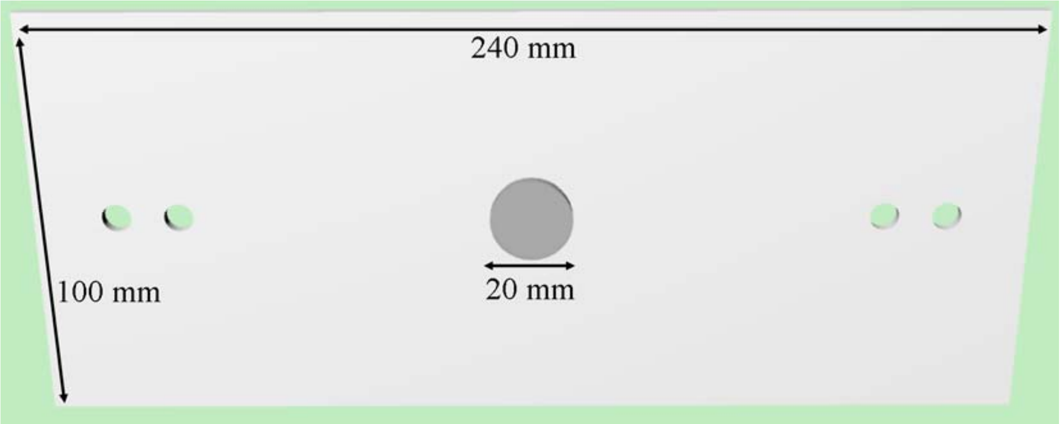

Figure 7.1 *The PTFE object, shown from the rear, which was used as the test sample for measurements made using the lathe. The aluminium disk is in the centre of the plate.*

7.1.2 The viewing apparatus frame

When it is in operation, the body of the lathe vibrates. The vibration of the lathe will induce a vibration in the fibre-bundle arms if they are in contact with the body of the lathe. Vibration of the bundles will result in a change in the relative phase of light propagating through the bundles between the reference and signal frames, resulting in a loss of fringe contrast. To avoid this occurrence, the viewing apparatus was mounted on a frame that was constructed using Flexlink components. This frame allowed the viewing apparatus to be mounted in such a way as to avoid any contact between the fibre-bundles and the body of the lathe. A schematic showing the frame used for mounting the viewing apparatus is shown in figure 7.2.

The frame was necessary for the measurements presented here because images were recorded at a rate of 10 Hz. For dual-pulsed measurements, with images recorded a few microseconds apart, the vibration of the lathe would not be significant on these timescales and the frame would therefore not be essential.

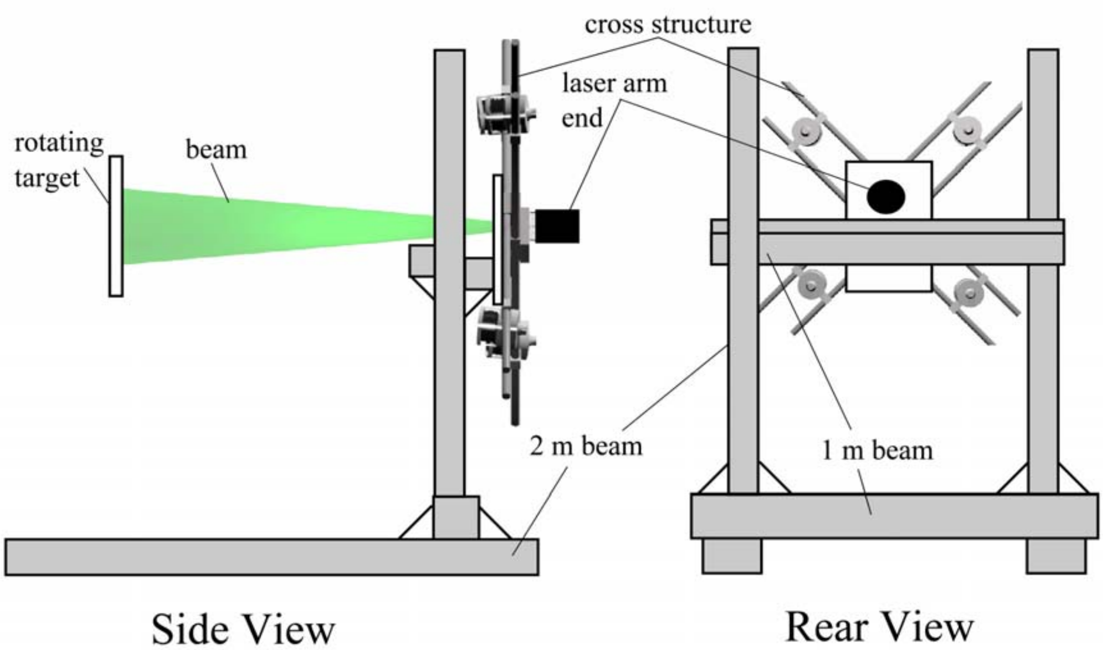

Figure 7.2 *A schematic of the frame built to mount the viewing apparatus so that no contact is made between the fibre bundles and the body of the lathe.*

Figures 7.3 and 7.4 show photographs of the viewing apparatus mounted on the frame built to isolate the bundles from the body of the lathe.

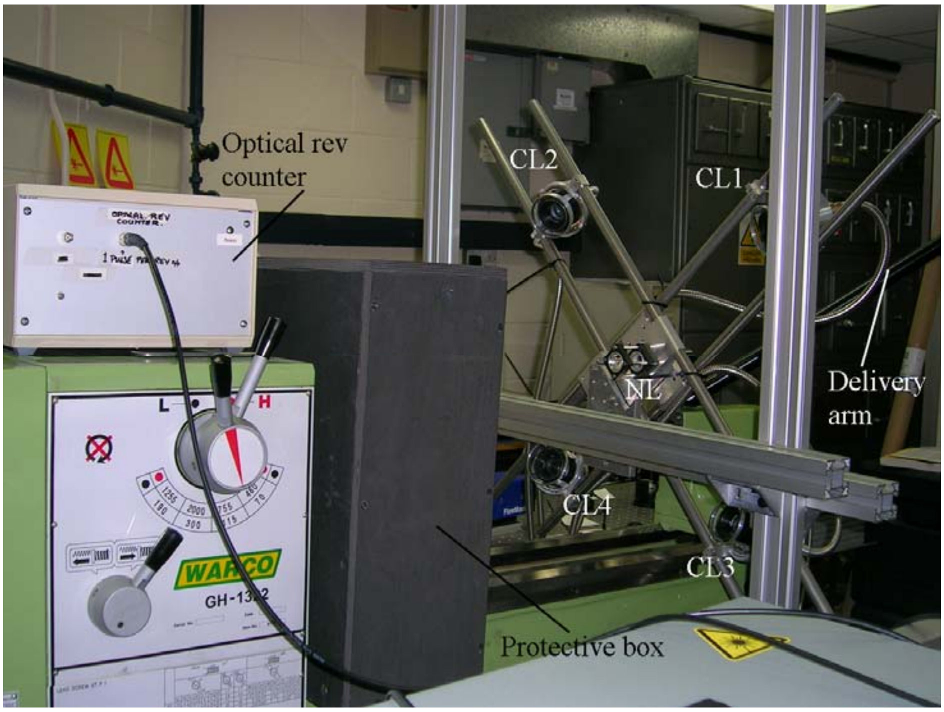

Figure 7.3 *Photograph of the viewing apparatus mounted on the frame built to isolate the bundles from the body of the lathe. CL 1-4 = camera lens, NL = negative lens.*

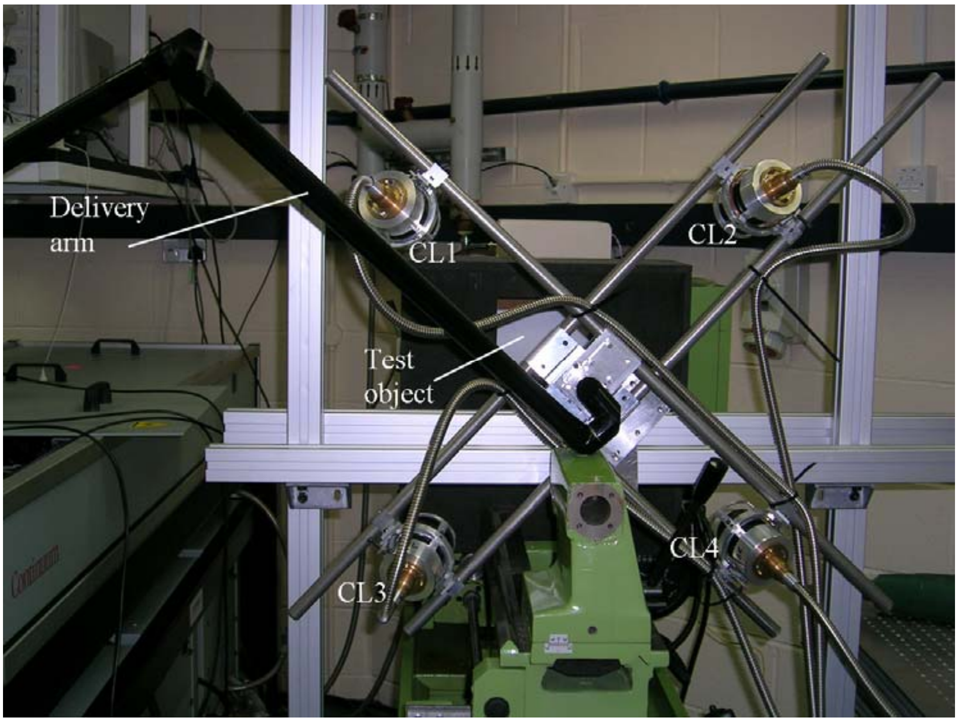

Figure 7.4 *Photograph of the viewing apparatus mounted on the frame built to isolate the bundles from the body of the lathe. CL 1-4 = camera lens, NL = negative lens.*

7.1.3 Laser synchronization

The laser synchronization timing scheme for the measurement of surface strain from the rotating object is shown in figure 7.5. A signal from the optical rev counter that was mounted on the lathe, indicated in blue in figure 7.5, was used to trigger the laser and CCD camera. The optical rev counter signal was obtained from an LED (light emitting diode) and photodetector pair that was housed within the protective box (shown in figure 7.3) to the right of the lathe wheel. A piece of reflective tape (area ~1 cm^2) was stuck to the edge of the lathe wheel. On each revolution of the wheel, light emitted by the LED was reflected from the reflective tape and was detected by the photodetector. A signal from the photodetector was transmitted to the optical rev counter electronics box (see figure 7.3). The electronics box produces a +5V pulse which was transmitted to a BNC (Berkeley Nucleonics Corporation) 555 eight channel pulse generator. The pulse generator then triggers the laser and the CCD camera.

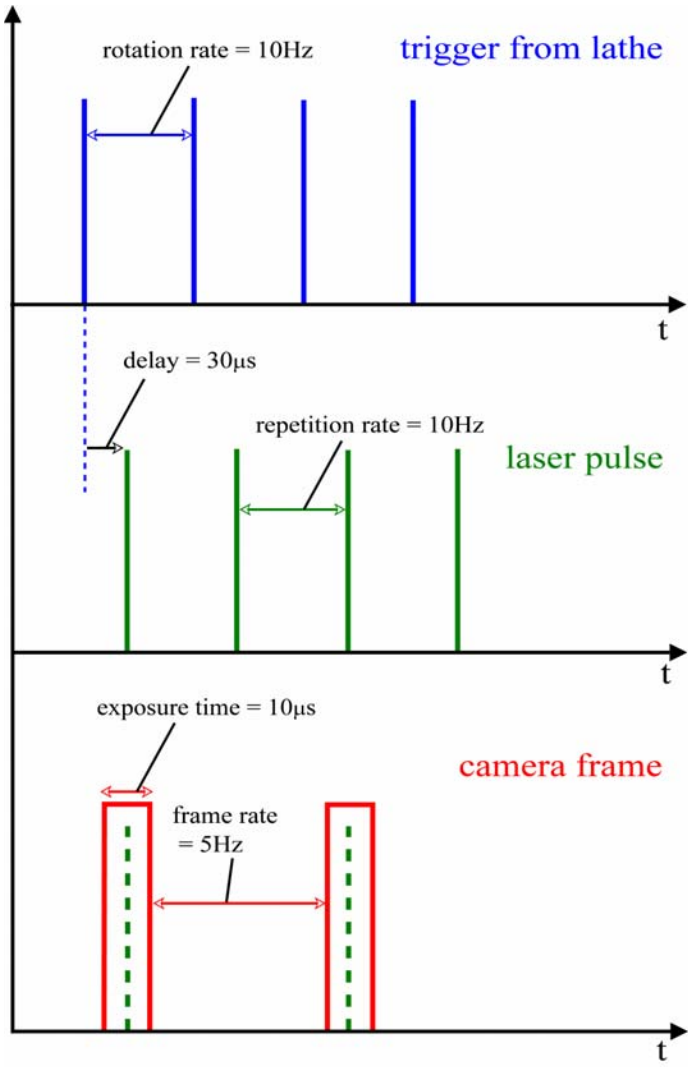

Figure 7.5 *The synchronization scheme for the lathe (blue), laser (green) and the camera (red).*

The repetition rate of the laser was set by the manufacturer to be 10 Hz. When externally triggering the laser, the repetition rate must be within the range of 9.8Hz – 10.2 Hz [5]. Operating the laser outside of this range will potentially cause damage to the optics within the laser due to thermal lensing. The rotation speed of the lathe was measured, using a rotation meter, to be 610 rpm. This corresponds to a rotational frequency of 10.17 Hz and is within the safe operating range for the laser.

After receiving the pulse from the optical rev counter, a delay was set on the pulse generator before triggering the laser, shown in green in figure 7.5. The magnitude of the delay determines the position that the object is in when it is illuminated by the laser pulse. A delay of 30 μs was used which ensured that the object was in the centre of the field of view of the four camera lenses when it was illuminated.

The camera was synchronized with the laser using the pulse generator to ensure that images were captured when the target was illuminated. The exposure time of each camera frame, indicated in red in figure 7.5, was chosen to be 10 μs. The acquisition rate of the camera was 5 Hz. The object was therefore able to complete two full rotations during the delay between capturing signal and reference frames.

7.1.4 Measurements from the rotating sample

To induce a measurable strain variation across the region of interest on the surface of the test object, the object was thermally loaded by locally heating the region of interest with a heat gun. This was done for approximately 1 minute with the object stationary. The temperature of the surface reached approximately 75°C after heating. This was measured using a thermocouple. The lathe was then switched on and allowed to accelerate to approximately 610 rpm. Carrier fringe patterns were then recorded using the Mach-Zehnder shearing interferometer described in section 5.3.2. The images were captured as the object cooled and correlation fringe patterns were generated from sequential subtraction of pairs of carrier fringe images. At first, no correlation fringes were visible because the temperature change in the time between the two frames was too great and the fringe density too high. Fringes started to become visible when the change in temperature between the signal and reference frame reached approximately 0.5°C. This temperature variation was measured with a thermocouple to an accuracy of ±0.1°C. When the correlation fringes began to appear, the signal and reference carrier fringe modulated speckle patterns were saved for further processing. Figure 7.6 shows a typical reference and signal frame obtained with the system and the correlation fringes obtained by subtraction of the two frames.

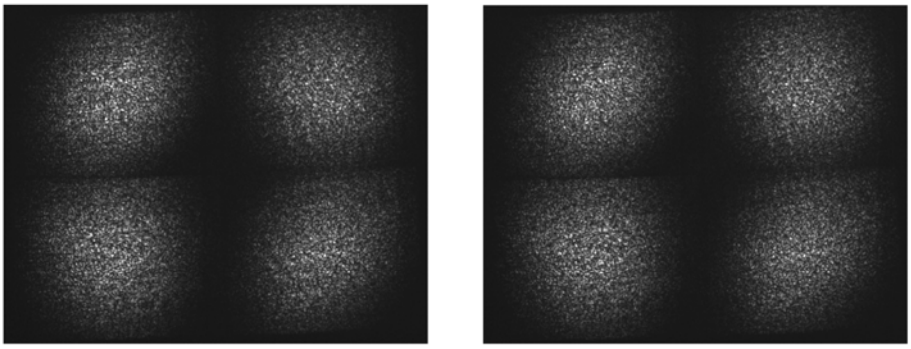

Reference frame Signal frame

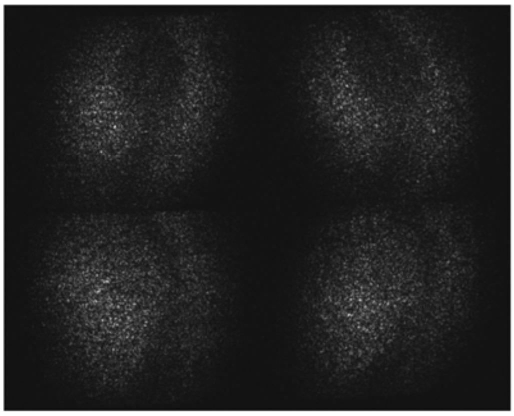

Correlation fringes

Figure 7.6 *Reference and signal frame carrier fringe modulated speckle patterns and the correlation fringes produced by subtraction of the two frames.*

Wrapped phase maps were calculated from saved reference and signal frames using the procedure described in section 3.3.2. Wrapped phase maps obtained with shear applied in the *x* and *y* directions are shown in figures 7.7(a) and 7.7(b) respectively. These wrapped phase maps are shown after the application of the iterative sine-cosine filter described in section 3.4.2. The phase maps from each of the measurement channels were isolated and then unwrapped using Goldstein's branch cut algorithm before being dewarped. Figures 7.7(c) and 7.7(d) show the phase maps after unwrapping and dewarping.

The lighter coloured region in the bottom left of the two right hand unwrapped phase maps shown in figure 7.7(d) was caused by errors in the unwrapping process which was due to the high noise content in this region. This region was windowed out of the phase maps prior to the displacement gradient calculation.

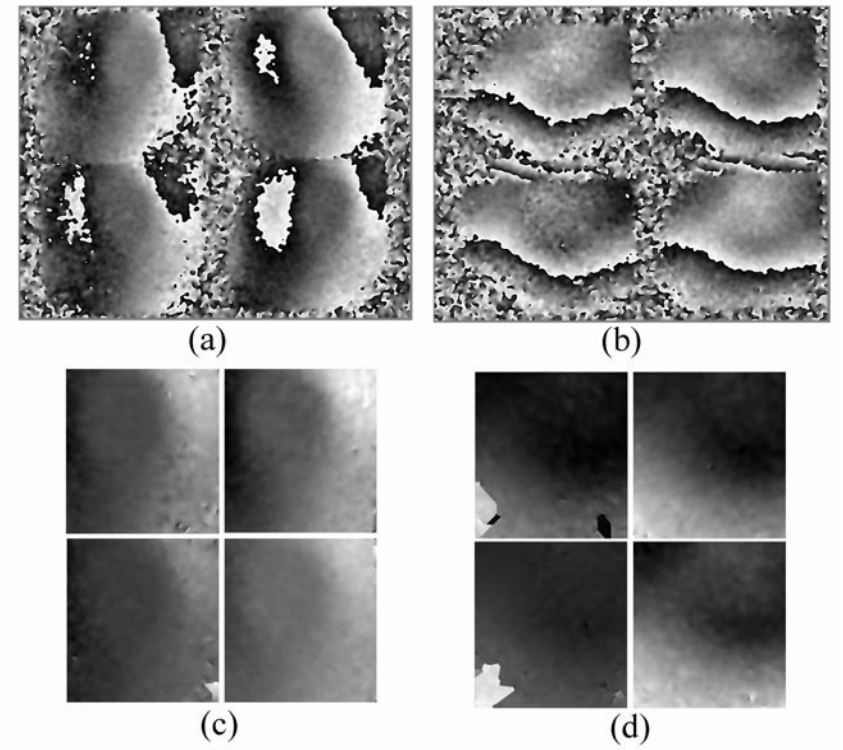

Figure 7.7 *Wrapped phase maps recorded with x-shear (a) and y-shear (b) obtained from the thermally loaded PTFE plate whilst rotating at a speed of 610 rpm. The unwrapped and dewarped phase maps for x-shear (c) and y-shear (d).*

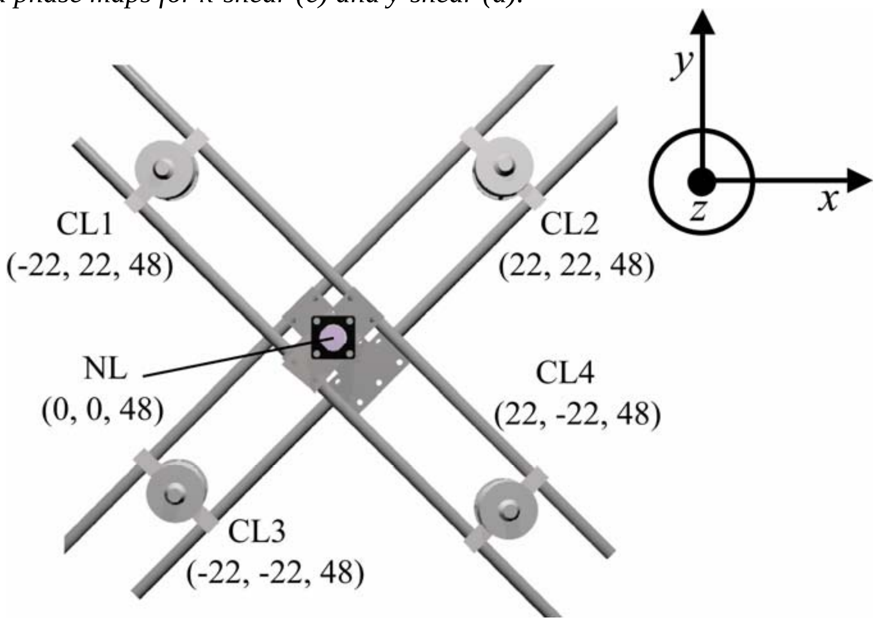

Figure 7.8 *Coordinate locations given in the form (x, y, z) of the observation and illumination positions used for the measurements of the rotating object. The coordinate system is indicated in the top right of the figure.*

The next step was to determine the sensitivity vector across the field of view for each of the four measurement channels. This was achieved using the method based on measurements of the observation and illumination positions that was discussed in section 6.2.1. The coordinate locations of the observation and illumination positions for the measurements made from the rotating object are illustrated in figure 7.8.

The magnitude of the applied shear across the full image was determined using the image correlation process presented previously in section 6.5.1. This method was necessary because the shear is function of position in the image plane, thus measurements from the different views have different shear magnitudes depending on their position within the composite image. Using this method, a shear magnitude of 8.3 mm was measured at the centre of the composite image for the images recorded with x-shear, with a shear variation of 0.6 mm across the composite image. For the images recorded with y-shear, the shear magnitude at the centre of the image was measured to be 8.0 mm with a shear variation of 0.8 mm across the image.

The orthogonal displacement gradient components were then calculated from the unwrapped phase maps, sensitivity vector components and the measurements of the shear magnitude using the matrix transformation given in equations (6.7) and (6.8). Figure 7.9 shows the calculated orthogonal displacement gradients across a field of view. This was approximately 40 x 35 mm^2 for the displacement derivatives in the x direction and approximately 35 x 30 mm^2 for the displacement derivatives in the y direction. This difference is due to the additional windowing required for the phase maps recorded with y-shear to remove the erroneous region that was discussed previously.

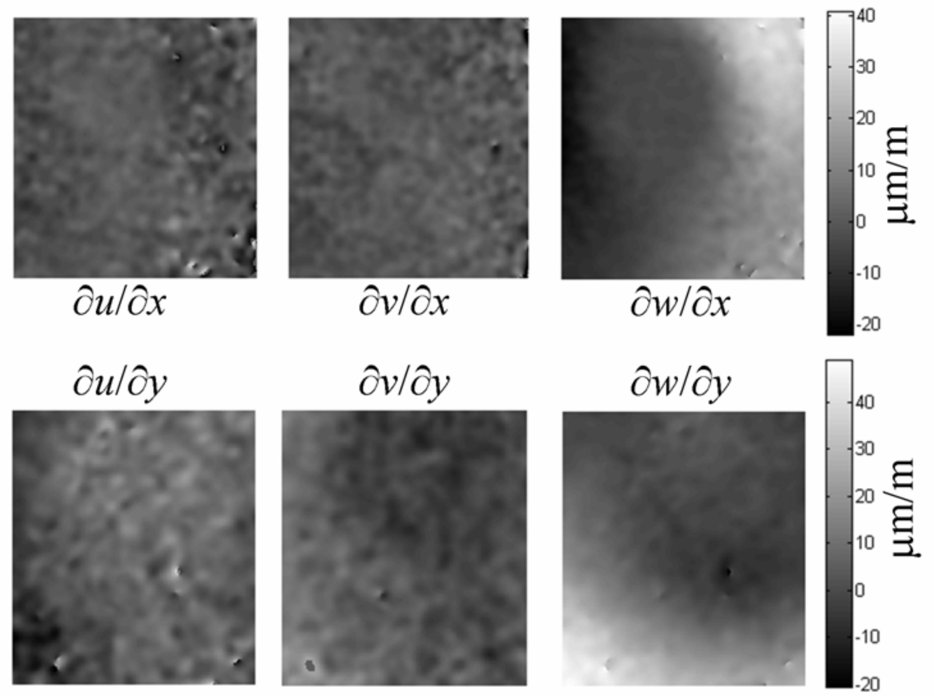

Figure 7.9 *The orthogonal displacement gradient components measured from the rotating test object.*

The results presented in figure 7.9 show relatively low in-plane strain in comparison to the out-of-plane strain components. Figure 7.10 shows the same displacement gradient component measurements plotted using the 'jet' colourmap. This colourmap varies from red for high values to blue for low values and shows the strain variation in the out-of-plane components more clearly.

Assuming a temperature variation of ΔT = 0.5°C and a thermal expansion coefficient of α_{PTFE} = $120\text{x}10^{-6}\text{k}^{-1}$, the strain induced by thermal expansion at a point on the PTFE plate can be calculated to be approximately $\varepsilon_{PTFE} = \Delta T^{*}\alpha_{PTFE}$ = 60 μm/m. Assuming a thermal expansion coefficient of α_{PTFE} = $23\text{x}10^{-6}\text{k}^{-1}$, the strain induced by thermal expansion calculated similarly is approximately $\varepsilon_{aluminium}$ = 11.5 μm/m. A difference in displacement gradient of approximately 48.5 μm/m can therefore be expected around the periphery of the aluminium disk. The positive strain values in the $\partial w/\partial x$ and $\partial w/\partial y$ components correspond approximately with this estimation. The negative strain values are less than this estimation due to the limited field of view of the images shown.

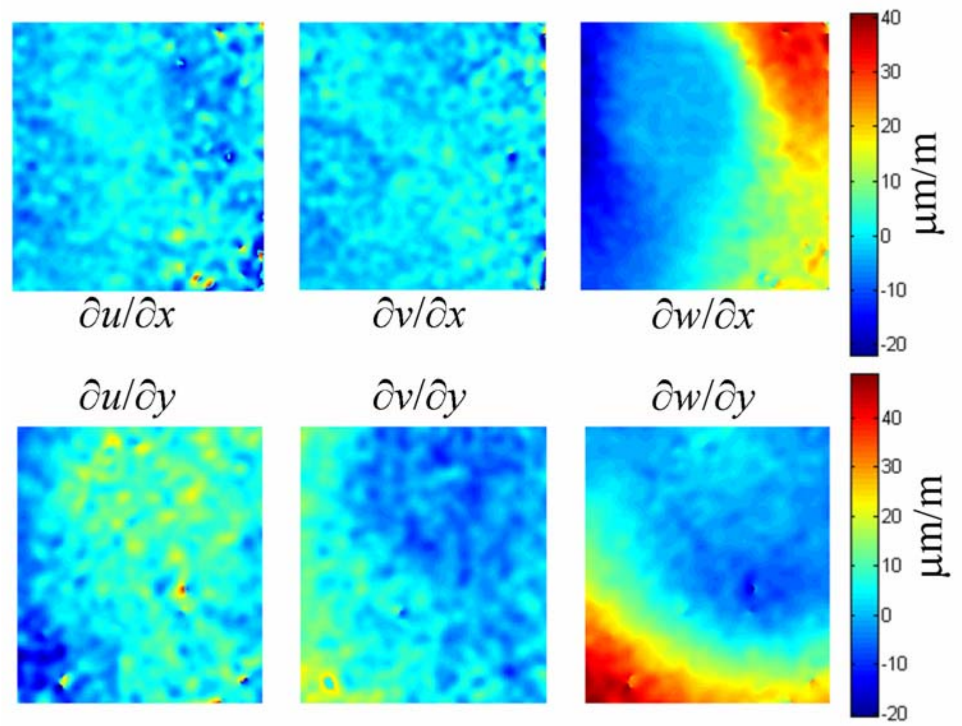

Figure 7.10 *The same orthogonal displacement gradient components as shown in figure 7.8 plotted with a different colourmap to highlight the strain variation around the periphery of the aluminium disk.*

7.2 Dual-pulse measurements from a vibrating test object

This section describes the use of the multiple-viewing-direction pulsed laser shearography system for the measurement of a vibrating test object. One advantage of using a pulsed laser system to investigate vibrating objects is that the fringes produced are cosinusoidal, as opposed to the Bessel fringes that are obtained from time-averaged vibration analysis using a continuous-wave laser [6]. Cosinusoidal fringe patterns are advantageous because the fringes are of uniform intensity and separation.

The results presented here were obtained from a speaker cone vibrating at a range of frequencies from 1.9 kHz to 4.5 kHz. These measurements were obtained using dual laser pulses separated by 1.6 μs. The two pulses effectively freeze the motion of the object at two points in the vibration cycle. Speckle patterns produced by the two laser pulses were recorded by the camera running in dual-frame mode. This mode allows the capture of images at a minimum of 200 ns separation. Subtraction of the two speckle patterns yields a correlation fringe pattern, where the fringes are dependent on the derivative of the vibration induced displacement. The spatial carrier technique was used to determine the phase variation introduced by the vibration of the object.

7.2.1 The test object

The test object used in this investigation was a speaker cone with a diameter of approximately 7 cm. The speaker cone was fixed in place in focal plane of the four camera lenses. A Stanford Research Systems DS345 function generator was used to generate a sine-wave signal. This signal was amplified using a current amplifier and used to drive the speaker cone.

7.2.2 Dual-pulse operation

The seed laser radiation is divided into pulses using a Kentech pulse shaper. This instrument, based on a Li:Tantalate pockels cell, is programmable and allows the operator to produce the desired pulse shape using the computer interface. With this tool, it is possible to divide the beam so that two pulses are emitted with a short separation between them. To measure the profile of the pulses emitted by the laser, a foam beam block was placed in the beam path. Light scattered from the foam block was collected with a high speed Melles-Griot 13DAH-0101 photodiode with a rise time of 0.35 ns – 1.0 ns. The signal from the photodiode was visualized using a Hewlett-Packard 54111D digitizing oscilloscope with a bandwidth of up to 250 MHz.

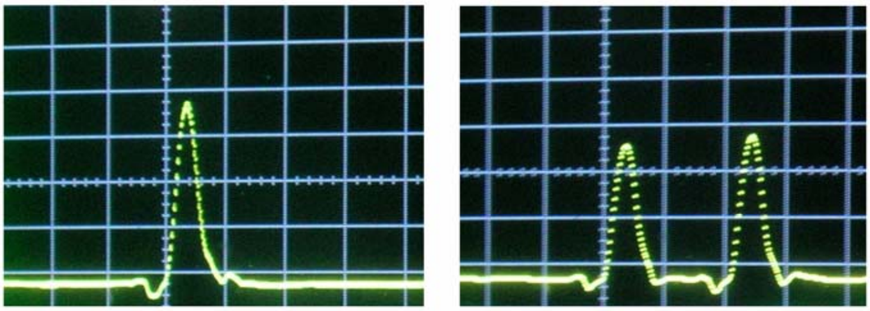

a) Single pulse b) 1.0 μs separation

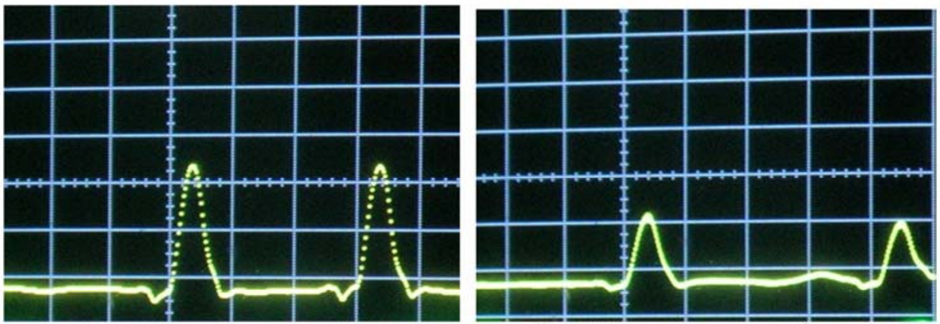

c) 1.6 μs separation d) 2.0 μs separation

Figure 7.11 *Photographs of the screen of the oscilloscope used to investigate the dual-pulsed operation of the laser. The images show (a) a single pulse and dual-pulses separated by (b) 1.0 μs, (c) 1.6 μs and (d) 2.0 μs.*

Figure 7.11 shows a series of photographs taken of the screen of the oscilloscope for a range of pulses. The trace shows the output from the photodiode. The timebase of the oscilloscope for each of the photographs shown in figure 7.11 was 500 ns. Figure 7.11(a) shows the profile for a single pulse. Figures 7.11(b) – (d) show the pulse profile for dual-pulses with separations of 1.0 μs, 1.6 μs and 2.0 μs, respectively. It can be seen from figure 7.11 that as the pulse separation increases, the amplitude of each pulse decreases. For the measurements presented in section 7.2.4, a pulse separation of 1.6 μs (figure 7.11(c)) was chosen since this seemed a good compromise between pulse separation and pulse amplitude.

7.2.3 Laser synchronization

The laser synchronization timing scheme used for measurements of the vibrating test object is shown in figure 7.12. For these measurements, both the laser and the CCD camera are triggered using the pulse generator. The timing of the laser pulses is shown in green in figure 7.12. The laser is triggered to emit dual pulses 1.6 μs apart at a rate of 10 Hz.

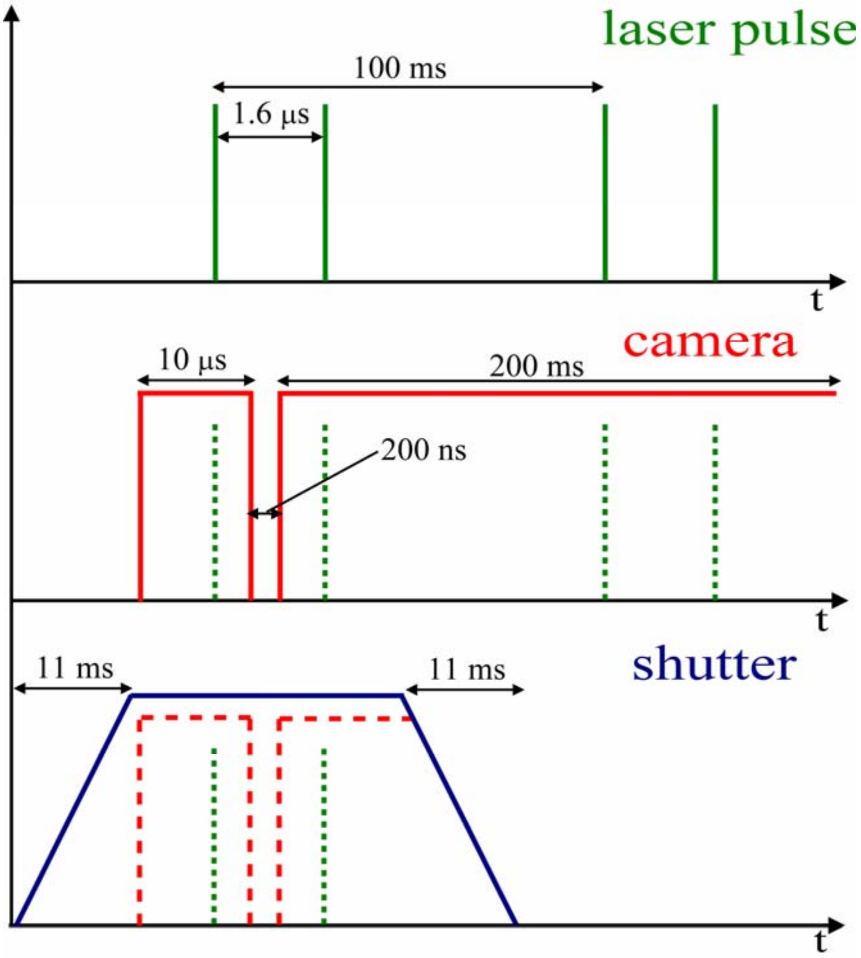

Figure 7.12 *The synchronization scheme for the laser (green), camera (red) and the mechanical shutter (blue).*

The exposure time of the camera is shown in red in figure 7.12. The camera was triggered to capture images whilst operating in dual-frame mode. In this mode, an initial frame with an exposure time of 10 μs was recorded and the data stored within the sensor. After a duration of 200 ns, a second frame is recorded and the two frames are read out to the computer simultaneously. This mode therefore allows pairs of images to be captured with a short separation between them.

The requirement to read out the dual-frame images to the computer simultaneously means that there is a fixed exposure time of 200 ms for the second frame. A Melles-Griot mechanical shutter was placed in front of the camera. The timing of the shutter is shown in blue in figure 7.12. The shutter was used to prevent multiple pulses being recorded by the second camera frame. The shutter takes approximately 11 ms to fully open. It is therefore important to trigger the shutter at least 11 ms before the camera in order to capture the image from the first pulse.

To capture images from the two pulses on the two frames of the camera, the delay on the shutter trigger was adjusted so that a pulse was seen only on the first camera frame. The delay on the camera trigger was then adjusted so that the second pulse falls on the second frame, with the first pulse remaining on the first frame.

]

7.2.4 Measurements from vibrating test object

Correlation fringe patterns were obtained from sequential subtraction of speckle patterns recorded with the two closely spaced laser pulses. The speaker cone was driven by a sinusoidal signal generated by the function generator with a range of frequencies from approximately 1- 5 kHz. Figure 7.13 shows a series of correlation fringe patterns recorded with vibrational frequencies of 1.9 kHz, 2.5 kHz, 3.9 kHz and 4.5 kHz. The images were recorded with a field of view of approximately 5 cm^2 and a shear of approximately 8 mm applied in the *x*-direction.

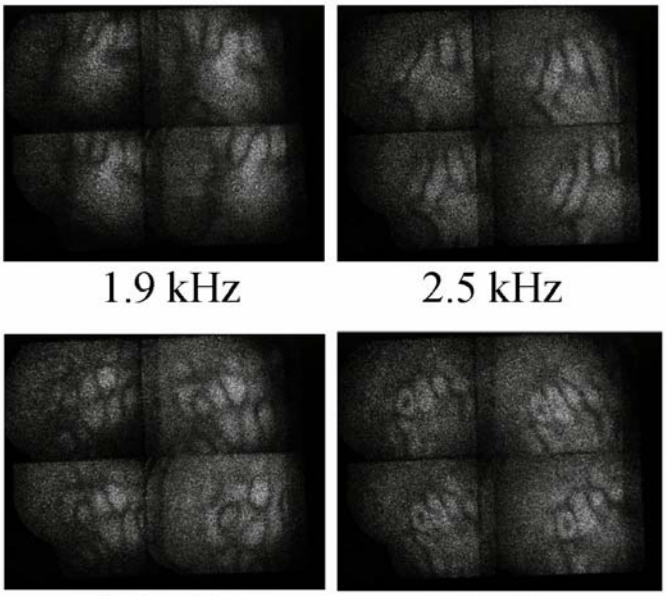

1.9 kHz 2.5 kHz

3.9 kHz 4.5 kHz

Figure 7.13 *Correlation fringes obtained through sequential subtraction of speckle patterns recorded from dual laser pulses with the dual-frame camera. The images were obtained with the speaker cone vibrating at frequencies of 1.9 kHz, 2.5 kHz, 3.9 kHz and 4.5 kHz.*

The Mach-Zehnder shearing interferometer was used to acquire carrier fringe patterns from the dual-pulsed illumination. Wrapped phase maps were calculated from the carrier fringe patterns using the subtraction technique described in section 3.3.2. Figure 7.14 shows wrapped phase maps calculated using the spatial carrier technique with the speaker vibrating at frequencies of 1.9 kHz, 2.5 kHz, 3.9 kHz and 4.5 kHz. Because the separation of the laser pulses is very short, the displacement of the speaker's surface between the pulses is small. This results in the low density of the 2π fringes seen in the wrapped phase maps. The areas were the phase values do exceed 2π can be seen in the black and white regions in figure 7.14. The positions of the features observed within the wrapped phase maps correspond with positions of the features seen in the correlation fringe patterns in figure 7.13.

The speaker cone used in this investigation was non-planar, unlike the other test objects presented in this thesis. An accurate determination of the vibration induced surface strain of the speaker therefore cannot be made without a correction for the objects shape. The orthogonal displacement derivatives were therefore not calculated for this object. This issue is discussed further in section 8.2.1.

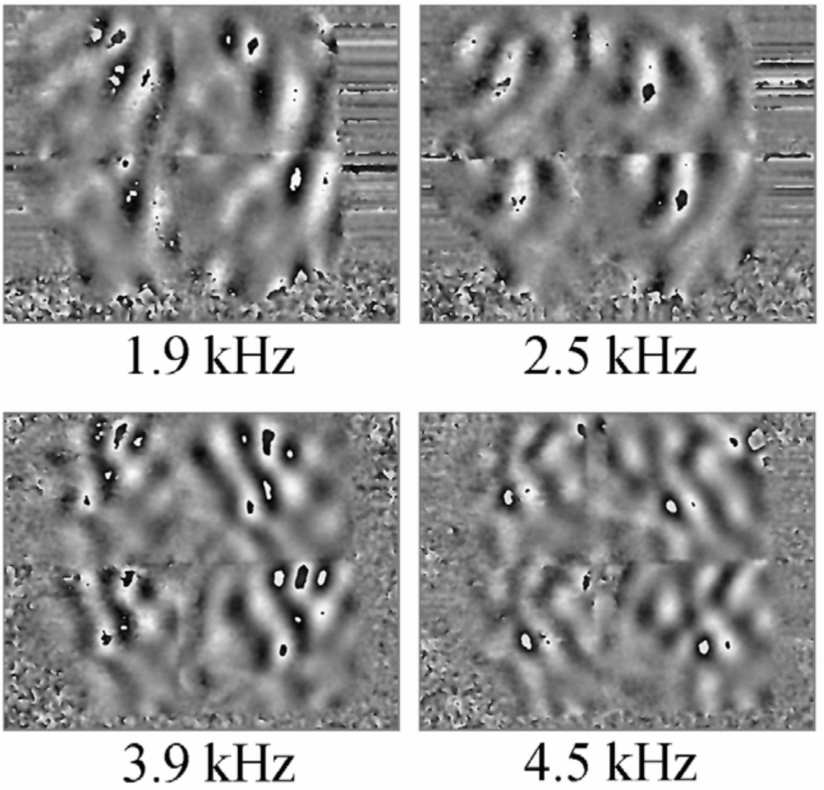

1.9 kHz

2.5 kHz

3.9 kHz

4.5 kHz

Figure 7.14 *Wrapped phase maps obtained using the spatial carrier technique with carrier fringe patterns recorded from dual laser pulses with the dual-frame camera. The images were obtained with the speaker cone vibrating at frequencies of 1.9 kHz, 2.5 kHz, 3.9 kHz and 4.5 kHz.*

7.3 Summary

In this chapter, the measurements made using the multiple-viewing-direction, pulsed laser shearography system from dynamic test objects have been presented. The first test object was a flat PTFE plate with an aluminium disk embedded in the rear of the plate. The object was secured to a lathe and set to rotate at a speed of 610 rpm. A signal from the lathe was used to trigger the laser and the CCD camera. The object was thermally loaded and allowed to cool as it rotated. Images were recorded with the object located at the same position but on separate revolutions. The spatial carrier technique was used to determine the phase distribution from the recorded images. A matrix transformation was then used to determine the orthogonal displacement gradient components using the unwrapped phase maps from each measurement channel. An out-of-plane strain variation was observed around the periphery of the aluminium disk embedded in the plate.

The second object that was investigated was a speaker cone that was driven by a sinusoidal signal at frequencies between 1.9 kHz and 4.5 kHz. Dual-pulses separated by 1.6 μs illuminated the object at two points in its vibrational cycle. Images from the two pulses were recorded on separate frames of a dual-frame CCD camera. Sequential subtraction of images from the two pulses resulted in correlation fringe patterns. The phase variation induced by the vibrational displacement was determined using the spatial carrier technique.

References

[1] Swain R. and Preater R, 'Investigation of windage heating effects on rotating components using pulsed ESPI', *Opt. Lasers Eng.* **26**, 377-94 (1997).

[2] Pérez-López C, Mendoza-Santoyo F. and Guerrero J. A, 'Decoupling the *x*, *y* and *z* displacement components in a rotating disc using three-dimensional pulsed digital holography', *Meas. Sci. Technol.* **14**, 97-100 (2003).

[3] RS Components, Mechanical Products and Tools: Catalogue volume 3, Northamptonshire (2007).

[4] http://en.wikipedia.org/wiki/Thermal_expansion_coefficient.

[5] McCoy D, Photonics Solutions, 40 Captains Road, Edinburgh, www.psplc.com, private communication.

[6] Atcha H. and Tatam R. P, 'Heterodyning of fibre optic electronic speckle pattern interferometers using laser diode wavelength modulation', *Meas. Sci. Technol.* **5**, 704-9 (2004).

8. Conclusions and future work

This thesis has presented the development of a novel multi-component, pulsed laser shearography system capable of making quantitative surface strain measurements of dynamic objects. This chapter summarizes the conclusions of the work presented in the previous chapters and suggests some possibilities for future work.

8.1 Summary of work presented in this thesis

In order to measure surface strain from dynamic test objects, a novel shearography instrument was developed. The novelty of the instrument lies in the fact that the multiple measurement channels required for quantitative measurement are made up of four observation directions and a single illumination direction and the use of fibre-optic imaging bundles to transport images from the four views to the shearing interferometer. Spatial multiplexing of the images onto the four quadrants of a CCD camera allows for simultaneous acquisition of data from the four measurement channels and thus, for the first time, quantitative surface strain measurement of dynamic objects can be made using shearography. The use of a pulsed Nd:YAG laser allows for the monitoring of dynamic test objects by effectively freezing the motion of the object for the duration of the laser pulse. The laser is also capable of dual-pulse emission with short separation between the pulses, which allows for the measurement of high speed deformations, such as objects vibrating at frequencies of the order of kilohertz.

A crucial step in making quantitative measurements using shearography is the determination of the phase variation across the field of view. A number of methods exist for calculating the phase from images recorded before and after deformation of the object. The most commonly used technique is temporal phase stepping. This method is convenient, easy to implement and provides good quality phase measurements. The method involves recording a series of images with a relative phase shift between them sequentially, before and after object deformation, and combining them using a phase stepping algorithm.

Measurements of dynamic objects made using pulsed laser speckle interferometry are made by combining images recorded from two pulses at two separate points in time. Temporal phase stepping is therefore unsuitable for dynamic measurements due to the requirement to record a series of at least four images. One of the main challenges of the work presented in this thesis was to implement a phase analysis procedure that requires only two images.

A number of solutions were investigated in chapter 5. One technique that is suitable for dynamic measurement is spatial phase stepping. This technique involves recording the images necessary for phase stepping simultaneously. One way to achieve this is to use a diffractive optical element (DOE) to divide the image into four and apply a relative phase shift to each of the diffracted images. The phase shifted images can then be recorded simultaneously on a single camera frame. In this multiple-viewing-direction shearography system, images from the four views are already recorded on a single camera frame. The use of this technique would therefore require the simultaneous recording of sixteen images. Each individual image would therefore be sampled by a relatively low number of pixels. Investigations of a DOE using a Michelson interferometer revealed that only fringe densities less than about 1 or 2 fringes per image could be observed with the camera that was available.

An alternative method that requires a minimum of two images is the spatial carrier technique. This method involves introducing a carrier frequency into the recorded image so that the desired phase information is spatially separated from the DC term in frequency space. The phase dependent spectral features can be accessed using a Fourier transform. The phase can be calculated from the inverse Fourier transform of the isolated spectral feature. One method of generating a carrier frequency that was investigated was to translate the illuminating lens along the optical axis in between the recording of the reference and signal frames. However, because of the limited spatial resolution of the camera, it proved to be difficult to generate a high enough carrier frequency to effectively separate the spectral features in frequency space.

Another carrier fringe method that was investigated was to apply a tilt between the beams propagating through the two arms of a Mach-Zehnder interferometer. This introduces a phase difference between the beams that varies linearly across the wavefront. A high frequency carrier fringe pattern was observed across the recorded images provided that the speckle size was large enough. The speckle size was increased by decreasing the aperture of an iris placed at the input of the interferometer. This method was deemed to be the most effective of the techniques investigated and was therefore used for the dynamic measurements presented in chapter 7.

The remaining steps in the processing to obtain quantitative measurements were described in chapter 6. Since each of the camera lenses views the object at an angle, errors due to perspective distortion are introduced into the measurements made from the recorded images. To correct for this, an image dewarping algorithm was used. This algorithm was also used to ensure pixel registration. The displacement gradient measurements obtained with the system are dependent on the sensitivity vector of each of the measurement channels. The sensitivity vector is defined as the bisector of the observation and illumination vectors. A calculation of the sensitivity vector at each pixel location in the images from the four views was required since the sensitivity vector varies across the field of view. In chapter 6, two methods of determining the sensitivity vector were presented. The first involved a calculation based on measurements of the observation and illumination positions relative to the point on the surface of the object at the centre of the field of view. The second technique, originally developed for full-field flow measurement, determines the observation vector at each pixel using the mapping functions generated during the dewarping process.

Quantitative surface strain measurements were made using the system from two test objects under static loading conditions. Since the loading was static, phase analysis could be performed using temporal phase stepping. The orthogonal displacement gradient components (two in-plane and one out-of-plane) were determined from a matrix transformation using the unwrapped phase maps and the sensitivity vector measurements. Measurements with shear applied in orthogonal directions were made sequentially. Displacement gradient measurements over a field of view of 35 x 30 mm^2 were made from a flat aluminium plate subjected to a central out-of-plane load. A strain variation of ±80 μm/m was observed in the out-of-plane displacement gradient components, which was greater than the in-plane components as expected considering the nature of the loading. The distribution of displacement gradient across the field of view was of a similar form to the results obtained using simulated phase maps. Displacement gradient measurements were also made from a flat perspex plate which showed both in-plane and out-of-plane strain. The strain variation across the field of view was approximately ±70 μm/m. The strain distributions across the field of view were similar to previous measurements made using a multiple-illumination-direction shearography system.

Measurements made from the flat aluminium plate were repeated using the spatial carrier technique. The density of fringes was discovered to vary for images from different measurement channels. This was believed to be due to a variation in the shear magnitude across the image introduced because of the tilt within the Mach-Zehnder interferometer. The variation in shear was across the composite image recorded by the camera and resulted in different sensitivities for each individual measurement channel. A measurement of the shear magnitude across the image was performed using an image cross-correlation technique. These measurements were then used in the displacement gradient calculation.

Measurements from two dynamic test objects were presented in chapter 7. The first object was a flat PTFE plate with an aluminium disk embedded in the rear of the plate. This object was mounted on a lathe and set to rotate at a speed of 610 rpm. The object was thermally loaded and allowed to cool. Phase maps were calculated from carrier fringe patterns recorded with the object in the same position but on subsequent revolutions. The orthogonal displacement gradient components were calculated from the unwrapped phase maps, sensitivity vector measurements and measurements of the applied shear across the image. A strain variation ranging from approximately -20 to +40 μm/m was observed around the periphery of the aluminium disk. This value corresponds approximately with a calculation based on the thermal expansion coefficients of aluminium and PTFE for a temperature change of 0.5°C between signal and reference frames.

The second object was a speaker cone that was made to vibrate through the application of a sine-wave signal produced by a function generator. The vibrational frequencies used were in the range of 1.9 – 4.5 kHz. The object was analysed with dual laser pulses separated by 1.6 μs. Images were recorded from the two pulses on separate frames of a dual framing camera. Sequential subtraction of speckle patterns recorded from the vibrating object yielded correlation fringe patterns were the fringes represent regions where the vibration induced displacement gradient is equal. The phase variation introduced by the vibrating surface between the two pulses was analysed using the spatial carrier technique.

The displacement gradient measurements presented in this thesis have shown variations ranging from approximately ±20 μm/m to ±80 μm/m. Further experiments are required to determine the range of strain measurement that is achievable with the system and resolution limit of the system. The rotation rates of objects measured using the method of recording images on separate rotations are at present limited by the fixed repetition rate of the laser. Measurements at different rotation rates could also be measured using the dual-pulse technique but would require sufficient loading such that a measurable deformation occurs in the time between recording the two images. This could be achieved if the object was vibrating and rotating simultaneously. If the dual-pulse method were to be used with rotation speeds greater than approximately 1500 rpm, the second image of the object would be displaced by at least one pixel relative to the first. The second image would therefore need to be translated back to the position of the first image before subtraction. This could be done in software using algorithms from digital speckle photography to determine the required shift.

8.2 Conclusions

The key points to arise from this work are as follows:

- Multi-component shearography using multiple-observation-directions is a suitable technique for surface strain measurement. Results from statically loaded test objects made with temporal phase stepping compare well to results made previously with a multiple-illumination-direction configuration.
- The spatial carrier technique within a Mach-Zehnder shearing interferometer is an effective phase analysis technique for the analysis of dynamic objects and requires no additional expensive components.
- To monitor high speed transient events, dual-pulsed illumination is required with a short duration between laser pulses. This instrument has shown that it is capable of operating under these conditions.

8.3 Future work

This section presents some ideas for future development of the multiple-viewing-direction system.

8.3.1 Surface strain measurement from non-planar objects

The work presented in this thesis involved the development and validation of the multiple-viewing-direction pulsed laser shearography. The next step in the development of the system would be to apply it to the dynamic measurement of surface strain of an actual component, for example, a helicopter rotor head or a gas turbine compressor blade.

All of the test objects presented in this thesis were planar, with the exception of the speaker cone discussed in section 7.2. Many components used in engineering are non-planar and accurate measurement of the surface strain from these components requires an additional correction for the shape of the object. Some techniques for making full-field shape measurements using speckle interferometry were discussed in section 2.5. An alternative technique that is relatively easy to apply and requires only a simple optical set up is fringe projection [1], shown in figure 8.1. This technique has previously been used with multi-component ESPI for the purpose of shape correction of strain measurements from non-planar objects [2].

The principle of shape measurement using fringe projection is as follows. First, a fringe pattern generated by, for example, a Wollaston prism or a Michelson interferometer, is projected onto a flat reference surface, Σ_1 that is placed in the in the observation plane of the camera and the fringe pattern is recorded. The reference surface is then replaced by the test object with a non-planar surface, Σ_2 and a second fringe pattern is recorded. The phase of the fringe patterns from Σ_1 and Σ_2 can be calculated using the Fourier transform technique. The resulting wrapped phase maps are subtracted and the result is unwrapped. The shape measurement can be obtained from the unwrapped phase, the sensitivity vector and the spacing of the projected fringes.

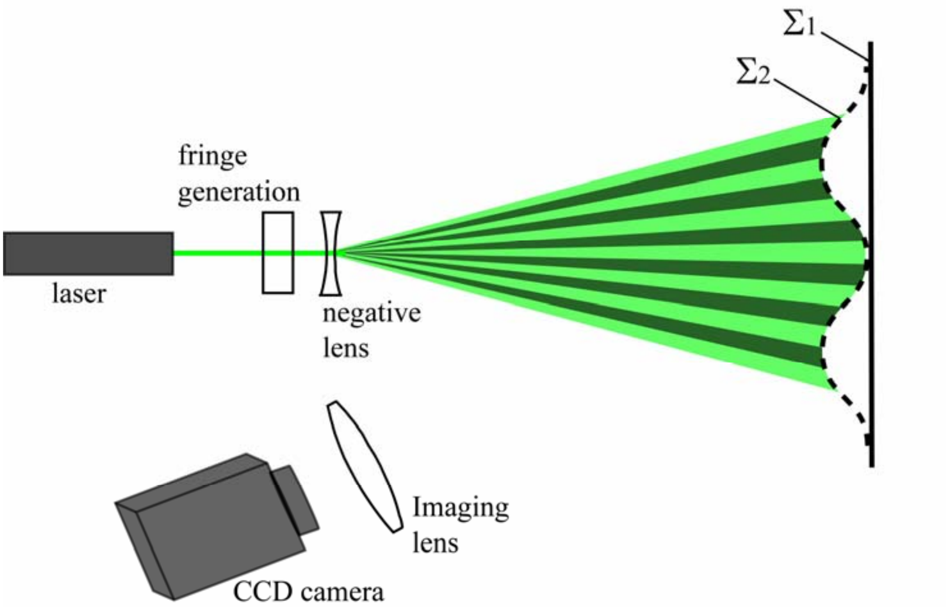

Figure 8.1 *Arrangement for measuring object shape with fringe projection.*

This technique could easily be incorporated into the multiple-viewing-direction shearography system by introducing a Wollaston prism or a Michelson interferometer in the beam path before the negative lens. The fringe pattern would be projected onto the object under investigation and the fringe pattern viewed by each of the camera lenses. A shape measurement could be made from each of the images recorded from the four camera lenses. The shape measurements made in this way would require image dewarping because of the off-axis viewing of each of the camera lenses.

Another measurement application for the system could be internal measurements, for example, inside engines. This could be achieved by fitting boroscopes to the ends of each of the fibre bundles, as shown in figure 8.2. Difficulties with performing image dewarping may make multi-component measurements difficult to achieve, but the system could still be used with a single measurement channel for the purpose of qualitative inspection.

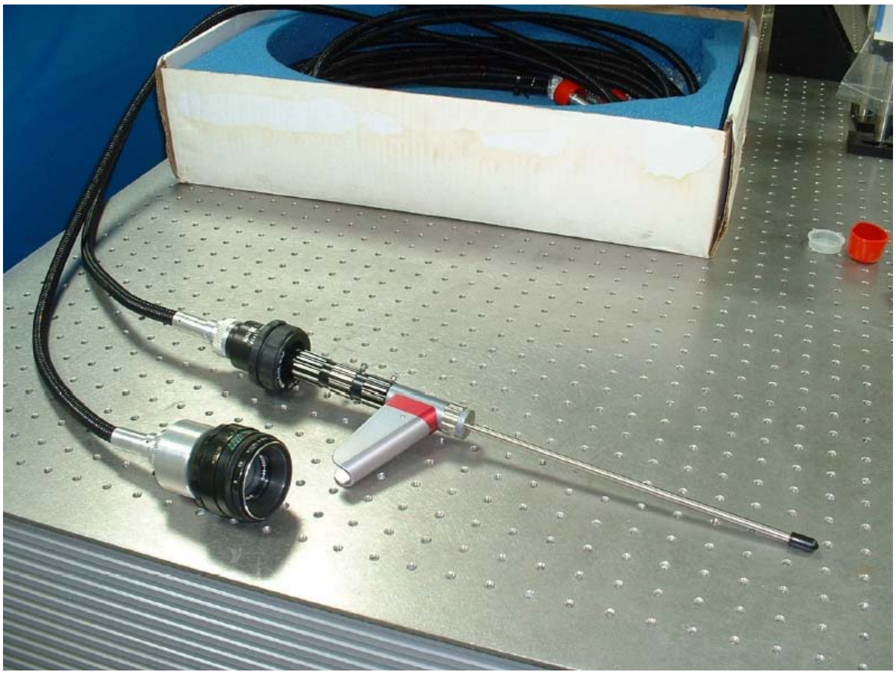

Figure 8.2 *Photograph showing fibre bundles coupled to an SLR camera lens and a boroscope.*

8.3.2 Combined ESPI and shearography

A multiple-viewing-direction ESPI system could be developed using the existing viewing configuration. This could be added to the existing shearography system so that simultaneous ESPI and shearography measurements could be made. Figure 8.3 shows a suggested configuration for a combined ESPI and shearography instrument. A small portion of the pulse energy needs to be split of from the main beam to form a reference beam for the ESPI system. This can be achieved, for example, by using a beamsplitter with a split ratio of 95:5. Light in the reference beam is coupled into a highly birefringent optical fibre, which is used to deliver the reference light to the ESPI head whilst preserving its polarization state. The remaining pulse energy is delivered to the target by a laser delivery arm. The scattered light is imaged by the camera lenses and transported to the ESPI and shearography imaging heads using fibre optic imaging bundles. A beamsplitter located at the distal end of the fibre bundles is used to split the received light and direct a proportion of the light towards the ESPI and shearography heads.

ESPI is directly sensitive to displacement of the surface under investigation. The results of ESPI measurements of vibrating surfaces are therefore easier to interpret than shearography vibration measurements because the fringes represent regions of the surface that experience equal displacement due to the vibration. ESPI correlation fringes are also typically of higher contrast than shearography correlation fringes. Phase analysis within the ESPI system can be performed using the spatial carrier technique. Carrier fringes can be generated by tilting the reference fibre at a slight angle so that a phase variation is introduced across the CCD detector [3].

One of the main issues with the proposed ESPI system is the polarization of the interfering beams. The highest fringe contrast is obtained when the polarization states of the beams are matched, with fringe contrast decreasing as we move further from this condition. With the proposed ESPI system, the fibre bundles form part of one of the interferometer arms. The effect of the fibres on the polarization state of light propagating through them is at present unknown, and was not needed for the shearography measurements reported within this thesis. Measurements of the effect of the bundles on the polarization state therefore need to be made in order to determine if this ESPI system can be developed.

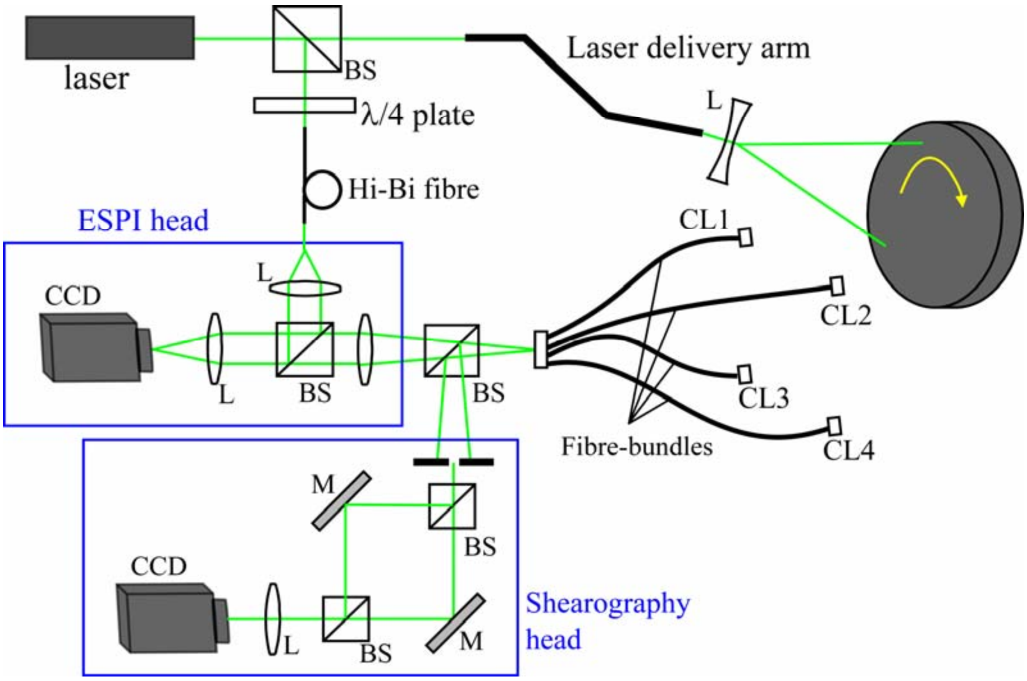

Figure 8.3 *A suggested arrangement for a combined ESPI and shearography instrument. BS = beamsplitter, L = lens, CL1 – 4 = camera lenses 1 – 4, M = mirror.*

8.3.3 Improvements in signal processing

The spatial carrier technique within a Mach-Zehnder shearing interferometer has proved to be an effective method of phase determination when making dynamic measurements. One of the issues with the method, however, is that the small iris aperture located at the input of the interferometer reduces the available light, meaning that high illumination intensities are required to use the technique effectively. This could prove to be a problem if a comparatively low power source were to be used.

A potential solution if available light levels are comparatively low could be to determine the phase from a single correlation fringe pattern. This would mean that the iris at the input of the interferometer is no longer necessary since large speckles would no longer be necessary. A number of techniques are available for determining the phase from a single fringe pattern. Two examples of single fringe pattern demodulation schemes are the regularized phase tracking (RPT) technique and the frequency guided sequential demodulation (FSD), which were described briefly in section 3.5.3. One of the problems with these techniques is that a lot of pre-processing is required to reduce the speckle noise to a sufficient level.

Another way to potentially improve the phase analysis would be to implement the DOE based spatial phase stepping technique with a camera with larger format CCD. The LaVision camera has a chip size of 1024 x 1280 pixels, but cameras with chip sizes of 4000 x 4000 pixels are not uncommon these days. Each of the individual images from the four views within the images recorded using the DOE in section 5.2.2 was sampled by approximately 50 x 50 pixels. This was found to be insufficient to effectively record images with fringe densities higher than 1 or 2 fringes across the field of view. This could be improved by using a camera with more pixels. The number of pixels per image could also be increased by using a DOE and imaging optics that makes better use of the available space on the CCD chip. In the results presented in figure 5.10 a lot of the available image space is wasted. Using a DOE where the ±1 diffracted orders are located in the four corners of the image plane would improve the situation. Also, the number of fringes per image for a particular deformation could be reduced by reducing the magnitude of the applied shear.

Another issue with the spatial phase stepping technique was that the large working distance required to effectively separate the diffracted orders in the image plane meant that only a small proportion of the available light was collected by the imaging lens. This situation could be improved by using a DOE with a greater divergence angle. The DOE used in section 5.2 had a divergence angle of 0.3° but DOEs with divergence angles of 1° and possibly higher are commercially available [4].

The orthogonal displacement gradient components were calculated from data from just three of the measurement channels, with data from the fourth channel being discarded. A four component calculation of orthogonal flow velocity using data from four measurement channels of PDV system has been utilized previously [5] and showed improved results over those obtained with the three component calculation.

The use of digital image correlation to calculate the shear magnitude across the composite image was an effective technique; however the results were somewhat pixellated due to the finite size of the correlation window. One technique that might provide results with a higher spatial resolution could be to compare the dewarping coefficients obtained with one of the interferometer mirrors blocked with those obtained with the other mirror blocked. This method could potentially provide a measurement of the image shear at each pixel in the CCD array.

8.4 Summary

A novel multiple-viewing-direction pulsed laser shearography system has been presented that is, for the first time, capable of quantitative surface strain measurement of dynamic objects. Surface strain measurement is made possible by the use of multiple measurement channels comprised of a single illumination direction and four observation directions. The instrument has been validated by measurements of static test objects, the results of which were compared to a numerical model and previous results obtained with a multiple-illumination-direction shearography system. In addition, measurements were made on an object rotating at 610 rpm and a speaker cone vibrating at frequencies from 1.9 kHz to 4.5 kHz.

The future directions that the system could take could be to measure dynamic, non-planar objects. For this, a correction for the object's shape is required. A suggested method for measuring the shape of an object is fringe projection. Another development that could be made is to combine the instrument with a multi-component ESPI system, which could lead to improved results for measurements of vibrating objects.

References

[1] Hung Y. Y, Lin L, Shang H. M, Park B. G, 'Practical three-dimensional computer vision techniques for full-field surface measurement', *Opt. Eng.* **39**:1, 143-9 (2000).
[2] Yang L. and Ettemeyer A, 'Strain measurement by three-dimensional electronic speckle pattern interferometry: potentials, limitations and applications', *Opt. Eng.* **42**:5, 1257-66 (2003).
[3] Fricke-Begemann T. and Burke J, 'Speckle interferometry: three-dimensional deformation field measurement with a single interferogram', *Appl. Opt.* **37**:19, 4116-22 (2001).
[4] SILIOS Technologies, Z. I. Peynier-Rousset, Rue Gaston Imbert prolongée, 13 790 Peynier, France. Web www.silios.com.
[5] Charrett T, 'Development of two-frequency planar Doppler velocimetry instrumentation', *PhD Thesis*, Cranfield University, Bedfordshire (2006).

List of Publications

Journal Publications

Francis D, James S. W. and Tatam R. P, ‘Surface strain measurement of rotating objects using pulsed laser shearography with coherent fibre-optic imaging bundles’, Submitted to *Meas. Sci. Technol.* (2008).

Francis D, James S. W. and Tatam R. P, ‘Surface strain measurement using multi-component shearography with fibre-optic imaging bundles’, *Meas. Sci. Technol.* **18**, 3583-91 (2007).

Conference Publications

Francis D, James S. W. and Tatam R. P, ‘Development of a multi-component shearography instrument for surface strain measurement on dynamic objects, *Interferometry XIV*, San Diego, USA (2008) [Accepted]. To be published in SPIE proceedings.

Francis D, James S. W. and Tatam R. P, ‘Surface strain measurement of rotating objects using shearography instrumentation based on fibre-optic imaging bundles’, *19th Conference on Optical Fibre Sensors [OFS-19]*, Perth, Australia (2008). *Proc. SPIE*, **7004**, 7004-259 (2008).

Francis D, James S. W. and Tatam R. P, ‘Surface strain measurement using multi-component shearography with fibre-optic imaging bundles’, *Optical Metrology*, Munich, Germany (2007). *Proc. SPIE*, **6616**, 6616-2S(1-10) (2007).

Francis D, James S. W. and Tatam R. P, ‘Comparison of multiple-viewing-direction shearography with multiple-illumination-direction shearography’, *Photon ’06*, Manchester, UK (2006) published in proceedings

Appendix A: Matlab for fringe pattern simulation

This appendix describes the use of Matlab in the generation of simulated fringe patterns used for figure 3.5 and figure 3.8.

A.1 Simulation of the Takeda method (figure 3.5)

First, a phase distribution was synthesized by generating a two-dimensional Gaussian derivative distribution using the equation

$$\phi(x,y) = -x \cdot \exp\left(2\left(-x^2 - y^2\right)\right) \qquad \text{(A.1)}$$

This can be done in Matlab using the code

```
for i = 1:512;                    % Phase distribution
    for j = 1:512;                % phi = -x*exp(2(-x^2 - y^2)) %
         phi(i,j) = (-(j-256)/256)*exp(2*(-((j-256)/256).^2 ...
                    -((i-256)/256).^2));
    end
end
```

for a 512x512 image. This was quick to execute and was therefore not deemed essential to vectorize the code. A greyscale map of the phase distribution produced using this code is shown in figure A.1(a). The phase distribution was then normalized between the limits of +1 and -1 and then multiplied by a factor which determines the final fringe density of the wrapped phase map. In Matlab this was done using

```
phi = phi + abs(min(min(phi)));
phi = phi*(2*phi/max(max(phi)) - 1);
phi = 12*pi*phi;
```

The carrier fringe pattern (figure A.1(b)) was produced using

```
cfreq = 50;
n = cfreq*(1/512);
for i = 1:512;
    for j = 1:512;
        Ic(i,j) = sin(2*pi*n*j);
    end
end
```

The carrier fringe pattern and the phase distribution were combined using

```
for i = 1:512;
    for j = 1:512;
        Im(i,j) = sin(2*pi*n*j + phi1(i,j));
    end
end
```

Random noise was added to the phase modulated carrier fringe pattern (figure A.1(c)) using

```
Im1 = Im + 2*rand(size(Im));
```

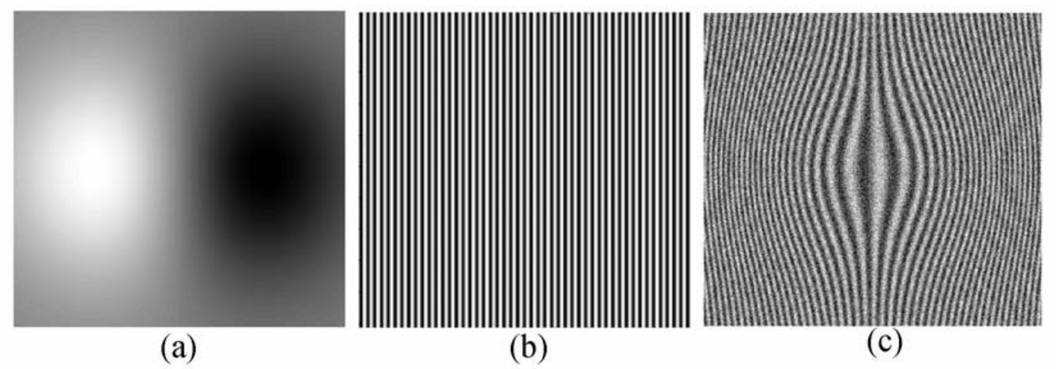

Figure A.1 *Simulated phase distribution (a), carrier fringes (b) and phase modulated carrier fringe pattern with added random noise.*

The Fourier transform of the phase modulated fringe pattern shown in figure A.1(c) was calculated and the side band isolated using

```
f = fftshift(fft2(Im1));
f(257,257) = 0;
f1 = f(221:291,260:330);
```

The fftshift() function serves to shift the spectral components to the centre of the image. An empty 512x512 array was produced and the isolated side band was placed at the centre of the empty array

```
tc = zeros(512,512);
tc(221:291,220:290) = f1;
```

The inverse Fourier transform was then calculated and wrapped phase determined using

```
rc = ifft2(fftshift(tc));
rc1 = 2*angle(rc);
```

A.2 Curved carrier fringes and the subtraction method (figure 3.8)

This describes the method used to produce the images shown figure 3.8. Curved carrier fringes were to illustrate the ability of this technique to successfully demodulate the phase independent of the fringe curvature.

The size of the image was chosen to be 512x512 pixels and carrier fringes are produced using the equation

$$I\left(x,y\right)=\sin\left(2\pi x^2+2\pi y^2\right) \qquad \text{(A.2)}$$

where

$$x = \frac{(256 - i)}{256} \qquad \text{and} \qquad y = \frac{(256 - j)}{256} \tag{A.3}$$

where i and j are the pixel coordinates in the x and y direction respectively. The result is a series of concentric rings with decreasing period and increasing radius of curvature away from the centre. Choosing the numerator of equations (A.3) to be 256 results in the rings being centred in the middle of the image, as shown in figure A.2(a). If we choose a value other than 256 in the numerator of one of the above equations then the centre of the image moves away from the centre of the ring pattern, either left or right if the x equation is changed or up or down if the y equation is changed. A value of 1500 was arbitrarily chosen to give a high enough frequency of ring fringes with large radii of curvature. These fringes form the reference curved carrier fringe pattern for the example and are shown in figure A.2(b).

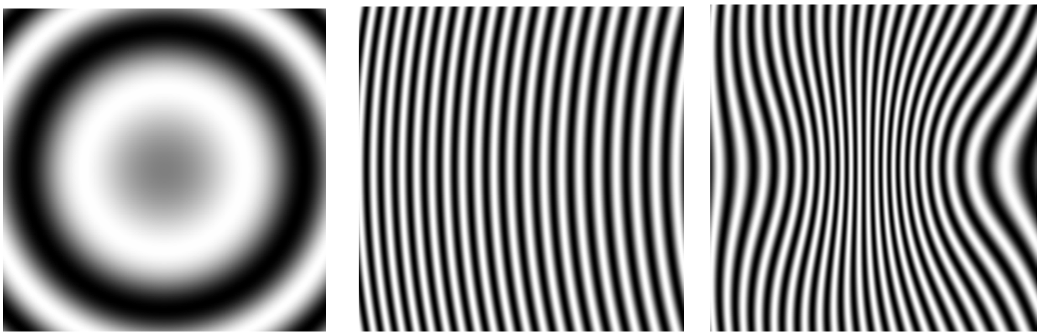

(a) **(b)** **(c)**

Figure A.2 *Image centered on the concentric ring fringes produced by equation (A.3) (a) and the image centered a distance to the left of the centre of the concentric fringes (b). Combining the fringes shown in (b) with the phase distribution shown in figure A.1(a) results in the phase modulated carrier fringe pattern shown in (c).*

The fringes shown in figure A.2(b) were combined with the phase distribution shown in figure A.1(a) to produce the phase modulated carrier fringe pattern shown in figure A.2(c). Random noise was then added to the reference carrier fringe pattern and the phase modulated carrier fringe pattern using the same code as before. The Fourier transform of the two fringe patterns was calculated and the side feature of each was isolated. The phase from each was calculated independently and the phase difference was calculated by subtracting the two.